

A Thesis Submitted for the Degree of PhD at the University of Warwick

Permanent WRAP URL:

<http://wrap.warwick.ac.uk/165007>

Copyright and reuse:

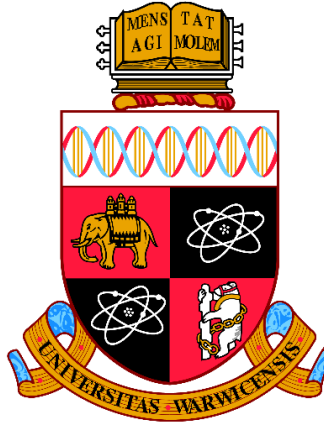
This thesis is made available online and is protected by original copyright.

Please scroll down to view the document itself.

Please refer to the repository record for this item for information to help you to cite it.

Our policy information is available from the repository home page.

For more information, please contact the WRAP Team at: wrap@warwick.ac.uk



Investigations of fast quality prediction and rivet/die optimization for self-piercing riveting joints

by

Huan Zhao

A thesis submitted in partial fulfilment of the requirements for
the degree of

Doctor of Philosophy in Engineering

School of Engineering, University of Warwick

September 2021

THE UNIVERSITY OF
WARWICK

Contents

Contents	i
List of Figures.....	v
List of Tables	xii
Acknowledgements	xiii
Declarations	xiv
Publications	xv
Abstract.....	xvi
Nomenclature	xvii
Abbreviations	xx
1. Introduction.....	1
1.1. Background	1
1.1.1. Lightweight design of automobiles	1
1.1.2. Self-piercing riveting (SPR) technique	3
1.2. Existing challenges and research objectives	7
1.2.1. Existing challenges	7
1.2.2. Research objectives	9
1.3. Thesis outline	11
2. Literature review	13
2.1. Joining parameters affecting SPR joint quality.....	13
2.1.1. Critical sheet parameters	14
2.1.2. Critical rivet parameters	23
2.1.3. Critical die parameters	29
2.1.4. Other critical setting parameters	35
2.2. Quality prediction models of SPR joints.....	36
2.2.1. FEA models	36
2.2.2. Mathematical prediction models	40

2.2.3. Artificial neural network (ANN) models	41
2.3. Optimization and selection approaches of SPR rivet/die combinations	43
2.3.1. Optimization strategies used in the welding field	43
2.3.2. Optimization approaches for other joining processes	44
2.4. Summary	44
3. Development and application of FEA model for the SPR process	46
3.1. Introduction.....	46
3.2. FEA model development	48
3.3. Validation of the FEA model.....	50
3.3.1. Effectiveness for the SPR joint quality prediction.....	50
3.3.2. Effectiveness for the joint formation prediction	53
3.4. Application of the FEA model on the analysis of SPR joint formation mechanism	56
3.4.1. Single factor experiments.....	56
3.4.2. Results and discussion	58
3.5. Summary	77
4. Quality prediction and interaction analysis for the SPR process with regression analysis.....	79
4.1. Introduction.....	79
4.2. Mathematical regression models for prediction of interlock and T_{\min}	81
4.2.1. Joint quality data collection	81
4.2.2. Analysis of variance.....	82
4.2.3. Development of the regression models	83
4.2.4. Evaluation of the regression models	84
4.2.5. Validation of the regression models.....	84
4.3. Interaction effects between rivet and die parameters on the interlock and T_{\min}	85
4.3.1. Between the rivet length (L_1) and die diameter (D_1).....	86
4.3.2. Between the rivet length (L_1) and die depth (H_1).....	89
4.3.3. Between the die diameter (D_1) and depth (H_1).....	91
4.4. Summary	93

5. Quality prediction and rivet/die parameters optimization for the SPR process with artificial neural network.....	94
5.1. Introduction.....	94
5.2. ANN models for SPR joint quality prediction	96
5.2.1. Joint quality data collection	96
5.2.2. ANN model architecture	97
5.2.3. Development of ANN for the interlock	98
5.2.4. Development of ANNs for the T_{cen} and T_{tip}	101
5.2.5. Validation of the ANN models	103
5.2.6. Graphical user interface (GUI)	105
5.3. Optimization of rivet and die parameters for a SPR joint.....	106
5.3.1. Optimization procedure.....	106
5.3.2. Optimization results	108
5.4. Interaction analysis between joining parameters	111
5.4.1. Interaction effects on the interlock.....	112
5.4.2. Interaction effects on the T_{cen} and T_{tip}	118
5.5. Summary	120
6. Auto-selection of rivet/die combinations for multiple SPR joints based on deep neural network	122
6.1. Introduction.....	122
6.2. DNN models for SPR joint quality prediction	124
6.2.1. Joint quality data collection	125
6.2.2. DNN architecture design.....	125
6.2.3. Establishment of SNNs and DNNs	126
6.2.4. Optimal network structure	130
6.2.5. Validation of the DNN model	136
6.3. Joint robustness evaluation	139
6.4. Auto-selection of rivet/die combinations for multiple SPR sheet combinations ..	144
6.4.1. Approach one	144
6.4.2. Approach two.....	150
6.4.3. Experimental validation	153

6.5. Summary	154
7. Conclusions and future work	156
7.1. Research conclusions	156
7.2. Future work	158
References	161

List of Figures

Figure 1.1 Exploded views of aluminium space frames and closures on (a) Audi A8 (D2) and (b) Audi A2 [15]	2
Figure 1.2 (a) Aluminium BIW of Jaguar XJ (X350) and (b) the corresponding material proportions [15]	2
Figure 1.3 (a) Aluminium BIW of Range Rover L405 and (b) the corresponding material proportions [15]	3
Figure 1.4 Schematic of the four major steps during the SPR process	4
Figure 1.5 Structures of SPR systems from (a) Henrob [18], (b) Böllhoff [19] and (c) Tucker [20]	4
Figure 1.6 Self-piercing rivets applied on the aluminium body of Jaguar XJ (X351) [15]	5
Figure 1.7 Joining techniques applied on the aluminium body structures of (a) Audi A8 (D2) and (b) Audi A2 [27].....	6
Figure 1.8 Schematic of the SPR joint cross-sectional profile and three quality evaluation indicators	6
Figure 1.9 Flow charts of (a) the general rivet/die selection process for a new SPR joint and (b) the faster selection process with a FEA model	8
Figure 1.10 Schematics of three approaches to simplify the selection of rivet/die for new SPR joints	10
Figure 2.1 Schematic of critical joining parameters affecting the SPR joint quality	14
Figure 2.2 Schematic of critical sheet parameters affecting the SPR joint quality	14
Figure 2.3 Cracks generated on the bottom sheet made of low ductility materials (a) AZ31B-H24 magnesium alloy sheets [51] and (b) AA7075-T6 aluminium alloy sheets [52]	15
Figure 2.4 Assistant technologies to improve the ductility of bottom sheet material (a) heating furnace [52], (b) induction coil [65], (c) direct current [66] and (d) laser [51].....	17
Figure 2.5 Experimentally tested joinability of (a) aluminium-steel sheets and (b) steel-aluminium sheets [11].....	19
Figure 2.6 Joinability of high strength steel sheet and aluminium alloy sheet (a) aluminum-SPFC440, (b) SPFC440-aluminium, (c) aluminum-SPFC590 and (d) SPFC590-aluminium [36]	19
Figure 2.7 Three types of defects generated in SPR joints with different sheet thicknesses (the t_u and t_l denote the top sheet thickness and the bottom sheet thickness) [11]	20
Figure 2.8 Force-displacement curve of 2.5 mm+2.5 mm carbon steel joint with rivet of 8 mm long and 555HV hardness [39].....	21
Figure 2.9 Failure modes of SPR joints with galvanized steel sheets (a) failure mode I, (b) failure mode II and (c) failure mode III [71]	22

Figure 2.10 Cross-sectional profiles of different rivets (a) a countersunk head semi-tubular rivet, (b) a pan head semi-tubular rivet, (c) a countersunk head solid rivet and (d) a countersunk tubular rivet [74]	24
Figure 2.11 Schematics of critical rivet factors affecting the SPR joint quality.....	24
Figure 2.12 Schematic of geometric parameters of the semi-tubular countersunk rivet	27
Figure 2.13 Different geometries of (a) rivets with varying rivet tip angles, leg lengths and inner diameters [83] and (b) rivets with a blunt or sharp tip [82]	28
Figure 2.14 Different geometries of (a) a new self-flaring rivet [86], (b) an inner flange pipe rivet [87] and (c) a double-side self-piercing rivet [89].....	29
Figure 2.15 Cross-sectional profiles of dies from published studies of (a) [91] , (b) [92], (c) [93], (d) [52], (e) [94], (f) [95], (g) [96], (h) [97] and (i) [35]	30
Figure 2.16 Schematics of the flat die and pip die parameters affecting the SPR joint quality.....	30
Figure 2.17 Cross-sectional profiles of the DF and DC dies employed by Li et al. [98].....	32
Figure 2.18 Relationship among the die diameter (D), depth of central die bottom (d) and the load for piercing middle sheet in 1.0 mm SPFC980+1.0 mm SPCC+2.5 mm A5052 SPR joints [43]....	34
Figure 2.19 Relationships between the joinability and tensile strength of top and middle steel sheets with an aluminium alloy bottom sheet using (a) a conventional die and (b) an optimized die [43]	34
Figure 2.20 Schematics of three specimen configurations for (a) lap shear test and (b) T-peel test [103]	36
Figure 3.1 Schematic of the SPR simulation model.....	48
Figure 3.2 Plastic stress-strain curves for (a) AA5754 (strain rate= 1 s^{-1}) [113] and (b) boron steel (strain rate= 0.01 s^{-1} and $20\text{ }^{\circ}\text{C}$).....	49
Figure 3.3 Cross-sectional profiles of the top sheet, the bottom sheet, the semi-tubular rivet and the pip die (in mm)	52
Figure 3.4 Specimens dimensions of the SPR joints (in mm)	52
Figure 3.5 Structure of the Tucker SPR system	52
Figure 3.6 Schematics of (a) specimen cutting position and (b) quality indicators measured on the joint cross-sectional profile.....	52
Figure 3.7 Comparisons of the joint cross-sectional profiles from the experimental tests and the FEA simulations.....	53
Figure 3.8 Comparisons of the experimentally tested and FEA simulated (a) interlock I and (b) T_{\min}	53
Figure 3.9 Dimensions of the (a) semi-tubular rivet and (b) pip die (Type-A) used in the interrupted tests (in mm)	54
Figure 3.10 Schematic of the four dimensions measured on the joint cross-sectional profile.....	55

Figure 3.11 Cross-sectional profiles of the joints 3-21~3-25 from (a) interrupted experimental tests and (b) FEA simulations.....	56
Figure 3.12 Comparisons between the experimentally tested and the simulated (a) deformed rivet shank diameter D_r , (b) remaining bottom sheet thickness at the joint centre T_{cen} and (c) interlock I in the joints 3-21~3-25	56
Figure 3.13 Dimensions of the pip die (Type-B) (in mm).....	57
Figure 3.14 Schematic of quality indicators measured on the joint cross-sectional profile	58
Figure 3.15 Comparisons between the experimentally tested and the simulated cross-sectional profiles of the SPR joints 3-26~3-36	59
Figure 3.16 Comparisons between the simulated and the experimentally tested (a) interlock I , (b) remaining bottom sheet thickness at the joint centre T_{cen} and (c) remaining bottom sheet thickness under the rivet tip T_{tip} in the joints 3-26~3-36	59
Figure 3.17 Comparisons between the simulated and the experimentally tested load-displacement curves of the joints 3-26~3-36.....	60
Figure 3.18 Experimentally tested cross-sectional profiles of the joints 3-26~3-29 with different top sheet thicknesses T_1 (a) 1.0 mm, (b) 1.2 mm, (c) 1.5 mm and (d) 2.0 mm	61
Figure 3.19 Experimentally tested and numerically simulated (a) interlock I , (b) D_{in} and D_{out} , (c) T_{cen} and (d) T_{tip} in the SPR joints 3-26~3-29	61
Figure 3.20 Numerically simulated cross-sectional profiles during riveting processes of the SPR joints 3-26~3-29 (a) $T_1=1.0$ mm, (b) $T_1=1.2$ mm, (c) $T_1=1.5$ mm and (d) $T_1=2.0$ mm	62
Figure 3.21 Numerically simulated (a) formation curves of the I and (b) formation curves of the two interlock boundaries during riveting processes of the joints 3-26~3-29	63
Figure 3.22 Simulated (a) variation curves of the deformed rivet shank diameter (D_r) and (b) load-displacement curves in the SPR joints 3-26~3-29 with different top sheet thicknesses T_1	64
Figure 3.23 Simulated variation curves of the T_{cen} with different top sheet thicknesses T_1	65
Figure 3.24 Equivalent stress distribution on the bottom sheet of the joint 3-26 ($T_1=1.0$ mm) (a) before and after top sheet separation and (b) before and after the rivet cavity fully filled	66
Figure 3.25 Experimentally tested cross-sectional profiles of the joints 3-30~3-33 with different bottom sheet thicknesses T_2 (a) 1.0 mm, (b) 1.5 mm, (c) 1.8 mm and (d) 2.0 mm	67
Figure 3.26 Experimentally tested and numerically simulated (a) I , (b) D_{in} and D_{out} , (c) T_{cen} and (d) T_{tip} in the SPR joints 3-30~3-33	67
Figure 3.27 Numerically simulated cross-sectional profiles during the riveting processes of the SPR joints 3-30~3-33 (a) $T_2=1.0$ mm, (b) $T_2=1.5$ mm, (c) $T_2=1.8$ mm and (d) $T_2=2.0$ mm	68
Figure 3.28 Numerically simulated (a) formation curves of the I and (b) formation curves of the two interlock boundaries during riveting processes of the joints 3-30~3-33	69

Figure 3.29 Simulated (a) variation curves of the deformed rivet shank diameter (D_r) and (b) load-displacement curves in the SPR joints 3-30~3-33 with different bottom sheet thicknesses T_2 ...	70
Figure 3.30 Simulated variation curves of the T_{cen} with different bottom sheet thicknesses T_2	70
Figure 3.31 Equivalent stress distribution on the bottom sheet of the joint 3-30 ($T_2=1.0$ mm).....	71
Figure 3.32 Equivalent plastic strain distribution on the bottom sheet of the (a) joint 3-30 and (b) joint 3-33.....	72
Figure 3.33 Tested cross-sectional profiles of the joints 3-34~3-36 with different rivet lengths L_1 (a) 5.0 mm, (b) 6.0 mm and (c) 6.5 mm	73
Figure 3.34 Experimentally tested and numerically simulated (a) I , (b) D_{in} and D_{out} , (c) T_{cen} and (d) T_{tip} in the SPR joints 3-34~3-36	73
Figure 3.35 Numerically simulated cross-sectional profiles during riveting processes of the SPR joints 3-34~3-36 (a) $L_1=5.0$ mm, (b) $L_1=6.0$ mm and (c) $L_1=6.5$ mm.....	74
Figure 3.36 Numerically simulated (a) formation curves of the I and (b) formation curves of the two interlock boundaries during riveting processes of the joints 3-34~3-36.....	75
Figure 3.37 Simulated (a) variation curves of the deformed rivet shank diameter (D_r) and (b) load-displacement curves in the SPR joints 3-34~3-36 with different rivet lengths L_1	75
Figure 3.38 Simulated variation curves of the T_{cen} with different rivet lengths L_1	76
Figure 4.1 Comparisons between the experimental values and the predicted values using the regression models (a) interlock and (b) T_{min}	85
Figure 4.2 Contour graphs of the (a) interlock and (b) T_{min} with different rivet lengths and die diameters (die depth $H_1=1.8$ mm)	87
Figure 4.3 Simulated joint cross-sectional profiles with different rivet lengths and die diameters (die depth $H_1=1.8$ mm)	87
Figure 4.4 Schematics of the (a) rivet volume V_r and (b) die cavity volume V_d	89
Figure 4.5 Joint cross-sectional profiles with (a) $V_d < V_r$ and (b) $V_d > V_r$ during the SPR processes ..	89
Figure 4.6 Contour graphs of the (a) interlock and (b) T_{min} with different rivet lengths and die depths (die diameter $D_1=9.0$ mm)	90
Figure 4.7 Simulated joint cross-sectional profiles with different rivet lengths and die depths (die diameter $D_1=9.0$ mm)	91
Figure 4.8 Contour graphs of the (a) interlock and (b) T_{min} with different die diameters and depths (rivet length $L_1=5.0$ mm).....	92
Figure 4.9 Simulated joint cross-sectional profiles with different die diameters and depths (rivet length $L_1=5.0$ mm).....	92
Figure 5.1 Six potential positions of the minimum remaining bottom sheet thickness (T_{min}) in SPR joints	97
Figure 5.2 Structure of the three-layer artificial neural network (ANN).....	98

Figure 5.3 The algorithm flow chart to select the optimal ANN model for the interlock	100
Figure 5.4 The performances of ANNs with different numbers of hidden layer neurons (N_h) for the interlock (a) MAE and (b) correlation coefficient (r)	100
Figure 5.5 Comparisons between the ANN predicted and the FEA simulated interlock values (a) training data and (b) testing data	101
Figure 5.6 The performances of ANNs with different numbers of hidden layer neurons (N_h) for the T_{cen} (a) MAE and (b) correlation coefficient (r)	102
Figure 5.7 Comparison between the ANN predicted and the FEA simulated T_{cen} values (a) training data and (b) testing data	102
Figure 5.8 The performances of ANNs with different numbers of hidden layer neurons (N_h) for the T_{tip} (a) MAE and (b) correlation coefficient (r)	102
Figure 5.9 Comparison between the ANN predicted and the FEA simulated T_{tip} values (a) training data and (b) testing data	103
Figure 5.10 Comparisons of the interlock from the experimental tests, the FEA simulation model and the ANN.....	105
Figure 5.11 Comparisons of the (a) T_{cen} and (b) T_{tip} from the experimental tests, the FEA model and the ANNs	105
Figure 5.12 The GUI for the SPR joint quality prediction	106
Figure 5.13 Flow chart to optimize the rivet and die with the ANNs and GA	107
Figure 5.14 Changing trends of the interlock, T_{cen} and T_{tip} with the optimized rivet and die (a) 1.0 mm+1.0 mm, (b) 1.0 mm+2.0 mm, (c) 1.5 mm+1.5 mm, (d) 2.0 mm+1.0 mm and (e) 2.0 mm+2.0 mm.....	110
Figure 5.15 Interaction plots of the five joining parameters on the (a) interlock, (b) T_{cen} and (c) T_{tip}	111
Figure 5.16 Contour graph of the interlock with varying bottom sheet thicknesses T_2 and die diameters D_1 ($T_1=1.2$ mm, $L_1=5.0$ mm, $H_1=2.0$ mm).....	112
Figure 5.17 Joint cross-sectional profiles with varying bottom sheet thicknesses T_2 and die diameters D_1 ($T_1=1.2$ mm, $L_1=5.0$ mm, $H_1=2.0$ mm).....	113
Figure 5.18 Contour graphs of the (a) interlock and (b) V_r-V_d with varying rivet lengths L_1 and die diameters D_1 ($T_1=1.2$ mm, $T_2=1.8$ mm, $H_1=2.0$ mm).....	114
Figure 5.19 Joint cross-sectional profiles with different rivet lengths L_1 and die diameters D_1 ($T_1=1.2$ mm, $T_2=1.8$ mm, $H_1=2.0$ mm)	115
Figure 5.20 Contour graphs of the (a) interlock and (b) V_r-V_d with varying die diameters D_1 and die depths H_1 ($T_1=1.2$ mm, $T_2=1.8$ mm, $L_1=5.0$ mm)	116
Figure 5.21 Joint cross-sectional profiles with different die diameters D_1 and die depths H_1 ($T_1=1.2$ mm, $T_2=1.8$ mm, $L_1=5.0$ mm).....	117

Figure 5.22 Contour graph of the (a) T_{cen} and (b) T_{tip} with varying top and bottom sheet thicknesses ($L_1=5.0$ mm, $D_1=10.0$ mm, $H_1=1.8$ mm)	119
Figure 5.23 Joint cross-sectional profiles with varying top and bottom sheet thicknesses ($L_1=5.0$ mm, $D_1=10.0$ mm, $H_1=1.8$ mm).....	119
Figure 5.24 Deformed rivet shank in the SPR joints with different top and bottom sheet thicknesses	120
Figure 6.1 Factors affecting the layout of a manufacturing line.....	123
Figure 6.2 Schematic of the research structure for auto-selection of rivet/die for multiple sheet combinations.....	124
Figure 6.3 Schematic of the DNN structure with multiple hidden layers.....	126
Figure 6.4 Schematic diagrams of (a) a SAE and (b) a single sparse autoencoder	127
Figure 6.5 Schematic diagram of the relationships between the DNN and the SAE.....	128
Figure 6.6 Illustration of detailed training procedures for the DNN with two or three hidden layers	129
Figure 6.7 Flow chart to select the optimal DNN with three hidden layers	130
Figure 6.8 Performance evaluation of SNNs with varying hidden neurons for the training data and testing data (a) interlock I , (b) T_{tip} and (c) T_{cen}	131
Figure 6.9 Performance evaluation of DNNs with two hidden layers for the training and testing data (a) interlock I , (b) T_{tip} and (c) T_{cen}	132
Figure 6.10 Performance evaluation of DNNs with three hidden layers for the training and testing data ($m=11$) (a) interlock I , (b) T_{tip} and (c) T_{cen}	134
Figure 6.11 Performance comparison between the three optimal SNN and DNNs for the testing data (a) MAE and (b) r	135
Figure 6.12 Comparisons between the optimal DNN (5-10-6-3) predicted and FEA simulated (a) interlock I , (b) T_{tip} and (c) T_{cen}	136
Figure 6.13 Comparisons of the I , T_{tip} and T_{cen} from the experimental SPR tests, the FEA model and the optimal DNN (5-10-6-3).....	139
Figure 6.14 Schematic diagram of joint robustness evaluation procedures with the Monte Carlo method and the DNN.....	141
Figure 6.15 Schematics of (a) frequency distributions, (b) identified normal distribution functions and (c) robustnesses of three quality indicators for the joint 6-1.....	142
Figure 6.16 (a) Comparisons between the experimentally tested and DNN predicted joint quality indicators with variation ranges, (b) DNN predicted robustness of three quality indicators and (c) DNN predicted robustness of each SPR joint	143
Figure 6.17 Schematic of the approach one for the rivet/die selection for multiple sheet combinations	144

Figure 6.18 Performance plot of a specific rivet/die combination for new sheet combinations using the DNN	145
Figure 6.19 Schematic diagram for automatic selection of minimum rivet/die combinations for multiple sheet combinations	145
Figure 6.20 Performance plots of the eight different rivet/die combinations for the target sixteen sheet combinations.....	148
Figure 6.21 Performances of the eight different rivet/die combinations and corresponding solutions for the target sixteen sheet combinations (a) without considering the joint robustness and (b) considering the joint robustness.....	149
Figure 6.22 The GUI of automatic rivet/die selection for multiple sheet combinations.....	149
Figure 6.23 Application range map of a rivet/die combination and the corresponding performance for multiple sheet combinations	150
Figure 6.24 Application range maps of the eight rivet/die combinations and performance evaluations for the target sixteen different sheet combinations	152
Figure 6.25 The identified minimum rivet/die combinations for the target sixteen sheet combinations with the approach two.....	152
Figure 6.26 Comparisons between the (a) experimentally tested, (b) DNN predicted and (c) application range maps identified joint quality results	154
Figure 7.1 Cross-sectional profiles of SPR joints with different rivet head heights.....	159
Figure 7.2 Schematics of locations the T_{\min} may appear (a) two locations considered in this thesis and (b) other possible locations can be further involved	159
Figure 7.3 Schematic diagram of procedures to facilitate the rivet and die selection in practical applications.....	160
Figure 7.4 Schematic diagram for the development and application of fast joint mechanical strength prediction model.....	160

List of Tables

Table 3.1	Mechanical properties of the rivet and sheet materials.....	49
Table 3.2	Friction coefficients between the different parts in the FEA model.....	50
Table 3.3	Validation experiments of the FEA model with different joint configurations	51
Table 3.4	Design of the interrupted experimental SPR tests	54
Table 3.5	Design of the single factor experiment.....	57
Table 4.1	Independent variables and levels of the orthogonal test	81
Table 4.2	$L_{27} (3^{13})$ orthogonal test design and simulation results.....	82
Table 4.3	Results of ANOVA for the interlock.....	83
Table 4.4	Results of ANOVA for the T_{\min}	83
Table 4.5	Evaluation results of the regression models for the interlock and T_{\min}	84
Table 4.6	Joint configurations and the results for the validation of the regression models	85
Table 4.7	Rivet volumes and die cavity volumes	89
Table 5.1	Full factorial design with five joint parameters and three levels (3^5).....	96
Table 5.2	Experiment design and results for the validation of ANNs	104
Table 5.3	Five top and bottom sheet combinations	108
Table 5.4	Setting parameters used in the GA	108
Table 5.5	Pareto optimal solution set for Case No.1 (1.0 mm+1.0 mm)	109
Table 6.1	Experiment design and results for validation of DNN model.....	137
Table 6.2	Tolerance bands and normal distribution equations for the five joining parameters [180]	140
Table 6.3	Twelve SPR joints for the robustness evaluation	142
Table 6.4	Sixteen sheet combinations (AA5754) to be self-piercing riveted	146
Table 6.5	Eight rivet/die combinations frequently used for AA5754 sheets	146
Table 6.6	Validation of the proposed two rivet/die selection approaches	153

Acknowledgements

First of all, I would like to express my sincerest gratitude to my two admirable supervisors: Prof. Xianping Liu and Dr Li Han, for their professional guidance, full support and encouragement on my doctoral study. In this special period, their patience, directions and technical suggestions are very helpful for me to obtain the current research progress and to complete this thesis. There are a lot of things I learnt from them, not only the correct attitude to scientific research, but also the sincere character of treating others. All of these teachings will benefit me all my life.

Many thanks to Jaguar Land Rover UK for funding this project, also special thanks to the School of Engineering, the University of Warwick for providing the scholarship during the four years of my study. Special appreciation to Dr Matthias Wissling, Paul Bartig and their team members from Tucker GmbH for their strong support for the experimental tests.

Special thanks to my panel committee: Prof. David Towers and Prof. Ken Mao, who always help me by caring about my needs, paying attention to my research progress, and putting forward valuable suggestions.

Special thanks to Prof. Keith Godfrey, who is not only a teacher but also a true friend, and takes me to appreciate the culture and scenery of the UK. Many appreciations to my friends, Zhen Yang, Yumeng Song, Yue Yang, Yiwei Ma, Lijin Deng, Wuweikai Xiang and Jiajing Zhu, for their mental support.

The biggest thanks to my father Xinfeng Zhao, my mother Xiang Feng, my grandparents, my sister, brother and other family members for their endless love and selfless support. Also, thanks to my mother-in-law and father-in-law for their understanding and kindness. Last but not least, heartfelt thanks to my dear husband for his meticulous care and support in my life and study during this special period. For you, a thousand times over.

Declarations

This thesis is submitted to the University of Warwick in partial fulfilment of the requirements for the degree of Doctor of Philosophy. The work presented here was conducted by candidate Huan Zhao under the supervision of Prof. Xianping Liu in the School of Engineering at the University of Warwick and Dr Li Han from Hansher Consulting Ltd. Any part of it has not been submitted for any degree at other institutions.

Publications

Published papers:

- [1] **Huan Zhao**, Li Han, Yunpeng Liu, and Xianping Liu. "Modelling and interaction analysis of the self-pierce riveting process using regression analysis and FEA." *The International Journal of Advanced Manufacturing Technology* 113.1 (2021): 159-176. {IF=3.226}
- [2] **Huan Zhao**, Li Han, Yunpeng Liu, and Xianping Liu. "Quality prediction and rivet/die selection for SPR joints with artificial neural network and genetic algorithm." *Journal of Manufacturing Processes* 66 (2021): 574-594. {IF=5.010}
- [3] **Huan Zhao**, Li Han and Xianping Liu. " Numerical study of deformation behaviour during self-pierce riveting process." *19th International Conference and Exhibition, EUSPEN* (2019): 416-419.
- [4] **Huan Zhao**, Li Han, Yunpeng Liu, and Xianping Liu. "Analysis of joint formation mechanisms for self-piercing riveting (SPR) process with varying joining parameters." *Journal of Manufacturing Processes*. (Under revision)

Others:

- [1] Yunpeng Liu, Li Han, **Huan Zhao**, and Xianping Liu. "Evaluation and correction of cutting position's effects on quality indicator measurement of self-piercing riveted joint." *Materials & Design* 202 (2021): 109583.
- [2] Yunpeng Liu, Li Han, **Huan Zhao**, and Xianping Liu. "Numerical modelling and experimental investigation of the Riv-Bonding process." *Journal of Materials Processing Technology* 288 (2021): 116914.
- [3] Yunpeng Liu, Li Han, **Huan Zhao**, and Xianping Liu. "Effects of the die parameters on the self-piercing riveting process." *The International Journal of Advanced Manufacturing Technology* 105, no. 7 (2019): 3353-3368.
- [4] Yunpeng Liu, Li Han, **Huan Zhao**, and Xianping Liu. " Experimental investigation of the adhesive layer's impact on the Riv-Bonding process and joint quality." *Thin-Walled Structures* 167 (2021): 108255.

Abstract

Self-piercing riveting (SPR) technique has achieved rapid development over the last three decades, and has already become one of the major connection approaches in the automotive industry. The selection of suitable rivets and dies for new SPR joints is always a big challenge because of the high requirements on engineers' joint design experience and the heavy costs of numerous experimental tests. Therefore, to shorten the design cycle and to quickly identify the suitable rivets and dies for new joints, this thesis carried out in-depth research in the development of fast joint quality prediction tools and rivet/die optimization strategies.

Firstly, in order to overcome the high investment in time and money of the great number of experimental SPR tests, a finite element analysis (FEA) model of the SPR process was established to collect sufficient joint quality data for the training and testing of fast quality prediction models. Then, fast quality prediction tools were developed using the multiple regression analysis, the shallow neural network (SNN) and the deep neural network (DNN) respectively, and their performances were evaluated and validated through experimental SPR tests. To obtain the desired quality for a specific single joint, a strategy that combined the developed SNNs with the genetic algorithm (GA) was proposed to automatically optimize the rivet and die parameters. Meanwhile, to simplify the selection of rivet/die for multiple new sheet combinations, two novel approaches suitable for inexperienced engineers were also proposed with the DNN. The first approach took the joint robustness into account and achieved automatic selection of rivet/die for multiple new sheet combinations. The Monte Carlo method was employed to evaluate the robustness of designed SPR joints. The second approach was developed based on application range maps of different rivet/die combinations, and was also approved effective to quickly determine the minimum rivet/die combinations for multiple sheet combinations.

In addition, to deepen understanding of the SPR process and to facilitate the selection of rivet and die, analysis of interaction effects between rivet, sheet and die parameters on the SPR joint quality was conducted with the developed regression models and the SNNs. The formation mechanisms of SPR joints with varying joining parameters were also numerically investigated with the FEA model. Moreover, two graphic user interfaces (GUIs) respectively integrating the developed fast quality prediction models and the automatic rivet/die selection approach were also developed to facilitate their practical applications in the industry sector. Overall, the results from this thesis are beneficial for simplifying the design process of new SPR joints, and have a great prospect in the automotive industry.

Nomenclature

$B_{i,j}^{(k)}$	Bias between the i th neuron in the $(k+1)$ layer and the j th neuron in the k th layer
D_1	Die diameter, mm
D_{in}	Diameter of inner interlock boundary, mm
D_{out}	Diameter of outer interlock boundary, mm
D_r	Deformed rivet shank diameter, mm
D_s	Rivet displacement, mm
F_{in}	Resistance force applied on the inner surface of the rivet shank, N
F_{out}	Resistance force applied on the outer surface of the rivet shank, N
F_r	Riveting force, N
H	Rivet head height, mm
H_1	Die depth, mm
I	Interlock, mm
L_1	Rivet length, mm
N	Total number of the SPR joints
N_h	Number of the hidden layer neurons
R	Die-to-Rivet volume ratio
R^2	Coefficient of determination
R^2_{adj}	Adjusted coefficient of determination
R^2_{pred}	Prediction coefficient of determination
R_f	Rivet flaring distance, mm
S	Standard error
T_1	Top sheet thickness, mm
T_2	Bottom sheet thickness, mm
T_{cen}	Remaining bottom sheet thickness at the joint centre, mm
T_{min}	Minimum remaining bottom sheet thickness, mm
T_{tip}	Remaining bottom sheet thickness under the rivet tip, mm
V_d	Die cavity volume, mm ³

V_r	Rivet volume, mm ³
$W_{i,j}^{(k)}$	Weight between the i th neuron in the $(k+1)$ layer and the j th neuron in the k th layer
$Y_{j,s}$	Matrix of the actual/simulation values by the FEA model for j th SPR joint
$Y_{j,p}$	Matrix of the predicted values by the DNN model for j th SPR joint
Y_s	Matrix of the actual/simulation results by the FEA model for all SPR joints
Y_p	Matrix of the predicted results by the ANN/DNN model for all SPR joints
$\Omega(h)$	Sparsity penalty term
a	Original input/output value
a_{max}	Maximum value among the original input/output values
a_{min}	Minimum value among the original input/output values
a_{norm}	Normalized input/output value
$\mathbf{b}^{(1)}$	Bias vector of the first layer in a sparse autoencoder
$\mathbf{b}'^{(1)}$	Bias vector of the second layer in a sparse autoencoder
\mathbf{h}	Representation matrix in the hidden layer
m	Number of neurons in the first hidden layer
n	Number of neurons in the second hidden layer
q	Number of neurons in the third hidden layer
r	Pearson's correlation coefficient
$\mathbf{w}^{(1)}$	Weight matrix of the first layer in a sparse autoencoder
$\mathbf{w}'^{(1)}$	Weight matrix of the second layer in a sparse autoencoder
\mathbf{x}	Input matrix in a sparse autoencoder
$\hat{\mathbf{x}}$	Output matrix in a sparse autoencoder
x_{input}	Original input value
x_{norm}	Normalized input value
$y_{j,s}$	Actual/simulation output value of the j th SPR joint
y_{max}	Maximum value among all the output values

y_{min}	Minimum value among all the output values
y_{norm}	Normalized output value
y_{output}	Original output value
$y_{j,p}$	Predicted output value of the j th SPR joint
μ	Mean value
σ	Standard deviation

Abbreviations

2D	Two-dimensional
3D	Three-dimensional
ALE	Arbitrary Lagrangian-Eulerian
ANN	Artificial neural network
ANOVA	Analysis of variance
ASF	Audi Space Frame
BIW	Body-in-white
BP	Back-propagation
CEL	Coupled Eulerian-Lagrangian
DNN	Deep neural network
FEA	Finite element analysis
FLD	Forming limit diagram
GA	Genetic algorithm
GBDT	Gradient boosted decision tree
GTN	Gurson-Tveergaard-Needleman
GUI	Graphical user interface
JLR	Jaguar Land Rover
k-NN	k-nearest-neighbour
LWV	Light Weight Vehicle
MAE	Mean absolute error
MAPE	Mean absolute percentage error
MSE	Mean squared error
NSGA- II	Non-dominated Sorting Genetic Algorithm II
NVH	Noise, vibration and harshness
PSO	Particle swarm optimization
RBF	Radial basis function
RSM	Response surface methodology

RSW	Resistance spot welding
SAE	Stacked autoencoder
SNN	Shallow neural network
SPG	Smoothed Particle Galerkin
SPH	Smoothed Particle Hydrodynamic
SPR	Self-piercing riveting
SVR	Support vector regression
TA-SPR	Thermally assisted self-piercing riveting
TIG	Tungsten inert gas arc

1. Introduction

1.1. Background

1.1.1. Lightweight design of automobiles

With the increasing legislative requirements to tackle global warming and climate change over the last three decades, lightweight design has become one of the main development directions in the automotive industry. Lightweight vehicles can effectively reduce fuel consumption, improve dynamic abilities and provide more opportunities for new useful features [1]. It was reported that fuel consumption could save up to 5~7 % if the weight of a vehicle is reduced by 10 % and the drivetrain system is also downsized [2]. During the lightweight vehicle design process, the design of body-in-white (BIW) structure is very crucial because the BIW accounts for around 60 % of the total investment cost and about 30~40 % of the entire vehicle weight [3,4]. Nowadays, the lightweight design of BIW is still a research hotspot in the automobile industry and academia. Except for optimizing the BIW structure, replacing the traditional steels with lightweight materials (i.e., aluminium alloys [5], magnesium alloys [6], composites and polymeric materials [7]) is also an effective way to reduce the weight of BIW. Among different types of lightweight materials, aluminium alloys are the most popular and have been widely applied on the vehicle BIW due to their excellent mechanical performance and good recyclability [4,8], especially the AA5xxx and AA6xxx series. The AA5xxx aluminium alloys have very good formability, high stiffness, good crashworthiness and durable properties [9]. The AA6xxx aluminium alloys also have good formability, high strength after coating and good corrosion resistance. Moreover, the density of aluminium alloy is just about 35 % of that of steel, which allows a 50 % mass reduction of the whole aluminium BIW compared to the conventional steel BIW [1].

Over the past thirty years, various aluminium-intensive vehicles have been developed by world-renowned automotive companies, such as Jaguar Land Rover (JLR), Audi and BMW [10]. In 1994, Audi launched the first-generation all-aluminium vehicle A8 (D2) with the Audi Space Frame (ASF) design technology. The vehicle body consists of 237 aluminium sheet stamping parts, 47 aluminium extrusion components and 50 aluminium casting parts as shown in **Figure 1.1** (a). The aluminium body weighs 249kg and is around 200kg less than the comparable steel one [11]. In 1999, Audi further developed the ASF technology and launched the first all-aluminium body mini car A2 [12]. **Figure 1.1** (b) illustrates its vehicle body structure. After that, more lightweight vehicle models were launched by Audi, such as the

Audi R8, Audi A8 (D4) and Audi A8 (D5). In 2003, Jaguar launched its first volume-production vehicle Jaguar XJ (X350), on which the aluminium body structure consists of 273 aluminium sheet stamping parts, 22 extruded aluminium components and 15 aluminium casting parts as shown in **Figure 1.2** (a). The proportions of different materials adopted are illustrated in **Figure 1.2** (b). An industrial breakthrough was achieved on this vehicle by introducing an all-aluminium monocoque chassis. By adopting lightweight aluminium alloys, the XJ (X350) model is 40 % lighter, but the body structure is 60 % stiffer than the previous XJ model. After that, Jaguar Land Rover (JLR) launched more new models with this Light Weight Vehicle (LWV) technique, such as the Jaguar XJ (X351), Jaguar XK (X150) and the Range Rover L405. The aluminium body of the Range Rover L405 shown in **Figure 1.3** (a) is more than 180kg lighter than the steel body of the previous vehicle model. The proportions of materials on this body structure are illustrated in **Figure 1.3** (b). It can be seen that the AA6xxx series aluminium alloys account for a much greater proportion than that in the Jaguar XJ (X350) (see **Figure 1.2** (b)). In recent years, the LWV technique has been further developed by JLR on its new vehicle models, such as the XE and XF [13,14].

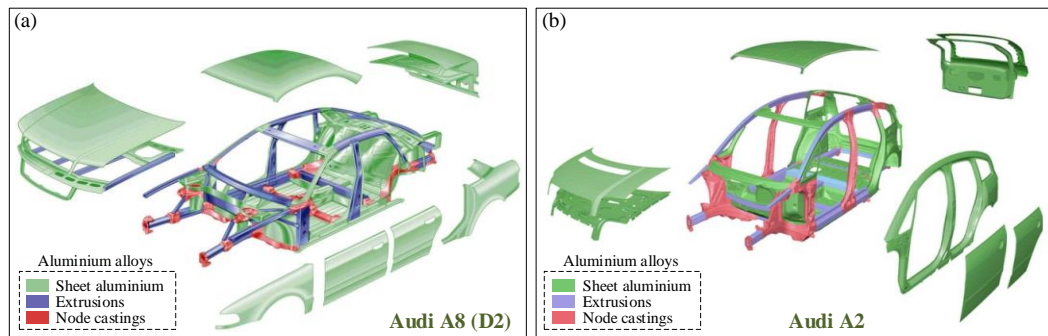


Figure 1.1 Exploded views of aluminium space frames and closures on (a) Audi A8 (D2) and (b) Audi A2 [15]

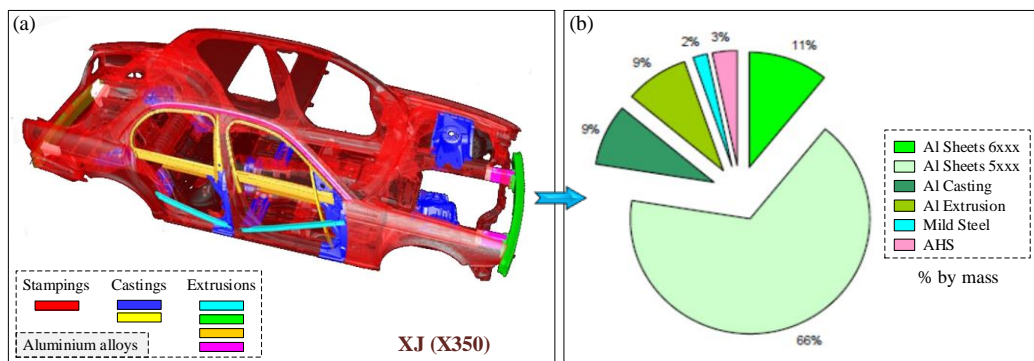


Figure 1.2 (a) Aluminium BIW of Jaguar XJ (X350) and (b) the corresponding material proportions [15]

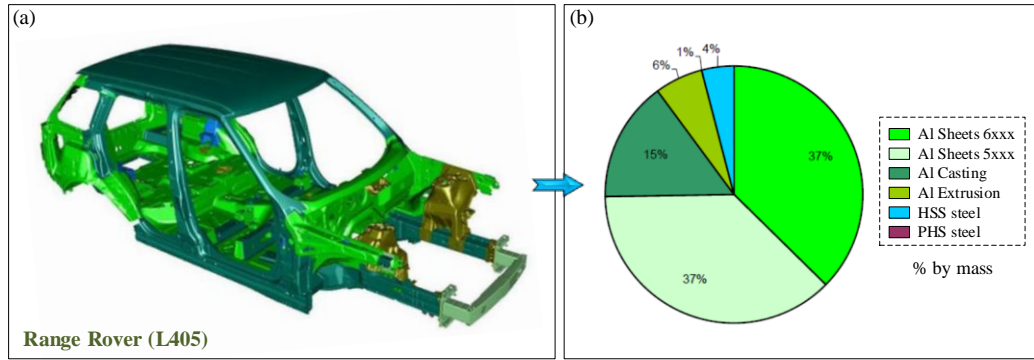


Figure 1.3 (a) Aluminium BIW of Range Rover L405 and (b) the corresponding material proportions [15]

With the increasing applications of aluminium alloys and other lightweight materials on vehicle BIW structures, the assembly of lightweight BIW structures becomes critical. The conventional resistance spot welding (RSW) technique demonstrates excellent performance for the connection of steel parts, but encounters many difficulties when joining the aluminium alloy parts. For instance, due to the high thermal and electrical conductivities of aluminium alloys [16], a higher welding current but a shorter welding time are required. This brings a big challenge to the welding equipment, especially the power sources. In addition, the relatively short lifetime of electrodes caused by the alloying effect also limits the applications of RSW in massive production [17]. Therefore, it is urgently needed to find out an alternative joining technique for the assembly of lightweight BIW structures in the automotive industry.

1.1.2. Self-piercing riveting (SPR) technique

Under such circumstances, the SPR technique was introduced into the car industry and has achieved rapid development in the past three decades [13]. Taking the two-layer joint as an example, the four steps during the SPR process are schematically shown in **Figure 1.4**. First, the blank-holder moves downward and clamps the two sheets together. Then, the punch moves downward and presses the rivet into the sheets. The rivet shank first pierces through the top sheet and then flares into the bottom sheet. Finally, the punch and blank-holder are lifted, and a SPR joint with a mechanical interlock is formed. In general, a SPR system is composed of a power and control unit, a driving unit, a rivet feeding unit, a C-frame structure, a punch, a blank-holder, dies and rivets. **Figure 1.5** illustrates the structures of three SPR systems manufactured by different companies [18–20]. The SPR systems are mostly driven by a hydraulic system or a servo-driving system. Compared with the hydraulic system, the servo-driving system is much lighter and easier to be integrated into the automotive production line. Some other driving systems (e.g., gunpower system [21]) have also been developed by researchers but are not yet widely employed in the industry sector.

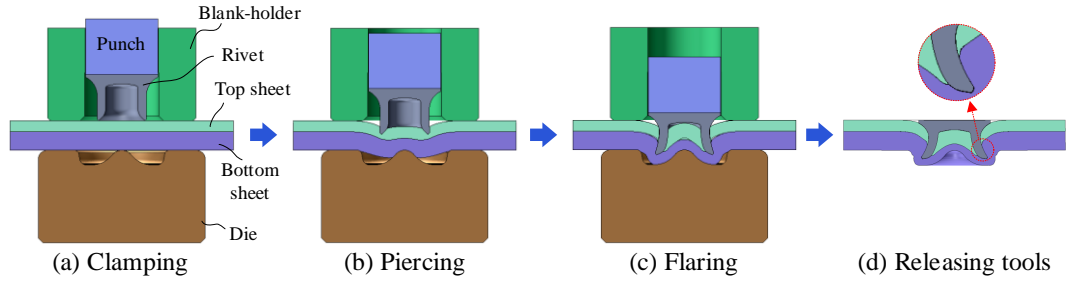


Figure 1.4 Schematic of the four major steps during the SPR process

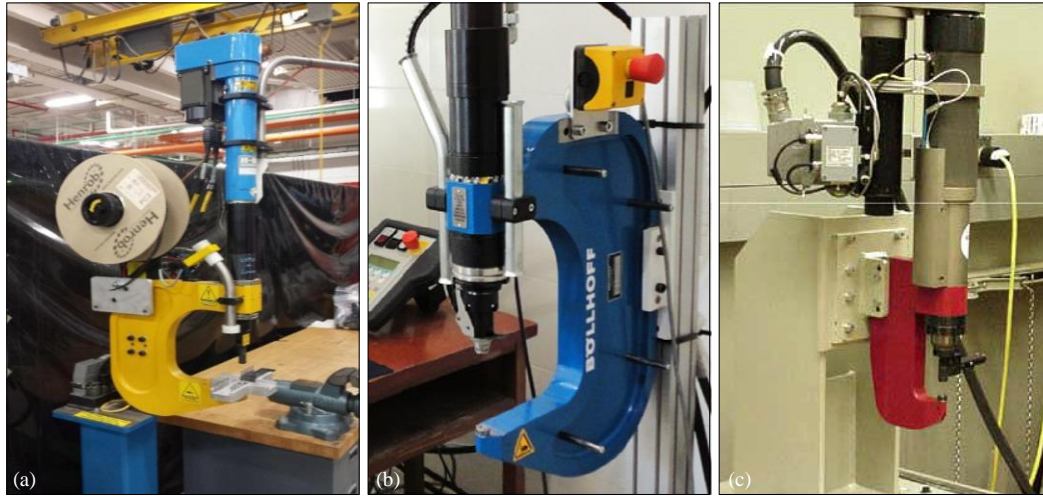


Figure 1.5 Structures of SPR systems from (a) Henrob [18], (b) Böllhoff [19] and (c) Tucker [20]

Different from the RSW technique, the SPR is a mechanical joining approach and thus does not need heat input to melt the materials to form a metallurgical connection [22]. It requires less energy than the RSW, and the formed SPR joints usually have a higher fatigue strength than RSW joints [23]. Moreover, the SPR technique is capable of connecting two or more layers of similar or dissimilar materials, such as aluminium alloys, magnesium alloys, steels and even composite materials [11,19]. It does not require pre-drilled holes and can be applied on coated or painted parts [24]. The main advantages of the SPR technique are summarised as follows [2,25,26]:

- No heat input required, no fumes, no sparks, no dust and environmental-friendly.
- Suitable for similar or dissimilar materials with different physical properties.
- Suitable for coated or pre-painted materials.
- No need for pre-drilled holes.
- High joining speed.
- Good mechanical behaviours of joints, including static strength and fatigue life.
- Could be used in combination with adhesives.
- Convenient to be integrated into the automatic production line.

Except for the above advantages, there are also some limitations as summarised below:

- Require access to both sides of the connected sheets.
- Not a flush joint, leaving a joint button on the backside of the bottom sheet.
- Require consumable items, i.e., the rivet.
- Require a relatively heavy rivet setting tool to provide the high riveting forces.
- Need to be combined with adhesive to form hybrid joints if sealing is required.

Owing to the advantages of the SPR technique in the connection of lightweight materials, it has now become one of the main joining approaches in the automotive industry and has been widely applied to assemble aluminium alloy BIW structures. For instance, nearly 3200 self-piercing rivets are used on the aluminium body structure of the Jaguar XJ (X350). The SPR is also the major joining approach for the Jaguar XJ (X351), and **Figure 1.6** shows the self-piercing rivets distributed on the corresponding aluminium body structure. High efficiency robotic SPR joining systems equipped with multi-feeding guns and blow feed systems are employed to assemble the Jaguar XE model, which effectively reduce the SPR cycle time. Audi also adopts the SPR technique as the main joining approach for aluminium vehicles. As shown in **Figure 1.7** (a), there are 1100 self-piercing rivets used on the aluminium body structure of Audi A8 (D2). The rivet number is further improved to around 1800 on the Audi A2 as shown in **Figure 1.7** (b) [27]. Other well-known automobile manufacturers, including Volvo, BMW, Daimler, Ford and Tesla, have also employed the SPR technique to assemble the aluminium-intensive vehicles [2,10].

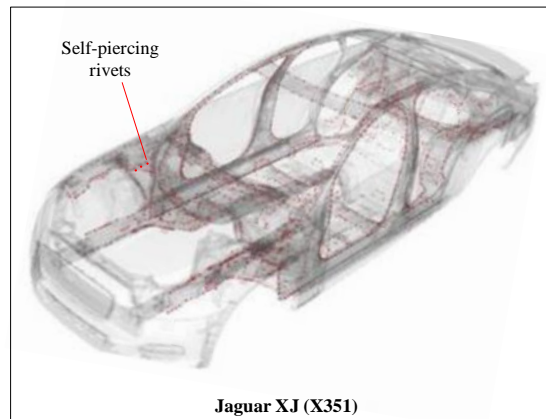


Figure 1.6 Self-piercing rivets applied on the aluminium body of Jaguar XJ (X351) [15]

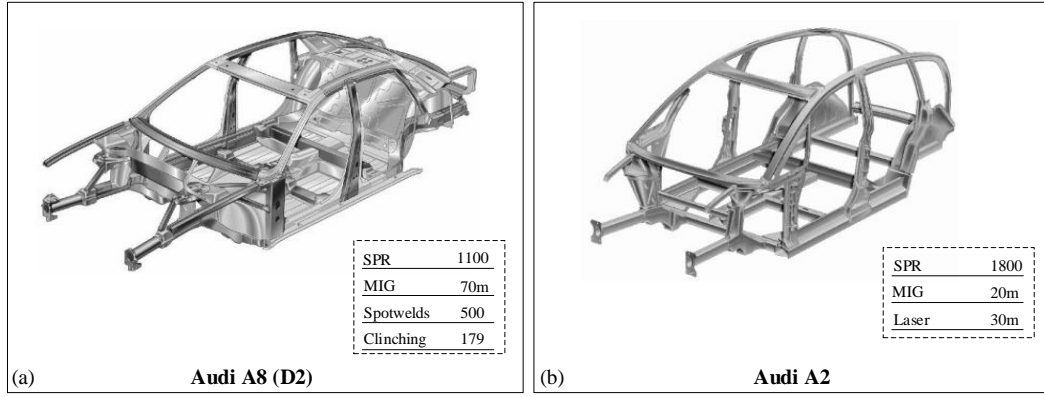


Figure 1.7 Joining techniques applied on the aluminium body structures of (a) Audi A8 (D2) and (b) Audi A2 [27]

Normally, the SPR joint quality is assessed by three critical indicators measured on the joint cross-sectional profile as shown in **Figure 1.8**: (1) the interlock (I); (2) the minimum remaining bottom sheet thickness (T_{\min}) and (3) the rivet head height (H). The magnitudes of these indicators are closely related to the joint mechanical performance [28,29]. The H directly affects the cosmetic appearance of the connected structure and the joint corrosion resistance [30]. A protruded rivet head usually causes gaps between the rivet and the connected sheets, and thus increases the risk of moisture or water invasion. The H also directly links with the final position of the rivet inserted into the sheets and thus affects the final values of the I and T_{\min} [30]. The I is critical for the joint mechanical strength and failure behaviour. Too small interlock values may result in pull-out failure of the rivet shank from the bottom sheet [31,32]. The T_{\min} is very important for the joint corrosion resistance and water-proof performance. If the T_{\min} is 0.0 mm or negative, moisture or water invasion will inevitably occur in service. This will accelerate galvanic corrosion between the steel rivet and the aluminium sheets, and result in premature corrosion failure of SPR joints. Zhang et al. [33] also reported that fatigue failure may occur on the bottom sheet if the T_{\min} was very small. In general, the assessment criteria for these three indicators are determined by the application requirements in different industry sectors. For example, according to the standard of a world-leading car manufacturer [2], the H should be between 0.3 mm and -0.5 mm to achieve a smooth surface. The I should be greater than 0.4 mm for joints with an aluminium alloy bottom sheet and greater than 0.2 mm with a steel bottom sheet. The T_{\min} should be always greater than 0.2 mm.

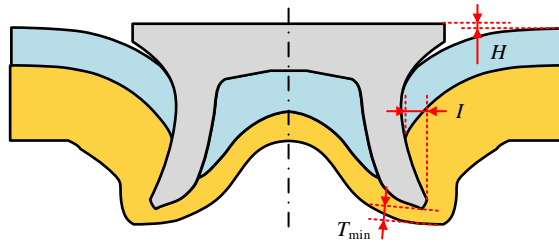


Figure 1.8 Schematic of the SPR joint cross-sectional profile and three quality evaluation indicators

During the SPR process, many joining parameters can affect the final joint quality: the sheet material [19,33], mechanical property [34], thickness [35], orientation [11,36] and surface conditions [37] are the main sheet parameters; the rivet shank diameter [38], length [39], material [32] and hardness level [35] are the important parameters for the rivet; the die type (e.g., flat die or pip die) [40], diameter [41], depth [42] and pip height [43,44] are the critical factors for the die. Moreover, the setting parameters, such as the clamping force, riveting velocity, and total rivet displacement, also affect the SPR joint quality to varying degrees [21,30]. In addition to single factor effects, these joining parameters also impose interaction effects on the joint quality. In other words, the influences of one joining parameter on the final joint quality might vary with the variations of other joining parameters [35,45]. Therefore, due to the complex relationships between these joining parameters and the final joint quality, the design of new SPR joints is always a challenge. Nowadays, the identification of suitable rivets and dies for new sheet combinations still heavily depends on engineers' experience and numerous experimental SPR tests [46]. It will be a great contribution to practical applications if a straightforward approach can be developed to simplify the design process of new SPR joints.

1.2. Existing challenges and research objectives

1.2.1. Existing challenges

In the new SPR joint design process, the joint quality is usually improved by choosing the optimal rivet/die combination based on the target sheet combination. Because of the complex relationships between the joining parameters and the final joint quality, as shown in **Figure 1.9 (a)**, the selection of rivet/die for new joints now still relies heavily on experienced joining engineers and is achieved through the trial-and-error method with the experimental SPR test. However, for a great number of new SPR joints, huge investment in time, materials and labour is needed in order to conduct all necessary experimental SPR tests. To speed up the design cycle of new joints and reduce financial investment, many FEA models for SPR joint quality prediction have been successfully developed and gradually utilized. As shown in **Figure 1.9 (b)**, using a high accuracy FEA model, the quality of all designed SPR joints can be numerically predicted and evaluated to identify the desired SPR joint. Then, experimental SPR tests are conducted to confirm the effectiveness of the numerically identified SPR joint. In this way, the number of experimental SPR tests required in the joint design process can be effectively reduced. The joint design cycle and investment can also be apparently reduced. However, developing and running such simulation models is a big challenge for general engineers without in-depth knowledge of FEA. Therefore, it will be beneficial for the design

of new SPR joints in practical applications if a straightforward and easy-to-use tool can be developed to predict the joint quality.

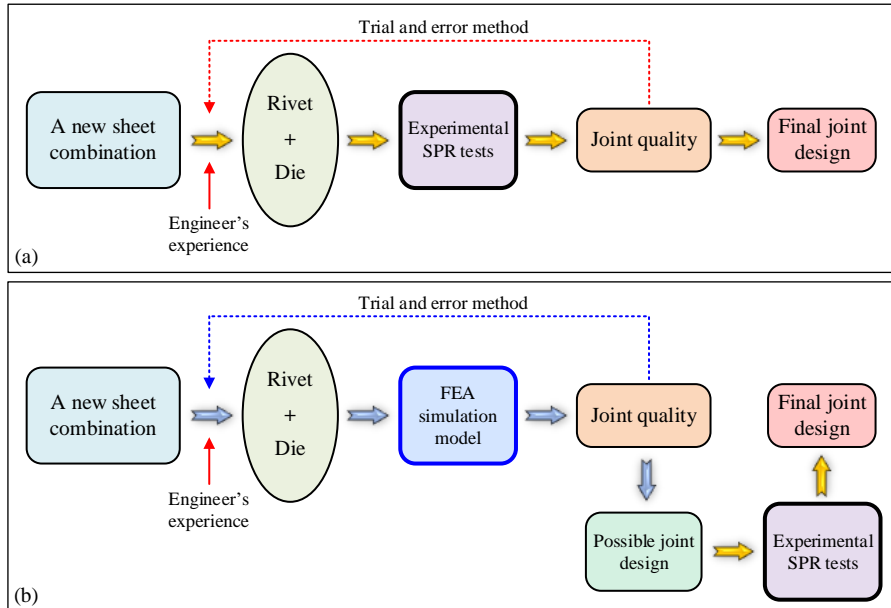


Figure 1.9 Flow charts of (a) the general rivet/die selection process for a new SPR joint and (b) the faster selection process with a FEA model

For experienced joining engineers, who are able to pre-define the most possible rivet and die combinations, fast joint quality prediction tools will be very helpful for the new joint design. However, for general engineers without professional knowledge of SPR process, the prediction tool itself is not sufficient to quickly select the suitable rivet/die because their experience is insufficient to preliminarily select the possible rivet and die. To the author's knowledge, there is still not an effective approach reported in the public domain that can be conveniently used by inexperienced engineers to select the rivet/die for new SPR joints. Therefore, to reduce the dependence of SPR joint design on engineers' experience and to further simplify the joint design process, it is also necessary to find out a straightforward approach that can automatically select the optimal rivet and die according to the target sheet combination and the joint quality standard.

Furthermore, when selecting the rivet/die for multiple new sheet combinations, in addition to ensuring the desired quality for each joint, the total number of rivet/die combinations should also be controlled. Due to the inflexibility of changing rivet and die during the SPR operation, the more rivet/die combinations are employed, the more joining robots are required. The total number of rivet/die combinations will directly affect the layout complexity, the initial investment and the subsequent maintenance of the manufacturing line for the vehicle BIW. This is a challenging task even for engineers with extensive experience in SPR joint design, not to mention inexperienced general engineers. Therefore, it will be meaningful for the design

of new SPR joints if a strategy can be proposed to automatically select the minimum rivet/die combinations for multiple new sheet combinations.

In practical applications, manufacturing tolerances of the sheets, rivet and die will inevitably affect the SPR joint quality [47]. If the joint robustness can be evaluated and took into account during the selection of rivet/die, the BIW structures connected with the SPR technique will become more reliable. So far, the only study relevant to the robustness design of SPR joints was reported by Tassler et al. [48], in which the robustness of SPR joints with rivets of different lengths was evaluated to determine the most suitable rivet for the studied joint configurations. However, although the die is critical for the final SPR joint quality, important die parameters (e.g., die depth and die diameter) are not involved in their evaluation model. Therefore, it will be very valuable for the design of new SPR joints if more crucial parameters of the rivet, sheets and die can be considered when evaluating the joint robustness.

Moreover, in the accessible literature, the influences of different joining parameters on the final joint quality have been widely studied. However, the conclusions in most studies were drawn by analysing the final joint cross-sectional profiles and the measured joint quality indicators. Little efforts were made to investigate the effects of joining parameters on the riveting process and the joint forming mechanisms (e.g., formation processes of the I and T_{\min}). Meanwhile, most accessible studies focused on single-factor effects of the sheets, rivet and die parameters on the final SPR joint quality, but ignored the interaction effects between these joining parameters. In fact, the sheet combinations, rivet properties and die profiles work together during the riveting process to affect the joint formation and the final joint quality. Therefore, to deepen understanding of the SPR process and to facilitate the rivet/die selection, it is also necessary to explore the formation mechanisms of SPR joints with varying configurations and to uncover the interaction effects between different joining parameters on the final joint quality.

Overall, although the SPR technique has been widely utilized in the industry sector, more efforts are still required to solve the problems encountered during its practical applications, especially the selection of rivet/die for new SPR joints.

1.2.2. Research objectives

Systematic research was conducted in this thesis to deal with the above-mentioned challenges. The main objectives are summarised as follows:

1. To avoid the professional knowledge required by the FEA model, straightforward and easy-to-use fast prediction tools for SPR joint quality will be developed. As shown in

Figure 1.10 (a), these tools can be conveniently used in the joint design process to reduce the number of experimental SPR tests and to shorten the joint design cycle.

2. To reduce the dependence of the new SPR joint design on engineers' experience, an effective approach will be developed to automatically optimize the rivet and die parameters according to the target sheet combination, as shown in **Figure 1.10** (b). This makes it possible for inexperienced engineers to design new joints even without in-depth understanding of the SPR process.
3. To simplify the selection of rivet/die for multiple new SPR joints and to reduce the complexity of the manufacturing line for vehicle BIW structures, an automatic rivet/die selection approach will be proposed as shown in **Figure 1.10** (c). A joint robustness evaluation strategy will also be developed and integrated into the rivet/die auto-selection system to improve the reliability of the designed joints in practical applications.
4. To facilitate the design of new SPR joints and have better understanding of the SPR technique, formation mechanisms of SPR joints with varying configurations and interaction effects between different joining parameters on the final joint quality will be investigated numerically and experimentally.

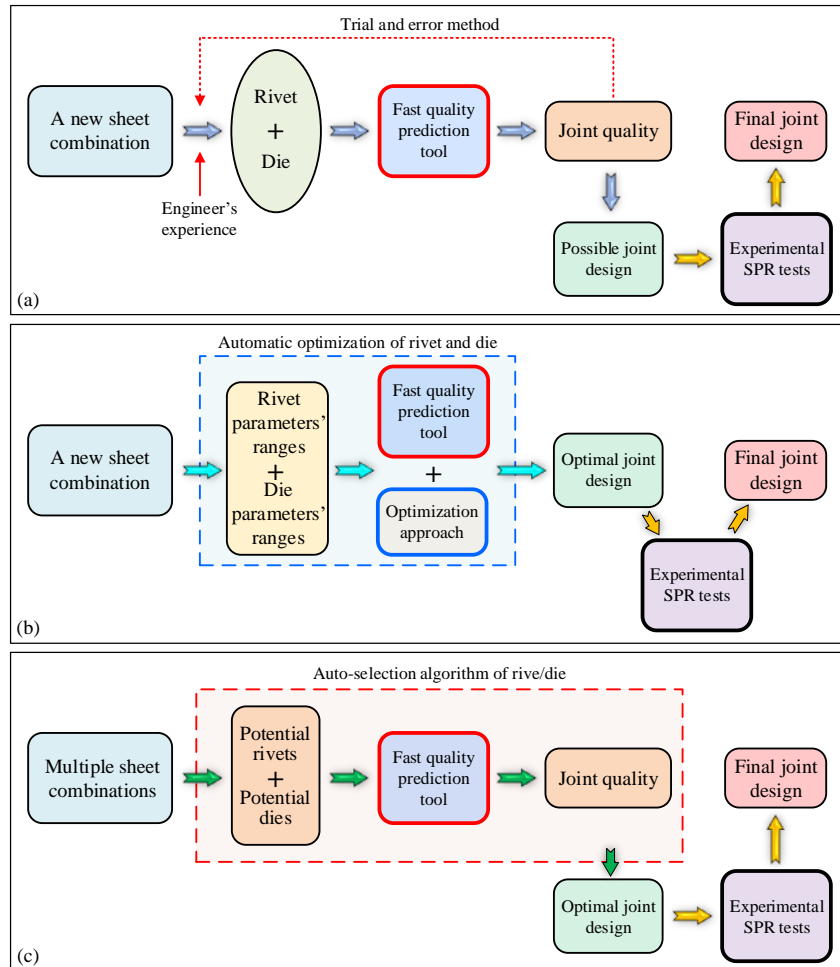


Figure 1.10 Schematics of three approaches to simplify the selection of rivet/die for new SPR joints

1.3. Thesis outline

This thesis is divided into seven chapters to present the development procedures and performances of fast joint quality prediction tools, rivet/die optimization tools and rivet/die auto-selection tools. The main contents of each chapter are summarised as follows:

Chapter 1 introduces the background of the SPR technique, the existing challenges in the design process of new SPR joints, the research objectives of this thesis and the thesis outline. Chapter 2 presents a detailed literature review to demonstrate the latest research status of the SPR technique in respect of the effects of different joining parameters (i.e., sheets, rivet and die parameters), the development of joint quality prediction models (i.e., FEA model, mathematical model and ANN model) and the selection approaches for rivet/die. Effective ways used to predict and optimize the joint quality in other joining techniques are also briefly reviewed.

Chapter 3 develops a FEA model of the SPR process with software Simufact.Forming. Normal experimental SPR tests and interrupted experimental SPR tests were conducted to verify its prediction accuracy in final joint quality (i.e., I and T_{\min}) and joint formation process (i.e., deformation behaviours of rivet and sheets). Then, the developed FEA model was employed as an alternative of the interrupted experimental SPR test to investigate the formation mechanisms of SPR joints with varying top sheet thicknesses (T_1), bottom sheet thicknesses (T_2) and rivet lengths (L_1). The interlock formation, the variation of remaining bottom sheet thickness at the joint centre, and the flaring behaviour of rivet shank were numerically monitored and analysed. Moreover, the FEA model was also utilized to collect training and testing data for the development of fast quality prediction tools in the following chapters.

In Chapter 4, fast quality prediction models were developed with multiple regression analysis method. The FEA model from Chapter 3 combined with the orthogonal experimental design method was employed to acquire the necessary joint quality data. Not only the rivet length (L_1), die diameter (D_1) and die depth (H_1), but also interaction factors between them (i.e., $L_1 \times D_1$, $L_1 \times H_1$ and $D_1 \times H_1$) were considered in the prediction tools. Experimental SPR tests were carried out to validate the performance of the developed quality prediction tools. Moreover, to better understand the influences of rivet/die parameters on the final joint quality, interaction effects between the L_1 , D_1 and H_1 on the SPR joint quality were systematically discussed by analysing the corresponding contour graphs plotted with the developed prediction models. The close relationships between the Die-to-Rivet volume ratio (R) and the joint quality were also highlighted.

To involve more joining parameters, broaden the application range and simplify the development procedures of fast prediction tools, Chapter 5 employs the artificial neural

network (ANN) to build fast quality prediction models. Five joining parameters, including the top sheet thickness (T_1), bottom sheet thickness (T_2), rivet length (L_1), die diameter (D_1) and die depth (H_1) were considered. The FEA model developed in Chapter 3 and the full factorial design method were used to collect the training and testing data for the ANN development. The trial-and-error method was adopted to identify the optimal network structures, and experimental SPR tests were conducted to validate the prediction accuracy of the developed ANNs. Moreover, to achieve the maximisation of joint quality for a new sheet combination, the ANNs were combined with the genetic algorithm (GA) to automatically optimize the rivet/die parameters. This can effectively reduce the dependence of SPR joint design on engineers' experience. In addition, interaction effects between these five joining parameters on the SPR joint quality were also investigated through the contour graphs plotted with the developed ANN models.

In Chapter 6, a fast quality prediction tool was developed with the deep neural network (DNN) to further improve the prediction accuracy. Performances of DNNs with different hidden layers and hidden neurons were systematically compared to identify the optimal DNN structure. Experimental SPR tests were carried out to confirm the prediction accuracy of the developed DNN. Then, with the DNN model and Monte Carlo method, the joint robustness was evaluated by considering the manufacturing errors of sheets, rivet and die. Furthermore, two novel approaches were proposed to quickly identify the minimum rivet/die combinations for multiple new sheet combinations. The first method considers the joint robustness during the design process, and can automatically select the rivet/die combinations. The second approach, once developed, can be used to manually select the minimum rivet/die combinations without calling the fast quality prediction tool. These two rivet/die selection approaches can effectively simplify the joint design process and reduce the dependence on engineers' experience.

Chapter 7 summarises the major conclusions and contributions of this thesis, and discusses the potential research directions that may be helpful to broaden the application of the SPR technique.

2. Literature review

The main objectives of this research are to develop fast joint quality prediction tools and to propose automatic rivet/die optimization and selection approaches for the design of new SPR joints. Therefore, the up-to-date development status of the SPR technique is reviewed in this chapter. First of all, the literature on relationships between different joining parameters (i.e., rivet, sheets and die) and the SPR joint quality is reviewed. Then, studies in the literature on SPR joint quality prediction are summarised and discussed. Finally, the development of rivet/die optimization and selection strategies for SPR and other joining techniques is also reviewed.

2.1. Joining parameters affecting SPR joint quality

The joining parameters, which can directly affect the SPR process and the joining results, can be roughly divided into four categories as presented in **Figure 2.1**, including sheet parameters, rivet parameters, die geometrical parameters and other setting parameters. Each category contains multiple parameters that should be considered carefully during the joint design process. Once all these parameters are determined, the SPR joint can be manufactured using a SPR system. In general, the joint assessment is conducted from two aspects: quality evaluation and mechanical performance evaluation. Magnitudes of the joint quality indicators (e.g., I , H and T_{\min}) directly affect the joint mechanical performance, and therefore they are widely adopted in the industry sector to determine whether the designed SPR joint is acceptable or not. To facilitate the design of new SPR joints, a great number of numerical and experimental investigations on the effects of different joining parameters have been carried out by researchers from both industry and academia [2,29,51].

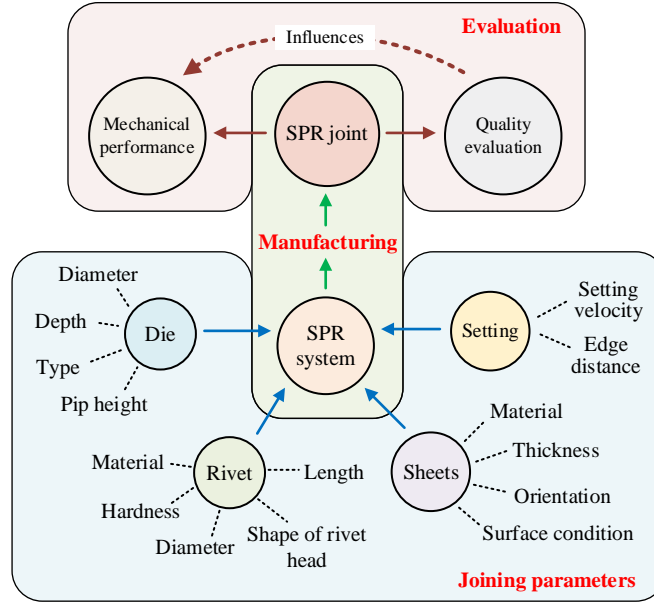


Figure 2.1 Schematic of critical joining parameters affecting the SPR joint quality

2.1.1. Critical sheet parameters

Sheet combinations on the vehicle BIW are usually determined at the structure design stage, and then delivered to the joint design department to find out the suitable joining parameters. The sheet configuration directly affects the joint design difficulty, and there are four critical sheet parameters should be considered, including the sheet material, sheet sequence, sheet thickness and surface condition as presented in **Figure 2.2** (in which the different box colours mean different materials of sheets, and the different box heights mean different thicknesses of sheets). Over the past three decades, a lot of efforts have been made by researchers to explore the influences of different sheet parameters on the joint quality (e.g., I , H and T_{\min}) and on the joint mechanical performance (e.g., tensile strength, fatigue life and failure modes) under various loading conditions.

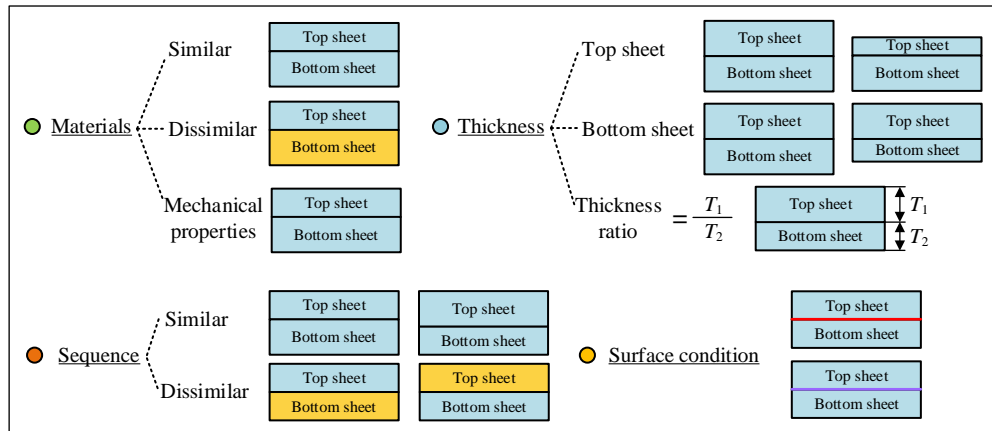


Figure 2.2 Schematic of critical sheet parameters affecting the SPR joint quality

2.1.1.1. Sheet material

The sheet material is a key factor for the SPR joint. Material properties can significantly affect the sheet deformation behaviour, and thus alter the joint quality and mechanical performance. As a mechanical joining approach, the SPR technique is very suitable for high ductility sheet materials (e.g., AA5754 [50] and H62 copper alloy [19]) and can also be employed to connect low ductility sheet materials (e.g., AZ31B-H24 magnesium alloy [51] and AA7075-T6 [52]) with the help of other assisted methods. During the riveting process, undesired cracks are more likely generated on the bottom sheet made of brittle or low ductility materials (see **Figure 2.3**), which is not acceptable in practical applications. To explore the application range of the SPR technique, the joinability of different sheet materials has been widely investigated in many studies.

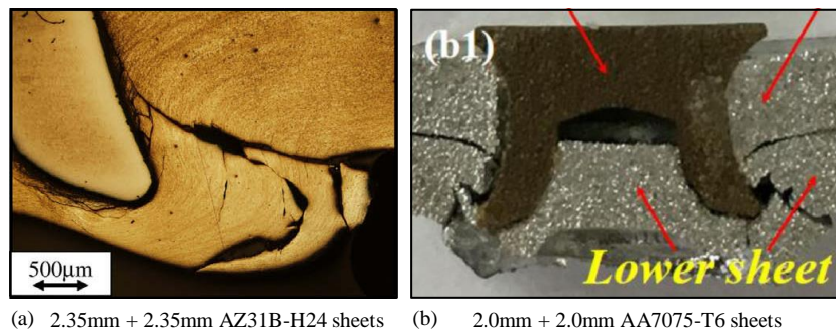


Figure 2.3 Cracks generated on the bottom sheet made of low ductility materials (a) AZ31B-H24 magnesium alloy sheets [51] and (b) AA7075-T6 aluminium alloy sheets [52]

Aluminium alloys, especially the AA5xxx and AA6xxx series, have become the main alternative materials to traditional steels for lightweight vehicles. Effectiveness of the SPR technique for aluminium alloy sheets has been repeatedly approved by researchers. For instance, Mucha [53] successfully adopted the SPR technique to connect aluminium alloy 5052 sheets. Li [54] and Liu et al. [41] successfully connected aluminium alloy AA5754 sheets with the SPR method. Hoang et al. [32] successfully applied the SPR to join aluminium alloy AA6060-W sheets. By optimizing the joining parameters, Li et al. [34] confirmed the suitability of SPR technique for the connection of aluminium alloys AA6008T61 and AA5754 sheets.

In addition to aluminium alloys, connections between aluminium alloy sheets and other types of material sheets (e.g., steels, magnesium alloys and carbon fibre reinforced plastics) are also inevitable in the assembly of lightweight BIW structures. Nowadays, this is still a research hotspot and a lot of efforts have been made to facilitate the design of this kind of SPR joints. For example, Abe et al. [11,36] numerically and experimentally investigated the joinability of the mild steel SPCC or high strength steel (SPFC440 and SPFC590) sheet with the aluminium alloy A5052-H34 sheet. The joinability of one 5000 series aluminium alloy sheet and two 980

MPa ultra-high strength steel sheets was also numerically studied by Abe et al. [55]. Similarly, Mori et al. [43] numerically and experimentally studied the joinability of multiple steel and aluminium alloy sheets (i.e., three or four sheets in total) and successfully realized the connection by optimizing the die profile. Experimental results from Han et al. [56] revealed that the SPR technique is effective in joining the aluminium alloy NG5754 and high strength low alloy steel (HSLA350) sheets. Kam et al. [31] reported that the vibration-damping steel and aluminium alloy Al5052 could be successfully connected with the SPR approach. Moraes et al. [57] found that the cast magnesium alloy AM60B and aluminium alloy AA6082 sheets could be successfully connected with the SPR technique. Ma et al. [58] reported successful applications of the SPR approach on the connection of the magnesium alloy AZ31B and aluminium alloy AA6061 sheets. Luo et al. [59] explored the joinability of the magnesium alloy and aluminium alloy, including the sheet combinations of AA6063-T6 and AM50, AA5754-O and AZ31B-O. He et al. [19] adopted the SPR technique to connect the aluminium alloy AA5052 and copper alloy H62 sheets, and found that the sheet materials could significantly affect the joint static strength and fatigue strength. The aluminium-lithium alloy AL1420 and titanium TA1 sheets were also successfully connected by Zhang et al. [33] with the SPR technique. Experimental tests carried out by Franco et al. [60] indicated that the SPR is an effective approach to connect the carbon fibres composite sheet and aluminium alloy AA2024 sheet. Similarly, the SPR technique was also successfully employed by Karim et al. [61] and Rao et al. [62] to join the carbon fibre reinforced plastic (CFRP) sheet with the aluminium alloy Al5052 or AA6111 sheet. Moreover, Franco et al. [63] reported the effectiveness of the SPR technique after adding an adhesive layer between the CFRP sheet and the aluminium sheet. In addition, Haque et al. [39] also explored the joinability of carbon steel sheets with the SPR technique.

Pressing and stamping, which are two important manufacturing processes of the vehicle BIW structure components, will unavoidably alter the sheet material properties [64]. To ensure that SPR joints designed under the laboratory conditions can still meet the quality standard after being applied to the vehicle body structure, the influences of sheet property variations on the joining results have been studied by some researchers. For example, Han et al. [64] investigated the influences of the pre-straining level of aluminium alloy NG5754 sheets on the joint quality and mechanical strength. The experimental results showed that the increment of pre-straining level (3 %, 5 % to 10 %) improved the tensile strength and hardness of the sheet material, and therefore led to an increase of the measured joint head height but a decrease of the interlock. The joint lap-shear strength and fatigue strength showed increasing tendencies. Li et al. [34] studied the impact of the yield strength variation of aluminium alloy AA6008T61 sheet on the joining results. The experimental results indicated that the yield strength of

AA6008T61 sheet affected the joint failure mode and the cracking level on the joint button, but did not obviously influence the joint strength during the lap-shear and T-peel tests. Jäckel et al. [42] numerically analysed the impact of sheet material pre-deformation and ultimate tensile strength variations on the aluminium alloy SPR joint quality. It was found that the increments of pre-deformation of top and bottom sheets led to a decrease of the interlock.

To improve the joinability of low formability sheet materials, assistant technologies have been employed in some studies, including heating furnace [52], induction coil [65], direct current [66] and laser [51], as shown in **Figure 2.4**. The key idea is to increase the ductility of bottom sheet material by improving the bottom sheet temperature. For instance, Ying et al. [52] successfully enlarged the joinability of the low ductility AA7075-T6 sheets by raising the sheet temperature to around 400 °C with a heating furnace. Deng et al. [65] proposed a thermally assisted self-piercing riveting (TA-SPR) process. By improving the ductility of the DP980 using the induction heating approach, the 2.0 mm AA6061-T6 top sheet and 1.2 mm DP980 bottom sheet were successfully connected. Lou et al. [66] applied a direct current on the DP780 sheet to improve its plasticity (electro plastic effect). The experimental results indicated that this method could effectively improve the SPR joint quality, and reduce the riveting force required during the joining process. Durandet et al. [51] integrated the laser heating technology into the SPR process, and successfully connected the 2.35 mm magnesium alloy AZ31B-H24 sheets (without cracks on the bottom sheet) by preheating the bottom sheet for 2.5~3.5 s using a laser beam.

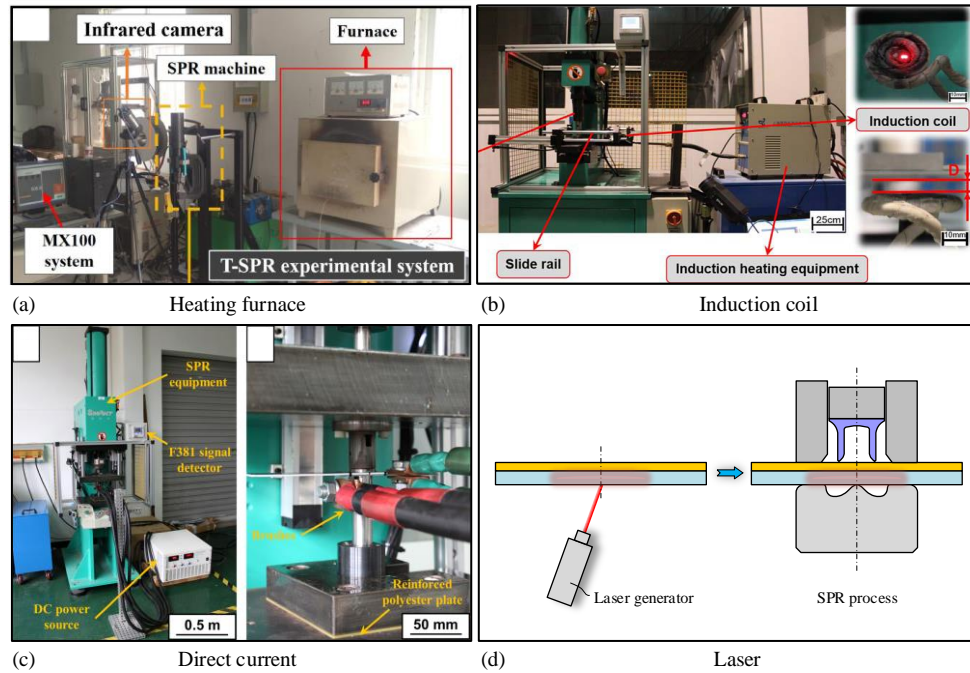


Figure 2.4 Assistant technologies to improve the ductility of bottom sheet material (a) heating furnace [52], (b) induction coil [65], (c) direct current [66] and (d) laser [51]

2.1.1.2. Sheet sequence

In the joint design process, the sheet sequence should also be considered carefully. A proper sheet sequence can effectively improve the joinability of sheets and the final joint quality. The optimal sheet sequence is closely related to the sheet materials and thicknesses. For sheets made of the same material, it is recommended to use the thicker one as the bottom sheet [67]. This will be beneficial for interlock and T_{\min} formations and therefore lead to a higher joint quality. Whilst for sheets made of dissimilar materials (e.g., aluminium alloy and high strength steel), not only the sheet thickness but also the sheet materials should be taken into account when arranging the sheet sequence. In general, the material with a higher ductility is more suitable to be used as the bottom sheet. This will be helpful to facilitate interlock formation and avoid cracks on the joint button [34]. A concrete analysis has to be made for a specific sheet combination before determining the optimal sheet sequence.

So far, the relationships between the sheet sequence and the joint quality have been widely discussed in many studies. For example, Li et al. [34] experimentally investigated the impact of sheet sequence on the joinability of AA6008T61 sheets with varying yield strength and AA5754 sheets with varying thicknesses by SPR technique. The results showed that the AA6008T61 sheet was more suitable as the top and middle layers to avoid severe cracks generated on the joint button. Abe et al. [11] studied the influences of sheet sequence on the joinability of mild steel SPCC and aluminium alloy A5052-H34 sheets, and found that the joining range was apparently extended when the mild steel sheet was used as the top sheet rather than as the bottom sheet, as shown in **Figure 2.5**. The same authors further studied other two types of steels in [36], and reported that the joining range was apparently extended with the steel SPFC440 as the top sheet (see **Figure 2.6** (a)(b)) but slightly narrowed with the steel SPFC590 as the top sheet (see **Figure 2.6** (c)(d)). Mori et al. [43] found that, for the SPR joints with three layers of steel and aluminium alloy sheets, the top sheet with a softer material could be pierced smoothly and thus improve the sheet joinability. Experimental results from the study of Kam et al. [31] revealed that the mechanical performance of the SPR joint with a vibration-damping steel sheet and an aluminium alloy Al5052 sheet was superior when the Al5052 was used as the top sheet due to the relatively larger interlock. Besides, all the tested SPR joints underwent the same failure mode: the rivet shank pull-out from the bottom sheet because of the insufficient mechanical interlock. Zhang et al. [33] studied the quality of SPR joints with aluminium-lithium alloy Al1420 and titanium TA1 sheets. It was found that, within the studied ranges, a higher static property was achieved when the aluminium-lithium sheet was used as the bottom sheet, but a longer joint fatigue life was observed with the titanium TA1 bottom sheet. Meanwhile, the fatigue mode was also influenced by the sheet sequence. Ma et al. [58] reported that the sheet sequence of AZ31B top sheet to AA6061-T6 bottom

sheet could avoid the appearance of cracks, achieve better joint quality and higher tensile strength. As for the connection of CFRP sheet and aluminium alloy sheet, it has been widely reported that the aluminium alloy sheet should be placed on the die side due to its high ductility [60–63].

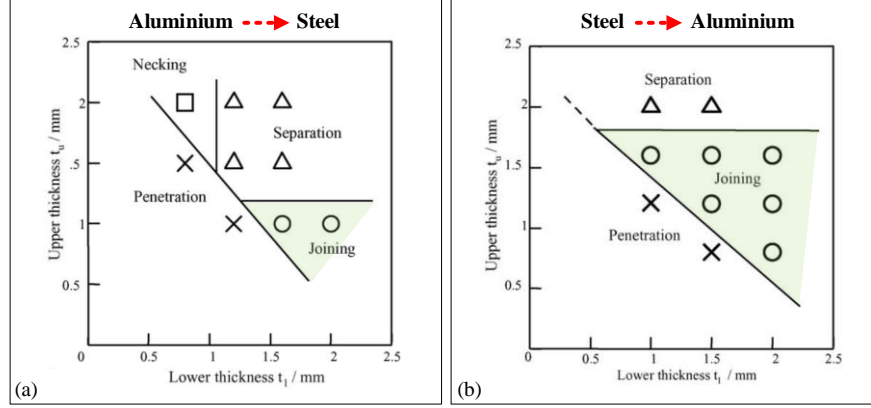


Figure 2.5 Experimentally tested joinability of (a) aluminium-steel sheets and (b) steel-aluminium sheets [11]

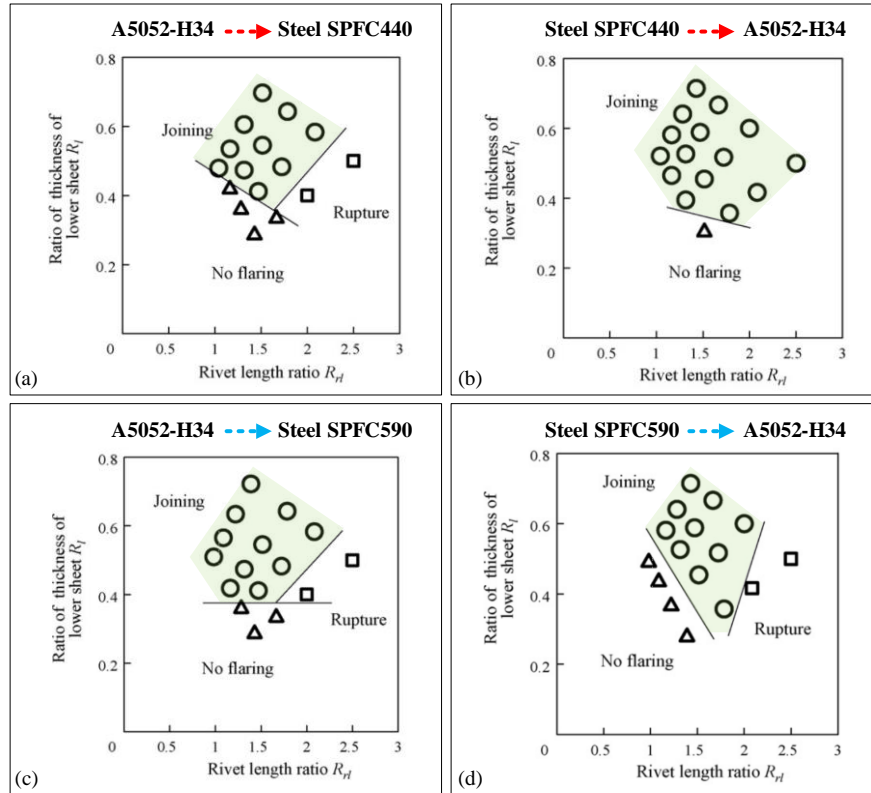


Figure 2.6 Joinability of high strength steel sheet and aluminium alloy sheet (a) aluminum-SPFC440, (b) SPFC440-aluminium, (c) aluminum-SPFC590 and (d) SPFC590-aluminium [36]

In practical applications, the joining direction of sheets sometimes has been determined because of special design or assembly requirements. It might not be possible to improve the joint quality by optimizing the sheet sequence. Under such circumstances, the joint quality can only be improved by optimizing the rivet and die parameters. So far, how to improve the

quality of SPR joints with a thick top sheet but a thin bottom sheet is still a challenge. In addition, most existing studies focused on the impact of sheet sequence on two-layer SPR joints. If there are three or more sheets, the arrangement of sheet sequence will become much more complicated because the sequence of the top and middle sheets may also affect the joining result. This problem was rarely discussed in the public domain, and more efforts are still needed.

2.1.1.3. Sheet thickness

The sheet thickness is also an important factor during the design of SPR joints. Because it could significantly affect the SPR process and the corresponding joint quality. For example, Zhao et al. [68] reported that the sheet thickness of aluminium alloy 5052 affected the joint fatigue life, failure mode and fretting wear behaviour. The fatigue life improved with the increase of sheet thickness (the ratio of top sheet thickness to bottom sheet thickness was kept at 1:1), and increased a greater value under a lower fatigue load. Moreover, the increment of sheet thickness transferred the fatigue failure position from the top sheet to the bottom sheet and reduced the fretting wear at the interface between two sheets in the single-lap fatigue tests. Li [34] also discovered that the increment of the top AA5754 sheet thickness could reduce the cracks on joint button when connecting with AA6008T61 bottom sheet. Moreover, the top sheet thickness imposed apparent effects on the joint static strength (i.e., the lap-shear strength and T-peel strength) and the joint failure mode.

For the SPR joints with mild steel and aluminium alloy sheets, Abe et al. [11] concluded that the sheet thickness could affect the appearance of defects in the final joint, including the penetration through the bottom sheet, the necking of bottom sheet and the separation of sheets as shown in **Figure 2.7**. These three defects were caused by the small total stack thickness, small bottom sheet thickness and large total stack thickness respectively.

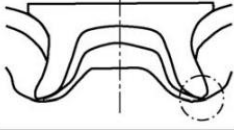

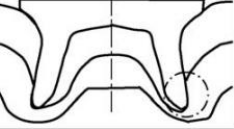
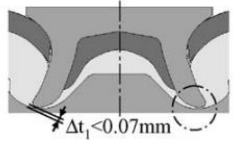
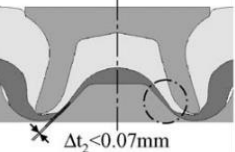
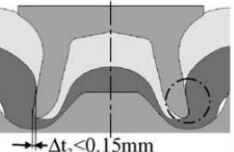
Defects	Penetration	Necking	Separation
Sheets	Steel-aluminum, $t_u=0.8\text{mm}$ and $t_f=1.5\text{mm}$	Aluminum-steel, $t_u=2.0\text{mm}$ and $t_f=0.8\text{mm}$	Aluminum-steel, $t_u=1.5\text{mm}$ and $t_f=1.6\text{mm}$
Experi mental			
Calcu lated			

Figure 2.7 Three types of defects generated in SPR joints with different sheet thicknesses (the t_u and t_f denote the top sheet thickness and the bottom sheet thickness) [11]

Haque et al. [39] also analysed the effects of sheet thickness on the quality of carbon steel SPR joints by comparing the force-displacement curves. With the interrupted experimental tests, the events occurred in the SPR process were revealed and linked with the force-displacement curves as shown in **Figure 2.8**. It was concluded that the length of the first stage decreased with the increase of stack thickness, but the force developed in this stage increased with a thicker joint because of the higher rigidity. Moreover, the displacement experienced in the second stage was dominated by the top sheet thickness. The total rivet displacement of the SPR process increased with the increase of stack thickness. Besides, it was also illustrated that the increase of sheet thickness could improve the joint strength under both cross-tension and lap-shear loading conditions [69].

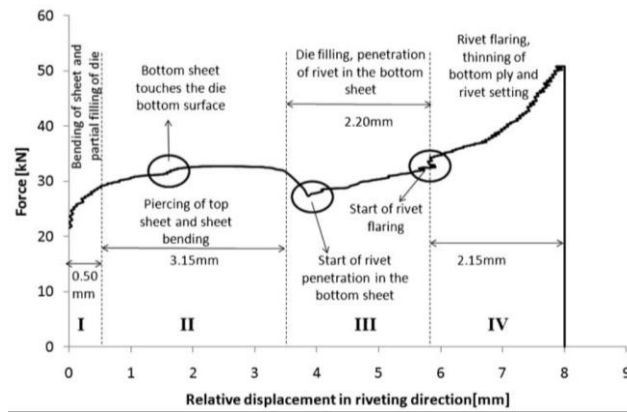


Figure 2.8 Force-displacement curve of 2.5 mm+2.5 mm carbon steel joint with rivet of 8 mm long and 555HV hardness [39]

Except for the individual top or bottom sheet thickness, the thickness ratio of top sheet to bottom sheet also plays an important role in the SPR joint quality. For two-layer AA5754 SPR joints, Mucha [44] illustrated that the increment of top to bottom sheet thickness ratio had negative effects on the interlock and the remaining bottom sheet thickness at the joint centre, but positive influences on the remaining bottom sheet thickness under the rivet tip. Xu [35] reported that, with the sheet combination changing from 1/1, 1/2, 2/1 to 2/2 (mm), the remaining bottom sheet thickness under the rivet tip increased, but the rivet flaring distance decreased in aluminium alloy AA5754 SPR joints. Moreover, the interlock achieved the maximum value with the combination of 1/2 and the minimum value with 2/1. Besides, the statistical analysis results showed that there was an interaction effect between the sheet combination and rivet length on the remaining bottom sheet thickness within the studied range.

For high strength steel and aluminium alloy SPR joints, it was mentioned in [36] that the ratio of the bottom sheet thickness to total stack thickness should not be too small to avoid no flaring of the rivet leg into the bottom sheet. The total stack thickness also should not be too small to avoid the bottom sheet rupture as shown in **Figure 2.6**. Xie et al. [70,71] illustrated that the thickness ratio of bottom sheet to top sheet played an important role in failure modes of cold-

formed galvanized steel SPR joints. The joint would fail by pulling out the rivet tail from the bottom sheet (i.e., failure mode I as shown in **Figure 2.9** (a)) if this ratio was equal to 1, but fail by tearing the top sheet and pulling out the rivet head (i.e., failure mode II as shown in **Figure 2.9** (b)) if this ratio was equal to or larger than 1.5. Whilst if this ratio was between 1 and 1.5, the joint would fail by combining the above two modes: pulling out the rivet tail from the bottom sheet and partly pulling the rivet head from the top sheet (i.e., failure mode III as shown in **Figure 2.9** (c)). Furthermore, the joint shear performance was also affected by the sheet thickness ratio [71].

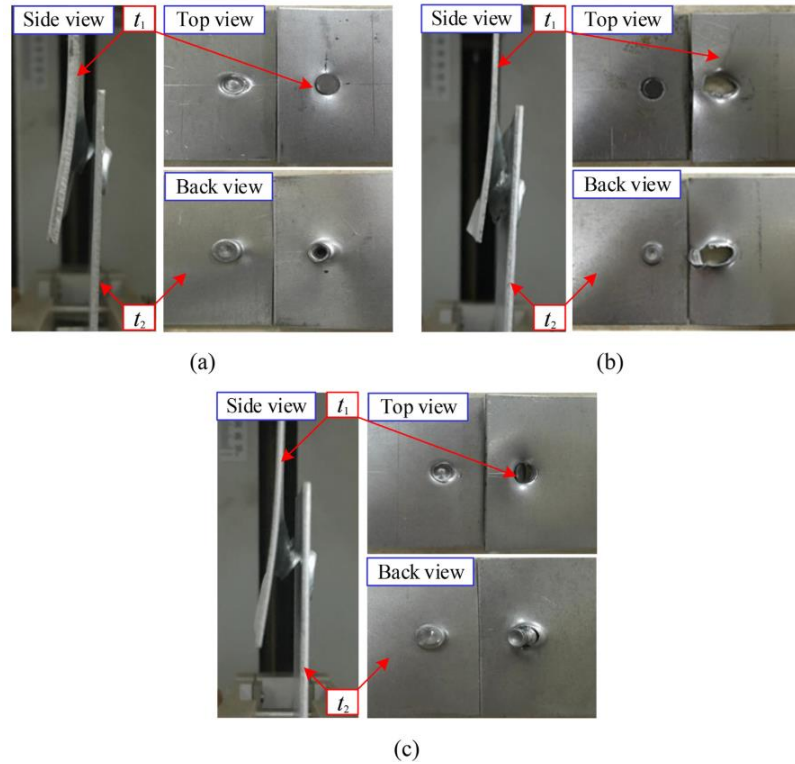


Figure 2.9 Failure modes of SPR joints with galvanized steel sheets (a) failure mode I, (b) failure mode II and (c) failure mode III [71]

2.1.1.4. Sheet surface condition

The SPR joint quality can also be altered by the sheet surface conditions. For instance, Li [54] experimentally analysed the effects of three different interface conditions between two sheets on the deformation behaviour of rivet shank, cross-sectional profile and static lap-shear strength of aluminium alloy AA5754 SPR joints. The results showed that only the grit-blasted sheets affected the riveting force, interlock and T_{\min} significantly. As for the effects on joint lap-shear strength, the significant order of these three interface conditions was grit blasting, sandpaper grinding and hot water washing respectively. Han et al. [38,73] also described the effects of E-coating and zinc plate coating on the quality of aluminium-steel SPR joints. The experimental results showed that the types of coating could affect the joint cross-sectional deformation characterises, the mechanical strength and the failure mechanisms. Moreover, the

effects of sheet coatings on the joint strength also could be changed by the setting parameters. It is necessary to optimize the setting parameters of SPR system according to sheet coatings to obtain qualified joints. Under corrosive environments, the effects of different coatings on the degradation and mechanical properties of SPR joints with aluminium alloy and steel sheets were also studied by Kotadia et al. [24]. The results showed that the joint lap-shear strength and failure mechanisms were influenced significantly by the coating types and pre-treatment ways.

Han et al. [73] investigated the effects of three interfacial conditions (i.e., uncoated, wax-based lubricant coating, inserting PTFE tape at the interface between two sheets) on fatigue life and fretting wear of aluminium alloy SPR joints. The results revealed that the joint fatigue life was affected by the different fretting behaviours with different coatings. The wax-based lubricant coating could delay the start of fretting damage and improve the joint fatigue life, which was more significant under low fatigue load levels. The PTFE insert between two sheets reduced the joint fretting damage or even eliminated the fretting at low fatigue loads, but led to reduction of the joint fatigue life. Meanwhile, the interfacial conditions in SPR joints also affected the joint load transfer mechanism and the joint failure mechanism.

2.1.2. Critical rivet parameters

The rivet is a critical component for the SPR joint, and plays an important role during the riveting process. To ensure a desired joint quality, different types of rivets have been developed considering the properties of target sheets (i.e., materials, thickness and number of layers). Roughly, the self-piercing rivets can be categorized into countersunk and pan types according to the rivet head geometry, or categorized into semi-tubular, hollow tubular [62] and solid types according to the rivet shank geometry. **Figure 2.10** shows four different types of rivets frequently used in the SPR process [74]. The shape of rivet head can affect the maximum riveting force required and influence the size of gap formed between the rivet head and the top sheet. The shape of rivet shank directly affects the rivet stability during the joining process, and should be selected carefully according to the sheet combination. Among these different types of rivets, the countersunk head semi-tubular rivet is the most commonly used in the automotive industry. There are many parameters involved to fully describe a countersunk head semi-tubular rivet, including the rivet material, rivet shank diameter, rivet length, rivet tip geometry and rivet coating as shown in **Figure 2.11**. All these factors will directly affect the rivet flare behaviour, and then influence the SPR joint quality. Therefore, it is important to choose the proper rivet parameters to obtain a sound joint. A lot of literature has explored the influences of these rivet parameters on the riveting process and joint quality from different aspects.

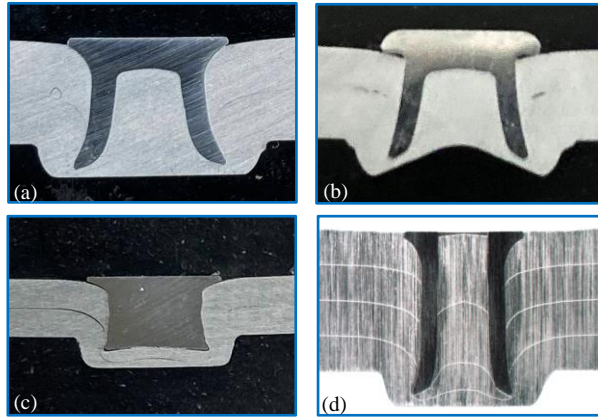


Figure 2.10 Cross-sectional profiles of different rivets (a) a countersunk head semi-tubular rivet, (b) a pan head semi-tubular rivet, (c) a countersunk head solid rivet and (d) a countersunk tubular rivet [74]

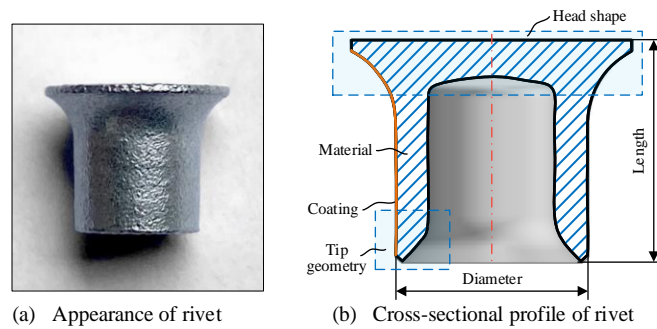


Figure 2.11 Schematics of critical rivet factors affecting the SPR joint quality

2.1.2.1. Rivet material

The rivet material can directly affect the rivet stiffness, and therefore influence the flare behaviour and stability of the rivet shank. To make sure that the rivet can successfully pierce into the sheets, the strength of the rivet material should be much higher than that of the sheet material. At the same time, to allow the rivet shank flaring into the bottom sheet sufficiently, the strength of the rivet material cannot be too high. Moreover, the rivets made of the same material are usually manufactured into different hardness levels or strength levels to meet the requirements for different sheet materials. In addition, the rivet material also has influences on the recyclability of the riveted structure [32,75] and the complexity of the rivet manufacturing process [76,77].

The most commonly used material for SPR rivets is boron steel in the automotive industry. There are also other types of materials that can be used for rivets. For example, Abe et al. [75] successfully connected the aluminium alloy A5052 sheets with the aluminium alloy A6061 rivet by optimizing the rivet and die geometries, and thus simplified the recycling of the riveted parts. Hoang et al. [32] employed the aluminium alloys 6082-T6, 7108-T5, and 7278-T6 instead of steel as the rivet materials to resolve the recycling problem, and studied the performances of these three kinds of aluminium alloys rivets. The results showed that the

AA7278-T6 rivet could join two aluminium alloy 6060-W sheets, but failed to join two aluminium alloy 6060-T4 and 6060-T6 sheets due to the rivet fracture. Besides, compared with the conventional steel rivet, the application of aluminium alloy rivet reduced the maximum riveting force and the displacement at maximum force, but decreased the joint interlock and mechanical performance to certain extends. It should also be noticed that the die geometry needed to be optimized accordingly to cooperate with the aluminium alloy rivet and to obtain a qualified SPR joint. Subsequently, the fracture mechanisms of the SPR joints connected by AA7278-T6 rivets were also investigated [78]. Uhe et al. [76] employed rivets made of stainless steel (i.e., high nitrogen steel 1.3815) to connect the high strength steel HCT780X and the aluminium alloy EN AW-5083 sheets, and evaluated the mechanical strength of the riveted joints. Compared with traditional steel rivets, the manufacturing process of stainless steel rivets is much simpler because coating and heat treatment are not required [77].

Variation of the rivet hardness can change the yield strength of rivet material, which will impose significant influences on the flaring behaviour of rivet shank during the riveting process. With the increment of the rivet hardness, it becomes easier for the rivet shank to pierce through the top sheet but may bring difficulties for the rivet shank to flare into the bottom sheet. The effects of rivet hardness on the SPR joints with two carbon steel sheets were investigated by Haque et al. [39]. It was uncovered that the rivet hardness altered the joint quality by affecting the riveting force at different stages of the force-displacement curve. Increment of the rivet hardness had negative effects on the lengths of the first stage and fourth stage (i.e., rivet flaring, thinning of bottom sheet as shown in **Figure 2.8**), but positive effects on the length of the third stage (i.e., die filling, penetration of rivet in bottom sheet), which led to less rivet shank flare and therefore a smaller interlock. Zhang et al. [33] studied the effects of rivet hardness on the SPR joints with dissimilar aluminium-lithium alloy AL1420 and titanium TA1 sheets. The results indicated that the rivet hardness could apparently affect the joint static performance and fatigue behaviours. Mucha [53] also numerically studied the influence of rivet material's yield strength on the AA5754 SPR joint quality by modifying the material plastic stress-strain curve.

2.1.2.2. Rivet diameter

The rivet diameter also affects the rivet performance. Two rivet diameters are normally designed for the semi-tubular countersunk rivet in the automotive industry, including 3.35 mm (nominal value 3 mm) and 5.3mm (nominal value 5 mm) [2]. The 3 mm diameter rivets produced by Henrob Ltd. are suggested to connect steel sheets up to 3 mm or aluminium sheets up to 5 mm. The 5 mm diameter rivets are designed for steel sheets up to 6 mm or aluminium

sheets up to 10 mm [25]. The effects of the rivet diameter on static strength and fatigue life of aluminium alloy 5754 joints were analysed by Fu et al. [79] using the statistical analysis method. Within the studied ranges, it was found that the rivet diameter did not affect the joint static strength significantly, but had a slightly higher contribution to the joint fatigue life than the rivet length, rivet hardness and rivet coating. For SPR and adhesively bonded hybrid joints, the rivet diameter showed significant effects on the joint failure mechanisms [80].

2.1.2.3. Rivet length

The rivet length is also an important factor for the SPR joint quality, and is usually selected according to the top sheet thickness and the total sheet thickness. To form a reliable mechanical interlock, the rivet length should be large enough to allow the rivet shank to flare sufficiently into the bottom sheet after penetrating the top sheet. Whilst it should also not be too long to avoid undesired remaining bottom sheet thickness or even penetration of the bottom sheet. Generally, a longer rivet is necessary for a thicker stack [39]. Researchers have made considerable efforts to investigate the influences of rivet length on the joint quality. For instance, Xu [35] illustrated that for aluminium alloy AA5754 SPR joints, the increment of rivet length had positive effects on the interlock and rivet flaring distance, but had negative effects on the remaining bottom sheet thickness under the rivet tip. Moreover, it was also found that there was an interaction effect between the rivet length and sheet combination on the remaining bottom sheet thickness, and an interaction effect between the rivet length and die type on the rivet flaring distance. The same conclusions for SPR joints of aluminium alloy AA6061-T6 and dual-phase high strength steel DP590 were made by Jin et al. [81]. The importance of rivet length on the SPR results of two-layer high strength steel and aluminium alloy sheets was also emphasized by Abe et al. [36]. The results demonstrated that rupture of the bottom sheet might occur when the ratio of the rivet length to the total sheet thickness (R_n) was too large, whilst no flaring of the rivet shank into the bottom sheet might happen when this ratio was too small. Besides, it was also investigated that the rivet length had the same effects on the riveting results of three-layer steel and aluminium alloy sheets [43]. Xie et al. [70,71] also concluded that the rivet length has significant effects on the shear strength of SPR joints. For the studied sheet combination, the joint shear capacity and stiffness increased firstly and then decreased with the increment of rivet length. An empirical model was proposed to determine the optimal rivet length based on the thickness of two steel sheets.

2.1.2.4. Rivet shank geometry

The rivet shank geometry has significant influences on the rivet performance, including the rivet tip angle, rivet shank length, inner and outer diameters of rivet shank as shown in **Figure**

2.12. The rivet tip angle directly affects the degree of difficulty for the rivet shank to pierce through the top sheet [82]. The rivet shank length, inner and outer diameters significantly influence the stability and bendability of the rivet shank. Meanwhile, for rivets with a constant length, variation of the shank length will affect the volume of rivet cavity, and thus change the interactions between the rivet shank and sheet materials filled in the rivet cavity [83]. As a result, changes of these factors will alter the flare behaviour of rivet shank and the final joint quality. Some studies have been conducted to explore the impact of rivet shank geometry on the SPR joint quality and joint mechanical strength. For example, Jiang et al. [83] experimentally studied the influences of three rivet shank geometric parameters, including the rivet tip angle, inner diameter and rivet shank length, on the final quality and mechanical properties of CFRP/Al and steel/Al joints as shown in **Figure 2.13** (a). The results showed that the increment of the rivet tip angle imposed positive influences on the interlock formation in CFRP/Al joints but negative effects in steel/Al joints. Li et al. [82] experimentally found that the aluminium alloy AA5754 SPR joint connected with the rivet with a sharp tip (see **Figure 2.13** (b)) achieved larger interlock and minimum remaining bottom sheet thickness (T_{\min}) than that with a blunt tip, and thus had a higher lap-shear strength. By optimizing the rivet geometry, Uhe et al. [38] realized the connection of two kinds of material combinations with one type of rivet, i.e., two-layer high strength steel sheets, and two-layer aluminium alloy and high strength steel sheets. The rivet geometry was improved by numerically analysing the material flow, deformation behaviours, stress and strain conditions during the SPR process. The optimal rivet owned larger hole depth and bevelled rivet shank, and could avoid the defects of the rivet compression and the bottom sheet fracture in these two material combinations respectively.

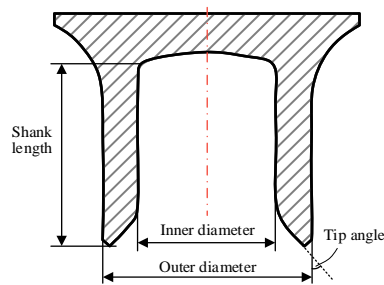


Figure 2.12 Schematic of geometric parameters of the semi-tubular countersunk rivet

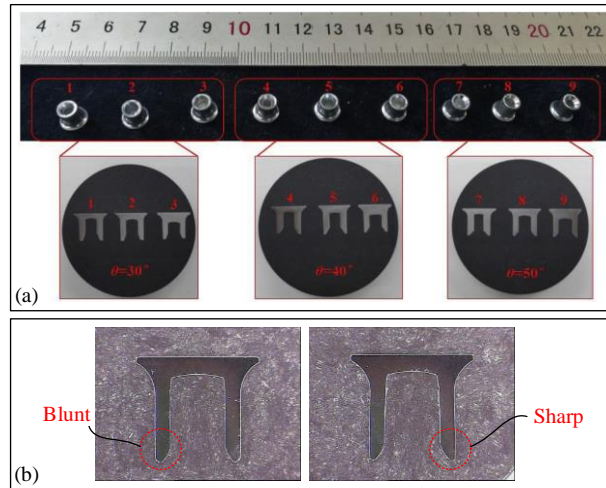


Figure 2.13 Different geometries of (a) rivets with varying rivet tip angles, leg lengths and inner diameters [83] and (b) rivets with a blunt or sharp tip [82]

2.1.2.5. Rivet coating

The rivet coating can not only affect the joining result, but also is important for the corrosion resistance of SPR joints. Different types of coatings have been applied on rivets to optimize the SPR joint performance under different conditions. For example, Karim et al. [61] investigated the effects of Almac[®]- and Zn-Ni-coated rivets on the corrosion resistance and the subsequent strength degradation of CFRP-aluminium alloy joints. The experimental results showed that the strength loss of Almac[®]-coated SPR joints was more than three times higher than that of Zn-Ni-Coated SPR joints due to severe rivet head corrosion. This was caused by the strong galvanic coupling between the Almac[®]-coated rivet head and the CFRP sheet, which directly led to the dissolution of the rivet head coating and early initial corrosion of the rivet base metal. Therefore, the mechanical locking between the rivet head and the top sheet significantly decreased in the Almac[®]-coated SPR joints. On the contrary, the corrosion resistance of Zn-Ni-coated SPR joints improved because of the weak galvanic coupling between the top sheet and the Zn-Ni-coated rivets. Furthermore, the frictional influence of these two rivet coatings on the quality and strength of aluminium alloy joints were also studied [84]. Due to the lower friction coefficient, the joints with Zn-Ni-coated rivets had a smaller rivet head height and a larger interlock under similar riveting conditions. While with similar joint quality, the joint with Almac[®]-coated rivets demonstrated higher lap-shear and cross-tensile strength because of the larger friction coefficient. Esfahani et al. [85] also reported that the Zn-Sn coating and Al coating experienced different deformations during the laser assisted self-pierce riveting.

2.1.2.6. Other types of rivets

Except for the commonly used self-piercing rivets, some new types of rivets were developed to realize the mechanical connection. For example, Kraus et al. [86] proposed a new self-flaring rivet as shown in **Figure 2.14** (a), and realized the self-flaring process without a die. Three mandrels were designed and arranged radially under the rivet head instead of the tubular shank, and completed the connection between two sheets at three points instead of a circle. Huang et al. [87,88] proposed an inner flange pipe rivet to connect aluminium alloy Al6063 sheets, as shown in **Figure 2.14** (b). The lap-shear testing results showed that the joint with a flange pipe rivet had higher strength than that with a conventional rivet. By optimizing the geometry of double-side self-piercing rivet, Alves et al. [89] successfully connected the polymer sheets at room temperature with the formed invisible lap joints as shown in **Figure 2.14** (c). Then, the same authors further extended the double-side self-piercing riveting technique to join dissimilar aluminium alloy AA5754-H111 and polyvinylchloride sheets with the proposed two-stroke riveting process [90].

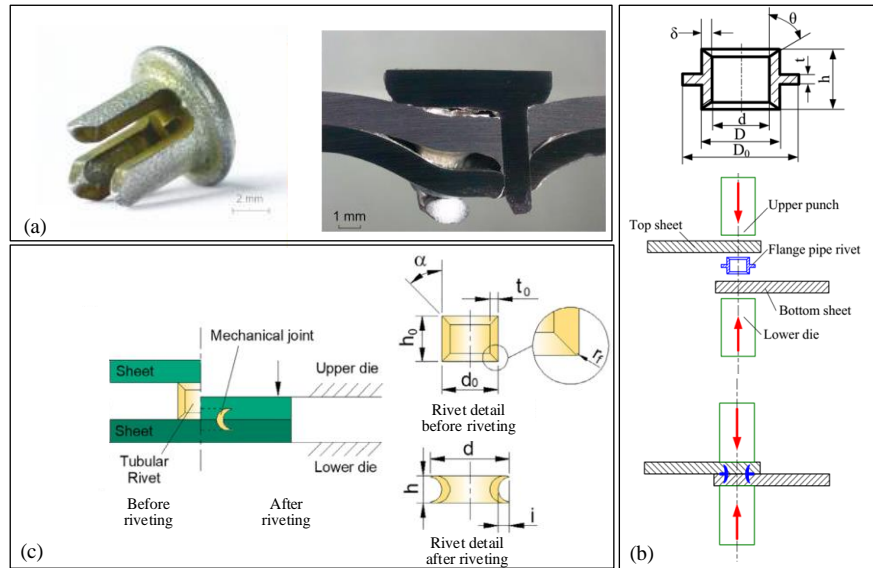


Figure 2.14 Different geometries of (a) a new self-flaring rivet [86], (b) an inner flange pipe rivet [87] and (c) a double-side self-piercing rivet [89]

2.1.3. Critical die parameters

During the SPR process, the die provides strong support on the riveted sheets, and guides the rivet to flare effectively into the bottom sheet to form the mechanical interlock. Dies are usually made of high strength tool steels to avoid plastic deformation [2]. The die geometry has critical influences on the flare behaviour of rivet and the plastic deformations of connected sheets. Figure 2.15 shows the cross-sectional profiles of dies employed in some published studies. Although the shapes of these dies are different from each other, they could be roughly categorized into the flat die and pip die according to whether the bottom of the cavity is flat

or has a bulge in the middle. **Figure 2.16** (a) shows the appearances of a flat die and a pip die frequently used in the automotive industry. There are many parameters involved to describe the die cavity profile, including the die diameter, die depth, die pip height, the angles of different sidewalls, the different chamfer values and so on, as shown in **Figure 2.16** (b). The influences of these parameters on SPR joints have been investigated by many researchers.

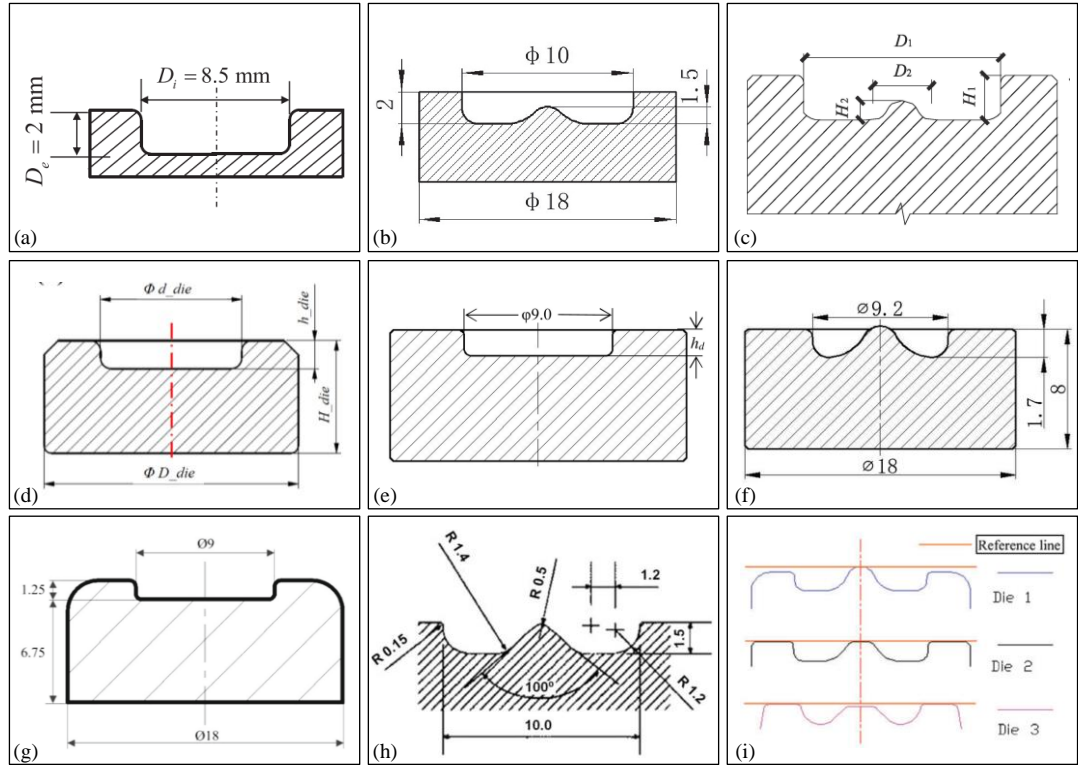


Figure 2.15 Cross-sectional profiles of dies from published studies of (a) [91], (b) [92], (c) [93], (d) [52], (e) [94], (f) [95], (g) [96], (h) [97] and (i) [35]

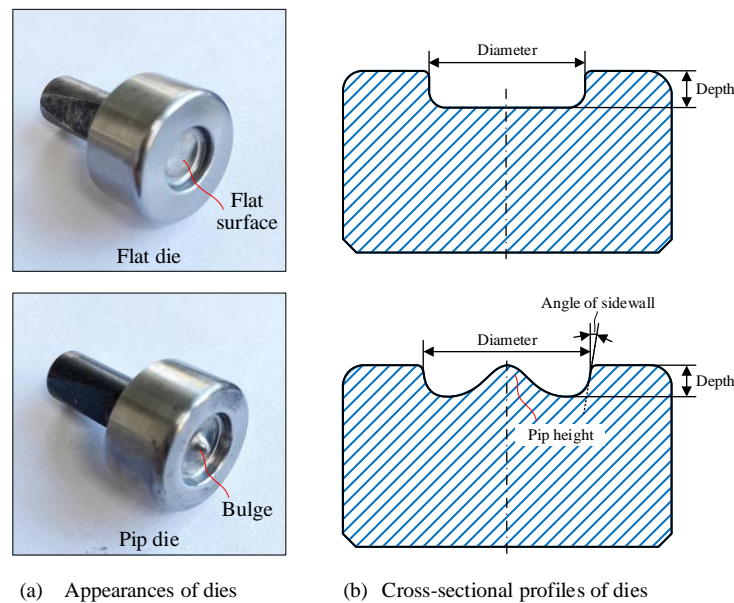


Figure 2.16 Schematics of the flat die and pip die parameters affecting the SPR joint quality

2.1.3.1. Flat die vs. pip die

The flat die and pip die have different guidance effects on the formation of SPR joints. Compared with the flat die, the pip die can apply a supporting force around the joint centre at an earlier time and impose a stronger guidance effect on the rivet shank flare [41]. A large amount of bottom sheet material will accumulate around the joint centre with the flat die. Whilst the bottom sheet material around the joint centre will partially flow outward with the pip die, which is helpful for the interlock formation. The performances of flat die and pip die have been widely analysed and discussed in some studies. For example, Kam et al. [31] experimentally compared the performances of five different flat dies and pip dies for SPR joints with dissimilar 1.5 mm vibration-damping steel and 1.2 mm aluminium alloy Al5052 sheets. It was found that the largest joint tensile shear load was obtained with one flat die. Moreover, the interlock and mechanical performance of joints decreased with the increase of the flat die taper angle and diameter due to the increase of die volume. The influences of pip die and flat die on the SPR process were also illustrated by Hoang et al. [32]. The experimental results showed that the adopted flat die had a better performance than the pip die in the connection of aluminium alloy AA6060-W sheets using an aluminium alloy AA7278-T6 rivet. Moreover, Haque et al. [39] studied the effects of die geometry on the riveting force of SPR joints with two carbon steel sheets. By comparing the recorded force-displacement curves, it was found that the die volume had significant effects on the riveting force of the third stage shown in **Figure 2.8**. Deng et al. [40] also experimentally and numerically investigated the influences of die type and geometric parameters on the SPR joint of aluminium alloy AA6061-T6 and mild steel SPF340. It was discovered that the geometric parameters of die cavity, especially the pip height, had significant effects on the joint quality within the studied range. The die with a moderate convex could avoid the generation of cracks on the bottom sheet by reducing the tangential tensile stress. Moreover, the SPR joints manufactured with a single conical-section die showed higher tensile strength and energy absorption than joints with a double conical-section die. Liu et al. [41] numerically compared the riveting processes with a flat die and a pip die. The simulation results showed that the existence of die pip speeded up the penetration of top sheet, led to a greater rivet shank flare but resulted in a higher maximum riveting force. A uniformly distributed bottom sheet was observed with the pip die, but a large variation of the remaining bottom sheet thickness was found with the flat die. Furthermore, it was also concluded that the flaring speed of the rivet shank depended heavily on the filling condition of the die cavity underneath the rivet cavity. A rapid flare of the rivet shank was observed after this space was fully filled.

2.1.3.2. Flat die parameters

For the flat die shown in **Figure 2.16** (a), the die diameter and depth are the two most important geometric parameters, and their magnitudes are usually selected based on the target sheet properties (e.g., material and thickness). Increment of the die diameter will involve more sheet material into the joining region, and thus reduce the stack stiffness. Whilst increment of the die depth will delay the appearance of fast riveting force increase, which is helpful to avoid the premature compression of rivet shank when piercing the top sheet but has negative influences on the rivet shank flare. For example, Li et al. [34,98] investigated the effects of two flat dies (i.e., DF and DC dies shown in **Figure 2.17**) on the quality of SPR joints with aluminium alloys AA5754 and AA6008T61 sheets. Due to the smaller diameter but larger depth, the DF die caused severe bending and tensile deformation of the bottom sheet, which resulted in cracks generated on the joint button. In contrast, the DC die had a larger diameter, a smaller depth and a truncated sidewall, which reduced the deformation level of bottom sheet and alleviated the generation of cracks on the joint button. For the mechanical behaviours, the SPR joints produced using the DF die demonstrated a smaller lap shear fatigue resistance because of the lower residual contact stress and severe cracks. Whilst the die type did not show obvious influences on the joint T-peel fatigue resistances and the fatigue modes. Moreover, the importance of the die diameter and die depth on the SPR joint quality varies from joint to joint, and thus should be analysed according to the specific sheet configurations. Haque et al. [69] illustrated that the die depth played a significant role in the deformation behaviour of the sheet material. A greater effective length of the rivet into the bottom sheet was achieved with a deeper die, and resulted in a higher joint mechanical strength within the studied range.

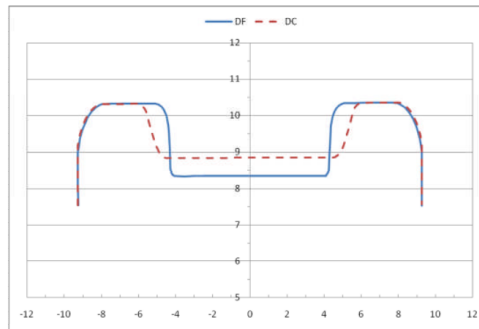


Figure 2.17 Cross-sectional profiles of the DF and DC dies employed by Li et al. [98]

2.1.3.3. Pip die parameters

For the pip die shown in **Figure 2.16** (b), the die diameter, depth and pip height are the three most important parameters. The impact of diameter and depth of the pip die on the joining process is similar to that of the flat die. The magnitude of pip height directly determines when the supporting force will be applied at the joint centre, and imposes varying influences on the

sheet deformation behaviour. With the decrease of the pip height, the performance of pip die will become more and more similar to that of flat die. Many studies have been carried out by researchers to explore the effects of different pip die parameters on the joining results.

For example, Jäckel et al. [42] numerically investigated the influences of five pip die parameters on the aluminium alloy SPR joint quality with a 2D simulation model. The sensitivity analysis results revealed that the die depth and die diameter were the most important factors for the interlock and the material damage value of the bottom sheet, which was related to the cracks generated on the joint button. Mucha [53] reported that the pip die geometry could significantly affect the riveting force and the quality of aluminium alloy SPR joints. Decrease of the die depth or die pip height was beneficial for both the interlock and the remaining bottom sheet thickness. For SPR joints with aluminium alloy AA6061-T6 and dual-phase high strength steel DP590 sheets, Jin et al. [81] also illustrated that the die diameter was the second important parameter for the interlock and the remaining bottom sheet thickness under the rivet tip, whilst the die depth was the most significant factor for the remaining bottom sheet thickness near the pip sidewall. Moreover, with the increment of die diameter, the remaining bottom sheet thickness under the rivet tip increased but the interlock showed a decreasing trend within the studied range. Han et al. [99] also numerically studied the main effects of nine independent pip die parameters on the interlock and the remaining bottom sheet thickness of magnesium alloy SPR joints. The importance sequences of the pip die parameters were obtained using the range analysis method. The results indicated that the die diameter and die depth are the most important parameter for the interlock and minimum remaining bottom sheet thickness respectively. Moreover, the optimal combination of these nine parameters was also selected to obtain the best joint quality. The experimental results from the studies conducted by Abe, Kato and Mori [11,36,43] showed that the die geometry was more important for the ultra-high strength steel (SPFC980) sheet than the mild and high strength steel sheets (i.e., SPCC, SPFC440 and SPFC590) when connected with the aluminium alloy A5052-H34 sheet. Because it is easy to cause insufficient driving through the top sheet or fracture of the bottom sheet due to the high hardness and low ductility of the ultra-high strength steel. The increment of the die diameter and decrease of the die pip height could effectively reduce the riveting force when piercing through the middle sheet as shown in **Figure 2.18**. By properly optimizing the die profile, the joining range of the harder sheets was successfully extended as shown in **Figure 2.19**. Similarly, by analysing the rivet and sheets deformation behaviours with a FEA model, Mori et al. [100] also optimized the pip die parameters for SPR joints of ultra-high strength steel and aluminium alloy. It was verified that the optimized die with a larger diameter, larger die depth and smaller die pip height was beneficial for the rivet to pierce through the upper ultra-high strength steel sheet and flare into

the lower aluminium alloy sheet, and could also avoid the appearance of defects, including rivet shank compression, fracture and bending.

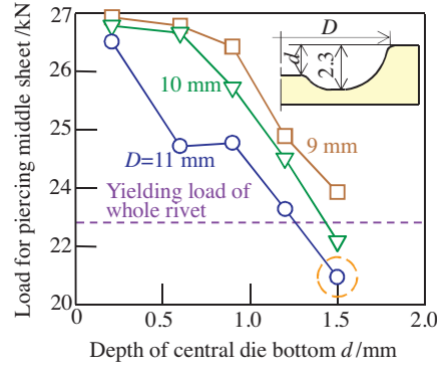


Figure 2.18 Relationship among the die diameter (D), depth of central die bottom (d) and the load for piercing middle sheet in 1.0 mm SPFC980+1.0 mm SPCC+2.5 mm A5052 SPR joints [43]

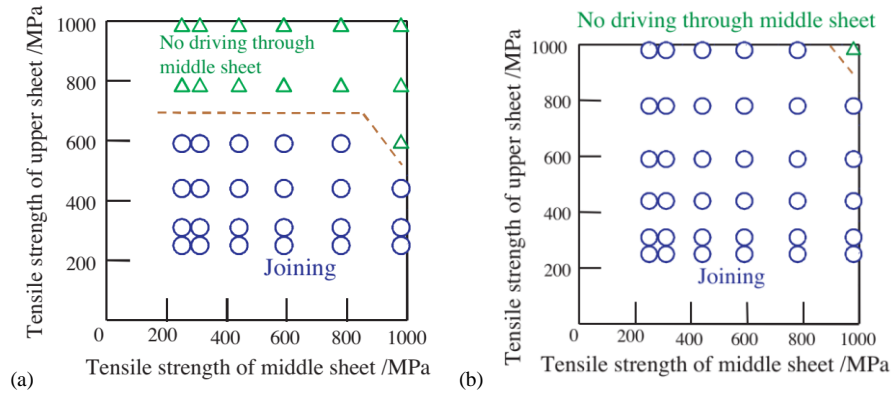


Figure 2.19 Relationships between the joinability and tensile strength of top and middle steel sheets with an aluminium alloy bottom sheet using (a) a conventional die and (b) an optimized die [43]

2.1.3.4. Interaction effects between the rivet and die

During the SPR process, the rivet and die work together to influence the joint formation and the final joint quality [35]. Therefore, in addition to individual effects of rivet or die parameters, the interaction effects between the rivet and die on the joining results are also important and necessary to be considered in the design of SPR joints. The Die-to-Rivet volume ratio is one of the most important factors to describe the matching degree between the selected rivet and die. Ma et al. [101] compared the performances of seven rivet and die combinations with different Die-to-Rivet volume ratios on the rivetability of SPR joints with aluminium alloy AA6061 and mild steel sheets. It was concluded that the rivetability range expanded with the softer rivet and larger die, but narrowed with the longer rivet and smaller die. The results also indicated that the Die-to-Rivet volume ratio should be slightly larger than 1.0 in order to achieve a qualified SPR joint. Similarly, Lou et al. [102] also obtained the same conclusions and emphasised the importance of the Die-to-Rivet volume ratio to the SPR joint quality. In addition to the Die-to-Rivet volume ratio, the rivet length should also match with the die depth

to avoid undesired remaining bottom sheet thickness. More efforts are still required to better understand the interaction effects between the rivet and die parameters.

2.1.4. Other critical setting parameters

Except for the above-mentioned sheet, rivet and die parameters, some other setting parameters may also affect the SPR joint quality and mechanical performance to varying degrees, such as the joining velocity, specimen configuration, distance from the rivet to sheet edge and so on. Some studies have been conducted to explore the influences of these setting parameters. For the velocity controlled SPR system, the initial punch velocity will directly affect the amount of energy carried by the punch and therefore affect the riveting result. Han et al. [30] experimentally found that the increment of riveting speed could lead to a smaller rivet head height, a greater interlock but a higher maximum riveting force. The influence of riveting speed on the joint shear strength depended on the joint quality and the consequent failure modes. For rivet pull-out failure, the increment of riveting speed imposed positive effects on the joint strength. But for mixed failure modes of rivet pull-out and sheet failure, the joint strength was determined by the sheet material strength.

For a specific sheet combination, different specimen configurations will lead to different joint mechanical performance. For example, the effects of specimen configuration on the joint static strength and failure mechanism were analysed by Han et al. [103] with the three-layer joints of 2.0 mm AA6111+1.5 mm NG5754+2.0 mm NG5754. Three groups of specimen configurations (i.e., G12, G21 and G111) were employed during the lap shear tests and T-peel tests as shown in **Figure 2.20**. The experiment results showed that the G111 group achieved the highest joint static strength and energy absorption, whilst the G21 had the lowest mechanical property. For the G21 specimens, the interlock failure was the only failure mode. While for the G111 group, the sheet material failure was observed in the lap shear test, but the interlock failure was captured in the T-peel test. For the G12 group, both interlock failure and sheet material failure happened in lap shear and T-peel tests.

By affecting the deformation behaviours of the connected sheets, especially the bottom sheet, distance from the rivet to the sheet edge can also influence the final SPR joint quality [113]. Li et al. [104] reported that the increment of the edge distance, either by varying the rivet pitch or by changing the specimen width, improved both the joint lap-shear strength and coach-peel strength. Besides, for the SPR joints made of two-layer 2.0 mm aluminium alloy AA5754 sheets, it was found that 11.5 mm was the optimal edge distance to achieve less joint distortion and higher strength. The 8.0 mm was the minimum edge distance to obtain the low deformation level and reasonable joint strength. Moreover, the fatigue performance of SPR joints was also affected by the edge distance.

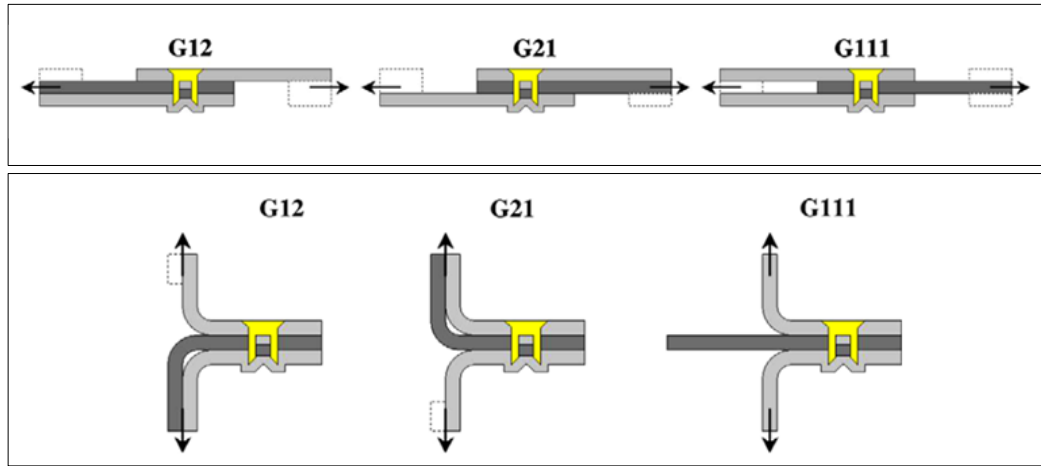


Figure 2.20 Schematics of three specimen configurations for (a) lap shear test and (b) T-peel test [103]

2.2. Quality prediction models of SPR joints

So far, the experimental SPR test is still the most reliable and frequently used approach to evaluate the quality of new SPR joints in the automotive industry. However, due to the complex effects of various joining parameters, numerous experimental tests are usually required before identifying the desirable joint design, which takes a lot of time and financial investment. Therefore, to reduce the number of experimental tests required and speed up the design process of new joints, different quality prediction models for SPR joints have been developed by researchers [105]. The existing prediction models can be classified into three groups according to the adopted methods, including the FEA simulation model, mathematical prediction model and ANN prediction model.

2.2.1. FEA models

During the last two decades, a great number of FEA models for SPR joint quality prediction have been developed, and their effectiveness was intensively verified through experimental SPR tests [2]. As a quasi-static problem, the SPR process can be simulated with both the implicit method and explicit method. Many types of commercial software can be used to simulate this process, including ABAQUS [106], LS-DYNA [107,108], DEFORM [42], MSC.Superform [109,110], MSC Marc [53,111], Forge2005 [112] and Simufact.Forming [113,114]. To improve efficiency, the SPR was assumed as an axisymmetric process in most existing studies and simulated with two-dimensional (2D) models [107,112,115]. Whilst there are also some three-dimensional (3D) models reported in the public domain [116]. In addition to predicting the joint quality, the FEA model for the SPR process can also provide useful information inside the riveting region that is hard to be accessed with the experimental method.

To properly describe the deformation behaviours of the rivet and sheets during the SPR process, different types of material constitutive models have been utilized, including the Power law hardening rule [117], Johnson and Cook material model [109], extended Voce isotropic hardening model [32,78], Voce hardening model [32,118], Ludwik hardening model [48,119], Krupkowski power law [120], Classic Hockett-Sherby model with a linear term [114] and Swift hardening law [121]. The unknown coefficients in these constitutive models are usually identified through experimental tensile test and inverse method. For simplicity, isotropic behaviour is assumed for sheet materials in the majority of accessible papers. However, because of the employed manufacturing technique, the sheets actually demonstrate an anisotropic deformation behaviour. The kinematic hardening law might be a more appropriate option [121]. Moreover, the mechanical properties of some materials are very sensitive to the temperature and strain rate. So taking the thermal softening and strain rate hardening effects into account will be beneficial for a higher prediction accuracy of FEA model. For instance, Carandente et al. [113] established a 2D model of SPR process in which the thermal softening and strain hardening effects on the sheet material strength were considered. Qu and Deng [109] also presented a 2D thermal-mechanical axisymmetric model using MSC.Superform to predict the joint deformation during the SPR process. However, the influences of temperature and strain rate effects on the sheet properties were neglected in most of the developed FEA models. So far, FEA models for SPR joints with similar or dissimilar sheet materials have been successfully developed, such as AA6181+AA6181 in [48], AA5754+AA5754 in [113], 6111T4+HSLA340 in [117] and DP600 + AA5182-O in [122].

During the riveting process, strong interactions will occur at the interfaces of contact parts, such as between the rivet and sheets, between the targeted sheets, and between the bottom sheet and die. Friction laws are generally used to model this phenomenon, including the constant shear friction factor law [106], the Coulomb friction law [107,109,113], and the combination of Coulomb friction law and shear friction law [114]. The magnitudes of friction coefficients will directly affect the friction forces at the contact interfaces, and thus influence the predicted deformation behaviours of the rivet and sheets [78]. Therefore, it is very important to correctly identify these friction coefficients used in the FEA model. Due to the difficulties to experimentally measure the friction coefficients at different interfaces [123], the inverse method is still the most simple but effective way and has been widely utilized in most existing SPR simulation models [106]. Some studies were conducted to investigate the impact of different friction coefficients on the simulation results [108]. For instance, Han et al. [124] explored the effects of friction coefficients on the predicted quality of SPR joints with AZ31 magnesium alloy sheets and 14NiCr14 rivet with the developed FEA model in DEFORM-2D. By comparing the simulation and experimental test results, Porcaro et al. [125] reported that

the friction coefficient between the rivet and sheets was not consistent for all the simulations, but a function of the rivet type and sheet thickness. With the help of a 2D FEA model, Mucha [53] numerically studied the influences of the friction coefficient between the rivet and sheets. Based on the simulation results from a 3D FEA model in ABAQUS, Moraes et al. [126] successfully proposed several multiple linear prediction models to optimize/adjust the friction coefficients used in the simulation model.

Modelling of the top sheet separation/fracture during the SPR process is also critical for the prediction accuracy of FEA model. In general, two algorithms are frequently utilized in the existing studies to simulate this phenomenon [127]. The first method is based on the geometrical criterion [32,53], and the second one relies on different material damage criteria. As for the geometrical criterion, only a threshold minimum thickness of the top sheet needs to be defined and no special data related to the sheet material is required. The top sheet will be penetrated by the rivet shank once the threshold thickness is reached during the simulation process. The value of threshold minimum thickness can be easily determined by comparing the joint cross-sectional profiles obtained from experiments and simulations. It needs to be noticed that this approach is suitable for top sheets made of ductile materials but becomes incapable for top sheet sheets made of low ductility or brittle materials, in which cracks occur and propagate at an early stage of the SPR process [113]. As for the second approach, the material failure criteria need to be selected based on the failure mode of the sheet material. The frequently employed material damage criteria include the Gurson-Tveergaard-Needleman (GTN) damage model [128], the Cockcroft-Latham damage law [109,129], the Lemaitre damage law [112,127], the Ductile Damage Model [130], the Bonora damage model [48], the Johnson-Cook damage model and the Forming limit diagram (FLD). Once one of the pre-defined failure criteria is satisfied, the elements that reach the critical damage value will be deleted from the simulation model and then the fracture of top sheet will happen [117]. To avoid too large volume loss caused by elements deleting, a small mesh size is required around the area where the material failure may occur. This approach is effective for top sheets made of ductile or brittle materials as long as a proper material failure criterion is chosen. In addition, except for the modelling of top sheet fracture, the second approach can also be extended to simulate the fractures of bottom sheet and rivet.

Mesh sizes of the rivet and sheets have critical influences on the simulation efficiency and accuracy. A suitable mesh size should be capable of producing an accurate simulation result without increasing too much simulation time. Sensitivity study of element mesh size is usually performed to determine the suitable mesh sizes when establishing a simulation model. Some studies have been conducted by researchers to explore the influences of element mesh size. For instance, Casalino et al. [131] explored the effect of sheet mesh size and threshold of the

failure criterion on the simulation results using a 2D simulation model in LS-DYNA. The results revealed that decreasing the mesh size of sheets without increasing the threshold value of failure criterion may lead to an earlier fracture of top sheet, whereas increasing the threshold value of the failure criterion without reducing the mesh size may cause instability problem for the rivet shank. Hoang et al. [78] numerically studied the effect of rivet mesh size on the SPR process. It was found that the rivet mesh size has no influence on the force-displacement curve, but a slight influence on the value of plastic strain, which increased somewhat with the decreasing of the rivet mesh size.

Until now, most of the FEA models for SPR process are developed based on the lagrangian method. Some studies also employed new simulation techniques to develop simulation models for SPR process. For example, Ishikawa and Aihara [132] simulated the SPR process using Arbitrary Lagrangian-Eulerian (ALE) approach, Coupled Eulerian-Lagrangian (CEL) approach and Smoothed Particle Hydrodynamic (SPH) method respectively in Abaqus/Explicit. It was found that the ALE method is not suitable because the upper sheet blanking could not be modelled. As for CEL approach, although the fracture of top sheet could be modelled, it required enormous CPU time which limited the application of this method. In contrast, the simulation results showed a possibility of using SPH method to simulate the SPR process. Huang et al. [133] simulated the SPR process using Smoothed Particle Galerkin (SPG) method combined with the largrangian method in LS-DYNA explicit with a 3D model. The material of the top sheet within the riveting zone was modelled using SPG particles, while other parts were modelled using largrangian elements. A bond-based failure criterion was introduced to model the fracture of the top sheet. A reasonable agreement between the simulation and experimental results was achieved in terms of the joint cross-sectional profile.

Taking the advantage of the high prediction accuracy of FEA models, numerical studies were also conducted by researchers to investigate influences of different joining parameters on the joining results. For example, Hoang et al. [78] numerically investigated the effects of different macroscopic parameters (i.e., fraction between the rivet and sheets, rivet mesh size) and the microscopic parameters (i.e., hard particles and narrow soft zones) on the fracture behaviour of the rivet shank. Han et al. [99] numerically studied the main effects of nine independent die parameters on the SPR joint quality, including the interlock and the remaining bottom sheet thickness. Jäckel et al. [42] also numerically studied the influences of five die geometrical parameters on the joint quality. Atzeni et al. [116] combined the established 3D FEA model with other optimization algorithms to facilitate the selection of rivet and die. Mucha [53] numerically evaluated the effects of the rivet material properties and the die geometries on the joint interlock and T_{\min} . To facilitate the optimization of tool geometry, Mucha [134] numerically investigated the stress distribution, pressure and deformations of tools (i.e., punch,

blank-holder, die) used in the SPR process. Moreover, simulation results from FEA models were further utilized to develop FEA models for SPR joint mechanical strength prediction (i.e., tensile strength, fatigue life and fracture behaviours) [106,110,112].

Overall, FEA models for the SPR process are capable of predicting the SPR joint quality, and thus can effectively reduce the number of experimental SPR tests required during the new SPR joint design process. However, for a huge number of SPR joints, it still requires a long time to set up and execute all the simulation models, and to extract all the joint quality results. Besides, establishing and running such FEA models is a huge challenge for general engineers without in-depth knowledge of FEA. Therefore, it will be a great contribution to the industry sector if a fast and easy-to-use tool can be developed to predict the SPR joint quality.

2.2.2. Mathematical prediction models

The mathematical model is a straightforward tool to predict the joint quality indicators (e.g., interlock and remaining bottom sheet thickness) and mechanical properties (e.g., static strength and fatigue life). Compared with FEA models, it can be used conveniently without any requirement on professional knowledge, and can give a prediction result almost immediately. By selecting the appropriate type of mathematical model and collecting enough joint quality data, the relationships between joining parameters and joint quality indicators can be established intuitively. In addition, the mathematical prediction model is also an effective tool to quantitatively analyse the influences of different joining parameters on the SPR joint quality and to optimize the joint design with the help of optimization algorithms.

Until now, some mathematical models have been reported in the public domain to predict the SPR joint quality or mechanical strength. For example, according to the sensitivity analysis results, Jäckel et al. [42] identified the main factors from the sheets and die parameters, and then deduced mathematical equations for the interlock and bottom sheet damage value with these main factors. By adopting the Kriging technique, Tassler et al. [48] also established a mathematical model to predict the quality of SPR joints with different sheet thicknesses and yield stresses, rivet lengths and blank-holder forces. The developed mathematical model was also combined with the Monte Carlo method to evaluate the joint robustness by considering the manufacturing errors of the rivet and sheets. Zhang et al. [135] developed response surface equations to predict the interlock and remaining bottom thicknesses of SPR joints with 2.0 mm aluminium alloys AA5052 and AA 6061 sheets. Optimization of rivet and die parameters was also performed with the developed mathematical models and the genetic algorithm (GA) to obtain a higher joint quality for the studied sheet combination. Based on the lower-bound limit-load analysis, Sun et al. [136] developed mathematical models to predict the static strength and failure mode of steel-aluminium SPR joints. Optimization of the joint strength

was also realized for the studied sheet configurations with these prediction models. By analysing the force-displacement curves from normal and interrupted experimental SPR tests, Haque et al. [137] deduced the linear mathematical model between the rivet shank flaring distance and two key points of rivet shank flare on the force-displacement curves (i.e., the start and end points). This specific linear relationship was affected by the sheet thickness, rivet parameters and die geometry. Ma et al. [101] found that there was a linear relationship between the interlock and the lap-shear strength of SPR joints. Mathematical equations could be deduced to predict the joint lap-shear strength with the top sheet thickness and interlock value. Xie et al. [70,71] proposed empirical equations to predict the shear strength of SPR joints based on different failure modes. Compared with models reported in previous studies [69,138], this calculation method could predict the shear strength more simply and reliably according to the sheet thickness and rivet length.

Overall, mathematical models have been widely proved effective to describe the relationships between joining parameters and the joint quality. Naturally, the development of mathematical models inevitably faces some challenges. Firstly, the types of mathematical equations need to be pre-defined. Performances of different mathematical models usually need to be compared during the model development process. Meanwhile, the mathematical expression equations would become complex with the extension of the joint design space. Subsequently, the identification of unknown coefficients in mathematical equations would also become increasingly difficult, especially for high order non-linear equations. Therefore, although the mathematical model is convenient to use, it still requires time and efforts to determine the most appropriate mathematical equation for the selected joint range.

2.2.3. Artificial neural network (ANN) models

The ANN has strong fitting ability and self-learning ability to describe complex relationships between inputs and responses [143,144], and therefore has been gradually adopted in the SPR field in recent years. Compared with the mathematical model, it is more suitable to be used to develop fast and easy-to-use prediction tools for SPR joint quality and mechanical performance. Because the ANN not only can give a prediction result almost immediately, but also has a simpler development procedure. Meanwhile, it can easily involve multiple joining parameters and quality indicators to achieve a wider application range. Nowadays, various types of ANNs have been increasingly applied to solve practical problems in different industrial sectors, such as rainfall-runoff forecasting [141], prediction of weld bead geometry [142] and optimization of reshaping rivets [143]. To the author's knowledge, there are already some studies in which the ANN was employed to predict the SPR joint quality or mechanical strength.

For instance, with the help of machine learning algorithms, Fang et al. [47] established surrogate models for the FEA model to predict the SPR joining results. By combining the Sobol sensitivity analysis method, the developed surrogate models were further used to analyse the impact of the variations of different joining parameters (i.e., the sheet and rivet material properties, clamping force and interfacial friction coefficients) on the joining results. The results showed that, except for the clamping force and the friction coefficient between the blank-holder and top sheet, the other parameters have significant influences on the joining results. Jiang et al. [144] successfully employed the ANN to identify cracks generated on the SPR joint button. Multi-class classification neural networks were first established to distinguish the cracks, edges and smooth surfaces on the sub-images. Then, combined with the search algorithm, the application range of the developed ANNs was extended to a full button image and the cracks on the joint button were identified automatically. Mylavarapu et al. [145] employed eleven ANNs to predict the temperature rise during the SPR process. A FEA model developed in ABAQUS was adopted to collect the subsection temperature values in different SPR processes as the training data for ANNs. The validation results showed that the developed ANNs could be used as an alternative to the FEA model to accurately predict the temperature in the SPR process. Using the FEA simulation model developed with Simufact.Forming software, Jäckel et al. [146] also collect numerous SPR results as different groups of training data for mathematical and machine learning models, including the Linear regression, Huber regression, Support vector regression (SVR), k-nearest-neighbour (k-NN), Gradient boosted decision tree (GBDT) and ANN. The comparisons between different models showed that the linear regression model and Huber regression model reached the best prediction accuracies with the filter numerical database, while the SVM, k-NN, GBDT and ANN models were much more accurate with the complete numerical database. This indicated that the size of training database had significant influences on the accuracy of different prediction models, and a larger database was beneficial for the accuracy of complex prediction algorithms.

However, although the ANN has been employed to develop joint quality prediction models in some studies, there is still not a comprehensive model in which critical rivet, sheet and die parameters are involved. More efforts are still required to extend the application of the ANN in SPR joint quality prediction and to explore its potential applications in the new SPR joint design process.

2.3. Optimization and selection approaches of SPR rivet/die combinations

Besides the development of fast quality prediction models for SPR joints, how to simplify the optimization/selection of rivet/die combinations for new SPR joints is the most urgent problem awaiting to be solved in the automotive industry. So far, the selection of rivet/die still depends heavily on experienced engineers in practical applications. The FEA model and other quality prediction models are helpful to reduce the number of experimental SPR tests required, but cannot directly optimize/select the rivet and die according to the target new sheet combinations. The optimization/selection of rivet/die for new joints have been discussed by some researchers [48,101,135]. However, to the author's knowledge, there is still not a straightforward way that can be used to quickly identify the suitable rivet/die combinations for new joints. More efforts are still required to facilitate the design of new SPR joints in practical applications.

To find more references, the related literature on welding and other joining techniques, for which the joint quality is also critical and affected by many processing parameters as the SPR process, is reviewed to provide some thoughts about optimization and selection of processing parameters.

2.3.1. Optimization strategies used in the welding field

Welding is one of the major joining methods applied in the industrial field, and its joint quality is significantly affected by many processing parameters. Similar to the SPR process, the optimization and selection of processing parameters are also crucial to the welding process and joint quality. Different strategies have been proposed by researchers to improve the quality of welded joints. For instance, Udayakumar et al. [147] proposed a multi-objective optimization method to optimize the processing parameters in the friction welding process by combining the response surface methodology (RSM) model and GA. The calculated Pareto Front could provide various solutions of the processing parameters for weighing the corrosion resistance and impact strength of the welded joints in practical applications. Similarly, Zhang et al. [148] also optimized the shear strength and peel strength of friction stir spot welding joint simultaneously with the RSM empirical models and Non-dominated Sorting Genetic Algorithm II (NSGA-II). Katherasan et al. [142] optimized the quality of flux cored arc welding joint by combining the ANN and particle swarm optimization (PSO) algorithms. The ANN model was developed to predict the weld bead geometry under different processing parameters, and then was embedded into the PSO algorithm to optimize the processing parameters and obtain the desired weld bead geometry. Park and Rhee [149] also used the ANN and GA to optimize processing parameters for laser welding. With the established ANN

prediction model and GA, the tension strength of laser welded joint was maximised by selecting the proper wire feed rate, laser power and welding speed. Nagesh and Datta [150] established two prediction models for the bead geometry of tungsten inert gas arc (TIG) weld with the multiple linear regression method and back-propagation (BP) neural network respectively. Both the main and interaction effects of the processing parameters were considered in the multiple linear equations, and four layers were included in the ANN model to make sure the prediction performance. Finally, the GA was used to search the optimal processing parameters to obtain the desired front height to front width ratio and back height to back width ratio of the weld bead.

2.3.2. Optimization approaches for other joining processes

Not only in the welding process, the optimization of processing parameters in other joining techniques are also very important for the joint quality. A variety of solutions to optimize and select the proper processing parameters have been proposed and investigated by many researchers. For example, Chen et al. [143] successfully optimized the rivet geometric parameters for the clinched joint of 2.0 mm+2.0 mm AA6061 sheets and maximised the joint strength based on the analysis of variance (ANOVA) and range analysis method. A 2D FEA model for clinched joint was developed and verified to obtain the clinching results quickly and conveniently. Zuperl and Cus [151] straightforwardly realized the multiple-objective optimization of cutting parameters during machining by combining the ANN and large-scale optimization algorithm. This approach was quite suitable for selecting important turning parameters quickly and efficiently without too much deep analysis.

Therefore, it can be seen that the processing parameters of different joining techniques can be effectively optimized by using different prediction models and optimization algorithms. Thus, combining one prediction model with an optimization algorithm is a feasible way to realize the optimization of joining parameters and maximisation of the corresponding joint quality indicators for SPR process.

2.4. Summary

This chapter reviews the up-to-date research status of the SPR technique from three aspects, including the effects of different joining parameters on joint quality, quality prediction models for SPR joint, and optimization/selection methods of rivet/die combination. In addition, optimization strategies for processing parameters of other joining techniques are also briefly reviewed. The limitations of current research and corresponding solutions proposed in this thesis are summarised as follows:

1. Single factor effects of different joining parameters on SPR joint quality are the main research direction in the existing studies, but in fact, the influences of these joining parameters are interactive. It is necessary to analyse the interaction effects between different joining parameters on the joint quality. Moreover, the final joint quality is concerned in most studies, but the detailed forming processes of joints with different configurations have not been fully investigated. Therefore, the formation mechanisms of SPR joints with varying joining configurations and the interaction effects between different joining parameters on joint quality are analysed and discussed in this thesis with the help of different prediction tools.
2. In the public domain, the FEA is still the most commonly used method to predict the SPR joint quality. However, it requires professional knowledge of FEA, and is not easy to be used straightforwardly by general engineers. Therefore, the mathematical models and ANN models, which have been successfully employed in other joining techniques, are applied in this thesis to develop easy-to-use and fast response prediction models for SPR joint quality.
3. Until now, the optimization and selection of rivet/die combinations for new SPR joints still heavily depend on engineers' experience and numerous experimental SPR tests. It will be quite helpful to simplify and speed up the design process of new joints if automatic optimization/selection approaches can be developed. Therefore, several novel approaches are proposed in this thesis to automatically optimize the rivet/die combination for an individual sheet combination and select minimum rivet/die combinations for multiple new sheet combinations.

3. Development and application of FEA model for the SPR process

The finite element analysis (FEA) model of the SPR process is an effective tool to speed up the new joint design by reducing the number of experimental SPR tests required. At the same time, it can also provide useful information inside the riveting region and thus facilitate the formation analysis of SPR joints. Therefore, a 2D axisymmetric simulation model was developed in this chapter using the software Simufact.Forming. Experimental SPR tests were conducted to verify the prediction accuracy of the developed FEA model on the joint quality indicators and final cross-sectional profile. Interrupted experimental SPR tests were also carried out to validate its prediction performance on the joint formation. Then, the developed FEA model combined with single factor experiments was employed to systematically analyse the formation mechanisms of SPR joints with varying top sheet thicknesses (T_1), bottom sheet thicknesses (T_2) and rivet lengths (L_1). This developed FEA model lays a foundation for the development of fast quality prediction tools in the following chapters.

3.1. Introduction

In the design process of new SPR joints, the selection of rivet and die is very crucial for the final joint quality but is usually a challenging task due to the complex joining parameters [2]. The rivet length, rivet shank diameter, rivet material and rivet hardness level are the most important rivet parameters [32,38,86]. The die type (e.g., flat die or pip die), die diameter, die depth and pip height are the most critical die parameters [40,41]. In addition, the property, thickness and sequence of the target sheets should also be considered in the joint design process [36,45]. So far, the trial-and-error method based on experienced engineers and experimental SPR tests is still the main approach in the automotive industry to find out the suitable rivet and die for new sheet combinations. However, it costs a lot of time and money to experimentally verify the effectiveness of all possible rivet/die combinations. To speed up the joint design process and to reduce financial investment, many FEA models for the SPR process have been successfully developed in the last two decades. These models can accurately predict the joint quality and be employed to partially replace the experimental SPR tests. For instance, Mucha [44] successfully developed a 2D axisymmetric SPR model in MSC Marc Mentat. Carandente et al. [113] established an improved 2D model of SPR process using Simufact.Forming, in which the thermal softening and strain hardening effects on the sheet material strength were considered. Atzeni et al. [152] established a 3D simulation model using

ABAQUS to predict the SPR joint quality. The effectiveness of FEA models on joint quality prediction has been intensively validated in the existing studies. Taking the advantage of high prediction accuracy, FEA models have also been utilized in some studies to assess the influences of joining parameters on the joint quality, such as the die geometric parameters [43,157], the initial sheet temperature [109] and the sheet thickness ratio [44].

In addition to joint quality prediction, the FEA model can also be conveniently used to inspect the SPR joint formation and to collect useful information inside the joining region, e.g., the flaring behaviour of rivet shank and the formations of the I and T_{\min} . However, to the author's knowledge, this useful function is rarely reported in the accessible studies. Most of the existing numerical and experimental investigations of the SPR process [21,31,45] focused on establishing the relationships between joining parameters and specific joint quality indicators (e.g., I and T_{\min}). Conclusions from these studies were mainly drawn by simply analysing the final joint cross-sectional profiles. The reasons behind the changes of joint quality are not clearly addressed from the perspective of joint formation. Interrupted experimental SPR test, in which the riveting process is stopped at different positions to capture the joint cross-sectional profiles, offers an effective way to experimentally observe the joint formation process but costs a lot of time and money even for just one joint configuration [39,54,137]. In contrast, the FEA model requires far less investment in time and money, and can be conveniently used to observe the whole joint formation process instead of only several joint cross-sectional profiles from interrupted experimental SPR tests [36,78,100]. Therefore, the FEA model is an excellent alternative to the interrupted experimental SPR test to investigate the joint formation mechanism, and is promising to become a mainstream research approach. In-depth understanding of the SPR joint formation mechanisms will be a great contribution to improving the joint quality via new joint designs or the development of new rivets and dies.

Therefore, a 2D simulation model for SPR process was developed in this chapter with the software Simufact.Forming. It was then adopted as an alternative to experimental SPR tests to collect joint quality data for the development of fast quality prediction models and optimization approaches in the following chapters. Previous studies reported the influences of the top sheet thickness (T_1), bottom sheet thickness (T_2) and rivet length (L_1) on the joint quality, but did not give a comprehensive explanation for the changing trends of joint quality indicators from the view of joint formation [35,44,45]. Thus, the developed FEA model combined with single factor experiments was also employed to systematically investigate the impact of these three joining parameters (i.e., T_1 , T_2 and L_1) on the SPR joint formation mechanisms. The results will contribute to better understanding of the joint formation mechanisms during the SPR process.

3.2. FEA model development

Due to the axisymmetric property of the SPR joint, axisymmetric deformations of the rivet and sheets were assumed. A 2D axisymmetric simulation model was therefore developed with the software Simufact.Forming as shown in **Figure 3.1**. The bottom of die was fixed whilst the sheet edges could move freely. A 5.3 kN clamping force (F_1) was applied on the top surface of the blank-holder to clamp the two sheets together. The punch moved downward at a constant speed ($v_1 = 300$ mm/s) to press the rivet into the sheets. During the riveting process, the punch, blank-holder and die undergo very limited elastic deformation and thus were modelled as rigid bodies. Whilst the boron steel rivet and the aluminium alloy AA5754 sheets undergo large plastic deformations and thus were modelled as elastic-plastic bodies. The mechanical properties of the boron steel rivet and the AA5754 sheets are listed in **Table 3.1**. The plastic stress-strain curves for AA5754 were provided by JLR and described in detail by Carandente [153], in which the thermal softening effect and strain rate hardening effect on the material strength were considered. However, the maximum strain rate on the sheets could reach up to approximately 500 s^{-1} during the SPR process, which is too high to be achieved due to the instrument limitation. Thus, the narrow strain rate range (0.01 s^{-1} , 0.1 s^{-1} and 1 s^{-1}) used by Carandente et al. [117,158] have very limited influences on the simulation results. Therefore, as shown in **Figure 3.2** (a), only the stress-strain curves at 1 s^{-1} strain rate considering the temperature effect of the AA5754 were utilized in this simulation model. The temperature change during the joining process ($20\sim 250 \text{ }^\circ\text{C}$) has very limited influence on the steel rivet properties [113], and thus only the plastic stress-strain curve (strain rate= 0.01 s^{-1}) at $20 \text{ }^\circ\text{C}$ of the boron steel was used to model the rivet deformation as shown in **Figure 3.2** (b).

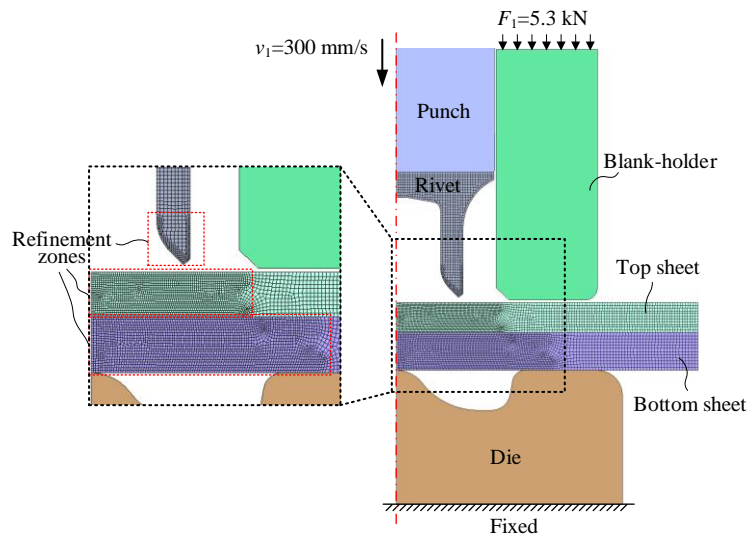
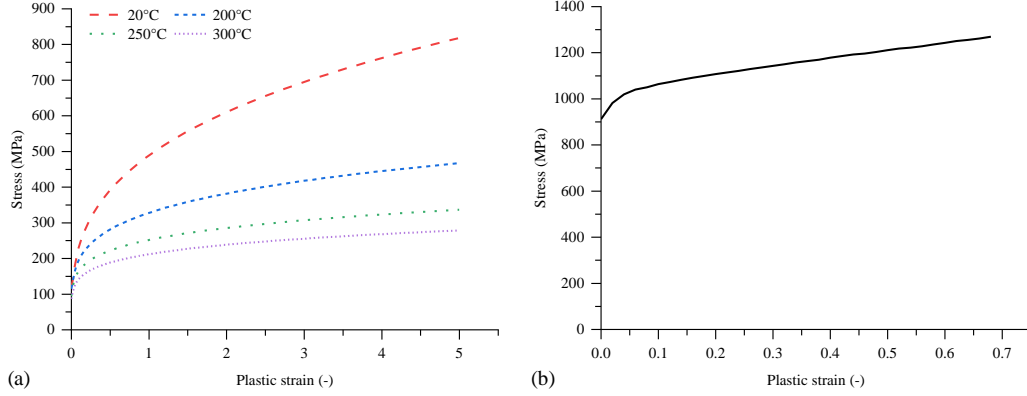


Figure 3.1 Schematic of the SPR simulation model

Table 3.1 Mechanical properties of the rivet and sheet materials

Material	Young's Modules (GPa)	Poisson's ratio	Elongation (%)
AA5754	70	0.33	22
Boron steel	200	0.30	--

**Figure 3.2** Plastic stress-strain curves for (a) AA5754 (strain rate=1 s⁻¹) [113] and (b) boron steel (strain rate=0.01 s⁻¹ and 20 °C)

The 4-nodes quadtree element with four gauss points was employed to mesh the rivet in order to allocate more elements on the rivet surface, whilst 4-nodes advancing front quad element was selected to mesh the top and bottom sheets to get uniform elements. To find out the suitable mesh sizes for the rivet and sheets, a mesh sensitivity study was carried out. The results indicated that, for industrial applications, the mesh sizes for the rivet, top sheet and bottom sheet could be set to 0.10 mm, 0.10 mm and 0.12 mm respectively, which makes a balance between the simulation efficiency and accuracy. To further improve the prediction accuracy without increasing too much simulation time, mesh refinement boxes were applied on the rivet tip and the central areas of the two sheets (i.e., red boxes in **Figure 3.1**). In the SPR process, the top and bottom sheets usually undergo severe plastic deformations, which will cause serious element distortions and convergence problems during the simulation [125]. To deal with this issue, an automatic re-meshing technique based on different re-meshing criteria was adopted for the top and bottom sheets. Whilst the automatic re-meshing was not applied on the rivet due to its small deformation. To simulate the fracture of top sheet, a geometrical criterion, which defines the occurrence of fracture when the top sheet thickness becomes lower than the pre-defined critical value, was implemented in the FEA model. The critical threshold thickness in the geometrical criterion has a significant influence on the predicted joint quality, especially for the interlock. In general, a too large critical thickness could lead to a premature fracture of the top sheet, while a too small critical thickness could cause an unrealistic deformation of the top sheet material around the fracture location. In this simulation model, the critical thickness was set to 0.04 mm through the inverse method.

The Coulomb friction model was chosen to describe the interactions between the contact components. The magnitudes of friction coefficients between different surfaces have significant influences on the deformation behaviours of the rivet and sheets [124]. For instance, the friction coefficient between the bottom sheet and the die could directly affect the final thickness distribution of the bottom sheet, whilst the friction coefficient between the top sheet and the rivet could directly influence the rivet shank flaring distance [22,78]. Due to the difficulties to measure these friction coefficients, the inverse method was used to determine the friction coefficients at different interfaces. As listed in Table 3.2, the friction coefficient between the bottom sheet and the die was set to 0.22, whilst the friction coefficients between other parts were set to 0.10 in the developed FEA model.

Table 3.2 Friction coefficients between the different parts in the FEA model

Contact pairs	Punch-Rivet	Blankholder-sheets	Rivet-Sheets	Top sheet-Bottom sheets	Bottom sheet-Die	Others
Friction-coefficients	0.10	0.10	0.10	0.10	0.22	0.10

3.3. Validation of the FEA model

To verify the prediction accuracy and capability of the developed FEA model, the results obtained from the simulations and laboratory experimental SPR tests were compared.

3.3.1. Effectiveness for the SPR joint quality prediction

As listed in **Table 3.3**, twenty SPR joints with different configurations and within the studied ranges were manufactured experimentally. **Figure 3.3** illustrates the cross-sectional profiles of the sheets, the semi-tubular rivet and the pip die used in the experiments. The aluminium alloy AA5754 sheets and boron steel rivets were used throughout all experiments. The rivets and dies were supplied by the Tucker GmbH, and the AA5754 sheets were provided by JLR. The rivet diameter, rivet hardness and die pip height were fixed at 5.3 mm, H0 (280±30 HV10) and 0.0 mm respectively. Different top sheet thicknesses (T_1), bottom sheet thicknesses (T_2), rivet lengths (L_1), die diameters (D_1) and die depths (H_1) were used to enhance the performance evaluation of the FEA model. All sheets were cut to 40 mm×40 mm as shown in **Figure 3.4** to eliminate possible influences of sheet dimensions on the joining result [154]. Three repetitions were made for each joint configuration using the Tucker servo SPR system shown in **Figure 3.5**. The punch speed and the clamping force were the same as that used in the FEA model.

All the specimens were sectioned along the joint central plane as shown in **Figure 3.6** (a), and the joint cross-sectional profiles were captured using an optical microscope. Then, the three

quality indicators (i.e., the rivet head height H , the interlock I and the T_{\min}) shown in **Figure 3.6** (b) were measured on the joint cross-sectional profiles. The mean values of these indicators from the three repetitions were calculated for each joint configuration, as listed in **Table 3.3**. All the twenty SPR joints were also simulated using the developed FEA model. For easier comparison between the experimental and simulation results, the mean value of the experimentally measured rivet head height for each SPR joint was implemented as the termination criterion of the corresponding SPR simulation. The simulated three quality indicators for each joint were also extracted as listed in **Table 3.3**.

Table 3.3 Validation experiments of the FEA model with different joint configurations

Joint configurations					Experimental and simulation results					
Joint No.	Stack /mm (AA5754)	Rivet Length L_1 /mm	Die		Rivet head height H /mm		Interlock I /mm		T_{\min} /mm	
			Diameter D_1 /mm	Depth H_1 /mm	Tested (Mean)	Simulated	Tested (Mean)	Simulated	Tested (Mean)	Simulated
3-1	1.0+1.5	5.0	10.0	1.8	0.03	-0.03	0.44	0.43	0.32	0.22
3-2	1.0+1.5	5.0	9.0	1.6	0.02	0.02	0.60	0.59	0.28	0.17
3-3	1.0+2.0	5.0	9.0	1.6	-0.09	0.01	0.76	0.64	0.51	0.43
3-4	1.5+1.0	5.0	10.0	1.8	-0.19	-0.01	0.16	0.12	0.36	0.23
3-5	1.5+1.0	5.0	9.0	1.6	-0.08	0.03	0.31	0.30	0.23	0.19
3-6	1.5+1.0	6.0	10.0	1.8	0.01	0.00	0.59	0.40	0.13	0.07
3-7	1.5+1.0	6.0	9.0	1.6	-0.08	0.10	0.74	0.68	0.10	0.18
3-8	1.5+1.5	5.0	10.0	2.0	-0.05	0.02	0.25	0.20	0.37	0.34
3-9	1.5+1.5	5.0	10.0	1.8	-0.07	0.01	0.33	0.27	0.48	0.43
3-10	1.5+1.5	5.0	9.0	1.6	0.02	0.03	0.42	0.39	0.53	0.48
3-11	1.5+1.5	5.0	8.0	2.0	-0.04	0.02	0.35	0.34	0.38	0.23
3-12	1.5+1.5	6.0	10.0	1.8	0.04	0.00	0.69	0.57	0.32	0.28
3-13	1.5+1.5	6.0	9.0	1.6	0.01	0.07	0.77	0.73	0.41	0.31
3-14	1.5+2.0	5.0	9.0	1.6	-0.06	0.03	0.56	0.46	0.72	0.70
3-15	1.5+2.0	6.0	10.0	1.8	-0.10	0.00	0.76	0.72	0.56	0.57
3-16	1.5+2.0	6.0	9.0	1.6	-0.12	0.06	0.93	0.76	0.43	0.62
3-17	2.0+1.5	6.0	10.0	1.8	-0.13	0.02	0.43	0.40	0.37	0.21
3-18	2.0+1.5	6.0	9.0	1.6	-0.11	0.05	0.61	0.56	0.22	0.25
3-19	1.8+2.0	6.0	9.0	1.6	0.06	0.01	0.71	0.64	0.39	0.55
3-20	2.0+2.0	6.0	9.0	1.6	0.02	0.04	0.65	0.58	0.37	0.37

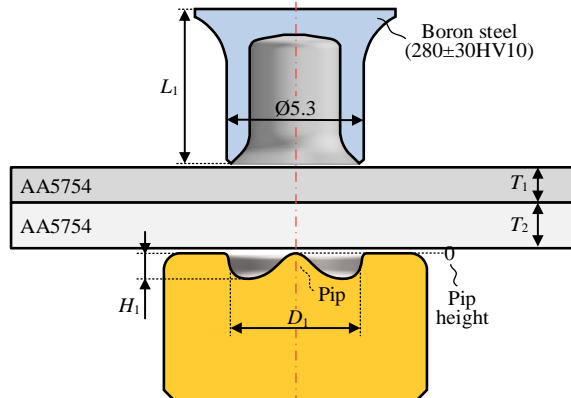


Figure 3.3 Cross-sectional profiles of the top sheet, the bottom sheet, the semi-tubular rivet and the pip die (in mm)

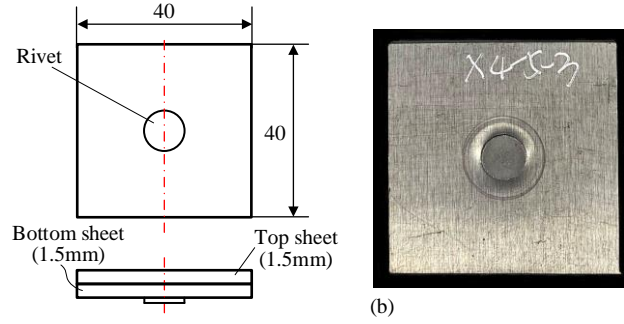


Figure 3.4 Specimens dimensions of the SPR joints (in mm)

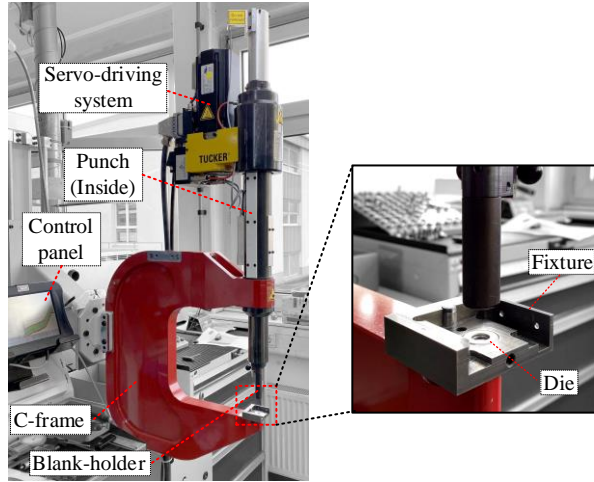


Figure 3.5 Structure of the Tucker SPR system

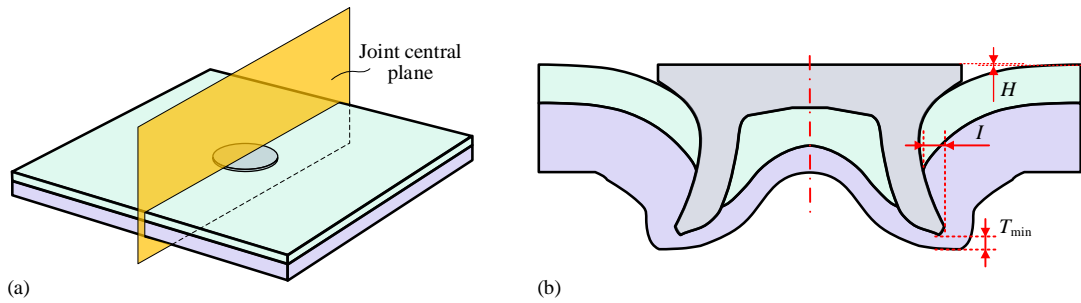


Figure 3.6 Schematics of (a) specimen cutting position and (b) quality indicators measured on the joint cross-sectional profile

The comparisons of joint cross-sectional profiles extracted from the experimental SPR tests and FEA simulations are presented in **Figure 3.7**. By visual observation, a reasonable agreement was found between the simulation and experimental results. The simulated shapes of the deformed rivet and sheets matched well with the experimentally tested ones. Comparisons between the tested and simulated interlock (I) and T_{\min} are given in **Figure 3.8**. The calculated mean absolute error (MAE) for the interlock and the T_{\min} were 0.064 mm and 0.079 mm respectively, and the corresponding Pearson's correlation coefficient (r) were 0.97

and 0.84. These results verified the high prediction accuracy of the FEA model on the I and the T_{\min} under various joint configurations.

From the analysis and comparisons above, it is reasonable to confirm that the developed FEA model is capable of predicting the cross-sectional profile and the quality of AA5754 aluminium alloy SPR joints with varying configurations.

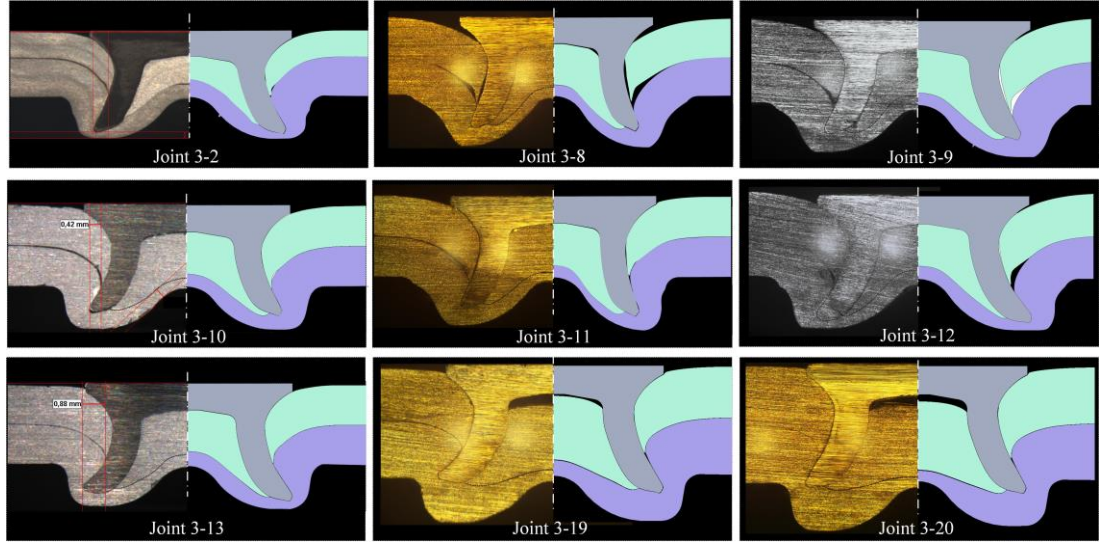


Figure 3.7 Comparisons of the joint cross-sectional profiles from the experimental tests and the FEA simulations

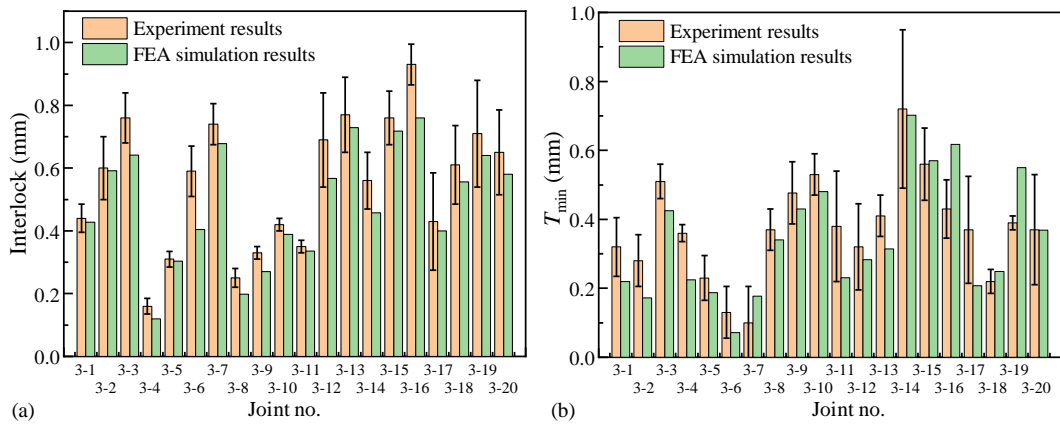


Figure 3.8 Comparisons of the experimentally tested and FEA simulated (a) interlock I and (b) T_{\min}

3.3.2. Effectiveness for the joint formation prediction

The interrupted experimental tests were also conducted to confirm the effectiveness of the developed FEA model on the prediction of SPR joint formation, including the deformation behaviours of sheets, the flare behaviour of rivet shank and the formation process of joint quality indicators. The interrupted experimental test means that a SPR process is manually stopped at the pre-defined position. It is the only approach to experimentally observe the joint formation at different riveting stages [155]. The Tucker SPR system as shown in **Figure 3.5**

is a servo-driven system, and the joining process is controlled by the rivet displacement. During the SPR process, the punch moves downward with a constant speed and presses the rivet into the sheet, then the SPR process is terminated when the pre-set rivet head height (H) is reached. In this section, the riveting process of the selected SPR joint (1.2 mm+2.0 mm AA5754 sheets and 6.0 mm long boron steel rivet) was interrupted at five positions by controlling the magnitude of H (i.e., 4.0 mm, 3.0 mm, 2.0 mm, 1.0 mm and 0.0 mm) as listed in **Table 3.4**. **Figure 3.9** shows the nominal dimensions of the semi-tubular rivet and pip die (Type-A) used in the interrupted tests. The size of the specimen and the other experimental conditions are the same as those used in 3.3.1. All the specimens were also sectioned through the joint central plane, and then slightly polished to capture the joint cross-sectional profiles. Meanwhile, the interlock (I), the remaining bottom sheet thickness at the joint centre (T_{cen}) and the deformed rivet shank diameter (D_r) as shown in **Figure 3.10** at each joint were also measured. The same SPR joint was also simulated with the developed FEA model, and the simulated SPR process was stopped at the same five positions to extract the corresponding cross-sectional profiles and measure the three indicators (i.e., I , T_{cen} and D_r).

Table 3.4 Design of the interrupted experimental SPR tests

Joint no.	Thickness (mm)		Rivet head height / H (mm)	Rivet (Boron steel)	Die
	Top sheet / T_1 (AA5754)	Bottom sheet / T_2 (AA5754)			
3-21			4.0		
3-22			3.0		
3-23	1.2	2.0	2.0	C5.3*6.0 H0	Pip die (Type-A)
3-24			1.0		
3-25			0.0		

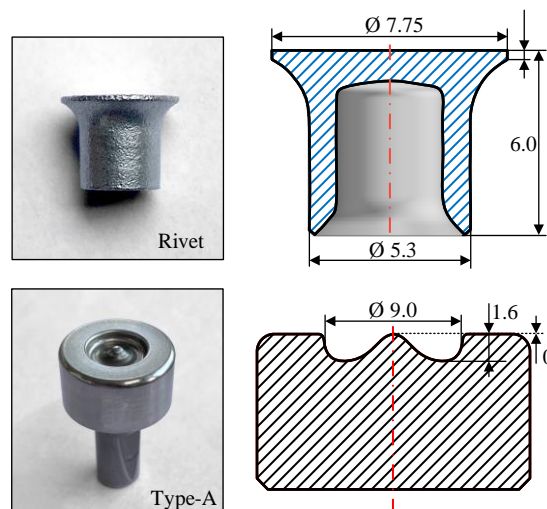


Figure 3.9 Dimensions of the (a) semi-tubular rivet and (b) pip die (Type-A) used in the interrupted tests (in mm)

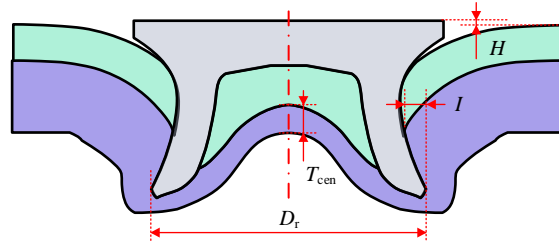


Figure 3.10 Schematic of the four dimensions measured on the joint cross-sectional profile

Comparisons of the cross-sectional profiles of the joints 3-21~3-25 from the FEA simulations and interrupted experimental tests are presented in **Figure 3.11**. It can be seen that the deformed shapes of the rivet and sheets at each riveting stage from the FEA model are matched well with that from the interrupted experimental tests. The gap formed between the two sheets (Zone1) and the local deformation on the bottom sheet (Zone3) were also accurately predicted by the FEA model (Zone2 and Zone4). The simulated and tested variation curves of the deformed rivet shank diameter (D_r), the remaining bottom sheet thickness at the joint centre (T_{cen}) and the interlock (I) are compared in **Figure 3.12**. It can be seen that both of the simulated and tested D_r first increased slowly and then increased rapidly with the decline of the H as shown in **Figure 3.12** (a). Both of the simulated and tested T_{cen} first decreased rapidly and then kept almost constant before the second rapid decline occurred as shown in **Figure 3.12** (b). Both of the simulated and tested I started increasing rapidly from around $H=3.0$ mm and its increasing speed kept almost constant with the decline of the H as shown in **Figure 3.12** (c). These results indicated that the changing trends of the D_r , T_{cen} and I were accurately predicted by the FEA model (red dash lines in **Figure 3.12**). It also can be found that the predicted and tested magnitudes of the D_r , T_c and I at varying H showed reasonable agreements. Therefore, the developed FEA model is capable of predicting the joint formation during the riveting process. It is also worth noting that, due to the limited number of stop positions in the interrupted experimental tests, the variation trend of the T_{cen} was not entirely captured (Region 1 in **Figure 3.12** (b)). This shortage can be easily overcome by the FEA model because the T_{cen} at any riveting stage can be conveniently extracted from the simulation results.

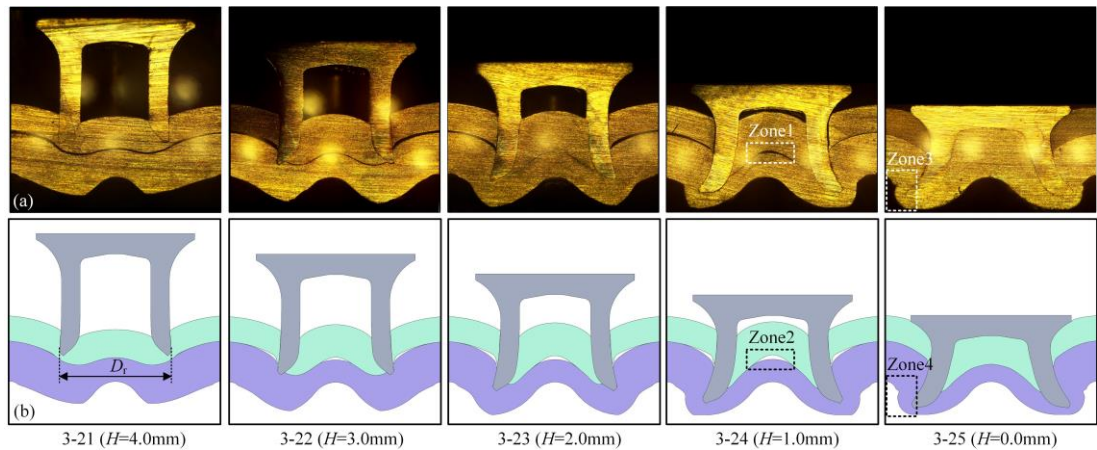


Figure 3.11 Cross-sectional profiles of the joints 3-21~3-25 from (a) interrupted experimental tests and (b) FEA simulations

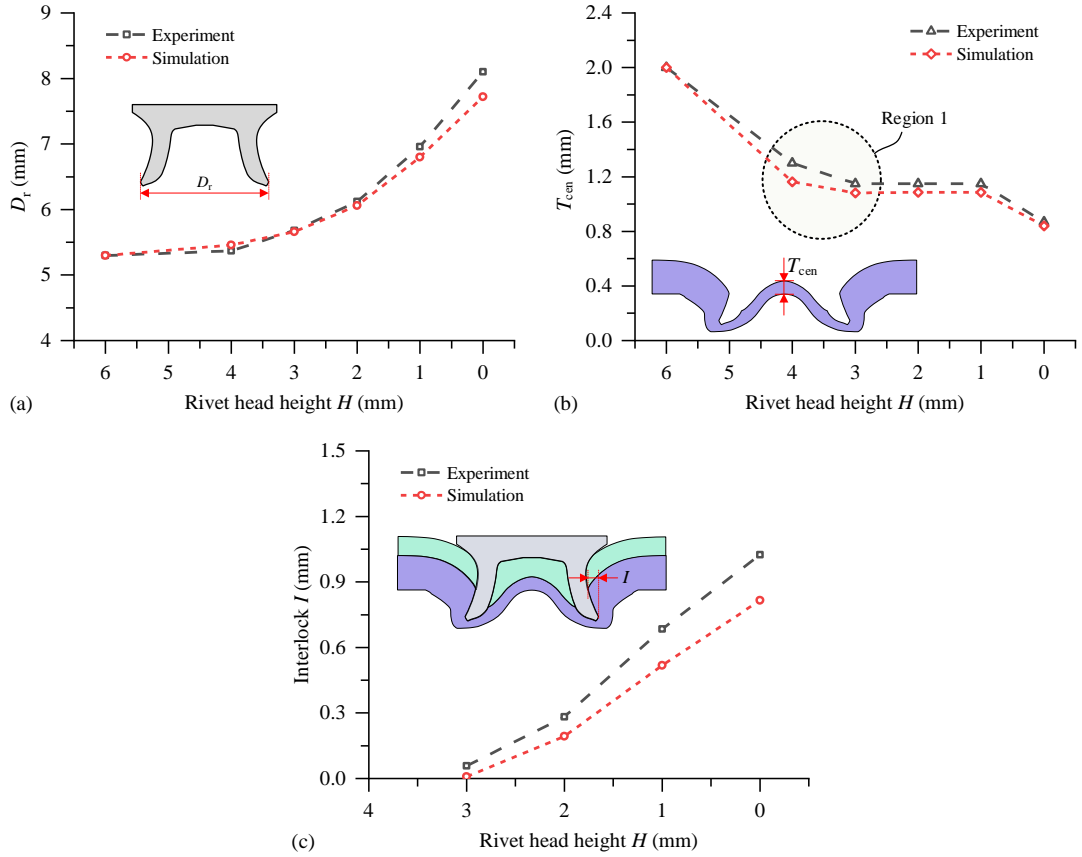


Figure 3.12 Comparisons between the experimentally tested and the simulated (a) deformed rivet shank diameter D_r , (b) remaining bottom sheet thickness at the joint centre T_{cen} and (c) interlock I in the joints 3-21~3-25

3.4. Application of the FEA model on the analysis of SPR joint formation mechanism

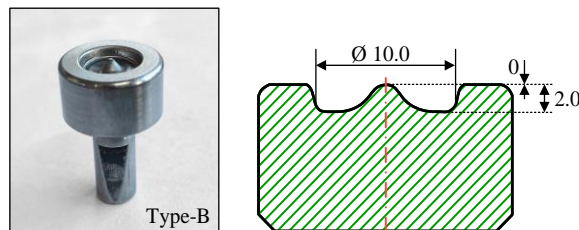
3.4.1. Single factor experiments

Single factor experiments listed in **Table 3.5** were carried out to investigate the impact of the top sheet thickness (T_1), bottom sheet thickness (T_2) and rivet length (L_1) on the formation of SPR joints, especially the formation mechanisms of the interlock (I) and the remaining bottom sheet thickness. The aluminium alloy AA5754 sheets and boron steel rivets adopted are the same as that used in **3.3.1**. Four top sheet thickness levels (i.e., 1.0 mm, 1.2 mm, 1.5 mm and 2.0 mm) were used in the joints 3-26~3-29. Four bottom sheet thickness levels (i.e., 1.0 mm, 1.5 mm, 1.8 mm and 2.0 mm) were utilized in the joints 3-30~3-33. Three rivet length levels (i.e., 5.0 mm, 6.0 mm and 6.5 mm) were used in the joints 3-34~3-36. A pip die (Type-B) was adopted throughout the single factor experiments as shown in **Figure 3.13**. The specimen size and the other experimental conditions are also the same as those used in **3.3.1**. For easier

comparison, the rivet head height (H) was controlled to the same value (i.e., -0.10 mm) in all the SPR joints by predefining the rivet displacement in the SPR system. To ensure the effectiveness of the experiment results, three repeats for each joint configuration were made. All the specimens were also sectioned through the joint central plane, and then slightly polished to capture the joint cross-sectional profiles. The rivet head height (H) and the interlock (I) for each joint were measured from the joint cross-sectional profiles as shown in **Figure 3.16**. The joint quality indicator T_{\min} is not suitable to be directly employed to evaluate the impact of joining parameters on the formation of remaining bottom sheet thickness. Because it can appear at any part of the deformed bottom sheet (green dashed line in **Figure 3.16**), and its position varies from joint to joint. Instead, the remaining bottom sheet thickness at the joint centre (T_{cen}) and under the rivet tip (T_{tip}) for each joint were measured in this section to represent the remaining bottom sheet thickness. In addition, the load-displacement curve of each joint was also recorded. All the eleven SPR joints in **Table 3.5** were also simulated using the developed FEA model. The simulation results were extracted and utilized to facilitate the analysis of the single factor experiment results.

Table 3.5 Design of the single factor experiment

Joint no.	Thickness (mm)		Rivet (Boron steel)	Die
	Top sheet/ T_1 (AA5754)	Bottom sheet/ T_2 (AA5754)		
3-26	1.0	1.8	C5.3*5.0	Pip die (Type-B)
3-27	1.2	1.8	C5.3*5.0	
3-28	1.5	1.8	C5.3*5.0	
3-29	2.0	1.8	C5.3*5.0	
3-30	1.2	1.0	C5.3*5.0	
3-31	1.2	1.5	C5.3*5.0	
3-32	1.2	1.8	C5.3*5.0	
3-33	1.2	2.0	C5.3*5.0	
3-34	1.2	1.8	C5.3*5.0	
3-35	1.2	1.8	C5.3*6.0	
3-36	1.2	1.8	C5.3*6.5	

**Figure 3.13** Dimensions of the pip die (Type-B) (in mm)

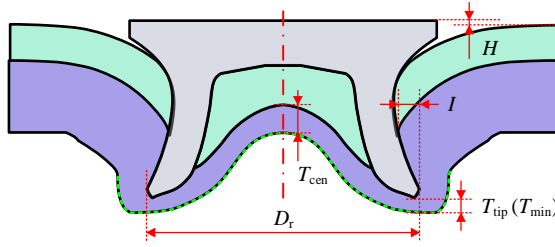


Figure 3.14 Schematic of quality indicators measured on the joint cross-sectional profile

3.4.2. Results and discussion

3.4.2.1. Comparisons between the experimentally tested and simulated results

Before using the FEA model to assist the analysis of joint formation mechanisms, its effectiveness on the SPR joints from single factor experiments (**Table 3.5**) was firstly confirmed. **Figure 3.15** shows the simulated and tested cross-sectional profiles of the joints 3-26~3-36. It can be seen that the predicted shapes of the rivet and sheets were in good agreement with the experimentally tested ones. The joint defects, such as the gaps formed between the top sheet and the rivet (e.g., Gap1 in **Figure 3.15** (d)), between the top and bottom sheets (e.g., Gap3 in **Figure 3.15** (b)), were accurately identified with the developed FEA model (e.g., Gap2 and Gap4). The severely localized deformation of the top sheet around the rivet shank (e.g., Zone 1 and Zone 3) was also accurately predicted (e.g., Zone 2 and Zone 4). Comparisons between the simulated and tested quality indicators are given in **Figure 3.16**. By visual observation, it can be found that the predicted values of the I , T_{cen} and T_{tip} matched well with that from the experimental SPR tests. The calculated MAE for the I , T_{cen} and T_{tip} are 0.066 mm, 0.042 mm and 0.115 mm respectively, and the corresponding mean absolute percentage error (MAPE) are 10.5 %, 12.9 % and 19.7 %. Because the changing trend of riveting force (F_r) is closely linked with the events happen during the riveting process [39], the simulated and experimentally measured load-displacement curves of the joints 3-26~3-36 are also compared as shown in **Figure 3.17**. It is obvious that the predicted changing trends and magnitudes of the F_r were almost identical to that from the experimental SPR tests. This also proved the good performance of the developed FEA model on the prediction of SPR joint formation. Based on the above comparison results, it can be concluded that the developed FEA model achieves a high prediction accuracy for the studied joint configurations and can be utilized to assist the analysis of SPR joint formation mechanisms.

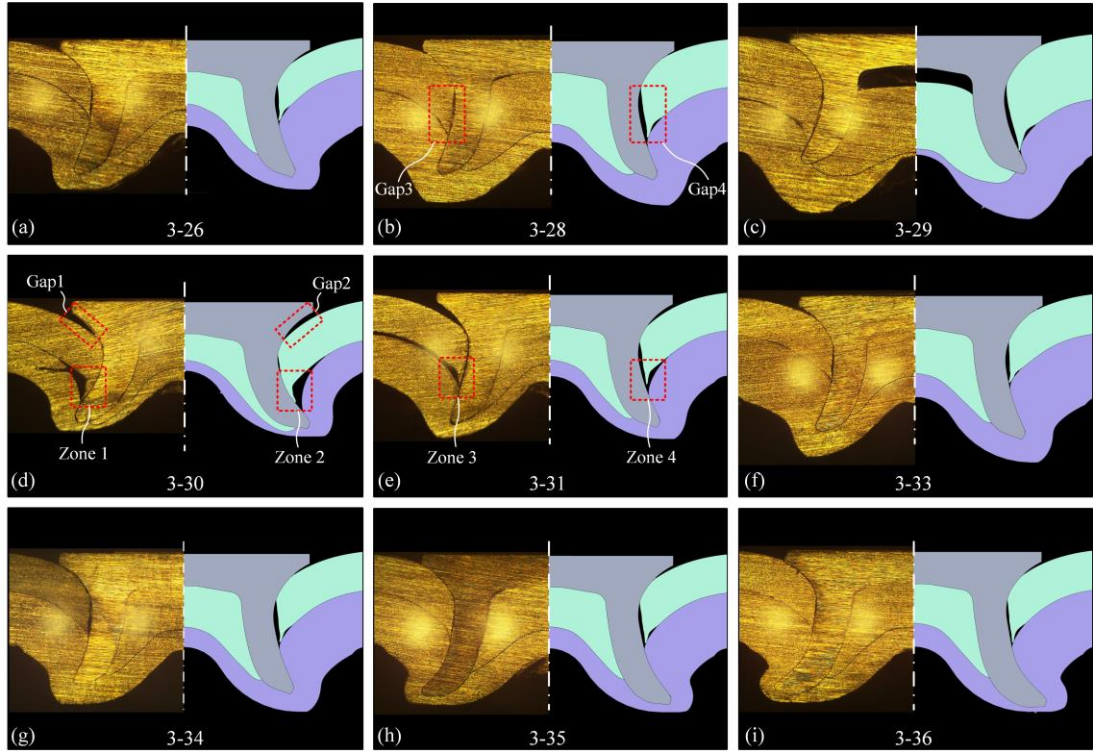


Figure 3.15 Comparisons between the experimentally tested and the simulated cross-sectional profiles of the SPR joints 3-26~3-36

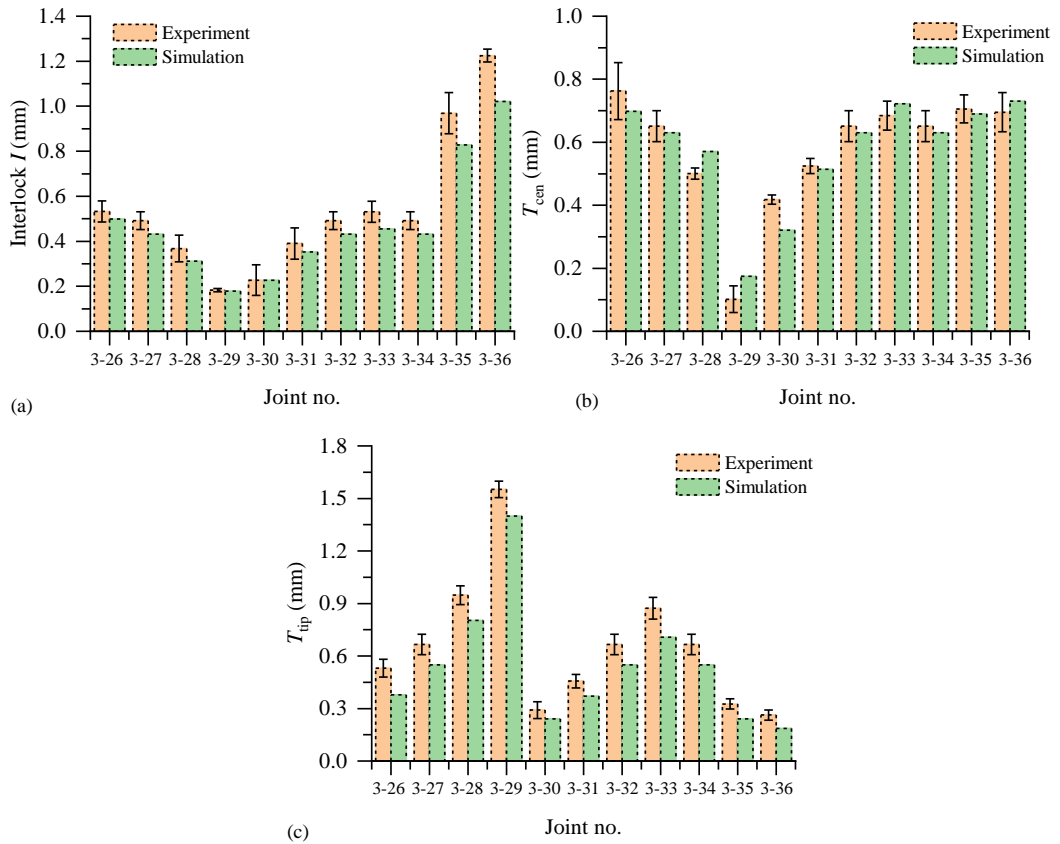


Figure 3.16 Comparisons between the simulated and the experimentally tested (a) interlock I , (b) remaining bottom sheet thickness at the joint centre T_{cen} and (c) remaining bottom sheet thickness under the rivet tip T_{tip} in the joints 3-26~3-36

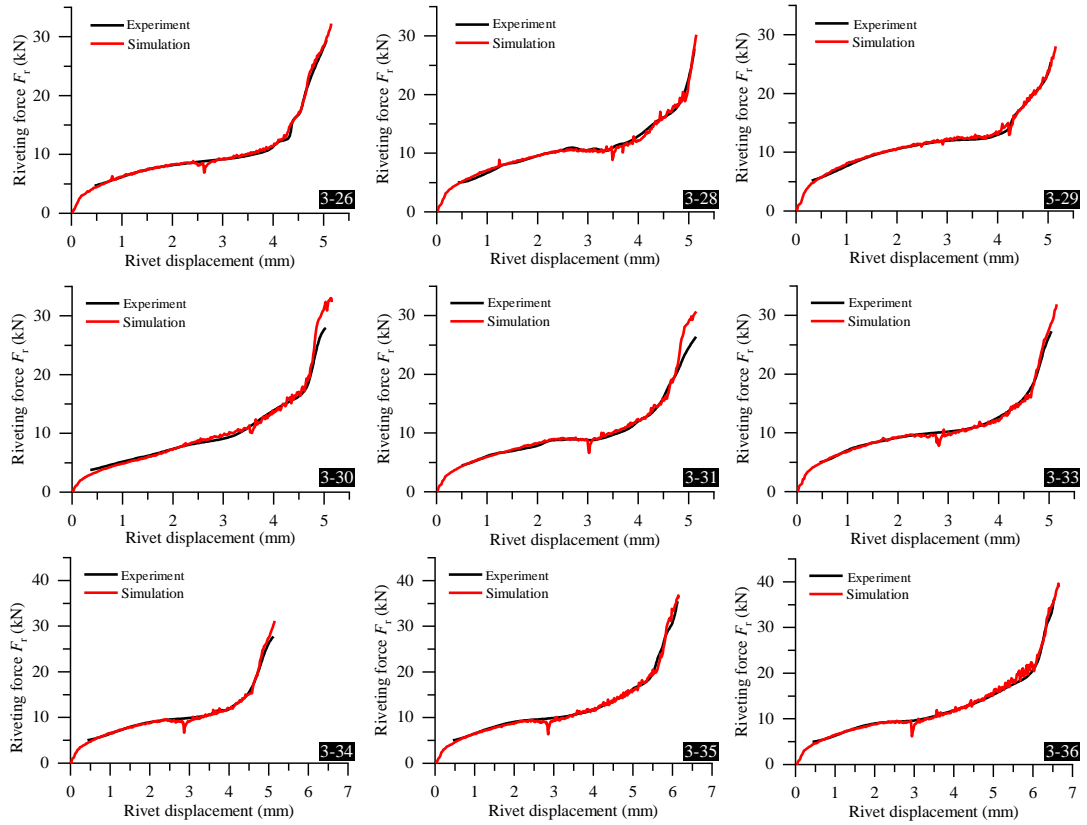


Figure 3.17 Comparisons between the simulated and the experimentally tested load-displacement curves of the joints 3-26~3-36

3.4.2.2. Formation mechanisms of SPR joints with varying T_1

Figure 3.18 shows the experimentally captured cross-sectional profiles of the joints 3-26~3-29 with different top sheet thicknesses (T_1). It can be seen that the final joint profile was significantly affected by the T_1 : the deformed shapes of rivet and sheets varies from joint to joint. Consequently, the magnitudes of the I , T_{cen} and T_{tip} were also apparently influenced. For easier comparison, the tested variation trends of the I , T_{cen} and T_{tip} with different T_1 are plotted into line charts as shown in **Figure 3.19** (black dash lines). It can be seen from **Figure 3.19** (a) that the increment of T_1 imposed negative effects on the interlock formation: the tested I decreased from 0.53 mm with $T_1=1.0$ mm to only 0.18 mm with $T_1=2.0$ mm. Actually, the magnitude of I is directly determined by the positions of two interlock boundaries, and can be expressed as a function of the diameters of inner interlock boundary (D_{in}) and outer interlock boundary (D_{out}) (i.e., $I = (D_{out} - D_{in})/2$). It can be seen from **Figure 3.19** (b) that the T_1 showed less influence on the D_{out} than on the D_{in} . With the increment of T_1 from 1.0 mm to 2.0 mm, the tested D_{out} fluctuated within a relatively narrow range (i.e., ± 0.07 mm), but the tested D_{in} increased rapidly from 5.84 mm to 6.53 mm. This revealed that the T_1 affected the interlock formation by mainly altering the position of the inner interlock boundary. Moreover, it can be seen from **Figure 3.19** (c)(d) that the increment of T_1 imposed negative effects on the

formation of T_{cen} but positive influences on the formation of T_{tip} . With the T_1 increasing from 1.0 mm to 2.0 mm, the tested T_{cen} decreased from 0.76 mm to 0.10 mm but the T_{tip} increased rapidly from 0.53 mm to 1.55 mm. By comparing the relative magnitudes of the T_{cen} and T_{tip} in each joint, it can be found that the position of the minimum remaining bottom sheet thickness (T_{min}) was also altered by the T_1 : around the rivet tip with a thin top sheet (e.g., $T_1=1.0$ mm) but around the joint centre with a thick top sheet (e.g., $T_1=2.0$ mm).

The information extracted from the experimentally tested joint profiles (see **Figure 3.18**) is sufficient for joint quality evaluation, but is not enough to analyse the joint formation mechanism. The developed FEA model could reasonably predict the changing trends and magnitudes of the I , D_{in} , D_{out} , T_{cen} and T_{tip} (red dash lines) as shown in **Figure 3.19**. Therefore, it was used in this section to extract more information during the riveting process to uncover the joint formation with varying T_1 .

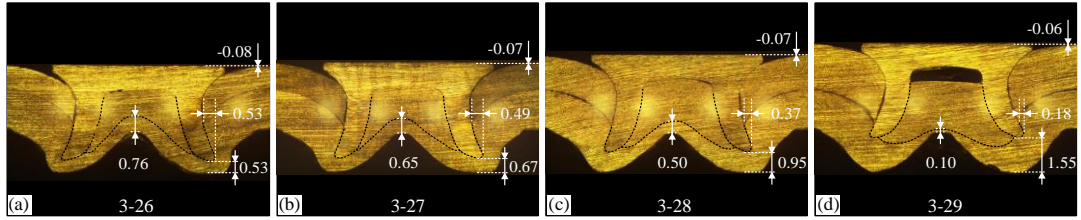


Figure 3.18 Experimentally tested cross-sectional profiles of the joints 3-26~3-29 with different top sheet thicknesses T_1 (a) 1.0 mm, (b) 1.2 mm, (c) 1.5 mm and (d) 2.0 mm

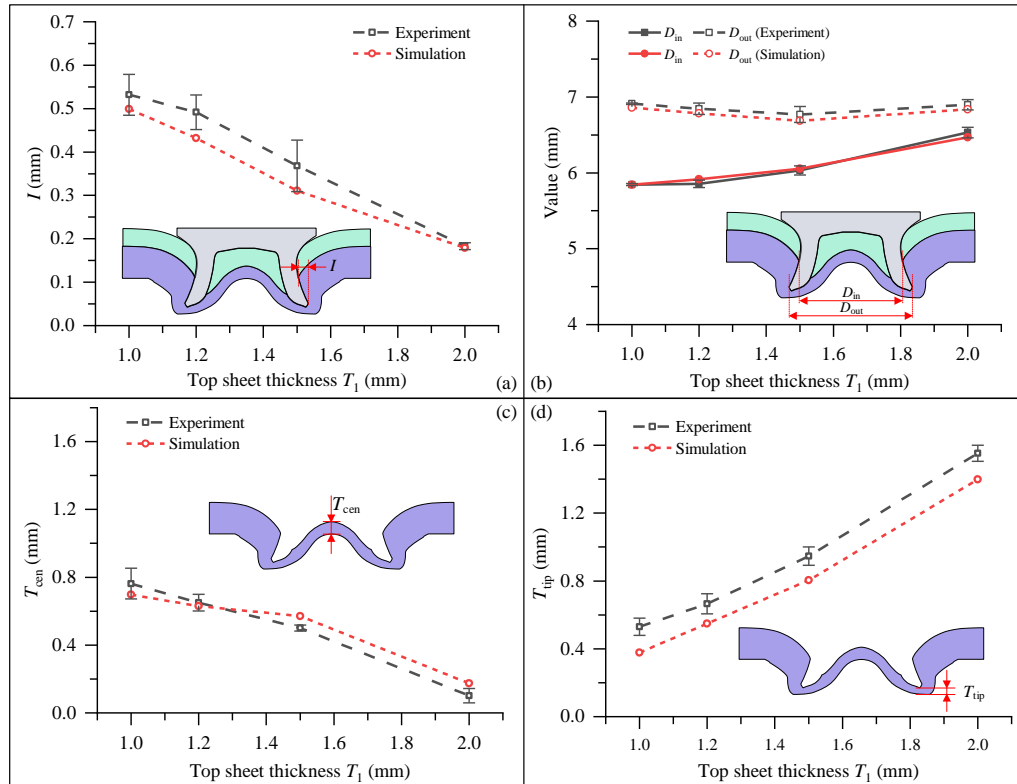


Figure 3.19 Experimentally tested and numerically simulated (a) interlock I , (b) D_{in} and D_{out} , (c) T_{cen} and (d) T_{tip} in the SPR joints 3-26~3-29

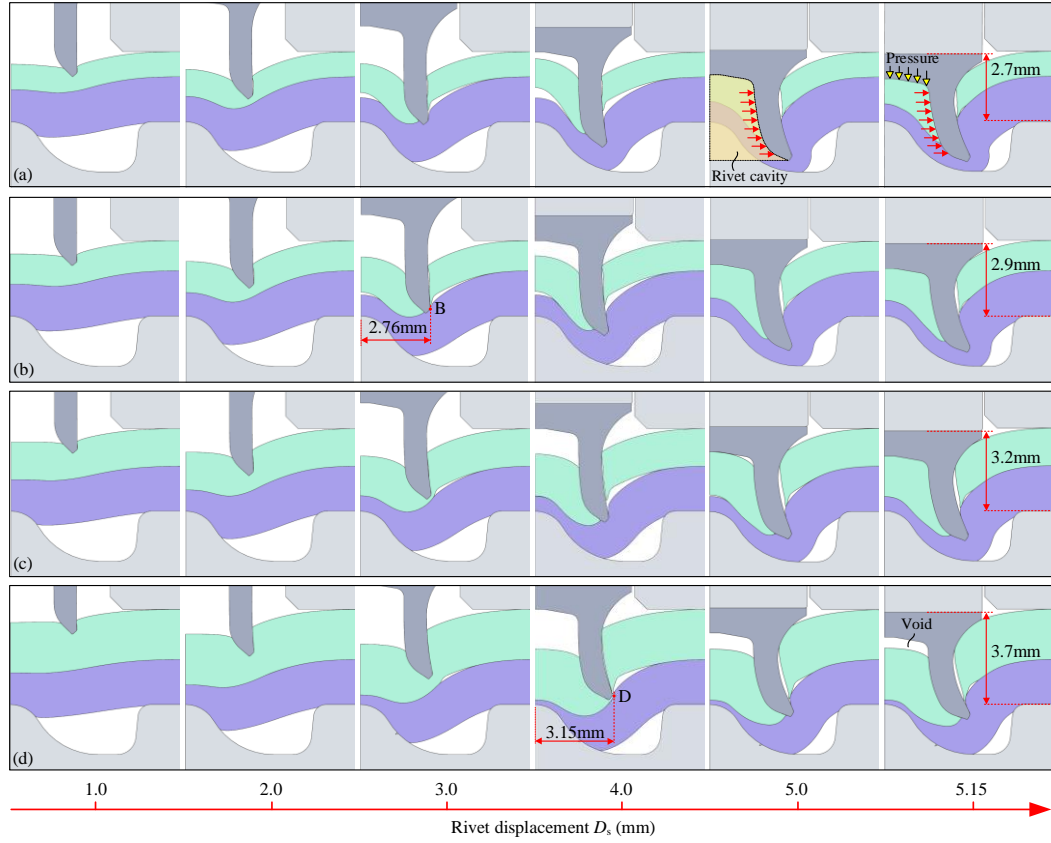


Figure 3.20 Numerically simulated cross-sectional profiles during riveting processes of the SPR joints 3-26~3-29 (a) $T_1=1.0$ mm, (b) $T_1=1.2$ mm, (c) $T_1=1.5$ mm and (d) $T_1=2.0$ mm

With the FEA model, the formation processes of the SPR joints 3-26~3-29 were visually inspected. **Figure 3.20** shows the numerically extracted joint cross-sectional profiles at six different rivet displacements (D_s). It can be seen that, with the increment of the T_1 , the top sheet became more and more difficult to be deformed. A greater rivet displacement was required before the top sheet was completely penetrated by the rivet shank. Consequently, the deformation behaviours of the rivet shank and the bottom sheet were also significantly affected, which resulted in the variations of the I , T_{cen} and T_{tip} .

To better understand the formation mechanism of interlock with different T_1 , the changing curves of the I during the riveting processes of the joints 3-26~3-29 were numerically extracted as shown in **Figure 3.21** (a). It can be seen that the starting point of interlock formation was apparently delayed with a greater T_1 (Zone 1), and a smaller rivet displacement was left to form the interlock. This is mainly attributed to the delayed penetration of the top sheet. Meanwhile, an equal or slightly smaller increasing speed of the I was also observed. The above changes directly caused the decline of the I with the increment of the T_1 . It is worth noting that the I increased almost linearly with the increment of the rivet displacement.

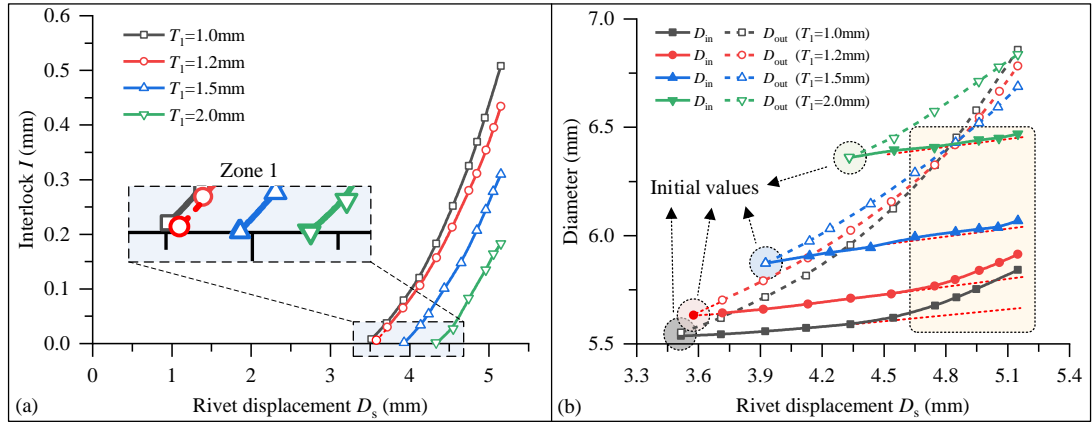


Figure 3.21 Numerically simulated (a) formation curves of the I and (b) formation curves of the two interlock boundaries during riveting processes of the joints 3-26~3-29

To find out the reasons for the different effects of the T_1 on the two interlock boundaries (see **Figure 3.19** (b)), the changing curves of the D_{in} (solid lines) and D_{out} (dash lines) during the four riveting processes were numerically extracted as shown in **Figure 3.21** (b). With the increment of the T_1 , it can be seen that the initial values of the D_{in} and D_{out} apparently increased. This is highly associated with the insertion position where the rivet shank started flaring into the bottom sheet. As shown in **Figure 3.20**, the rivet shank underwent a greater deformation when penetrating the thicker top sheet, and thus flared into the bottom sheet at a position farther away from the joint centre (e.g., point B in **Figure 3.20** (b) vs point D in **Figure 3.20** (d)). As a result, greater initial values of the D_{in} and D_{out} were observed in joints with a larger T_1 . However, it can be seen from **Figure 3.21** (b) that the increasing speed and the duration of D_{out} apparently decreased. So the initial difference of the D_{out} with varying T_1 was gradually eliminated, and the final value of the D_{out} was not significantly affected by the T_1 . In contrast, although a shorter duration of the D_{in} was also observed with a greater T_1 , the initial difference of the D_{in} with varying T_1 was just slightly reduced. This is because the different increasing speeds of the D_{in} appeared at the end of the riveting processes, and just lasted a short period (yellow region). So the final value of the D_{in} was apparently affected by the T_1 . It is also worth mentioning that the different increasing speeds of the D_{in} were directly linked to the filling conditions of the rivet cavity. For example, the rivet cavity was fully filled before the end of the SPR process with the $T_1=1.0$ mm as shown in **Figure 3.20** (a). With further downward movement of the rivet, the rivet head applied high pressure on the sheet materials filled in the rivet cavity. As a result, the entire rivet shank was pushed towards the radial direction and the D_{in} experienced a faster increment speed (i.e., black solid line). In contrast, the rivet cavity was still not fully filled at the end of the SPR process with the $T_1=2.0$ mm as shown in **Figure 3.20** (d). So the increasing speed of the D_{in} kept almost constant throughout the joining process (i.e., green solid line).

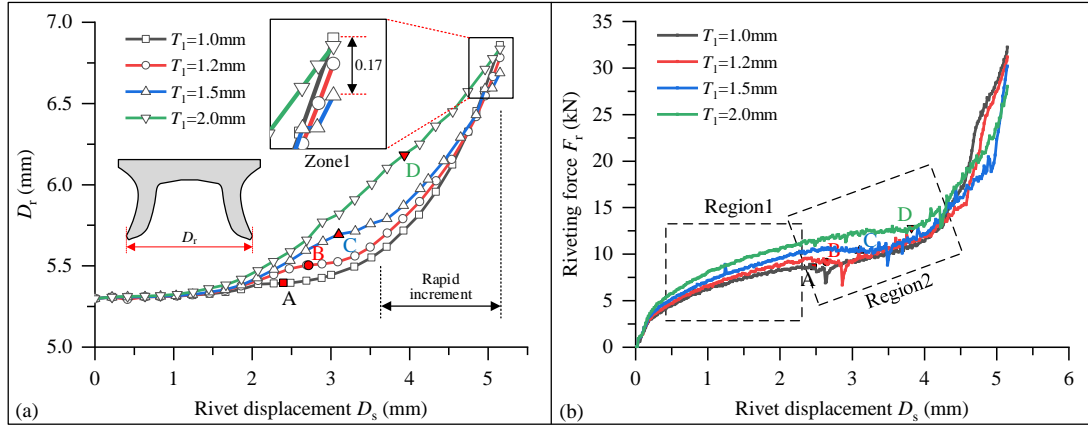


Figure 3.22 Simulated (a) variation curves of the deformed rivet shank diameter (D_r) and (b) load-displacement curves in the SPR joints 3-26~3-29 with different top sheet thicknesses T_1

Since the flare behaviour of rivet shank is so important for the interlock formation, the changing curves of the deformed rivet shank diameter (D_r) during the four joining processes were also numerically extracted and analysed as shown in **Figure 3.22** (a). Because the rivet shank flare behaviour is highly associated with the resistance force that the rivet encountered, the simulated load-displacement curves during the four riveting processes were also recorded as shown in **Figure 3.22** (b). It can be seen from **Figure 3.22** (a) that the four curves of the D_r demonstrated similar increment patterns but different magnitudes. The D_r always first increased slowly at the early stage, and then increased sharply until the end of the joining process. An almost constant increasing speed of the D_r was observed during the rapid increment phase. By comparing the four curves, it was also found that the slow increment of the D_r lasted for a shorter period whilst the rapid increment of the D_r lasted for a longer period in the joints with a larger T_1 . This can be explained by the greater increasing speed of the riveting force (F_r) at the early stage of the joining process with a larger T_1 (Region1 in **Figure 3.22** (b)), which resulted in a higher F_r and thus an earlier start of the rapid increment phase of the D_r . However, due to the slightly smaller rapid increasing speed of the D_r , the maximum value of the D_r was not significantly affected by the T_1 (Zone1 in **Figure 3.22** (a)). The points A, B, C and D in **Figure 3.22** (a) indicate the positions where the top sheet was penetrated by the rivet shank. It can be seen that the increment speed of the D_r was negatively affected by the separation/fracture of the 1.0 mm, 1.2 mm and 1.5 mm top sheets (points A, B, C), but almost not influenced by the fracture of the 2.0 mm top sheet (point D). This might be attributed to the slow increment of the F_r around the points A, B, C but the immediate sharp increment of the F_r following the point D (Region2 in **Figure 3.22** (b)). With the $T_1 = 1.0$ mm, the D_r just increased a limited value before the top sheet was penetrated at the point A (i.e., black line). The major growth of the D_r mainly occurred when the rivet shank flared into the bottom sheet. In contrast, with the $T_1 = 2.0$ mm (i.e., green line), a larger increment of the D_r was observed before the top sheet was penetrated at the point D, whilst a smaller increment of

the D_r was observed when the rivet shank flared into the bottom sheet. Overall, the flare behaviour of the rivet shank can be significantly influenced by the T_1 .

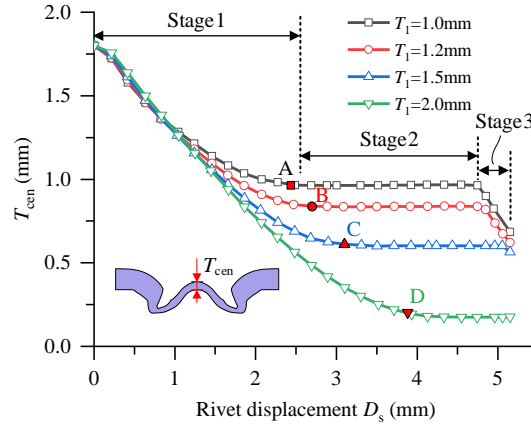


Figure 3.23 Simulated variation curves of the T_{cen} with different top sheet thicknesses T_1

To understand the formation mechanism of the T_{cen} with different T_1 , the changing curves of the T_{cen} during the four riveting processes were numerically extracted as shown in **Figure 3.23**. It can be seen that the T_{cen} on the four curves underwent three different decline stages: it first decreased rapidly (Stage1), and then kept almost constant for a period (Stage2) before the second rapid decline occurred (Stage3). Stage1 started at the beginning of the riveting process, and ended after the top sheet was completely penetrated by the rivet shank (points A, B, C and D). The fracture of top sheet directly changed the magnitudes of stress distributed around the centre of the bottom sheet, which terminated the rapid decline of the T_{cen} . For instance, **Figure 3.24** (a) shows the equivalent stress distribution on the bottom sheet of the joint 3-26 before and after the top sheet separation. Quite large stress was found around the centre of the bottom sheet before the top sheet was penetrated (Zone1), but relatively small stress was found around the same region after the fracture of the top sheet (Zone2). With the increment of the T_1 , the length of Stage1 apparently increased because a larger rivet displacement was required before the top sheet was penetrated. It can also be found that the decreasing speed of the T_{cen} was less influenced by the T_1 and remained almost constant at Stage1. During Stage2, the stress around the centre of the bottom sheet was maintained at a relatively low level, and thus the decreasing speed of the T_{cen} was equal to almost zero. Once the rivet cavity was fully filled with the top sheet material, Stage3 started and the T_{cen} rapidly decreased again. This is because the rivet head applied high pressure on the sheet material trapped in the rivet cavity, and the stress around the centre of the bottom sheet increased to a high level. For instance, **Figure 3.24** (b) shows the equivalent stress distribution on the bottom sheet of the joint 3-26 before and after the rivet cavity was fully filled. The relatively small stress in Zone3 and the large stress in Zone4 clearly explained the appearance of Stage3. With the increment of the T_1 , the length of Stage3 apparently decreased or even disappeared. This is because the filling of the rivet cavity

was apparently delayed as shown in **Figure 3.20**. Furthermore, the increment of the T_1 directly increased the distance from the final position of the rivet to the bottom of the die cavity as shown in **Figure 3.20**, and thus caused the increasing trend of the T_{tip} . It is also worth noting that the increment of the T_{tip} is almost equal to the increment of the T_1 , which can be attributed to the similar magnitudes of the final rivet shank diameter (D_r).

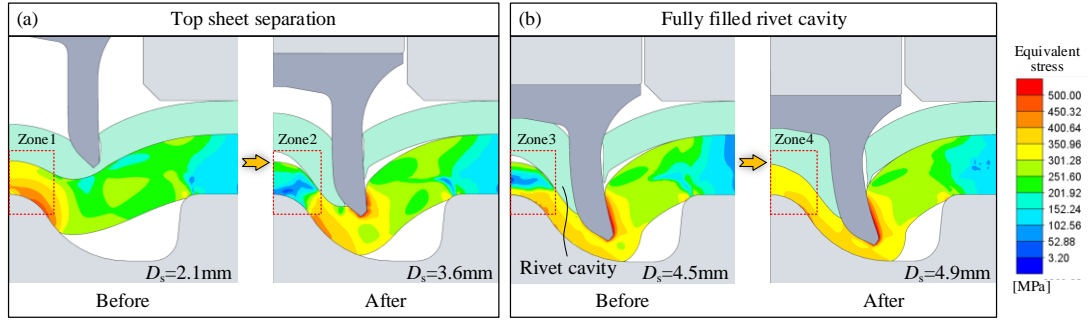


Figure 3.24 Equivalent stress distribution on the bottom sheet of the joint 3-26 ($T_1=1.0$ mm) (a) before and after top sheet separation and (b) before and after the rivet cavity fully filled

3.4.2.3. Formation mechanisms of SPR joints with varying T_2

Figure 3.25 presents the experimentally captured cross-sectional profiles of the joints 3-30~3-33 with different bottom sheet thicknesses (T_2). With the increment of the T_2 , it can be seen that both of the top sheet and bottom sheet underwent less plastic deformation. The rivet shank also flared a smaller distance towards the radial direction. As a result, the defects (i.e., large gaps formed between two sheets and formed between the rivet head and the top sheet in **Figure 3.25** (a)) appeared in the joint 3-30 with $T_2=1.0$ mm were reduced or even eliminated (i.e., Zone1 in **Figure 3.25** (d)) in the joint 3-33. The joint quality was also apparently improved with the increment of the T_2 , including the I , T_{cen} and T_{tip} . The line charts in **Figure 3.26** show the variation trends of the tested three quality indicators (black dash lines) with different T_2 . It can be seen from **Figure 3.26** (a) that the increment of the T_2 imposed positive effects on the interlock formation: the tested I increased from 0.23 mm with $T_2=1.0$ mm in the joint 3-30 to 0.53 mm with $T_2=2.0$ mm in the joint 3-33. A smaller increasing speed of the I was noticed when the T_2 changed from 1.8 mm to 2.0 mm. The position variations of the two interlock boundaries with different T_2 are illustrated in **Figure 3.26** (b). Different from the T_1 , the T_2 imposed significant influences on both of D_{in} and D_{out} . With the T_2 increasing from 1.0 mm to 2.0 mm, the experimentally tested D_{in} declined from 7.06 mm to 5.66 mm whilst the tested D_{out} decreased from 7.48 mm to 6.72 mm. The greater reduction of the D_{in} compared to the D_{out} directly caused the increment of the I . Moreover, it can be seen from **Figure 3.26** (c)(d) that the increment of the T_2 also showed positive influences on the formations of the T_{cen} and T_{tip} . With the T_2 increasing from 1.0 mm to 2.0 mm, the experimentally tested T_{cen} and T_{tip} increased from 0.42 mm to 0.69 mm and from 0.23 mm to 0.53 mm respectively. By

comparing the relative magnitudes of the T_{cen} and T_{tip} in each joint, it can be found that the T_2 also affected the formation position of the minimum remaining bottom sheet thickness (T_{min}): the T_{min} was captured around the rivet tip with $T_2=1.0$ mm in the joint 3-30 but around the joint centre with $T_2=2.0$ mm in the joint 3-33. This position change of the T_{min} can be explained by the greater increasing speed of the T_{tip} than that of the T_{cen} .

To uncover the influences of the T_2 on the SPR joint formation, the developed FEA model was employed again to extract more information during the four riveting processes. The reasonable agreements between the simulated (red short dash lines in **Figure 3.26**) and experimentally tested (black dash lines in **Figure 3.26**) variation trends and magnitudes of the I , D_{in} , D_{out} , T_{cen} and T_{tip} confirmed the effectiveness of the following analyses.

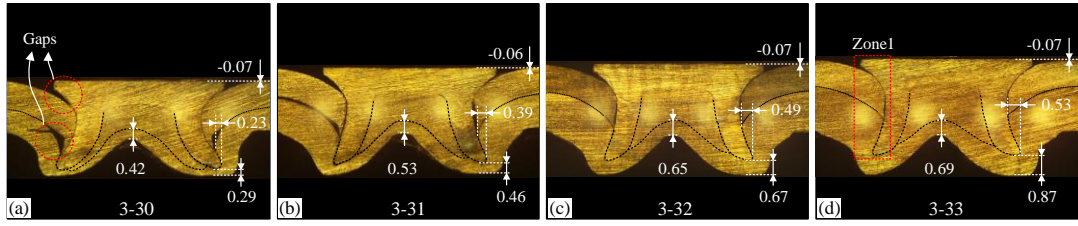


Figure 3.25 Experimentally tested cross-sectional profiles of the joints 3-30~3-33 with different bottom sheet thicknesses T_2 (a) 1.0 mm, (b) 1.5 mm, (c) 1.8 mm and (d) 2.0 mm

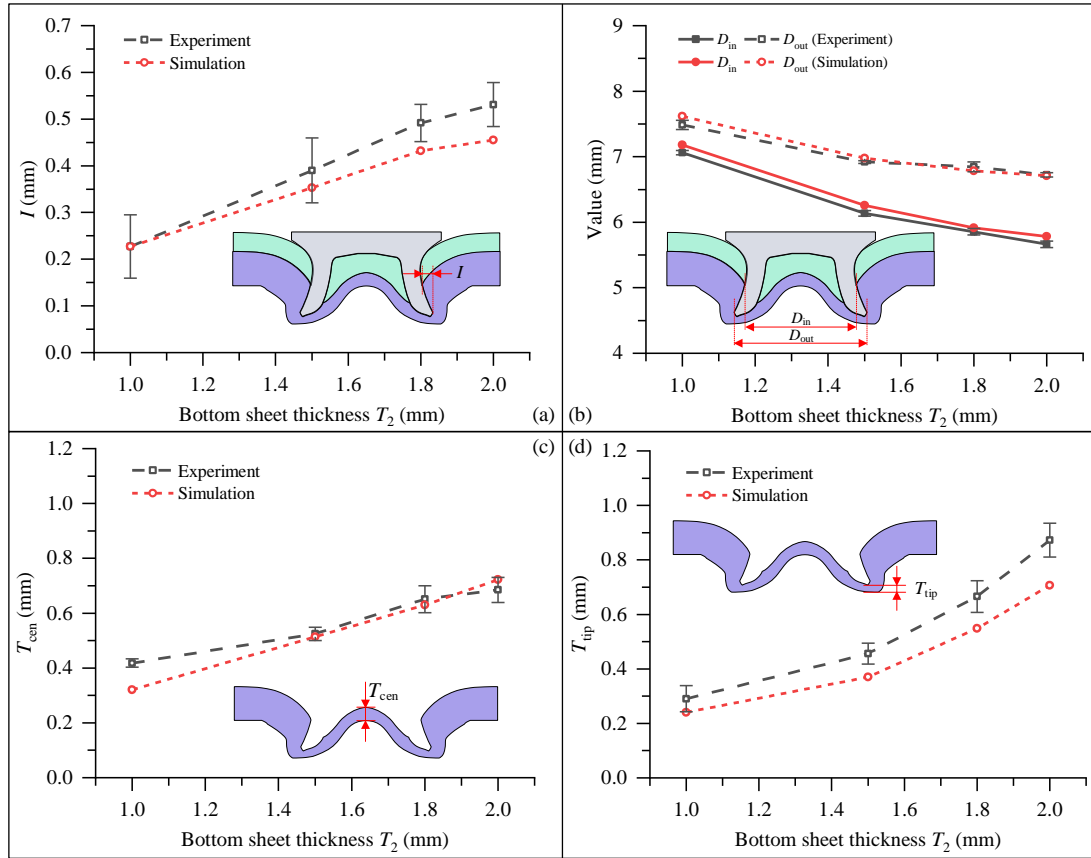


Figure 3.26 Experimentally tested and numerically simulated (a) I , (b) D_{in} and D_{out} , (c) T_{cen} and (d) T_{tip} in the SPR joints 3-30~3-33

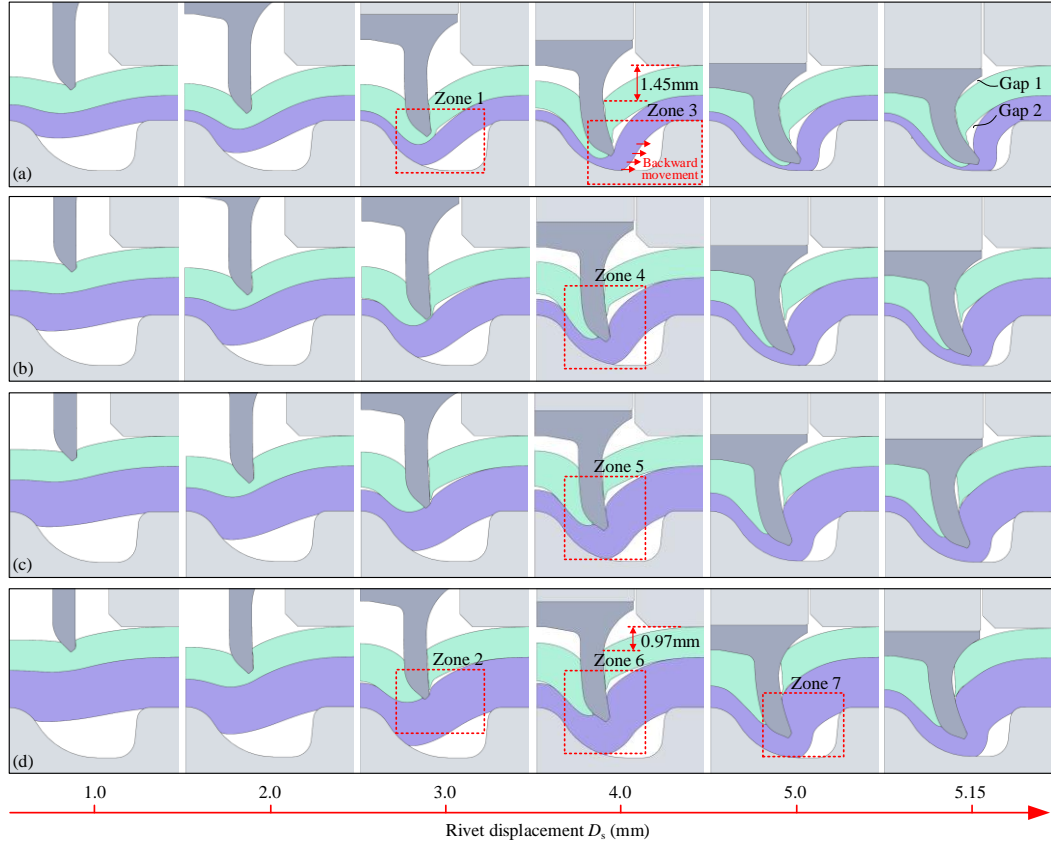


Figure 3.27 Numerically simulated cross-sectional profiles during the riveting processes of the SPR joints 3-30~3-33 (a) $T_2=1.0$ mm, (b) $T_2=1.5$ mm, (c) $T_2=1.8$ mm and (d) $T_2=2.0$ mm

To visually inspect the formation mechanism of the joints 3-30~3-33, the joint cross-sectional profiles at six different rivet displacements (D_s) of each riveting process were numerically extracted as shown in **Figure 3.27**. By comparing the deformation behaviour of the bottom sheet, it can be found that the increment of the T_2 apparently made the bottom sheet more difficult to be deformed. Correspondingly, the downward movement of the top sheet was apparently restricted. For instance, when the $D_s=4.0$ mm, the top sheet underwent a 1.45 mm downward displacement with the $T_2=1.0$ mm in **Figure 3.27** (a) but a 0.97 mm downward displacement with the $T_2=2.0$ mm in **Figure 3.27** (d). The smaller downward displacement of the top sheet and the smaller backward movement of the bottom sheet effectively avoided the formation of gaps appeared in the final joints (e.g., Gap 1 and Gap 2 in **Figure 3.27** (a) vs no gap in **Figure 3.27** (d)). This indicates that a tightly connected joint is more likely formed with a thicker bottom sheet than with a thinner one.

To uncover the impact of the T_2 on the interlock formation, the changing curves of the I during the four riveting processes were numerically extracted as shown in **Figure 3.28** (a). It can be seen that, with the increment of the T_2 , the interlock formation started at an earlier time (Zone 1). This is because the thicker bottom sheet provided a greater resistance force on the top sheet, which allowed the top sheet to be penetrated by the rivet shank at a faster speed rather than to be pressed downward rapidly (e.g., Zone 1 vs Zone 2 in **Figure 3.27**). The rivet shank started

piercing into the bottom sheet at an earlier time, and therefore the formation of interlock also occurred at an earlier time. Moreover, similar increasing speeds of the I were observed on the four curves, whilst the interlock formation process lasted for a longer period when with a thicker bottom sheet. As a result, the I showed an increasing trend with the increment of the T_2 as shown in **Figure 3.26** (a).

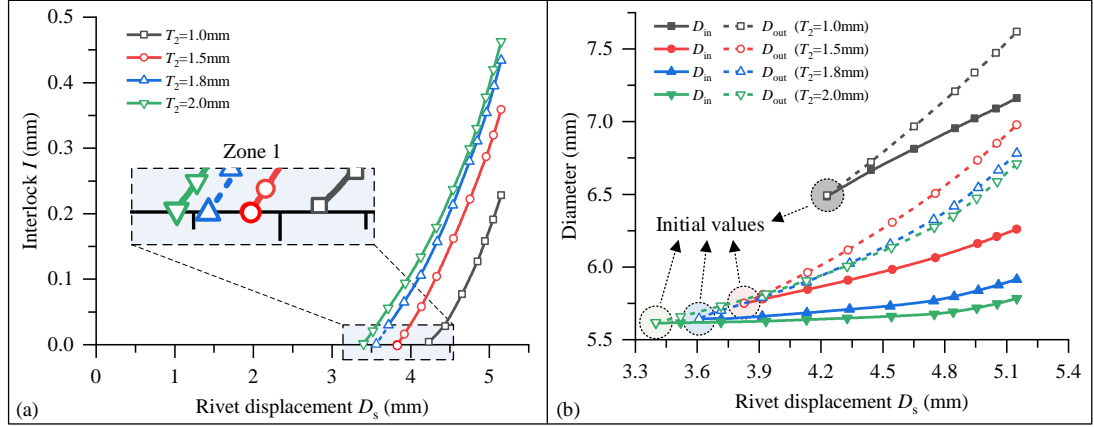


Figure 3.28 Numerically simulated (a) formation curves of the I and (b) formation curves of the two interlock boundaries during riveting processes of the joints 3-30~3-33

Figure 3.28 (b) shows the numerically extracted changing curves of the D_{in} (solid lines) and D_{out} (dash lines) during the four riveting processes. It can be seen that the initial values of the D_{in} and D_{out} apparently decreased with the T_2 increasing from 1.0 mm to 1.5 mm (marked with black and red circles), but just slightly decreased with the T_2 increasing from 1.5 mm to 2.0 mm (marked with red, blue and green circles). This can be explained by the different rigidities of bottom sheets with varying T_2 . Compared with the 1.5 mm, 1.8 mm and 2.0 mm bottom sheets, the 1.0 mm bottom sheet had a much lower rigidity and thus was easily pushed backward rather than pierced by the rivet shank after the completely penetration of the top sheet (Zone 3 in **Figure 3.27** (a)). As a result, the rivet shank started piercing into the bottom sheet at a very late time, and the initial values of the D_{in} and D_{out} were apparently greater than that in the other three joints. In contrast, the rigidity of the 1.5 mm bottom sheet was already large enough to avoid fast backward movement of the bottom sheet. The increment of the T_2 from 1.5 mm to 2.0 mm further restricted the backward movement of the bottom sheet, and led to an earlier start of the rivet shank flaring into the bottom sheet. Due to the similarly limited rivet shank deformation in the three riveting processes (Zone 4, Zone 5 and Zone 6 in **Figure 3.27** (b)(c)(d)), the initial values of the D_{in} and D_{out} just slightly changed. From **Figure 3.28** (b), it can also be found that the increasing speed of the D_{in} showed a decreasing trend with the increment of the T_2 . Similar phenomenon was also observed for the increasing speed of the D_{out} . As a result, the initial differences of the D_{in} and D_{out} during the four riveting processes could not be eliminated and therefore both of the D_{in} and D_{out} showed a decreasing tendency with the increment of the T_2 as shown in **Figure 3.26** (b).

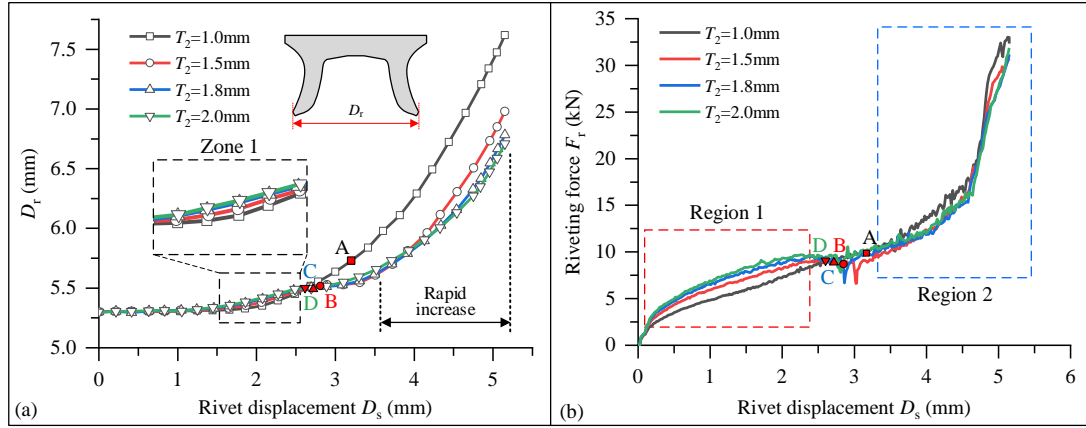


Figure 3.29 Simulated (a) variation curves of the deformed rivet shank diameter (D_r) and (b) load-displacement curves in the SPR joints 3-30~3-33 with different bottom sheet thicknesses T_2

Figure 3.29 (a) shows the numerically extracted changing curves of the deformed rivet shank diameter (D_r) during the four joining processes. It can be seen that the flare behaviour of rivet shank was apparently affected by the T_2 . Before the top sheet was completely penetrated by the rivet shank (marked as points A, B, C and D), the D_r on the four curves increased slowly and its magnitude just increased a little bit with the increment of the T_2 (Zone 1). This is attributed to the slightly greater riveting force (Region 1 in **Figure 3.29** (b)) induced by the higher rigidity of the thicker bottom sheet. Obvious differences between the four curves were observed after the penetration of the top sheet. Although similar magnitudes of the F_r were observed during this period (Region 2 in **Figure 3.29** (b)), the increasing speed of the D_r demonstrated a decreasing trend with the increment of the T_2 . This is also because the thicker bottom sheet is increasingly difficult to be pushed backward. The rivet shank pierced into the thicker bottom sheet quickly along the vertical direction rather than along the radial direction. As a result, the maximum D_r showed a decreasing trend with the increment of the T_2 . From the above analyses, it can be concluded that the increment of the T_2 had negative effects on the rivet shank flare under the studied joint configurations.

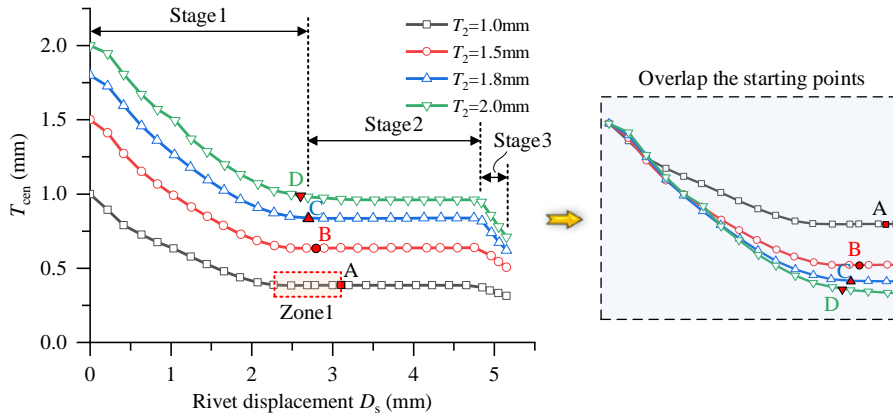


Figure 3.30 Simulated variation curves of the T_{cen} with different bottom sheet thicknesses T_2

To figure out the impact of the T_2 on the formation of the T_{cen} , the numerically extracted changing curves of the T_{cen} during the four riveting processes are presented in **Figure 3.30**. For easier comparison, the starting points of the four curves were overlapped together. It can be seen that the lengths of the first rapid decrease (i.e., Stage1) were almost the same on the four curves. However, with the increment of the T_2 , the T_{cen} reduced a greater value during this stage. It was also noticed that Stage1 stopped before the top sheet was completely penetrated with $T_2=1.0$ mm in the joint 3-30 (point A on the black line). This is attributed to the changes of the stress distribution around the central area of the bottom sheet. As shown in **Figure 3.31**, quite high stress was observed on the bottom sheet when the rivet displacement was equal to 2.1 mm (Zone 1), but the magnitudes of stress reduced to a low level when the rivet displacement increased to 2.7 mm (Zone 2). The earlier reduction of the stress was directly caused by the large deformation of the low rigidity 1.2 mm top sheet. Moreover, by comparing the four curves, it can also be seen that the second rapid decrease (i.e., Stage3) started almost at the same time. This is because the T_2 showed limited influences on the filling condition of the rivet cavity. However, a greater decreasing speed of the T_{cen} was found with a thicker bottom sheet during this stage. This might be explained by the larger amount of bottom sheet material and the lower-level equivalent strain around the centre of the thicker bottom sheet (e.g., Zone 1 and Zone 2 in **Figure 3.32**). Finally, although the T_{cen} reduced greater values during Stage1 and Stage3, the final magnitude of the T_{cen} still showed an increasing trend with the increment of the T_2 .

Furthermore, similarly to the T_1 , the increment of the T_2 also significantly increased the distance from the final position of the rivet to the bottom of the die cavity, and thus caused the increment of the T_{tip} . It is worth mentioning that the increased value of the T_{tip} is smaller than the increment of the T_2 . This can be explained by the reduction of the rivet shank flare with a thicker bottom sheet.

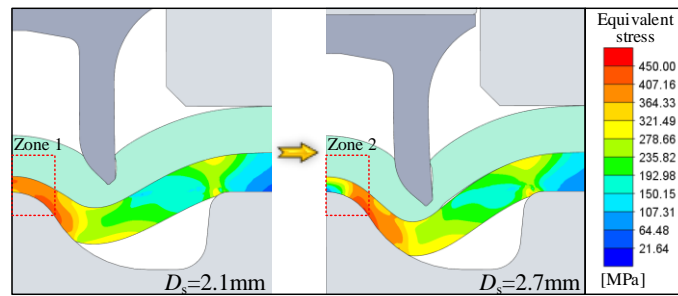


Figure 3.31 Equivalent stress distribution on the bottom sheet of the joint 3-30 ($T_2=1.0$ mm)

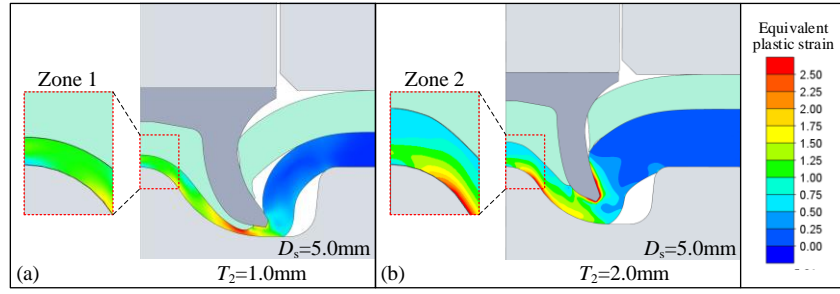


Figure 3.32 Equivalent plastic strain distribution on the bottom sheet of the (a) joint 3-30 and (b) joint 3-33

3.4.2.4. Formation mechanisms of SPR joints with varying L_1

Figure 3.33 shows the experimentally captured cross-sectional profiles of the joints 3-34~3-36 with different rivet lengths (L_1). It can be seen that the final profiles of these SPR joints were also significantly affected by the L_1 , especially the deformed bottom sheet around the rivet tip. Consequently, the magnitudes of the I , T_{cen} and T_{tip} were also influenced. For easier comparison, the tested variation trends of the I , T_{cen} and T_{tip} with different L_1 are plotted into line charts as shown in **Figure 3.34** (black dash lines). It can be seen from **Figure 3.34** (a) that the increment of the L_1 imposed positive influences on the interlock formation: the experimentally tested I rapidly increased from 0.49 mm with $L_1=5.0$ mm in the joint 3-34 to 1.23 mm with $L_1=6.5$ mm in the joint 3-36. **Figure 3.34** (b) shows the position variations of the two interlock boundaries. It can be seen that the L_1 demonstrated significant influences on the D_{out} but limited effects on the D_{in} . With the L_1 increasing from 5.0 mm to 6.5 mm, the D_{out} increased rapidly from 6.84 mm to 8.48 mm but the D_{in} just slightly increased from 5.85 mm to 6.03 mm. This indicates that the L_1 affected the interlock formation by mainly altering the position of the outer interlock boundary. From **Figure 3.34** (c)(d), it is obvious that the increment of the L_1 had negative effects on the formation of the T_{tip} but imposed limited influences on the formation of the T_{cen} : the tested T_{tip} rapidly decreased from 0.67 mm to 0.26 mm but the tested T_{cen} only fluctuated within a narrow range (i.e., 0.65~0.71 mm) with the increment of the L_1 . By comparing the relative magnitudes of the T_{cen} and T_{tip} in each joint, it can be found that the formation position of the T_{min} was also affected: around the joint centre with the $L_1=5.0$ mm but around the rivet tip with the $L_1=6.0$ mm and 6.5 mm.

The numerically predicted variation trends and magnitudes of the I , D_{in} , D_{out} , T_{cen} and T_{tip} (red short dash lines) showed reasonable agreements with that from the experimental SPR tests (black dash lines) in **Figure 3.34**. Thus, the developed FEA model was also employed to analyse the formation mechanisms of the SPR joints 3-34~3-36.

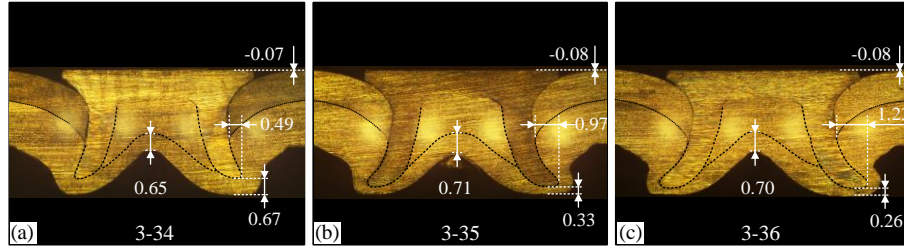


Figure 3.33 Tested cross-sectional profiles of the joints 3-34~3-36 with different rivet lengths L_1 (a) 5.0 mm, (b) 6.0 mm and (c) 6.5 mm

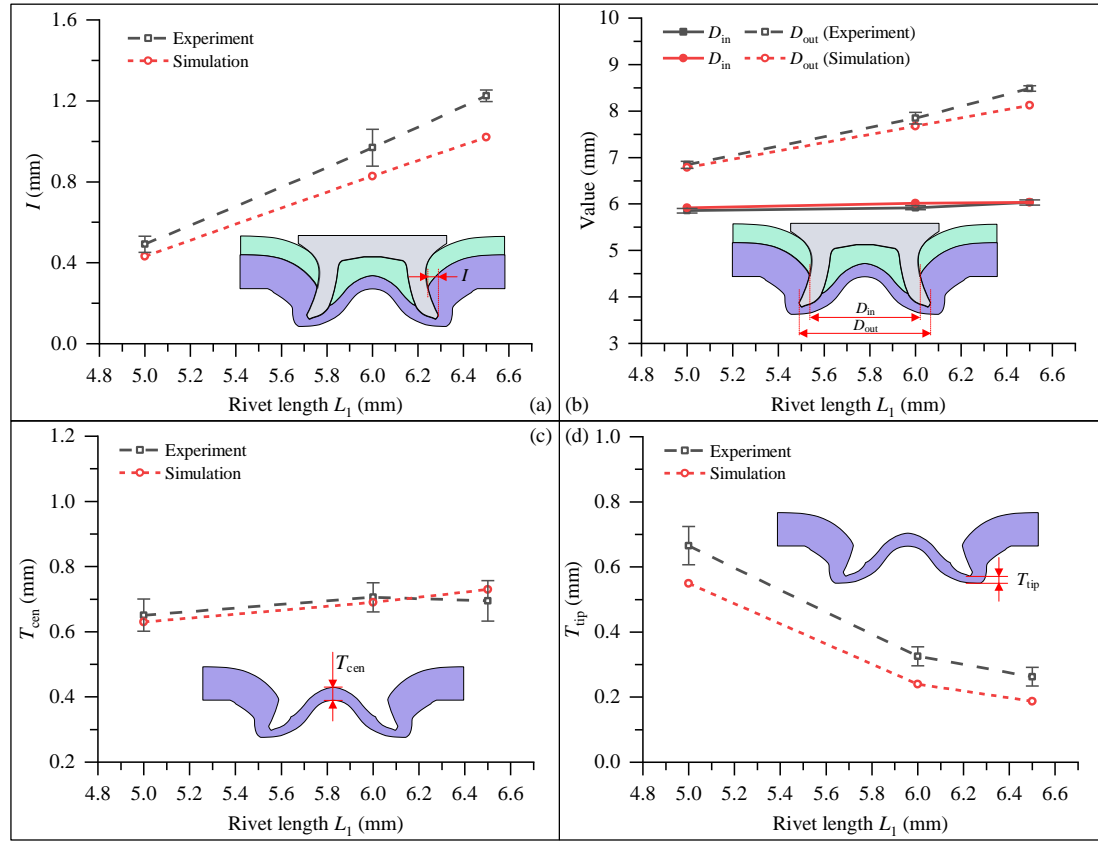


Figure 3.34 Experimentally tested and numerically simulated (a) I , (b) D_{in} and D_{out} , (c) T_{cen} and (d) T_{tip} in the SPR joints 3-34~3-36

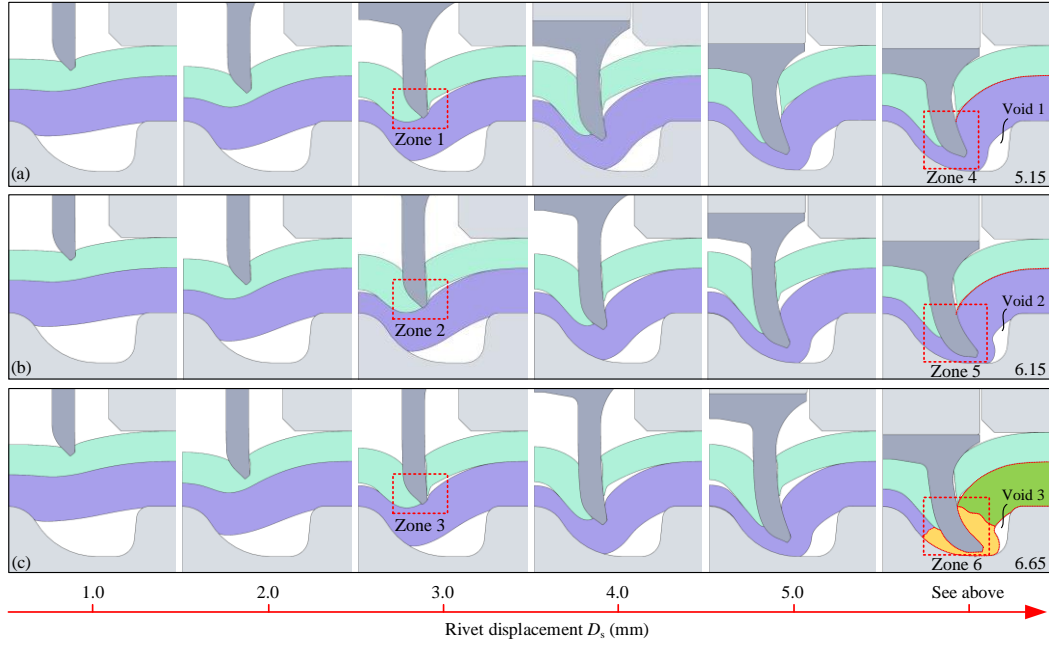


Figure 3.35 Numerically simulated cross-sectional profiles during riveting processes of the SPR joints 3-34~3-36 (a) $L_1=5.0$ mm, (b) $L_1=6.0$ mm and (c) $L_1=6.5$ mm

With the help of the FEA model, the joint cross-sectional profiles at six different rivet displacements (D_s) were numerically extracted to observe the joint formations with different L_1 as shown in **Figure 3.35**. Before the head of the 5.0 mm long rivet started pressing the top sheet ($D_s \approx 4.0$ mm), it can be seen that the deformed shapes of the top and bottom sheets during the three riveting processes were almost identical. The penetration of the top sheet was not obviously affected by the L_1 and occurred at almost the same time (Zones 1, 2 and 3). Main differences were observed at the later stage of these joining processes. The rivet shank apparently flared a larger distance into the bottom sheet with the increment of the L_1 (Zones 4, 5 and 6). As a result, a greater localized deformation of the bottom sheet was found around the rivet tip (yellow region in **Figure 3.35** (c)), whilst the final shape of the bottom sheet far from the rivet tip (green and violet regions in **Figure 3.35** (c)) remained almost the same in the three joints. Consequently, the final magnitudes of the quality indicators I , T_{cen} and T_{tip} were affected to different degrees.

Figure 3.36 (a) shows the impact of the L_1 on the formation process of interlock I . It can be seen that the starting points of interlock formation were nearly the same (Zone 1), and the increasing speeds of the I were almost identical on the three curves. The only difference is that the quick increase of the I lasted for a longer period with the increment of the L_1 . With the increment of the rivet displacement, the nearly same increasing patterns and magnitudes of the I on the three curves explained the linear increment of the final I shown in **Figure 3.34** (a).

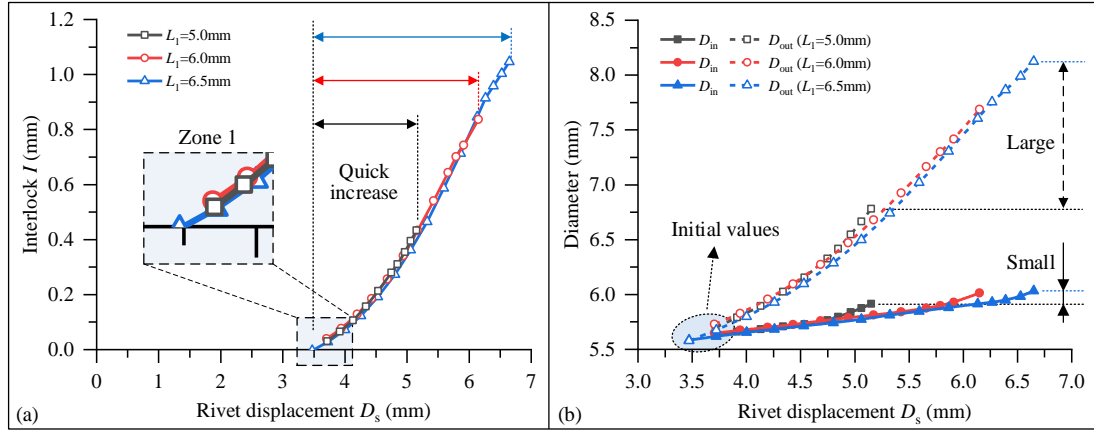


Figure 3.36 Numerically simulated (a) formation curves of the I and (b) formation curves of the two interlock boundaries during riveting processes of the joints 3-34~3-36

Figure 3.36 (b) shows the numerically extracted changing curves of the D_{in} (solid lines) and D_{out} (dash lines) during the three riveting processes. It can be seen that the D_{in} experienced a similar increasing pattern but lasted for a longer period with the increment of the L_1 . Similar phenomenon was also identified from the three changing curves of the D_{out} . The large enough space of the die cavity successfully accommodated the materials of sheets and rivets with varying L_1 , and contributed to the similar increasing patterns of the D_{in} and D_{out} . However, due to the relatively low increasing speed of the D_{in} , the maximum D_{in} increased a limited value with the L_1 increasing from 5.0 mm to 6.5 mm. In contrast, because of the high increment speed of the D_{out} , the maximum D_{out} increased a quite large value with the increment of the L_1 . The increasing patterns of these curves clearly uncovered the different influences of the L_1 on the two interlock boundaries shown in **Figure 3.34** (b). Overall, the L_1 affected the interlock formation by mainly altering the position of the outer interlock boundary under the studied joint configurations.

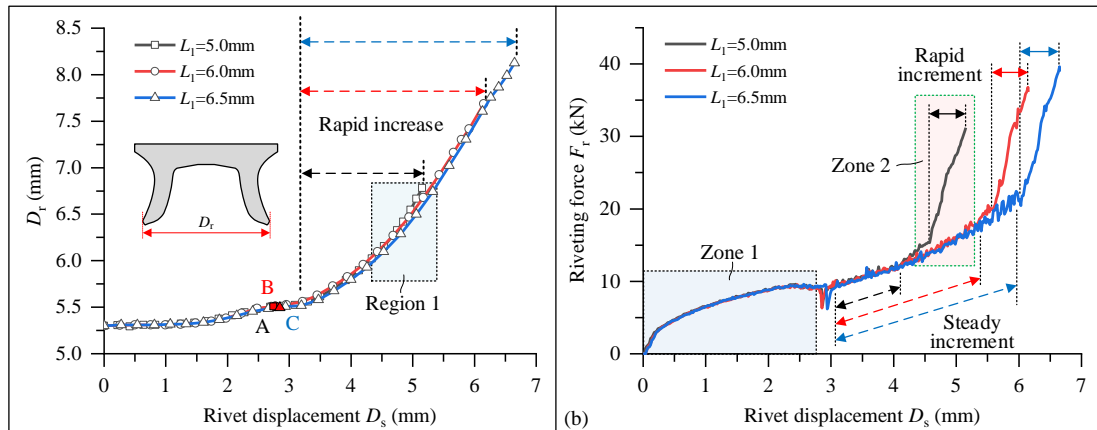


Figure 3.37 Simulated (a) variation curves of the deformed rivet shank diameter (D_r) and (b) load-displacement curves in the SPR joints 3-34~3-36 with different rivet lengths L_1

The numerically extracted changing curves of the deformed rivet shank diameter (D_r) during the three riveting processes are shown in **Figure 3.37** (a). It can be seen that the magnitudes

of the D_r were almost the same at the slow increment stage on the three curves. This can be explained by the same riveting forces (F_r) during this period (Zone 1 in **Figure 3.37** (b)). The increasing speeds of the D_r at the rapid increase stage were nearly identical on the three curves. Compared with the steady increment of the F_r with the $L_1=6.0$ mm and 6.5 mm (Zone 2 in **Figure 3.37** (b)), the F_r with $L_1=5.0$ mm experienced a much faster increment but contributed very little to the rivet shank flare (Region 1 in **Figure 3.37** (a)). This is because a large part of the F_r was used to overcome the resistance force applied on the rivet head instead of that applied on the rivet shank. This phenomenon indicates that, by properly optimizing the rivet head geometry, it might be possible to reduce the maximum riveting force without affecting too much of the rivet shank flare behaviour. For example, reducing the thickness around the central area of the rivet head to delay the occurrence of the rapid increment of the F_r . As shown in **Figure 3.37** (a), the main difference between the three curves is that the rapid increment of the D_r lasted for a longer period with a greater L_1 . This directly caused the almost linear increment trends of the I and the D_{out} shown in **Figure 3.34** (a)(b). By comparing the three load-displacement curves in **Figure 3.37** (b), it is also found that the increment of the L_1 led to a larger length of the steady increment of the F_r , but showed little influence on the increasing pattern and speed at the rapid increment stage of the F_r . In general, the L_1 had significant influences on the flare behaviour of the rivet shank.

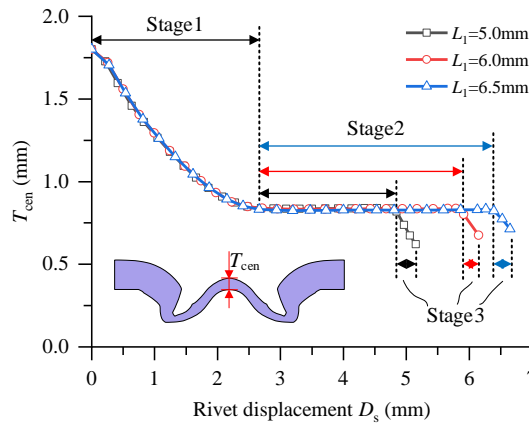


Figure 3.38 Simulated variation curves of the T_{cen} with different rivet lengths L_1

Figure 3.38 shows the influences of the L_1 on the formation of the T_{cen} . By comparing the three changing curves of the T_{cen} , it can be found that the increment of the L_1 had no influence on the speed and length of the first rapid decrease of the T_{cen} (i.e., Stage1). However, it led to a longer length of Stage2 and delayed the appearance of the second rapid decrease of the T_{cen} (i.e., Stage3). During Stage3, a slightly smaller decreasing speed of the T_{cen} was observed with a larger L_1 . This difference might be attributed to the different filling conditions of the die cavity. With the increment of the L_1 , the decreasing void space in the die cavity (i.e., Void 1 > Void 2 > Void 3 in **Figure 3.35**) restricted the deformations of the rivet and bottom sheet, and

thus led to the slightly smaller speed of the T_{cen} . As a result, the increment of the L_1 imposed very limited influences on the maximum T_{cen} shown in **Figure 3.34** (c). Moreover, the increment of the L_1 directly shortened the relative distance between the final position of the rivet tip and the die as shown in **Figure 3.35**, and therefore caused the rapid decline of the T_{tip} shown in **Figure 3.34** (d).

From the above analyses of joint formation processes with varying T_1 , T_2 and L_1 , it can be found that the FEA model of SPR process is a powerful tool for investigating the joining parameters' impact on the SPR joint formation. Information within the joining region can be easily extracted with the FEA model to inspect the events happened during the riveting process. This makes the analysis of experimental results much easier and more intuitive. By linking the deformation behaviours of the rivet and sheets with the joint quality indicators, the formation mechanism of the SPR joint can be clearly understood. Therefore, the FEA model has great potentials to become a mainstream research approach to speed up the development of SPR technique.

3.5. Summary

A 2D FEA model of the SPR process was established in this chapter, and its accuracy was verified with both the general experimental SPR tests and interrupted experimental SPR tests. Then, the verified FEA model combined with the single factor experiments was utilized to investigate the formation mechanisms of SPR joints with varying top sheet thicknesses (T_1), bottom sheet thicknesses (T_2) and rivet lengths (L_1). The main conclusions obtained are summarised below:

1. The comparisons between the experimental and simulation results showed that the developed FEA model not only could accurately predict the SPR joint quality indicators and the final joint cross-sectional profile, but also could predict the joint formation during the riveting process. It was proved that the FEA model is an excellent alternative to the interrupted experimental test for the study of SPR joint formation mechanisms.
2. Increment of the T_1 showed negative influences on the interlock formation by mainly affecting the position of the inner interlock boundary. In contrast, increment of the L_1 imposed positive influences on the interlock formation by mainly altering the position of the outer interlock boundary. Increment of the T_2 was also beneficial for interlock formation by affecting both the inner and outer interlock boundaries.
3. Increment of the T_1 showed negative effects on the formation of remaining bottom sheet thickness at the joint centre (T_{cen}), whilst increment of the T_2 imposed positive influences on the T_{cen} . Increment of the L_1 showed very limited influences on the formation of the

T_{cen} . The rapid decline of the T_{cen} mainly occurred before the top sheet was completely penetrated and after the rivet cavity was fully filled.

4. Increments of the T_1 and T_2 demonstrated positive influences on the remaining bottom sheet thickness under the rivet tip (T_{tip}), but increment of the L_1 imposed negative influences on the T_{tip} . All the three joining parameters affected the T_{tip} by directly altering the relative distance between the final position of rivet tip and the bottom surface of the die cavity.
5. The formation position of the minimum remaining bottom sheet thickness (T_{min}) was significantly affected by the T_1 , T_2 and L_1 . Increment of the T_1 and T_2 will increase the possibility of the T_{min} formed around the joint centre, whilst increment of the L_1 will increase the possibility of the T_{min} formed around the rivet tip.
6. When piercing the top sheet, the flare behaviour of the rivet shank was significantly affected by the T_1 , but only slightly affected by the T_2 and L_1 . When piercing the bottom sheet, the flare speed of the rivet shank decreased with the increment of the T_1 and T_2 , but remained almost constant with the increment of the L_1 . For the studied joint configurations, the final value of the deformed rivet shank diameter (D_r) fluctuated within a small range with the increment of the T_1 . In contrast, it obviously decreased with the increment of the T_2 , but increased almost linearly with the increment of the L_1 .

4. Quality prediction and interaction analysis for the SPR process with regression analysis

To meet the demand from the automotive industry for fast and easy-to-use quality prediction tools, this chapter adopted the regression analysis method to establish fast response prediction models for the SPR joint quality. The FEA model developed in Chapter 3 together with the orthogonal experimental design were used to collect the necessary joint quality data for regression model development. Analysis of variance (ANOVA) was performed to determine the importance of different rivet and die parameters on the interlock (I) and the minimum remaining bottom sheet thickness (T_{\min}). Then, two regression models considering three joining parameters (i.e., rivet length L_1 , die diameter D_1 and depth H_1) were developed to respectively predict the magnitudes of interlock and T_{\min} in SPR joints with varying configurations, and their performances were validated through experimental SPR tests. In addition, taking advantage of the developed two regression prediction models, interaction effects between the L_1 , D_1 and H_1 on the interlock and T_{\min} were also systematically studied by plotting corresponding contour graphs. The reasons behind these interaction effects were explained from the view of rivet and sheet material deformations with the FEA model. The importance of the Die-to-Rivet volume ratio (R) on the SPR joint quality was also highlighted.

4.1. Introduction

Over the last two decades, the fast development of high prediction accuracy FEA models for the SPR process [42,44,99] offers a promising way to shorten the design cycle and reduce the financial investment of new SPR joints. Many vehicle manufacturers, such as Audi and JLR, have gradually applied such FEA models to assist the selection of rivet and die in the new joint design process. However, for engineers without in-depth knowledge of the FEA, developing and running such simulation models is still a big challenge. It will be a great contribution for the automotive industry if a fast and easy-to-use tool can be developed to predict the joint quality.

The multiple regression model is simple but effective to describe the relationships between independent and dependent variables, and has already been widely applied in different industrial fields to solve practical problems. For example, Bhushan [156] proposed second order regression models to investigate the cutting parameters' influences during the turning of aluminium alloy 7075. Singh and Ahuja [157] developed regression models to study the influences of two swellable polymers on the bioadhesive strength and release pattern of the

drug. Anawa and Olabi [158] successfully predicted the welding pool geometry of the CO₂ continuous laser welded joints using the proposed multiple regression models. Bitondo et al. [159] also proved the effectiveness of multiple regression models in prediction of welding force and mechanical strength of friction-stir welded aluminium joints. Zhao et al. [160] developed a nonlinear mathematical model using the stepwise regression analysis method to predict the nugget diameter of the resistance spot welded DP600 joint with three welding parameters. To the author's knowledge, there are few reports on the application of regression model in the SPR joint quality prediction.

As previously discussed, the SPR joint quality can be significantly affected by the rivet and die parameters [28,136]. To facilitate the selection of rivet and die for new SPR joints, it is necessary to find out the impact of different rivet and die parameters on the joint quality. So far, a great number of studies have been carried out on this topic but most of them focused on single-factor effects of the rivet or die parameters on the SPR joint quality [35,45,82]. In fact, the rivet and die work together during the riveting process to affect the joint formation and the final joint quality. It is very important and necessary to investigate the interaction effects between rivet and die parameters on the joint quality. Although the experimental method is the most reliable approach for the study of SPR joints, it is not a good option to explore the interaction effects considering the heavy investment (e.g., materials, equipment and labour) and long testing time for a huge number of SPR joints. Similarly, the FEA model cannot provide a straightforward result to demonstrate the interaction effects between different rivet and die parameters on the joint quality. In contrast, the regression model can be conveniently used to visualize the interaction effects between different input variables on the output response by drawing the corresponding contour graphs [158–160]. It is a promising way to analyse the interaction effects between rivet and die parameters on the SPR joint quality.

Therefore, fast response and easy-to-use multiple regression models were developed in this chapter to predict the quality of aluminium alloy AA5754 SPR joints with different configurations, and to uncover the interaction effects between rivet and die parameters (i.e., rivet length (L_1), die diameter (D_1) and die depth (H_1)) on the joint quality. The FEA model developed in Chapter 3 was adopted to collect the necessary joint quality data for the model development. The close connection between the Die-to-Rivet volume ratio (R) and the interaction effects of rivet and die was also highlighted.

4.2. Mathematical regression models for prediction of interlock and T_{\min}

4.2.1. Joint quality data collection

To minimise the number of SPR joints but collect enough joint quality data for the regression model development, the orthogonal design method was adopted in this section. The rivet length (L_1), die diameter (D_1) and depth (H_1) are the three independent variables considered in the regression model, and each independent variable has three levels as listed in Table 4.1. Moreover, to investigate the interaction effects of the L_1 , D_1 and H_1 on the joint quality, the interaction terms between these joining parameters ($L_1 \times D_1$, $L_1 \times H_1$ and $D_1 \times H_1$) were also considered in the orthogonal test design. Each interaction terms should take two columns in the orthogonal test table (i.e., $(L_1 \times D_1)1$, $(L_1 \times D_1)2$, $(L_1 \times H_1)1$, $(L_1 \times H_1)2$, $(D_1 \times H_1)1$ and $(D_1 \times H_1)2$) because there are three levels of each independent variables. According to the numbers of independent variables, interaction terms and levels, the L_{27} (3^{13}) orthogonal table with 13 columns and 27 rows was selected and designed as listed in **Table 4.2**. Four null columns were left and treated as error terms.

The 27 SPR joints with different configurations in **Table 4.2** were simulated using the FEA model developed in Chapter 3. For consistency, all the simulations were terminated when the rivet head height (H) reached 0.0 mm. After all these simulations were completed, the cross-sectional profile and joint quality indicators (i.e., interlock I and T_{\min}) of each joint were extracted from the simulation results. By observing the 27 simulated joint cross-sectional profiles, it was found that the T_{\min} appeared around the rivet tip in most joints. Therefore, to keep the data uniformity and to simplify the prediction model development, the minimum bottom sheet thickness around the rivet tip in each joint was measured as the T_{\min} in this section. **Table 4.2** shows the simulated values of the I and T_{\min} for the 27 SPR joints.

Table 4.1 Independent variables and levels of the orthogonal test

Level	Rivet length L_1/mm	Die diameter D_1/mm	Die depth H_1/mm
1	5.0	8.0	1.6
2	6.0	9.0	1.8
3	6.5	10.0	2.0

Table 4.2 $L_{27} (3^{13})$ orthogonal test design and simulation results

Joint no.	Variables and levels													Results	
	L_1	D_1	$(L_1 \times D_1)_1$	$(L_1 \times D_1)_2$	H_1	$(L_1 \times H_1)_1$	$(L_1 \times H_1)_2$	$(D_1 \times H_1)_1$	--	--	$(D_1 \times H_1)_2$	--	--	I /mm	T_{\min} /mm
4-1	1	1	1	1	1	1	1	1	1	1	1	1	1	0.367	0.558
4-2	1	1	1	1	2	2	2	2	2	2	2	2	2	0.394	0.552
4-3	1	1	1	1	3	3	3	3	3	3	3	3	3	0.349	0.521
4-4	1	2	2	2	1	1	1	2	2	2	3	3	3	0.379	0.506
4-5	1	2	2	2	2	2	2	3	3	3	1	1	1	0.330	0.504
4-6	1	2	2	2	3	3	3	1	1	1	2	2	2	0.267	0.524
4-7	1	3	3	3	1	1	1	3	3	3	2	2	2	0.283	0.556
4-8	1	3	3	3	2	2	2	1	1	1	3	3	3	0.239	0.573
4-9	1	3	3	3	3	3	3	2	2	2	1	1	1	0.198	0.594
4-10	2	1	2	3	1	2	3	1	2	3	1	2	3	0.566	0.264
4-11	2	1	2	3	2	3	1	2	3	1	2	3	1	0.595	0.321
4-12	2	1	2	3	3	1	2	3	1	2	3	1	2	0.611	0.341
4-13	2	2	3	1	1	2	3	2	3	1	3	1	2	0.739	0.263
4-14	2	2	3	1	2	3	1	3	1	2	1	2	3	0.713	0.266
4-15	2	2	3	1	3	1	2	1	2	3	2	3	1	0.700	0.249
4-16	2	3	1	2	1	2	3	3	1	2	2	3	1	0.594	0.271
4-17	2	3	1	2	2	3	1	1	2	3	3	1	2	0.550	0.276
4-18	2	3	1	2	3	1	2	2	3	1	1	2	3	0.523	0.249
4-19	3	1	3	2	1	3	2	1	3	2	1	3	2	0.615	0.159
4-20	3	1	3	2	2	1	3	2	1	3	2	1	3	0.658	0.202
4-21	3	1	3	2	3	2	1	3	2	1	3	2	1	0.688	0.239
4-22	3	2	1	3	1	3	2	2	1	3	3	2	1	0.892	0.226
4-23	3	2	1	3	2	1	3	3	2	1	1	3	2	0.876	0.225
4-24	3	2	1	3	3	2	1	1	3	2	2	1	3	0.862	0.204
4-25	3	3	2	1	1	3	2	3	2	1	2	1	3	0.752	0.255
4-26	3	3	2	1	2	1	3	1	3	2	3	2	1	0.748	0.192
4-27	3	3	2	1	3	2	1	2	1	3	1	3	2	0.719	0.176

4.2.2. Analysis of variance

Before developing the mathematical prediction models for the interlock and T_{\min} , the ANOVA was performed using the orthogonal test results to evaluate the significances of the three independent variables (L_1 , D_1 and H_1) and their interaction terms ($L_1 \times D_1$, $L_1 \times H_1$ and $D_1 \times H_1$) on the interlock and T_{\min} with software Minitab 19. **Table 4.3** and **Table 4.4** list the results of the ANOVA for the interlock and the T_{\min} respectively. The significance of the assessed variable is reflected by the magnitude of the p-value. In general, the smaller the p-value is, the more significant the variable is. A variable is usually considered to be significant for the response if the corresponding p-value is smaller than 0.05 or 0.10, depending on the selected significant level (0.05 or 0.10). According to the ANOVA results, it was apparent that all the

three independent variables and their interaction terms had significant influences on the interlock as the p-values were less than 0.05. However, under the studied joint configurations, the rivet length (L_1) showed a significant influence on the T_{\min} , whilst the other two independent variables (D_1 and H_1) and the three interaction terms ($L_1 \times D_1$, $L_1 \times H_1$ and $D_1 \times H_1$) did not show remarkable effects on the T_{\min} .

Table 4.3 Results of ANOVA for the interlock

Source	DF	Adj SS	Adj MS	F-Value	p-Value
L_1	2	0.93608	0.468041	4322.59	0.000
D_1	2	0.08224	0.041120	379.77	0.000
$L_1 \times D_1$	4	0.06324	0.01581	146.00	0.000
H_1	2	0.00424	0.002121	19.59	0.001
$L_1 \times H_1$	4	0.00465	0.001163	10.74	0.003
$D_1 \times H_1$	4	0.00937	0.00234	21.64	0.000
Error	8	0.00087	0.000108	--	--
Total	26	1.10069	--	--	--

Table 4.4 Results of ANOVA for the T_{\min}

Source	DF	Adj SS	Adj MS	F-Value	p-Value
L_1	2	0.561094	0.280547	266.93	0.000
D_1	2	0.002480	0.001240	1.18	0.356
$L_1 \times D_1$	4	0.00833	0.00208	1.98	0.191
H_1	2	0.000168	0.000084	0.08	0.924
$L_1 \times H_1$	4	0.00071	0.00018	0.17	0.948
$D_1 \times H_1$	4	0.00324	0.00081	0.77	0.574
Error	8	0.008408	0.001051	--	--
Total	26	0.584434	--	--	--

4.2.3. Development of the regression models

Multiple regression analysis was carried out using the software Minitab 19 to develop the prediction models for the interlock (I) and the T_{\min} . According to the results of the ANOVA, the three independent variables and three interaction terms were significant for the I . So, all of them were included in the multivariable regression model of the I in Eq. (4.1). As for the T_{\min} , although only the rivet length (L_1) was a statistically significant variable under the studied joint configurations, the influences of other variables on the T_{\min} were also considered in this section. Therefore, all of them were also involved in the regression model of the T_{\min} in Eq. (4.2).

$$I = \alpha_0 + \alpha_1 L_1 + \alpha_2 D_1 + \alpha_3 H_1 + \alpha_4 L_1 \times D_1 + \alpha_5 L_1 \times H_1 + \alpha_6 D_1 \times H_1 \quad (4.1)$$

$$T_{\min} = \beta_0 + \beta_1 L_1 + \beta_2 D_1 + \beta_3 H_1 + \beta_4 L_1 \cdot D_1 + \beta_5 L_1 \cdot H_1 + \beta_6 D_1 \cdot H_1 \quad (4.2)$$

The unknown coefficients in the regression models (i.e., α_1 to α_6 , and β_0 to β_6) were identified with the orthogonal test results. The final regression models of the interlock and the T_{\min} are shown in Eq. (4.3) and Eq. (4.4).

$$I = 2.030 - 0.543L_1 - 0.196D_1 + 0.280H_1 + 0.069L_1 \cdot D_1 + 0.125L_1 \cdot H_1 - 0.120D_1 \cdot H_1 \quad (4.3)$$

$$T_{\min} = -0.360 - 0.093L_1 + 0.206D_1 + 0.793H_1 - 0.012L_1 \cdot D_1 - 0.016L_1 \cdot H_1 - 0.076D_1 \cdot H_1 \quad (4.4)$$

4.2.4. Evaluation of the regression models

The fitting accuracy of the developed regression models was evaluated statistically by five indicators, including the coefficient of determination (R^2), adjusted R^2 (R^2_{adj}), prediction R^2 (R^2_{pred}), mean absolute error (MAE) and standard error (S). The R^2 describes how close the predicted and the actual values lie, and the R^2 close to 1 indicates the good fitting achieved using this regression model. The R^2_{adj} is effective at eliminating the influence of the independent variables' numbers. The evaluation results for the regression models of interlock and T_{\min} are listed in **Table 4.5**. Both of the R^2 and R^2_{adj} for the interlock were over 0.860, and the value of the R^2_{pred} was up to 0.828. The corresponding MAE and S for the interlock were 0.055 mm and 0.076 mm. For the T_{\min} , the R^2 , R^2_{adj} and R^2_{pred} were as high as 0.949, 0.934 and 0.885 respectively. The corresponding MAE and S were 0.029 mm and 0.039 mm. Therefore, the developed regression models are accurate enough to predict the interlock and the T_{\min} . In other words, it is proved that the developed multiple regression models could be used to replace the FEA model for the SPR joint quality prediction under the studied joint configurations.

Table 4.5 Evaluation results of the regression models for the interlock and T_{\min}

Quality indicator	R^2	R^2_{adj}	R^2_{pred}	MAE/mm	S /mm
I	0.896	0.865	0.828	0.055	0.076
T_{\min}	0.949	0.934	0.885	0.029	0.039

4.2.5. Validation of the regression models

To verify the performance of the developed regression models in real applications, seven groups of SPR joints with different rivets and dies, as shown in **Table 4.6**, were made using laboratory experimental method. All of the experimental conditions were the same as that used in the validation tests for the FEA model in 3.3. Three repetitions for each group were performed. The average values of the interlock and the T_{\min} from the experimental SPR tests and the predicted values from the regression models are recorded in **Table 4.6** and compared graphically in **Figure 4.1**. The calculated MAE between the predicted and experimental results for the interlock and the T_{\min} were 0.047 mm and 0.053 mm respectively, and the

corresponding MAPE were 10.4 % and 12.3 %. The calculated Pearson's correlation coefficient (r) for the interlock and T_{\min} were 0.987 and 0.964 respectively. Thus, the predicted interlock and T_{\min} matched well with the experimental ones. This also indicated the high prediction accuracy of the developed regression models for the interlock and the T_{\min} .

According to the statistical evaluation and experimental verification results, it is reasonable to conclude that the developed multiple regression models are effective for the quality prediction of the studied SPR joints. Meanwhile, the model development method used in this chapter has also been proved to be valid.

Table 4.6 Joint configurations and the results for the validation of the regression models

Joint configurations					Experimental and predicted results					
Joint no.	Stack /mm (AA5754)	Rivet length L_1 /mm	Die		Rivet head height H /mm		Interlock I /mm		T_{\min} /mm	
			Diameter D_1 /mm	Depth H_1 /mm	Tested (Mean)	Predicted	Tested (Mean)	Predicted	Tested (Mean)	Predicted
4-28	1.5+1.5	5.0	8.0	2.0	-0.04	0	0.35	0.40	0.57	0.55
4-29		5.0	9.0	1.6	0.02	0	0.42	0.38	0.53	0.54
4-30		5.0	10.0	1.8	-0.07	0	0.33	0.27	0.59	0.55
4-31		5.0	10.0	2.0	-0.05	0	0.25	0.22	0.66	0.54
4-32	6.0	6.0	9.0	1.6	0.02	0	0.69	0.66	0.36	0.31
4-33		6.0	10.0	1.8	-0.05	0	0.69	0.65	0.38	0.31
4-34		6.5	10.0	1.8	-0.06	0	0.91	0.83	0.25	0.19

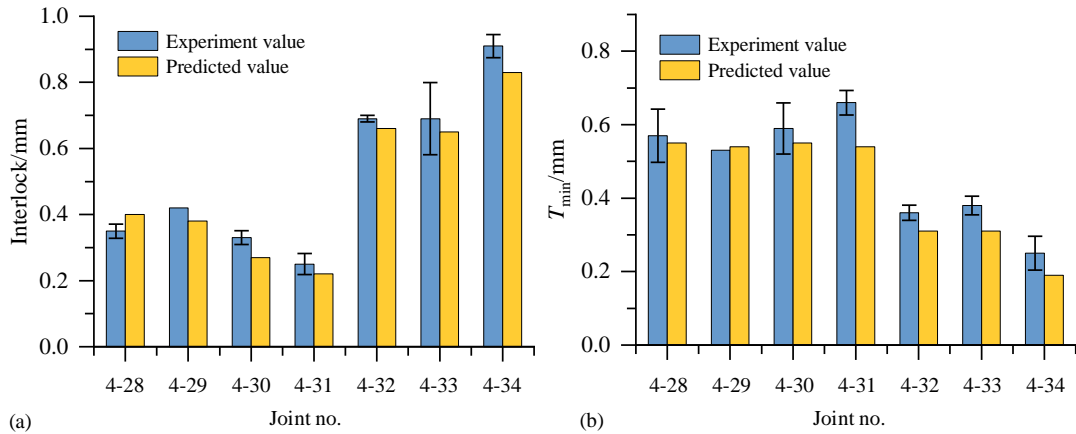


Figure 4.1 Comparisons between the experimental values and the predicted values using the regression models (a) interlock and (b) T_{\min}

4.3. Interaction effects between rivet and die parameters on the interlock and T_{\min}

Unlike the experimental SPR test or the FEA model, the interaction effects between different joining parameters on the joint quality can be easily inspected by observing the contour graphs drawn from the developed regression models. In this section, the interaction effects between

the three rivet and die parameters (i.e., L_1 , D_1 and H_1) on the interlock and the T_{\min} were systematically analysed. Some simulated joint cross-sectional profiles are also presented to further verify the contour graphs and to explain the changing trends of the interlock and the T_{\min} . All the discussions were carried out on the basis of a uniform rivet head height ($H=0.0$ mm). To avoid repetition, not all representative contour graphs and interaction effects were presented and discussed in detail.

4.3.1. Between the rivet length (L_1) and die diameter (D_1)

When the die depth (H_1) was fixed at 1.8 mm, the contour graphs of the interlock and the T_{\min} with varying rivet lengths (L_1) and die diameters (D_1) are plotted in **Figure 4.2**. Apparent interaction effects between the rivet length and die diameter on the interlock were indicated by the non-parallel lines shown in **Figure 4.2** (a). With the die diameter increased from 8.0 mm to 10.0 mm, the interlock demonstrated a decreasing trend when the rivet length was smaller than 6.0 mm, but an increasing tendency when the rivet length was greater than 6.0 mm. With the rivet length increased from 5.0 mm to 6.5 mm, a higher increasing rate (a larger gradient density) of the interlock was observed when the die had a larger diameter. In contrast, very weak interaction effects on the T_{\min} were found because of the almost parallel contour lines in **Figure 4.2** (b). When the die diameter increased from 8.0 mm to 10.0 mm, the T_{\min} kept almost constant with different rivet lengths. While when the rivet length increased from 5.0 mm to 6.5 mm, the T_{\min} rapidly decreased at almost the same rate with different die diameters. The rivet length almost dominated the magnitude of the T_{\min} , which is in agreement with the ANOVA results in **Table 4.4**.

To assist the contour graph analysis, the simulated joint cross-sectional profiles at the points a~i in **Figure 4.2** are presented in **Figure 4.3**. In both figures, the interlock showed an increasing trend as the rivet length increased, but irregular changes when the die diameter varied. In contrast, the T_{\min} decreased as the rivet length increased, but remained almost constant as the die diameter increased. A good agreement between the predicted results from the developed regression models and the FEA simulation model was found, except for the interlock values in **Figure 4.3** (e) and (f) underestimated by the regression model. This might be attributed to the inherent limitation of the adopted regression model, which could only describe a monotonous growth or decline trend.

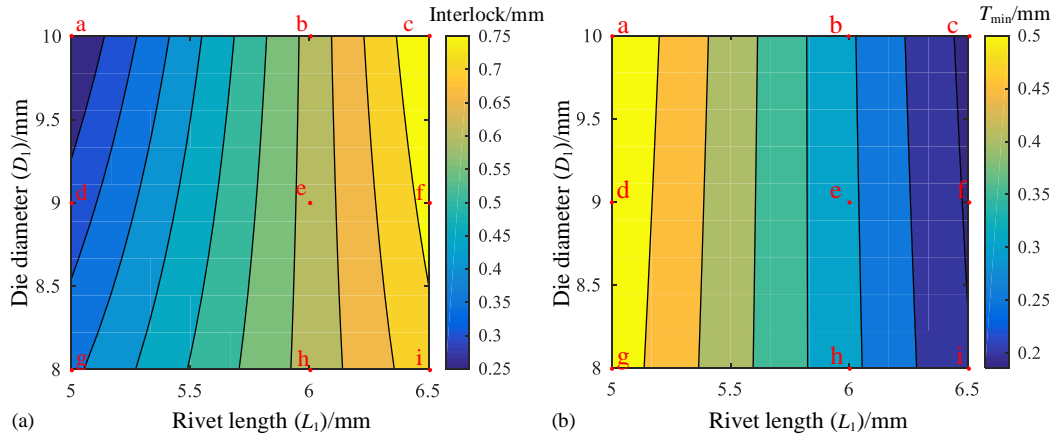


Figure 4.2 Contour graphs of the (a) interlock and (b) T_{min} with different rivet lengths and die diameters (die depth $H_1=1.8$ mm)

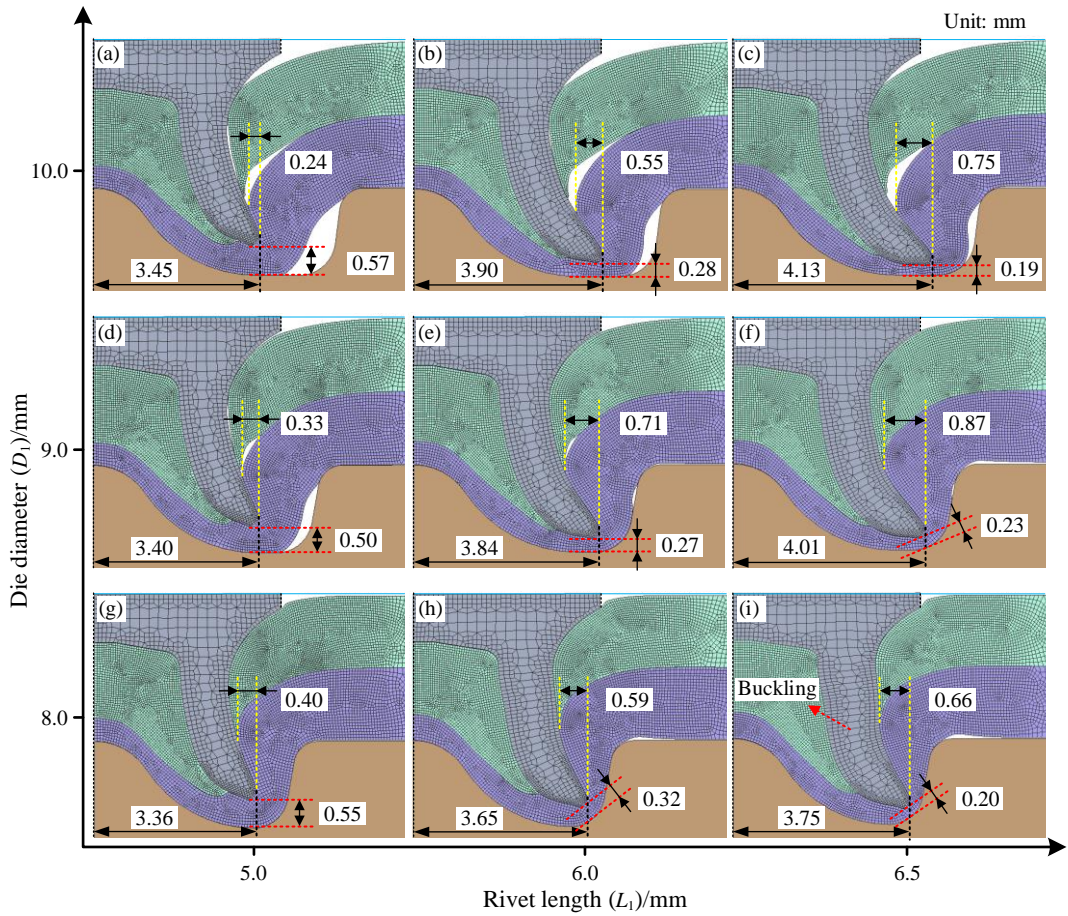


Figure 4.3 Simulated joint cross-sectional profiles with different rivet lengths and die diameters (die depth $H_1=1.8$ mm)

Such interaction effects between the rivet and die parameters on the interlock are attributed directly to the deformation behaviours of the rivet and sheets. As two key components in the SPR process, the rivet is used to pierce through the top sheet and flare into the bottom sheet. The specially designed die is used to guide the rivet flaring and the sheet deforming into its cavity. To achieve a sound SPR joint with a flush head height (approximately 0.0 mm), the

rivet volume (V_r) should be equal to the die cavity volume (V_d) or slightly larger if considering the rivet and sheet material compressions, as shown in **Figure 4.4**. **Table 4.7** lists the volumes of the rivets and dies used in this section. In practice, if the V_d was much smaller than the V_r , as shown in **Figure 4.5** (a), the die cavity could not accommodate all the material pressed into it. Once the die cavity was fully filled, the die would provide a high resistance force to prevent further downward movement of the rivet. This would lead to buckling of the rivet shank, and impose negative effects on the interlock formation. In contrast, if the V_d became much larger than the V_r by increasing the die diameter (D_1) as shown in **Figure 4.5** (b), there would be always a void space underneath the bottom sheet. So, the bottom sheet became easier to be deformed into the die cavity and imposed less resistance force on the outer surface of the rivet shank (F_{out}). Whilst the resistance force applied on the inner surface of the rivet shank (F_{in}) kept almost unchanged considering the similar filling conditions of the rivet cavity. As a result, the rivet shank flared a larger distance, but was not effectively inserted into the bottom sheet to form the interlock. Therefore, the maximum interlock would be always achieved when the V_d was close to the V_r , in which the rivet shank could be inserted effectively into the bottom sheet to form the interlock without buckling.

When the die diameter increased from 8.0 mm to 10.0 mm, due to the different initial Die-to-Rivet volume ratios ($R=V_d/V_r$), the interlock demonstrated different changing trends at the rivet lengths of 5.0 mm, 6.0 mm and 6.5 mm. For the 5.0 mm long rivets, the values of the R in **Figure 4.3** (g), (d) and (a) were 0.88, 1.14 and 1.44 respectively, which resulted in a rapid decrease of the interlock from 0.40 mm to 0.24 mm. Whilst for the 6.0 mm and 6.5 mm rivets, severe rivet shank buckling was observed in **Figure 4.3** (h) and (i) due to the small values of the R (0.77 and 0.73). With the increment of the die diameter, the reduction of the rivet shank buckling imposed a positive effect on the interlock formation in **Figure 4.3** (e) and (f), but then the interlock decreased when the R became much larger (i.e., 1.26 in **Figure 4.3** (b) and 1.19 in **Figure 4.3** (c)). Thus, with the 6.0 mm or 6.5 mm rivets, the interlock first increased but then decreased as the die diameter increased.

When the rivet length increased from 5.0 mm to 6.5 mm, the interlock had a smaller increasing speed with the 8.0 mm die diameter shown in **Figure 4.3**. This is because the rivet shank underwent more and more severe buckling with the reduction of the R value.

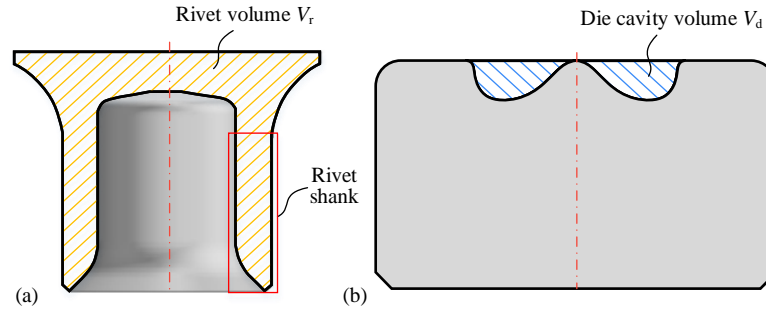


Figure 4.4 Schematics of the (a) rivet volume V_r and (b) die cavity volume V_d

Table 4.7 Rivet volumes and die cavity volumes

Rivet		Die		
Length L_1/mm	Volume V_r/mm^3	Diameter D_1/mm	Depth H_1/mm	Volume V_d/mm^3
5.0	90.0	8.0	1.6	70.07
			1.8	79.54
			2.0	89.07
6.0	102.3	9.0	1.6	91.58
			1.8	103.02
			2.0	111.03
6.5	108.6	10.0	1.6	116.21
			1.8	129.26
			2.0	142.84

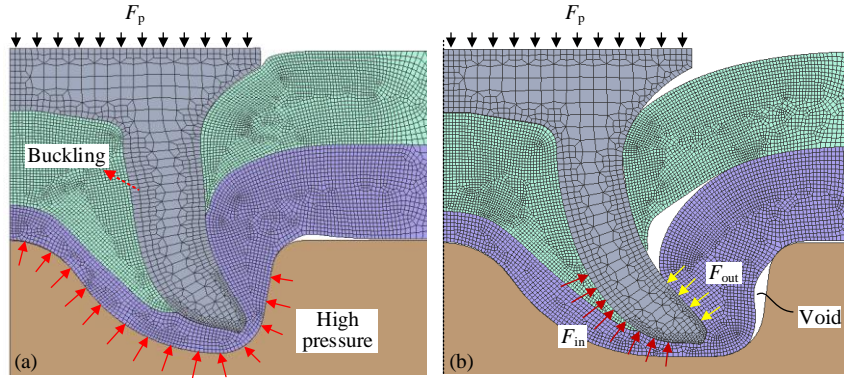


Figure 4.5 Joint cross-sectional profiles with (a) $V_d < V_r$ and (b) $V_d > V_r$ during the SPR processes

4.3.2. Between the rivet length (L_1) and die depth (H_1)

Figure 4.6 shows the contour graphs of the interlock and the T_{\min} with different rivet lengths (L_1) and die depths (H_1) when the die diameter (D_1) was fixed at 9.0 mm. As shown in **Figure 4.6** (a), significant interaction effects indicated by the unparallel lines were also found on the interlock. When the die depth increased from 1.6 mm to 2.0 mm, the interlock showed a decreasing trend and its reducing speed slowly decreased as the rivet length increasing from 5.0 mm to 6.0 mm. Once the rivet length became greater than 6.0 mm, the interlock remained almost constant with the increment of the die depth. In contrast, the parallel lines shown in

Figure 4.6 (b) indicated the weak interaction effects on the T_{\min} . The rivet length showed a dominant influence on the value of the T_{\min} , whilst the die depth demonstrated little effect on the T_{\min} under the studied joint configurations. To assist the contour graphs analysis, the simulated joint cross-sectional profiles at the points a~i in **Figure 4.6** are presented in **Figure 4.7**. It can be seen from these two figures that the predicted joint quality by the developed regression models matched well with that from the FEA model. For a given die depth, the interlock increased but the T_{\min} decreased as the rivet length increased from 5.0 mm to 6.5 mm. For a given rivet length, the interlock decreased but the T_{\min} remained almost unchanged as the die depth increased from 1.6 mm to 2.0 mm.

The increment of die depth could also increase the V_d and result in a larger Die-to-Rivet volume ratio (R). While different from the die diameter, a larger die depth could lead to an easier downward movement of the bottom sheet. As a result, the rivet shank flared less and a smaller interlock was formed. Such effect was more significant for the 5.0 mm long rivets than the 6.0 mm and 6.5 mm rivets: the interlock showed a larger decrease with the 5.0 mm long rivets, but reduced a smaller value with the 6.0 mm and 6.5 mm rivets because of the reduction of the rivet shank buckling degrees in **Figure 4.7** (e) and (f).

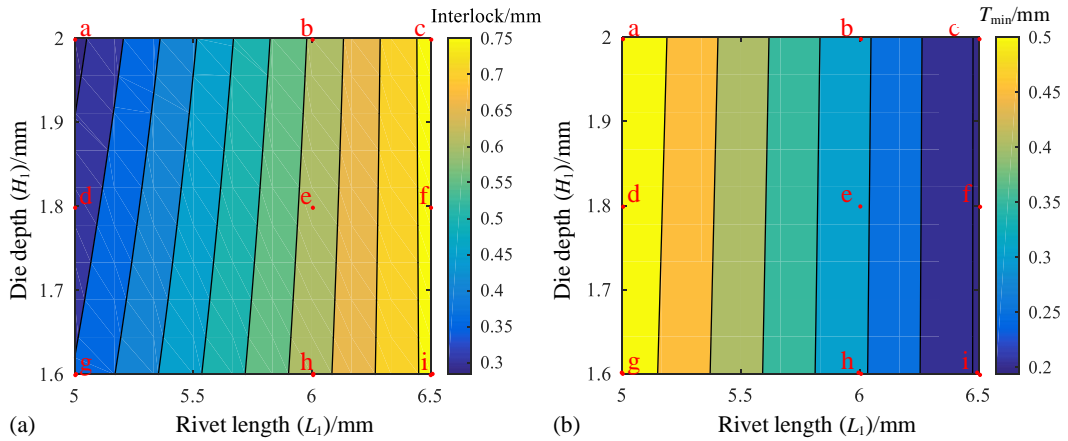


Figure 4.6 Contour graphs of the (a) interlock and (b) T_{\min} with different rivet lengths and die depths (die diameter $D_1 = 9.0$ mm)

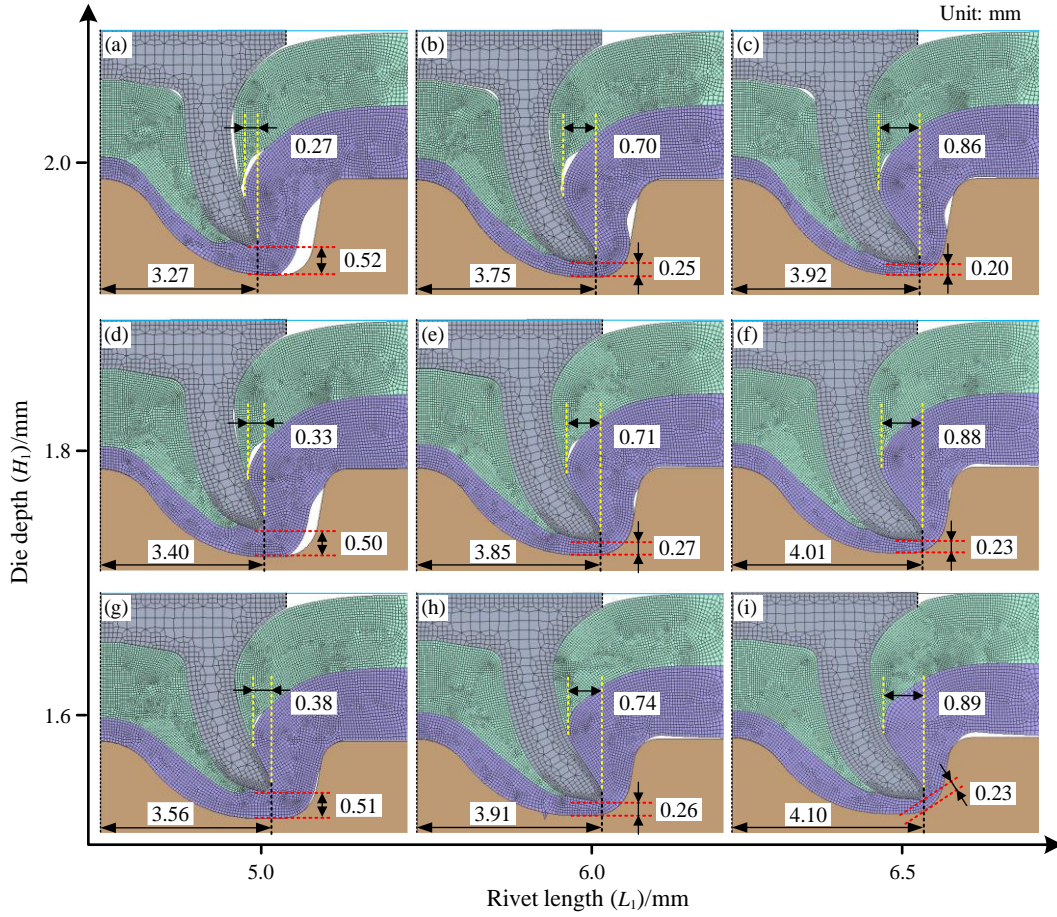


Figure 4.7 Simulated joint cross-sectional profiles with different rivet lengths and die depths (die diameter $D_1=9.0$ mm)

4.3.3. Between the die diameter (D_1) and depth (H_1)

When the rivet length (L_1) was fixed at 5.0 mm, the contour graphs of the interlock and the T_{\min} with different die diameters (D_1) and depths (H_1) are shown in Figure 4.8. Significant interaction effects were indicated by the unparallel lines on the interlock, as shown in Figure 4.8 (a). When the die depth increased from 1.6 mm to 2.0 mm, the interlock decreased at a slower speed with a small diameter die (e.g., $D_1=8.0$ mm) than with a larger one (e.g., $D_1=10.0$ mm). Similarly, when the die diameter increased from 8.0 mm to 10.0 mm, the interlock also showed a smaller decreasing speed with a small depth die (e.g., $H_1=1.6$ mm) than with a larger one (e.g., $H_1=2.0$ mm). However, considering the relatively small changing range (from 0.51 mm to 0.555 mm) of the T_{\min} in Figure 4.8 (b) and the prediction accuracy of the regression model (MAE=0.029 mm), the interaction effects on the T_{\min} was not confident to be evaluated and therefore not discussed in detail.

The simulated joint cross-sectional profiles at the points a~i in Figure 4.8 are presented in **Figure 4.9**. A good agreement between the predicted results from the developed regression models and the FEA simulation model was also found. For a given die diameter, the increased

die depth was accompanied by the decreased interlock and the almost unchanged T_{\min} . For a given die depth, the increased die diameter also lead to the decreased interlock and the almost constant T_{\min} . It is worth mentioning that both of the interlock and the T_{\min} varied within narrow ranges (i.e., 0.18 mm and 0.045 mm respectively) in Figure 4.8 than that in **Figure 4.2** or **Figure 4.6**. This indicates the smaller influences of the die diameter and depth on the SPR joint quality than that of the rivet length under the studied joint configurations.

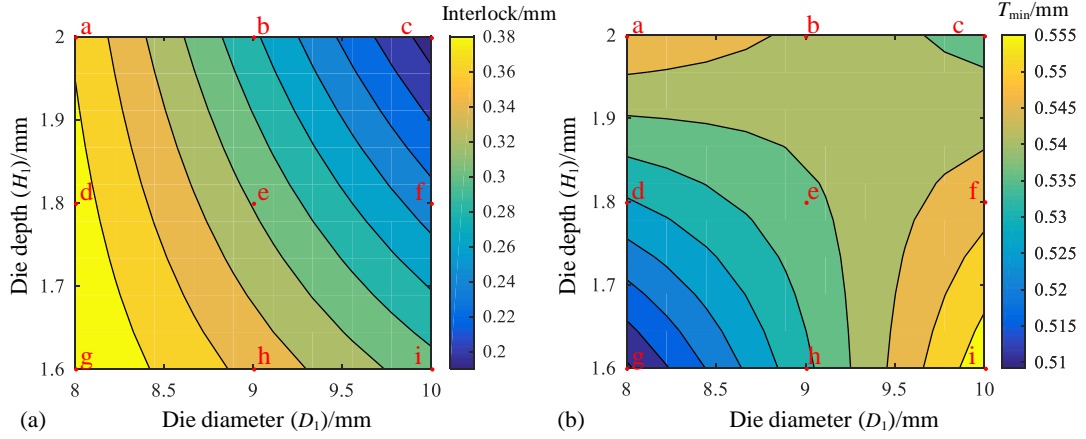


Figure 4.8 Contour graphs of the (a) interlock and (b) T_{\min} with different die diameters and depths (rivet length $L_1=5.0$ mm)

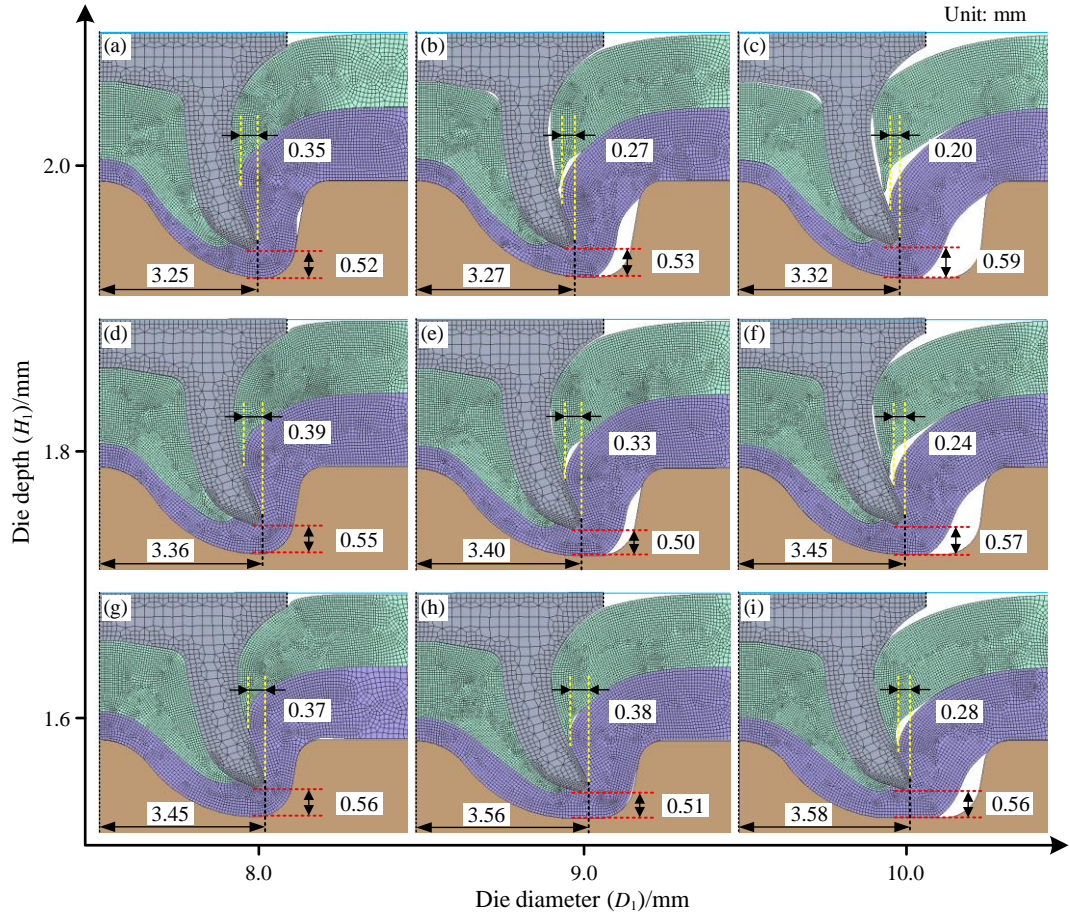


Figure 4.9 Simulated joint cross-sectional profiles with different die diameters and depths (rivet length $L_1=5.0$ mm)

The relationship between the formation of the interlock and the Die-to-Rivet volume (R) was discussed previously, hence here will not discuss further. It is just worth mentioning that the maximum interlock was achieved on the lower left corner of Figure 4.8 (a) with the R closer to 1.0, while the minimum interlock was observed on the upper right corner of Figure 4.8 (a) when the R equals to 1.59. In addition, such interaction effect also revealed that when the R value is less than 1.0, the increment of the R value could lead to a larger interlock; but when the R value is greater than 1.0, the increment of the R value could result in a smaller interlock. Except for the R , the die depth is also very important because it directly determines when the rivet shank starts flaring rapidly. Therefore, the die depth should be considered together with the R during the selection of rivet and die. For the studied material combination, a shallower die is better for the interlock formation. For other material combinations, further study is required.

4.4. Summary

In this chapter, simple but effective multiple regression models were proposed to predict the SPR joint quality. The interaction effects between the rivet and die parameters on the joint quality were graphically analysed and numerically validated. The main conclusions are listed as below:

1. The developed multiple regression models were proved effective to describe the relationships between the SPR joining parameters and the joint quality. The MAE values between the experimental results and regression predictions for the interlock and T_{\min} were 0.047 mm and 0.053 mm respectively, and the corresponding MAPE were 10.4 % and 12.3 % under the studied joint configurations.
2. It is straightforward to analyse the interaction effects between the joining parameters on the joint quality by observing the contour graphs drawn from the developed regression models. Significant interaction effects between the rivet length, die diameter and die depth were identified on the interlock, but not on the T_{\min} within the studied range.
3. By affecting the deformation behaviours of the rivet and sheets, the Die-to-Rivet volume ratio (R) significantly influenced the magnitude and changing trend of the interlock under varying joining parameters. A larger interlock was more likely to be achieved when the R was close to 1.0.

The introduction of the regression model is the first step towards more complicated and more practical industrial applications by involving more joining parameters, such as the sheet thickness, the rivet hardness, etc. In addition, it also offers the possibility to optimize the SPR joint quality by using the mathematical model together with other optimization algorithms.

5. Quality prediction and rivet/die parameters optimization for the SPR process with artificial neural network

Due to the straightforward development procedure and the strong self-learning ability, the artificial neural network (ANN) is more suitable for the development of fast quality prediction tools than mathematical models (e.g., regression analysis model), especially when multiple joining parameters and quality indicators need to be considered. Therefore, this chapter adopted the ANN to develop fast response prediction tools for SPR joint quality. To overcome the high time and money investment of numerous experimental SPR tests, the FEA model developed in Chapter 3 combined with the full factorial design was utilized to collect enough training and testing data for ANN models development. Then, three ANN models considering five joining parameters (i.e., T_1 , T_2 , L_1 , D_1 and H_1) were respectively built for the interlock (I), the remaining bottom sheet thickness at the joint centre (T_{cen}) and under the rivet tip (T_{tip}) to ensure the high prediction accuracy. Experimental SPR tests were conducted to validate the performance of these ANN models. Moreover, an innovative approach that combines the developed ANN models and the genetic algorithm (GA) was proposed to automatically optimize the rivet and die parameters during the new SPR joint design. Interaction effects between the five joining parameters on the SPR joint quality were also investigated by analysing the contour graphs plotted with the ANN models.

5.1. Introduction

Due to the intrinsic properties of SPR joints, changes of the sheet [36,44], rivet [38,86] and die [40,41] parameters will inevitably affect the final joint quality. So far, the selection of rivet and die for new joints still heavily depends on experimental SPR tests designed and assessed by experienced engineers. There is not a straightforward way that can be used by inexperienced engineers to select suitable rivet and die for new SPR joints. It will be a great contribution to practical applications if a simpler approach of rivet and die selection can be developed. This goal can be achieved by combining a fast joint quality prediction tool with an optimization tool. The quality prediction tool can effectively reduce the experimental SPR tests required during the joint design process, and the optimization tool can automatically identify the suitable rivet and die to reduce the dependence on engineers' experience.

As for the joint quality prediction tool, many FEA models of SPR process have been successfully developed in recent years and proved effective to give accurate prediction results [44,113,152]. However, professional knowledge of FEA is required in order to establish and

run such simulation models, which brings new challenges to inexperienced engineers. Meanwhile, a large number of FEA simulations might be required for each new joint prior to experimental confirmation. This will cost a lot of time and efforts to complete all the simulations needed for multiple new SPR joints. The mathematical prediction model can effectively minimise the above-mentioned limitations of FEA models because it is easy-to-use and can give a prediction result almost immediately. In the public domain, some mathematical prediction models for SPR joint quality have been reported and their effectiveness was also confirmed through experimental tests [48,135]. However, during the mathematical model development, one challenge is to predefine the relationships between the inputs (i.e., joining parameters) and outputs (i.e., joint quality indicators) in order to determine the appropriate expression. With the expansion of joint design space (i.e., the number and scopes of joining parameters), the variation trends of joint quality indicators will become highly nonlinear. This raises the complexity of relationships between the joining parameters and the quality indicators, and therefore increases the difficulties for the model structure selection. Another challenge is the identification of unknown coefficients in the mathematical model. The model structure will become increasingly complicated with the increment of joining parameters considered. This will inevitably increase the number of unknown coefficients and therefore increase the difficulties in coefficient identification [48]. Compared with mathematical prediction models, ANN is much more suitable to develop easy-to-use quality prediction tools because of its excellent fitting and self-learning ability to describe complex relationships between inputs and outputs [140,161]. It can involve multiple joining parameters and joint quality indicators, and thus achieve a wide application range. Successful applications of the ANN in predictions of surface roughness [162], weld morphology of welding-rivet hybrid bonding joint [163] and workpiece deformation [164] have been reported in the public domain. However, there are only a few studies relevant to the application of ANN in the SPR joint quality prediction [47]. Considering the advantages of the ANN, it was employed in this chapter to develop fast prediction tools for the SPR joint quality. In addition, taking advantage of ANNs, the interaction effects between the five joining parameters (i.e., T_1 , T_2 , L_1 , D_1 and H_1) on the SPR joint quality were also systematically investigated by plotting the corresponding contour graphs.

As for the optimization tool, GA is a popular optimization algorithm inspired from the biological evolution process [165], and very powerful to deal with multi-objective optimization problems. So far, the GA has been widely applied to solve practical issues raised from different industrial fields, such as the geometry optimization of the composite honeycomb tip [166], the parameter optimization of friction welding process [147] and the mechanical strength optimization of friction stir spot welding joints [148]. Effectiveness of

the GA in dealing with multiple-objective problems has been widely confirmed through experimental tests. Considering the multiple quality indicators of SPR joints, the GA is a promising tool to identify the optimal parameters of rivet and die to maximise these quality indicators simultaneously. Therefore, the GA combined with the ANN was utilized in this chapter to facilitate the selection of rivet and die for new SPR joints.

5.2. ANN models for SPR joint quality prediction

5.2.1. Joint quality data collection

In this chapter, the five critical joining parameters (T_1 , T_2 , L_1 , D_1 and H_1) were involved in the ANN prediction models for aluminium alloy AA5754 SPR joints. To collect enough training and testing data for the development of ANN models, the full factorial design (3^5) with five parameters and three levels was adopted as listed in **Table 5.1**. A total of 243 joints with different configurations were simulated using the developed FEA model in Chapter 3. For consistency, a uniform rivet head height (i.e., $H=0.0$ mm) was set for all SPR joints by controlling the rivet displacement.

Table 5.1 Full factorial design with five joint parameters and three levels (3^5)

Level	Top sheet thickness T_1 /mm	Bottom sheet thickness T_2 /mm	Rivet length L_1 /mm	Die diameter D_1 /mm	Die depth H_1 /mm
1	1.0	1.0	5.0	8.0	1.6
2	1.5	1.5	5.5	9.0	1.8
3	2.0	2.0	6.0	10.0	2.0

After all of the simulations were completed, the quality indicators of the 243 joints were measured on the simulated joint cross-sectional profiles. The interlock is always formed around the rivet tip and thus relatively easy to measure. In contrast, the formation position of the T_{\min} is not fixed but changes under different joint configurations. **Figure 5.1** illustrates six positions that the T_{\min} may appear. Because of the uncertain position of the T_{\min} , it is very difficult to establish a single ANN model to predict the T_{\min} directly. By analysing formation positions of the T_{\min} in the 243 joints, it was found that the T_{\min} had a higher possibility to locate at the joint centre (as shown in **Figure 5.1** (a)) or under the rivet tip (as shown in **Figure 5.1** (d)). Therefore, in this section, the remaining bottom sheet thickness at the joint centre (T_{cen}) and under the rivet tip (T_{tip}) were measured in each SPR joint. To keep data consistency, the T_{cen} and the T_{tip} were always measured along the vertical direction. All of the interlock, T_{cen} and T_{tip} values in the 243 joints were recorded as the training and testing data to develop the ANN models.

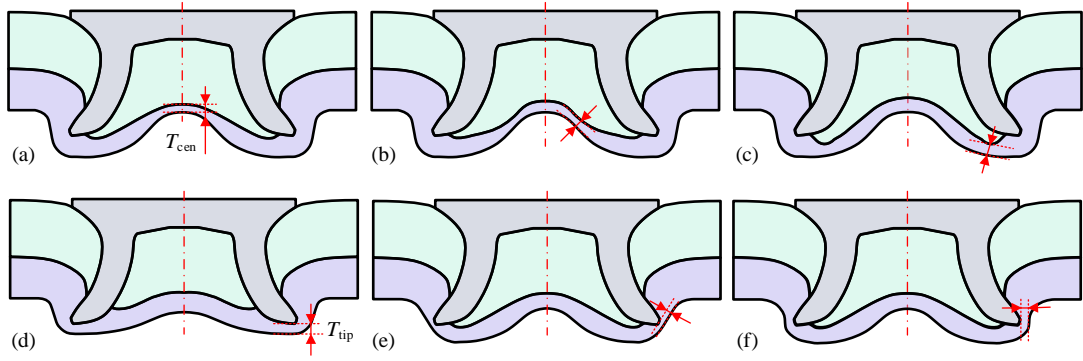


Figure 5.1 Six potential positions of the minimum remaining bottom sheet thickness (T_{min}) in SPR joints

To eliminate the influences of scope difference between the input parameters, all the five inputs of the 243 SPR joints were normalized using the z-score method (Eq. (5.1)). Similarly, all the outputs were calculated with the min-max normalization into the range 0~1 using the Eq. (5.2). During the training of ANN, the learning rate was set to 0.001 to ensure a high probability of global convergence and a maximum of 5000 iterations was selected to determine the weights.

$$x_{norm} = \frac{x_{input} - \mu}{\sigma} \quad (5.1)$$

where x_{norm} is the standardized input value, x_{input} is the original input value, μ and σ are the mean and the standard deviation of all input values.

$$y_{norm} = \frac{y_{output} - y_{min}}{y_{max} - y_{min}} \quad (5.2)$$

where y_{norm} is the normalized output value, y_{output} is the original output value, y_{min} and y_{max} are the minimum and maximum values among all the output values.

5.2.2. ANN model architecture

The ANN has very powerful self-learning ability, strong robustness and high fault tolerance. It is suitable to describe the complex nonlinear relationships between the inputs and outputs [167] of the SPR process. Compared with the mathematical prediction models (e.g., Kriging technique), the development process of an ANN is much more straightforward and faster because the ANN can automatically learn the highly nonlinear relationships between the multiple joining parameters and quality indicators. The ANN model employed in this section is classified as the feedforward neural network. As shown in **Figure 5.2**, it consists of one input layer, one hidden layer and one output layer. The five joint parameters, including the top sheet thickness (T_1), bottom sheet thickness (T_2), rivet length (L_1), die diameter (D_1) and die

depth (H_1), were designed as the inputs. To improve the prediction accuracy and to reduce the difficulty of model training, only one of the joint quality indicators (i.e., interlock, T_{cen} or T_{tip}) was selected as the output. There is also one bias neuron in the input and hidden layer respectively. The neurons in each layer are connected to all neurons in the adjacent layer. The weight ($W_{i,j}^{(k)}$) assigned to each connection indicates the intensity of the signal transmission between the connected neurons [168]. In the $W_{i,j}^{(k)}$, the i and j denote the numbers of the two connected neurons in the later layer and in the previous layer respectively, and the k denotes the layer number in the ANN. The back-propagation (BP) algorithm was utilized to optimize the internal weights and biases in the ANN model. The activation functions are the ‘*tansig*’ for the hidden layer and the ‘*purelin*’ for the output layer. The ANN model was established and trained using the software MATLAB R2020a.

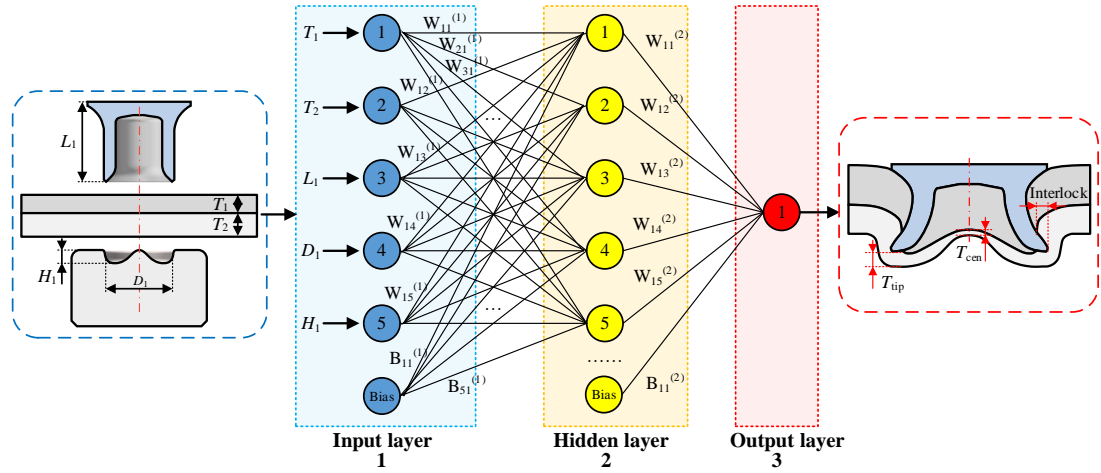


Figure 5.2 Structure of the three-layer artificial neural network (ANN)

5.2.3. Development of ANN for the interlock

The trial-and-error method was applied to select the appropriate number of hidden layer neurons (N_h). **Figure 5.3** illustrates the procedures to determine the optimal ANN for the interlock. First, the ANN with three hidden layer neurons ($N_h=3$) was set up. The 243 SPR joints were divided randomly into training data (70 %) and testing data (30 %) in each circle. As shown in Eq. (5.3), the mean squared error (MSE) between the actual output values and the predicted output values was selected as the performance function during the ANN training. Then the training and testing stages for the neural network were carried out, and the performance indexes of this developed ANN were calculated and recorded, including the MAE in Eq. (5.4) and the correlation coefficient (r) in Eq. (5.5) between the FEA simulated and ANN predicted values. The smaller MAE value, the more accurate the developed ANN model. The closer the r value is to 1, the more relevant the predicted and actual results are.

$$MSE = \frac{\sum_{j=1}^N (y_{j,s} - y_{j,p})^2}{N} \quad (5.3)$$

$$MAE = \frac{\sum_{j=1}^N |y_{j,s} - y_{j,p}|}{N} \quad (5.4)$$

where the $y_{j,s}$ and $y_{j,p}$ denote the simulated value by the FEA model (i.e., actual value) and the predicted value by the ANN model of the j th SPR joint respectively. The N is the total number of the SPR joints.

$$r = \frac{\sum Y_s Y_p - \frac{\sum Y_s \sum Y_p}{N}}{\sqrt{(\sum Y_s^2 - \frac{(\sum Y_s)^2}{N})(\sum Y_p^2 - \frac{(\sum Y_p)^2}{N})}} \quad (5.5)$$

where the Y_s and Y_p are the matrixes of the FEA simulation results and the predicted results from the ANN model separately.

To eliminate the influences of data partitioning and the weights initialization on the performance of ANN, the above development steps were repeated 20 times. The mean values of all the recorded MAE and r were calculated to evaluate the performance of the current ANN. Seven ANN models with 3~9 neurons in the hidden layer were individually trained and tested. Finally, the performances of these ANNs were compared to choose the optimal one.

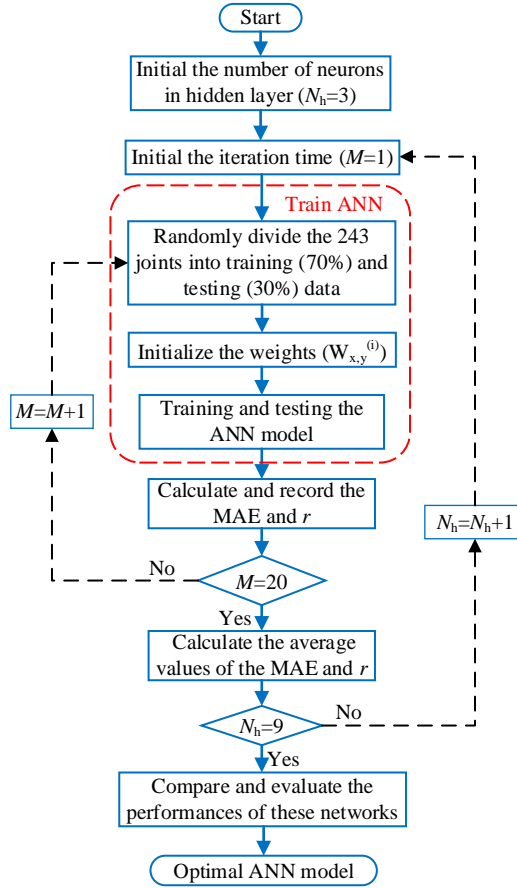


Figure 5.3 The algorithm flow chart to select the optimal ANN model for the interlock

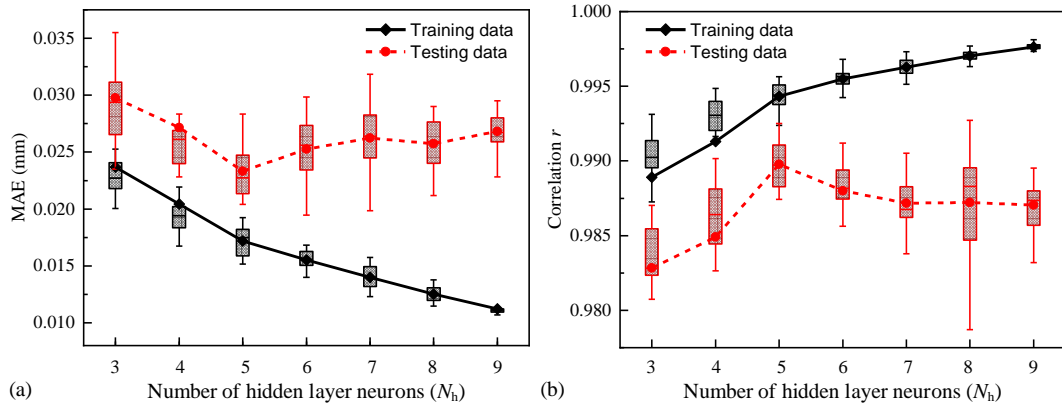


Figure 5.4 The performances of ANNs with different numbers of hidden layer neurons (N_h) for the interlock (a) MAE and (b) correlation coefficient (r)

The values of average MAE and r for the seven ANNs are compared in **Figure 5.4**. For the training data, it can be seen that the value of MAE rapidly decreased, and the corresponding value of r gradually increased when the number of hidden layer neurons (N_h) increased from 3 to 9. However, for the testing data, the MAE value firstly decreased but then increased, whilst the corresponding r value firstly increased and then decreased with the increment of the N_h . The smallest MAE and the largest r were observed in the ANN with 5 hidden layer neurons. This indicated that the ANN with 5 hidden layer neurons had the best fitting degree. The

performance degradation of the ANNs with the N_h greater than 5 might attribute to the over-fitting problem. Therefore, the ANN with 5 hidden layer neurons was selected as the optimal one for the interlock. Comparisons between the FEA simulated and the ANN predicted interlock values are shown in **Figure 5.5**. Good correlations were found for both of the training and testing data. The mean values of MAE for the training and testing data were 0.017 mm and 0.023 mm respectively, and the corresponding average correlation coefficient (r) were 0.994 and 0.990. Therefore, the optimized ANN for the interlock demonstrated a very high prediction accuracy.

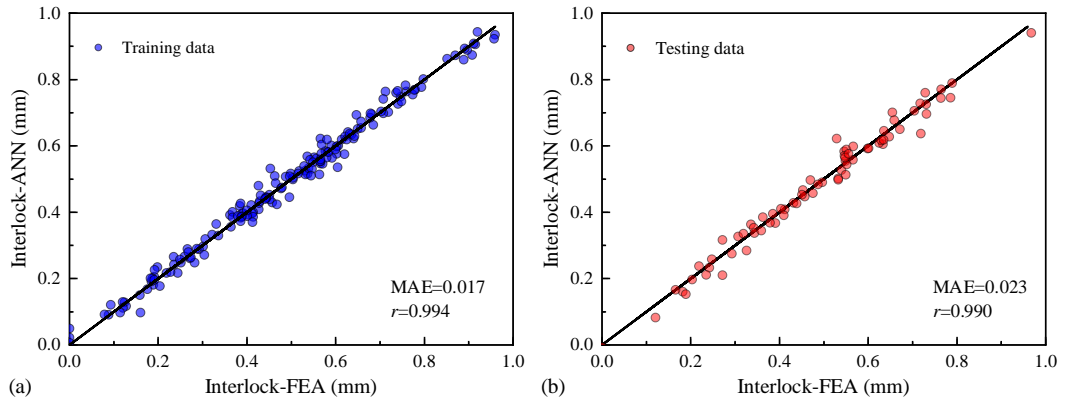


Figure 5.5 Comparisons between the ANN predicted and the FEA simulated interlock values (a) training data and (b) testing data

5.2.4. Development of ANNs for the T_{cen} and T_{tip}

Similar selection procedures, as the optimal ANN for the interlock illustrated in **Figure 5.3**, were also carried out to determine the optimal structures of ANNs for the T_{cen} and T_{tip} . The performances of nine ANNs for the T_{cen} with different hidden layer neurons ($N_h=3 \sim 11$) are presented in **Figure 5.6**. It can be seen that the ANN with 8 hidden layer neurons achieved the smallest MAE and the second largest r for the testing data, and thus was selected as the optimal ANN for the T_{cen} . Comparisons between the FEA simulated and the optimal ANN predicted T_{cen} in **Figure 5.7** indicated the good correlations for the training and testing data. The mean values of MAE for the training and testing data were 0.011 mm and 0.022 mm respectively, and the corresponding average values of r reached up to 0.998 and 0.992. Similarly, according to the performances of the nine ANNs for the T_{tip} shown in **Figure 5.8**, the ANN with 7 hidden layer neurons was chosen as the optimal one. **Figure 5.9** also demonstrates the good correlations between the FEA simulated and the optimal ANN predicted T_{tip} for the training and testing data. The mean values of MAE were 0.018 mm and 0.033 mm respectively for the training and testing data, and the average values of r reached 0.998 and 0.994. Thus, the optimal ANNs for the T_{cen} and T_{tip} also achieved high prediction accuracies for SPR joints within the studied ranges.

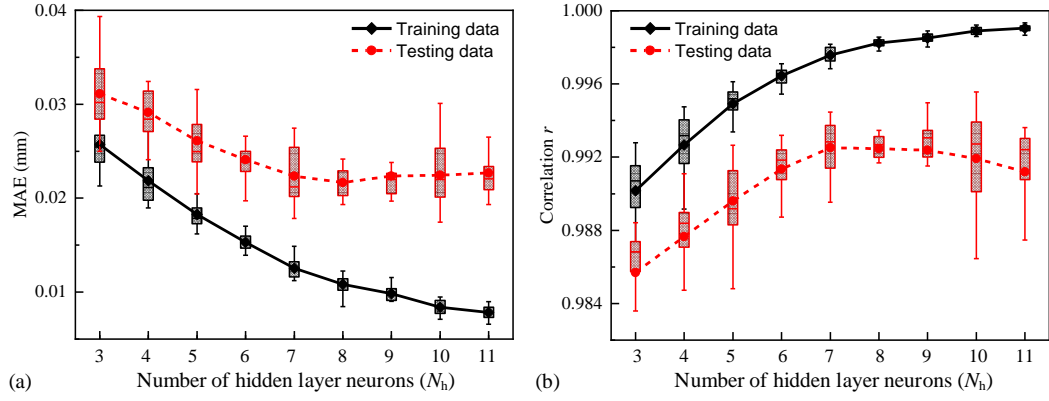


Figure 5.6 The performances of ANNs with different numbers of hidden layer neurons (N_h) for the T_{cen} (a) MAE and (b) correlation coefficient (r)

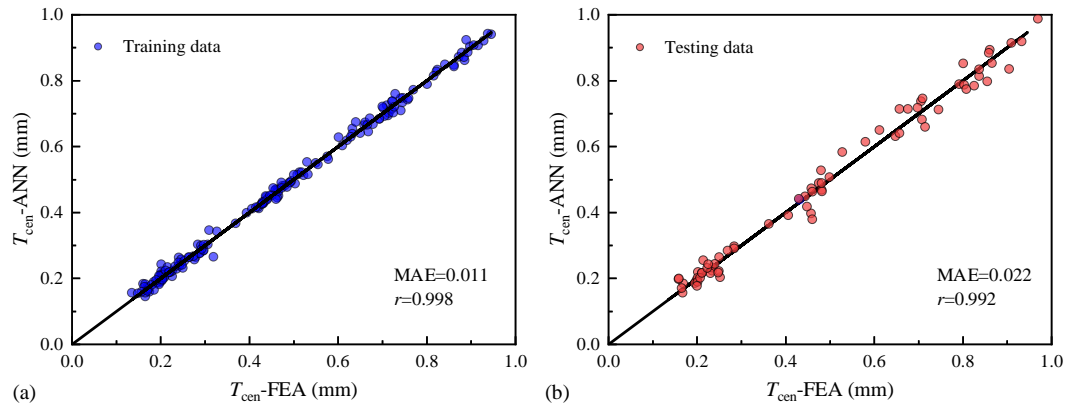


Figure 5.7 Comparison between the ANN predicted and the FEA simulated T_{cen} values (a) training data and (b) testing data

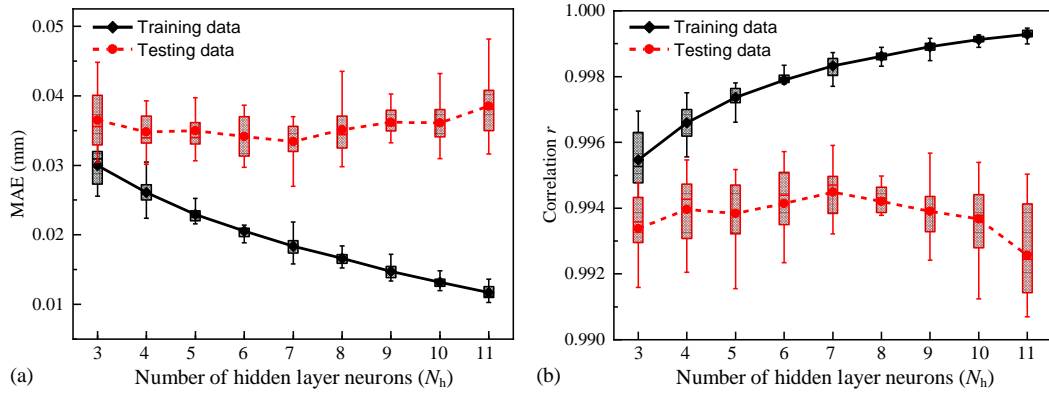


Figure 5.8 The performances of ANNs with different numbers of hidden layer neurons (N_h) for the T_{tip} (a) MAE and (b) correlation coefficient (r)

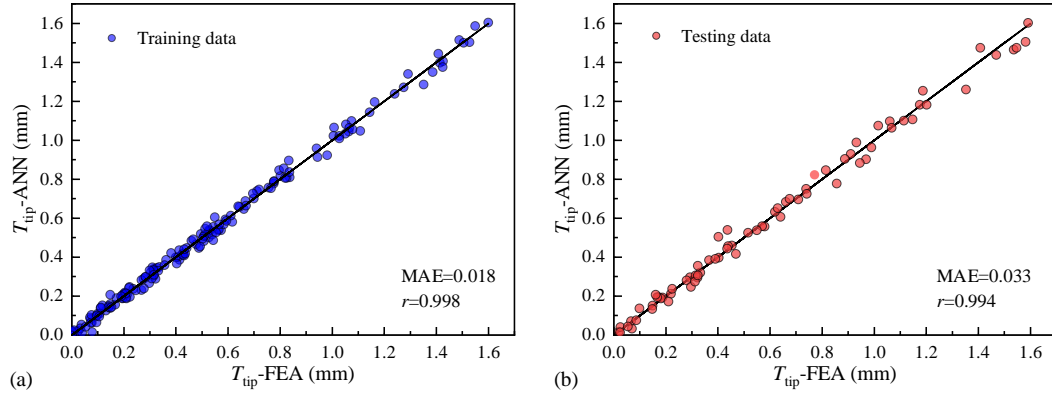


Figure 5.9 Comparison between the ANN predicted and the FEA simulated T_{tip} values (a) training data and (b) testing data

5.2.5. Validation of the ANN models

To validate the prediction accuracy of the developed ANNs, another 23 new SPR joints with different configurations listed in **Table 5.2** were experimentally made. All of the experimental conditions were the same as that used in the experimental SPR tests for the FEA model validation in **3.3**. Three repetitions were performed for each joint configuration, and the mean values of the interlock, T_{cen} and T_{tip} were recorded in **Table 5.2**. Moreover, the three quality indicators of the 23 joints were also predicted with the FEA model and the developed ANNs, as shown in **Table 5.2**. For easier comparisons, the joint quality data in **Table 5.2** are also plotted in line graphs as shown in **Figure 5.10** and **Figure 5.11**.

Comparisons between the interlock values from the experimental tests, the FEA model and the developed ANN are presented in **Figure 5.10**. It can be seen that the changing trends of the interlock were almost the same on the three curves. The interlock values predicted by the ANN agreed well with that from the experimental tests in 20 out of the 23 SPR joints, except for the joints 5-3, 5-14 and 5-16. The MAE, MAPE and r between the experimentally tested and ANN predicted interlock values were 0.058 mm, 14.2 % and 0.978 respectively. In SPR joints with relatively small interlock values, such as in 5-6 and 5-22, the small absolute errors (0.04 mm, 0.03 mm) between the tested and the ANN predicted interlock values still led to large absolute percentage errors (22.2 %, 23.1 %). This directly caused the relatively large MAPE for the interlock (i.e., 14.2 %). Considering the magnitudes of the MAE and r , it can be concluded that the developed ANN for the interlock could give accurate prediction results for SPR joints within the studied ranges. In addition, the interlock values predicted by the ANN were quite consistent with that predicted by the FEA model. The calculated MAE, MAPE and r values between the ANN predicted and FEA simulated interlock values were 0.039 mm, 9.7 % and 0.994. This means that the prediction accuracy of the ANN reached almost the same level as the FEA model.

Table 5.2 Experiment design and results for the validation of ANNs

Joint configurations					Experiment, prediction and simulation results								
Joint no.	Stack /mm (AA5754)	Rivet Length L_1 /mm	Die		Interlock/mm			T_{cen} /mm			T_{tip} /mm		
			Diameter D_1 /mm	Depth H_1 /mm	Predicted (ANN)	Simulated (FEA)	Tested (Mean)	Predicted (ANN)	Simulated (FEA)	Tested (Mean)	Predicted (ANN)	Simulated (FEA)	Tested (Mean)
5-1	1.0+1.8	5.0	8.0	2.0	0.53	0.58	0.59	0.71	0.66	0.70	0.33	0.35	0.39
5-2	1.5+1.8				0.38	0.37	0.41	0.54	0.56	0.22	0.85	0.75	0.90
5-3	2.0+1.8				0.19	0.18	0.30	0.18	0.16	0.02	1.42	1.24	1.51
5-4	1.0+1.8		10.0	2.0	0.46	0.51	0.49	0.73	0.70	0.76	0.37	0.38	0.47
5-5	1.5+1.8				0.29	0.31	0.33	0.59	0.57	0.50	0.89	0.80	0.93
5-6	2.0+1.8				0.14	0.19	0.18	0.16	0.18	0.11	1.39	1.40	1.54
5-7	1.2+1.0	5.0	8.0	2.0	0.49	0.50	0.48	0.29	0.34	0.33	0.10	0.14	0.12
5-8	1.2+1.5				0.48	0.52	0.51	0.52	0.56	0.35	0.29	0.32	0.34
5-9	1.2+2.0				0.48	0.55	0.52	0.7	0.72	0.62	0.71	0.73	0.80
5-10	1.2+1.0		10.0	2.0	0.20	0.23	0.16	0.27	0.32	0.41	0.25	0.24	0.27
5-11	1.2+1.5				0.33	0.36	0.34	0.54	0.51	0.56	0.35	0.37	0.41
5-12	1.2+2.0				0.42	0.46	0.49	0.71	0.72	0.68	0.76	0.71	0.83
5-13	1.2+1.8	5.0	8.0	2.0	0.47	0.51	0.53	0.63	0.64	0.55	0.50	0.50	0.57
5-14	1.2+1.8	6.0			0.68	0.73	0.86	0.67	0.75	0.67	0.28	0.33	0.36
5-15	1.2+1.8	5.0			0.39	0.44	0.47	0.65	0.63	0.66	0.57	0.55	0.63
5-16	1.2+1.8	6.0	10.0	2.0	0.76	0.84	0.90	0.71	0.69	0.71	0.23	0.24	0.29
5-17	1.2+1.8	5.0	9.0	1.6	0.53	0.60	0.59	0.7	0.61	0.73	0.44	0.46	0.47
5-18	1.2+1.8		10.0	1.8	0.42	0.47	0.48	0.67	0.63	0.65	0.49	0.51	0.48
5-19	1.2+1.2	5.0	10.0	1.8	0.28	0.32	0.36	0.39	0.40	0.49	0.28	0.29	0.24
5-20	1.2+1.8				0.42	0.47	0.47	0.67	0.63	0.64	0.49	0.51	0.50
5-21	1.5+1.5				0.27	0.27	0.33	0.45	0.43	0.48	0.54	0.56	0.63
5-22	1.8+1.2				0.10	0.13	0.13	0.25	0.21	0.19	0.62	0.63	0.63
5-23	1.8+1.8				0.23	0.25	0.26	0.44	0.40	0.21	1.16	1.04	1.26

Figure 5.11 (a) shows the values of the T_{cen} from the ANN, FEA model and experimental tests. It can be seen that, in the majority of the 23 SPR joints, the changing trend and magnitudes of the T_{cen} predicted by the ANN showed reasonable agreements with that from the experimental tests. The corresponding MAE, MAPE and r values were 0.075 mm, 22.4 % and 0.881 respectively. The joint 5-3 was excluded when calculating the MAPE because the absolute percentage error in this joint was extremely large (800 %). The predicted T_{cen} from the FEA model and the ANN were almost the same for all joints, and the calculated MAE, MAPE and r values were 0.033 mm, 7.5 % and 0.978 respectively. This means that the prediction accuracy of the ANN for T_{cen} also reached almost the same level as the FEA model.

Figure 5.11 (b) illustrates the values of the T_{tip} obtained from the experimental tests, the FEA model and the ANN. It can be seen that the developed ANN not only successfully predicted the changing trend of the T_{tip} but also accurately predicted the magnitudes of the T_{tip} in almost all of the 23 SPR joints. The calculated MAE, MAPE and r values for T_{tip} between the experimental tested and the ANN predicted results were 0.059 mm, 10.9 % and 0.996 respectively. These indicate that the developed ANN is capable of accurately predicting the

T_{tip} within the studied ranges. Moreover, The MAE, MAPE and r values between the predicted T_{tip} from the FEA model and the ANN were 0.038 mm, 7.0 % and 0.993 respectively. This means that the prediction accuracy of the ANN for T_{tip} is also as high as that of the FEA model. Based on the above results, it is reasonable to conclude that the developed ANNs for the interlock, T_{cen} and T_{tip} reached the same prediction accuracy levels as the FEA model, and can be used to predict the SPR joint quality within the studied ranges.

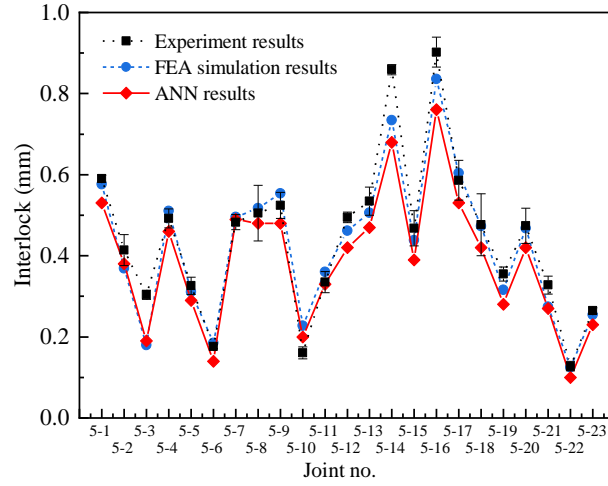


Figure 5.10 Comparisons of the interlock from the experimental tests, the FEA simulation model and the ANN

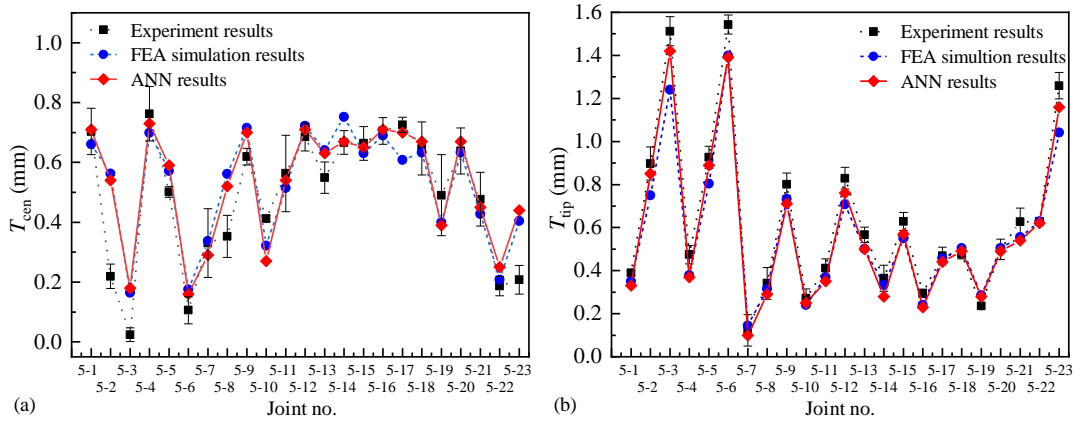


Figure 5.11 Comparisons of the (a) T_{cen} and (b) T_{tip} from the experimental tests, the FEA model and the ANNs

5.2.6. Graphical user interface (GUI)

For the convenience of practical applications, a GUI integrating the three established ANNs was developed using the App Designer in MATLAB R2020a, as shown in **Figure 5.12**. By simply entering the five pre-defined joint parameters, this GUI will call the three ANNs to calculate the interlock, T_{cen} and T_{tip} , and then display the prediction results to the user within seconds. Compared with the experimental SPR test and the FEA model, this GUI is quicker, more user-friendly and more suitable for industrial applications.

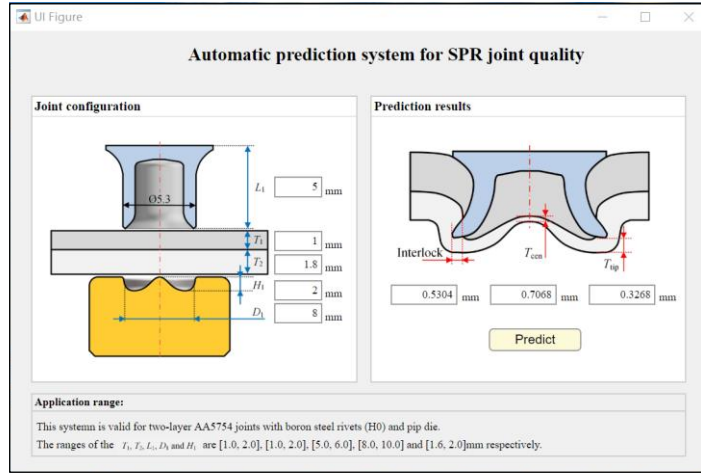


Figure 5.12 The GUI for the SPR joint quality prediction

5.3. Optimization of rivet and die parameters for a SPR joint

The ANNs are capable to predict the joint quality, but cannot automatically select suitable rivets and dies for a given sheet combination. To reduce the dependence on engineers' experience, the developed ANNs in combination with the GA are used to simplify and optimize the selection of rivet and die. This can be achieved by maximising the interlock, T_{cen} and T_{tip} . However, because of the contradictory relationships among the three quality indicators, it is impossible to achieve the maximum values of the three quality indicators concurrently [148]. The optimal combination of rivet and die always changes with the variation of the selected joint quality criteria. Therefore, instead of only one optimal solution, in this section, a Pareto optimal solution set of rivet and die combinations was generated using the GA to meet the different joint quality standards.

5.3.1. Optimization procedure

The optimization process was carried out using the Global Optimization Toolbox in MATLAB R2020a. The built-in function '*gamultiobj*', which integrates a controlled elitist GA (i.e., a variant of NSGA- II), was employed to get the Pareto optimal solution set. This controlled elitist GA has a very good exploration performance [148] and can effectively maintain the population diversity [169]. **Figure 5.13** illustrates the multi-objective optimization procedures with the GA and the three ANNs. Firstly, the population size was assigned, and the initial population was created. Then, the scores for the population were generated by calculating the objective functions, and were also evaluated to determine whether the termination conditions were met or not. If yes, the optimization iteration was terminated and the Pareto optimal solutions were obtained. Otherwise, the main iteration in function '*gamultiobj*' was processed, including the selection of parents for next generation, creation of the next generation with

mutation and crossover, scoring the children, combining the children to the extended population, trimming the extended population for diversity conservation and forming a new population. The evaluation procedure continued until the stopping criterion was met. The three ANNs for the interlock, T_{cen} and T_{tip} were called to calculate the scores of the population. For a specific sheet combination, the rivet length (L_1), die diameter (D_1) and die depth (H_1) were optimized using the GA by maximising the three joint quality indicators. By predefining the scopes of three quality indicators, the GA can directly generate a Pareto optimal solution set satisfying the selected joint quality standard. In this section, to recognize optimal rivet and die combinations complying with different quality standards, the variation ranges of the quality indicators were not constrained.

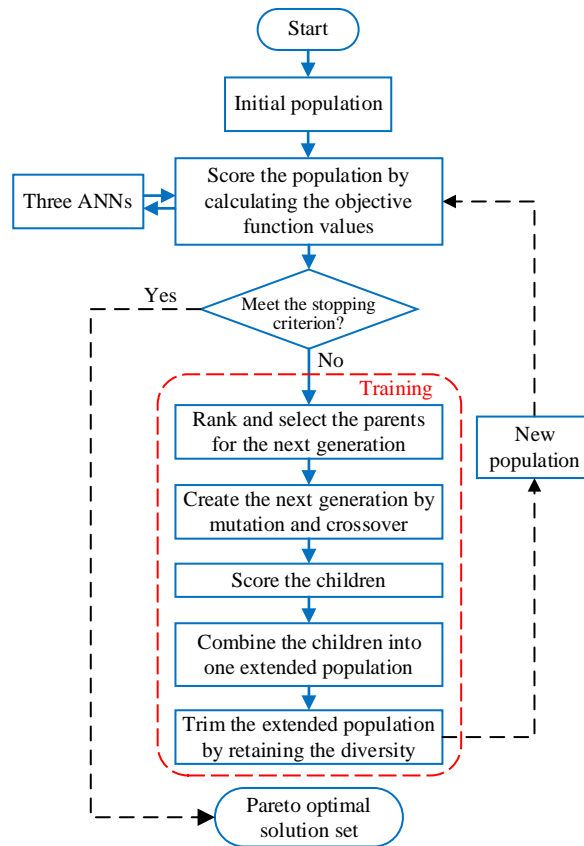


Figure 5.13 Flow chart to optimize the rivet and die with the ANNs and GA

As listed in **Table 5.3**, five different sheet combinations were used to demonstrate the proposed optimization procedures for the selection of rivet and die in practical applications.

Table 5.4 shows the detailed setting parameters of the GA and the bounds of the L_1 , D_1 and H_1 . The population size was set to 50, and the maximum generation was 500. The crossover and migration rates were 0.80 and 0.20 respectively. The Pareto front population fraction was set to 0.35 to get 18 Pareto optimal solutions for each sheet combination. These Pareto optimal solutions are non-dominated with respect to each other. In other words, when moving from

one Pareto solution to another, a certain amount of gain in one objective(s) is always accompanied with a certain amount of sacrifice in the other(s).

Table 5.3 Five top and bottom sheet combinations

Case No.	Top sheet thickness T_1 /mm (AA5754)	Bottom sheet thickness T_2 /mm (AA5754)
1	1.0	1.0
2	1.0	2.0
3	1.5	1.5
4	2.0	1.0
5	2.0	2.0

Table 5.4 Setting parameters used in the GA

Optimization options	Setting condition
Rivet and die bounds	$5.0 \leq L_1 \leq 6.0$
	$8.0 \leq D_1 \leq 10.0$
	$1.6 \leq H_1 \leq 2.0$
Population size	50
Selection function	Tournament with size 2
Creation function	Feasible population
Crossover fraction	0.80
Mutation function	Adaptive feasible
Crossover function	Scattered
Migration direction	Forward
Migration fraction	0.20
Distance measure function	Distance crowding
Pareto front population fraction	0.35

5.3.2. Optimization results

For Case No. 1 (i.e., 1.0 mm+1.0 mm), the eighteen Pareto optimal solutions are listed in **Table 5.5**. It can be seen that the interlock, T_{cen} , and T_{tip} reached their maximum values in different Pareto optimal solutions: the maximum interlock (0.89 mm) in Solution No.18, the maximum T_{cen} (0.58 mm) in Solution No.13 and the maximum T_{tip} (0.21 mm) in Solution No.1. To clearly show the changing trends of these quality indicators within the 18 optimal solutions, the joint quality results in **Table 5.5** were plotted in **Figure 5.14** (a). Obviously opposite changing trends were found between the interlock and the T_{tip} . By optimizing the L_1 , D_1 and H_1 , the interlock increased from 0.30 mm to 0.89 mm, whilst the corresponding T_{tip} decreased from 0.21 mm to nearly zero. The T_{cen} was less affected by the rivet and die, and just fluctuated within the range of 0.46 mm to 0.58 mm.

Using **Figure 5.14** (a), the optimal rivet and die under different quality standards for the 1.0 mm+1.0 mm sheet combination can be easily identified. For example, according to the

standard of a world-leading car manufacturer, the interlock and T_{\min} should be greater than 0.4 mm and 0.2 mm respectively for SPR joints with an aluminium alloy bottom sheet [2]. By adding two reference lines (black for the interlock and green for the T_{\min}) onto **Figure 5.14** (a), it can be clearly seen that the 1.0 mm+1.0 mm sheet combination could not be successfully connected by optimizing the L_1 , D_1 and H_1 within the studied ranges. Further optimization of other rivet and die parameters, such as the rivet diameter, rivet type and die type, is required in order to improve the joint quality. However, if reducing the quality standard of the T_{\min} from 0.2 mm to 0.1 mm (yellow reference line), there would be five Pareto optimal solutions (in Zone1) conforming to the modified quality standard. Considering the importance of the interlock for the joint mechanical strength, Solution No.8 with a larger interlock (0.59 mm) might be the best solution for the 1.0 mm+1.0 mm sheet combination.

Table 5.5 Pareto optimal solution set for Case No.1 (1.0 mm+1.0 mm)

Solution No.	Sheets /mm	Optimized rivet and die			Joint quality results (ANN)		
		Rivet length L_1 /mm	Die diameter D_1 /mm	Die depth H_1 /mm	Interlock /mm	T_{cen} /mm	T_{tip} /mm
1	1.0+1.0	5.0	10.0	1.6	0.30	0.47	0.21
2	1.0+1.0	5.0	10.0	1.6	0.30	0.47	0.21
3	1.0+1.0	5.0	10.0	1.7	0.30	0.45	0.20
4	1.0+1.0	5.3	9.8	1.6	0.43	0.47	0.17
5	1.0+1.0	5.0	9.5	1.7	0.46	0.44	0.16
6	1.0+1.0	5.2	9.5	1.6	0.51	0.47	0.16
7	1.0+1.0	5.3	9.5	1.6	0.56	0.47	0.14
8	1.0+1.0	5.3	9.5	1.7	0.59	0.46	0.13
9	1.0+1.0	5.3	9.0	1.6	0.61	0.48	0.10
10	1.0+1.0	6.0	10.0	1.7	0.61	0.49	0.08
11	1.0+1.0	6.0	9.8	1.6	0.67	0.51	0.07
12	1.0+1.0	5.9	8.0	1.6	0.70	0.57	0.02
13	1.0+1.0	6.0	8.0	1.6	0.71	0.58	0.01
14	1.0+1.0	6.0	8.0	1.7	0.74	0.53	0.01
15	1.0+1.0	6.0	8.0	1.7	0.76	0.52	0.00
16	1.0+1.0	6.0	8.1	1.7	0.78	0.51	0.00
17	1.0+1.0	6.0	9.5	1.8	0.81	0.49	0.04
18	1.0+1.0	6.0	9.0	1.7	0.89	0.49	0.02

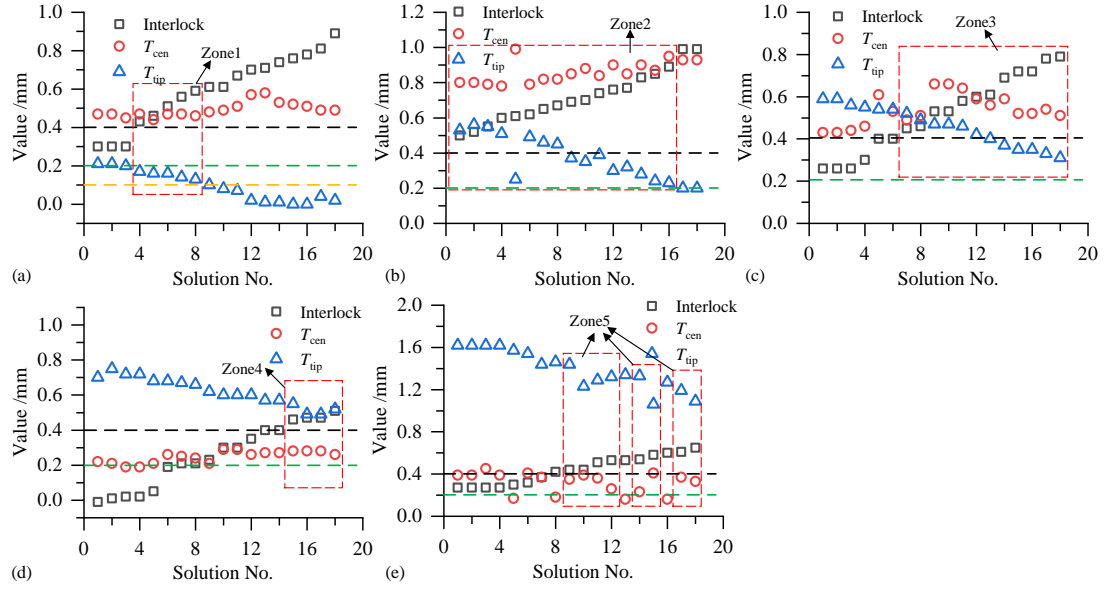


Figure 5.14 Changing trends of the interlock, T_{cen} and T_{tip} with the optimized rivet and die (a) 1.0 mm+1.0 mm, (b) 1.0 mm+2.0 mm, (c) 1.5 mm+1.5 mm, (d) 2.0 mm+1.0 mm and (e) 2.0 mm+2.0 mm

The Pareto optimal solutions for the other four sheet combinations are also plotted in **Figure 5.14** (b)(c)(d)(e) to facilitate the selection of optimal rivet and die. For clarity, the detailed Pareto optimal solutions are not presented in tabular form anymore. It can be seen that the interlock, T_{cen} and T_{tip} in **Figure 5.14** (b)(c)(d)(e) demonstrated very similar changing trends to that in **Figure 5.14** (a): the increment of interlock was always accompanied by the rapid decrease of T_{tip} and the fluctuation of T_{cen} within a small range. According to the joint quality standard from [2] (i.e., interlock > 0.4 mm and T_{min} > 0.2 mm), all of the four sheet combinations can be successfully connected by optimizing the L_1 , D_1 and H_1 . From the acceptable solutions in Zone2 of **Figure 5.14** (b), the optimized rivet and die in Solution No.16 might be the best option for the 1.0 mm+2.0 mm sheet combination. Similarly, the best solutions for the rest three sheet combinations were also easily identified from the acceptable solutions shown in Zone3 of **Figure 5.14** (c), Zone4 of **Figure 5.14** (d) and Zone5 of **Figure 5.14** (e): Solution No.18 for the 1.5 mm+1.5 mm sheet combination, Solution No.18 for the 2.0 mm+1.0 mm sheet combination and Solution No.18 for the 2.0 mm+2.0 mm sheet combination.

By comparing the acceptable solution ranges (Zone2, Zone3 and Zone4) in **Figure 5.14** (b)(c)(d), it was also found that the sheet combination with a thin top sheet and a thick bottom sheet (e.g., 1.0 mm+2.0 mm) is more compatible with the rivet and die, and therefore much easier to be successfully connected. In contrast, the sheet combination with a thick top sheet and a thin bottom sheet (e.g., 2.0 mm+1.0 mm) is more demanding for the rivet and die, and thus more difficult to be connected successfully. This is in good agreement with the results reported in study [44]. Meanwhile, the T_{min} was more likely formed around the rivet tip in the sheet combination with a thin top sheet and a thick bottom sheet ($T_{tip} < T_{cen}$ in **Figure 5.14**

(b)), but more likely formed around the joint central area in the sheet combination with a thick top sheet and a thin bottom sheet ($T_{\text{tip}} > T_{\text{cen}}$ in **Figure 5.14** (d)).

Based on the above case studies, it can be concluded that the developed joint quality optimization tool could effectively simplify the selection of rivet and die according to different joint quality standards.

5.4. Interaction analysis between joining parameters

Another useful application of the developed ANNs is to analyse the interaction effects between different joining parameters on the joint quality. **Figure 5.15** shows the interaction plots of the five joining parameters (i.e., T_1 , T_2 , L_1 , D_1 and H_1) on the interlock, T_{cen} and T_{tip} . The almost parallel trend lines suggest weak interactions, whilst the non-parallel trend lines indicate significant interactions between these parameters. Under the studied joint configurations, significant interaction effects on the interlock were observed between the D_1 and any of the other three parameters (T_2 , L_1 and H_1) as shown in **Figure 5.15** (a). Whilst only the T_1 and T_2 demonstrated apparent interaction effects on the T_{cen} and T_{tip} as shown in **Figure 5.15** (b)(c). Therefore, the corresponding five contour graphs of the interlock, T_{cen} and T_{tip} were plotted with the ANNs, and discussed in the following sections.

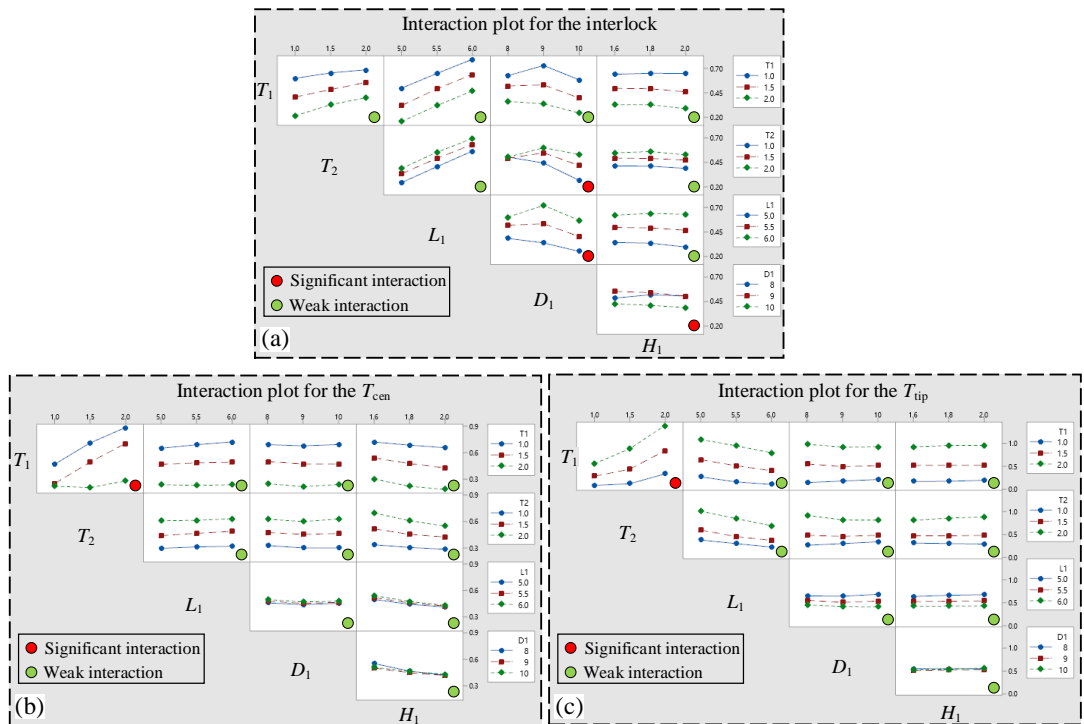


Figure 5.15 Interaction plots of the five joining parameters on the (a) interlock, (b) T_{cen} and (c) T_{tip}

5.4.1. Interaction effects on the interlock

5.4.1.1. Between the bottom sheet thickness (T_2) and die diameter (D_1)

When the T_1 , L_1 and H_1 were fixed at 1.2 mm, 5.0 mm and 2.0 mm, the contour graph of the interlock with varying T_2 and D_1 is plotted in **Figure 5.16**. The non-parallel contour lines indicated the apparent interaction effects between the T_2 and D_1 on the interlock. It can be seen that the interlock always increased with the increment of the T_2 . A greater increasing speed of the interlock was found with a larger D_1 . In contrast, the interlock always decreased with the increment of the D_1 . A greater decreasing speed of the interlock was found with a smaller T_2 . To confirm such interaction effects, the cross-sectional profiles of joints corresponding to the points a ~ i were obtained from experimental SPR tests and FEA simulations, as shown in **Figure 5.17**. Six of the nine joints were made experimentally due to the availability of dies. It can be seen that not only the changing trends but also the magnitudes of interlock matched well between **Figure 5.16** and **Figure 5.17**.

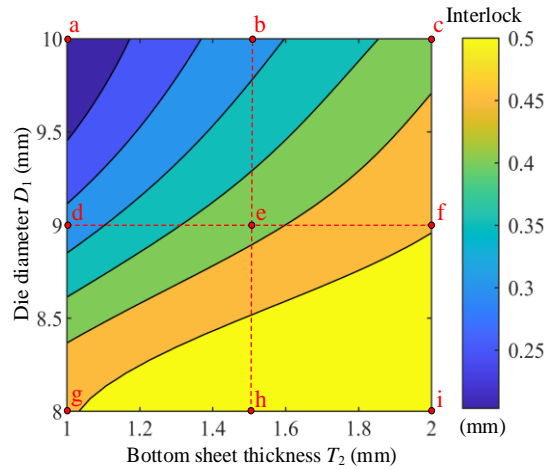


Figure 5.16 Contour graph of the interlock with varying bottom sheet thicknesses T_2 and die diameters D_1 ($T_1=1.2$ mm, $L_1=5.0$ mm, $H_1=2.0$ mm)

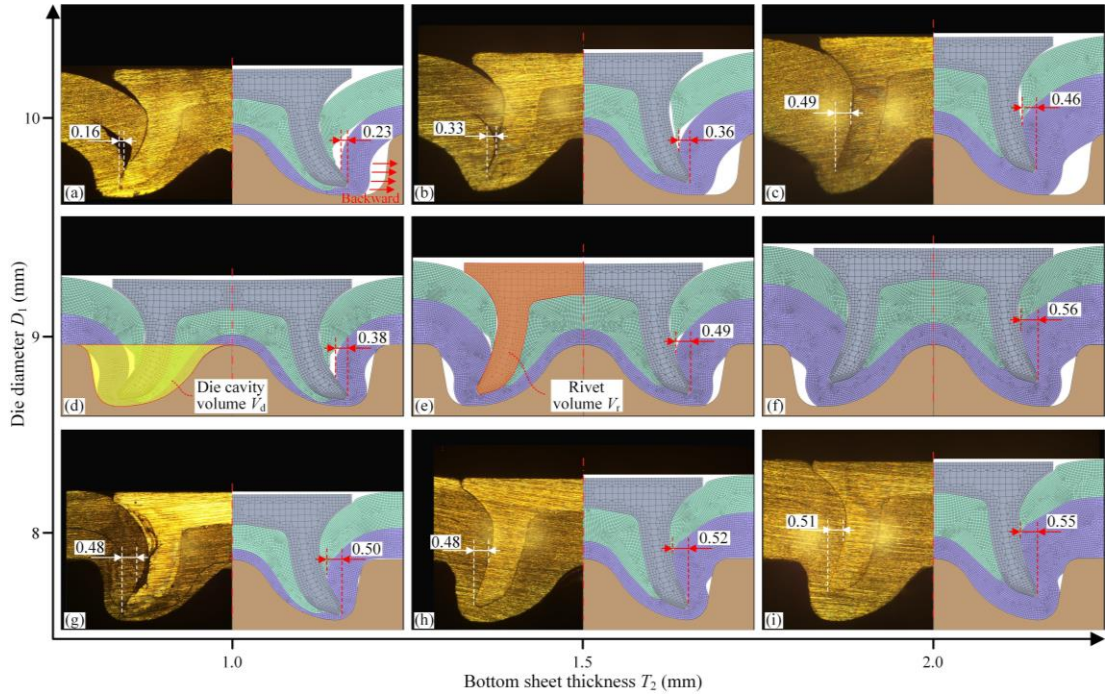


Figure 5.17 Joint cross-sectional profiles with varying bottom sheet thicknesses T_2 and die diameters D_1 ($T_1=1.2$ mm, $L_1=5.0$ mm, $H_1=2.0$ mm)

By analysing the gradients of contour lines in **Figure 5.16**, it can be seen that the interlock demonstrated a higher sensitivity to the T_2 with a large die diameter (e.g., 10.0 mm at the points a to c) than with a small one (e.g., 8.0 mm at the points g to i). This is mainly attributed to the different bottom sheet rigidities and the relative magnitudes of the rivet volume (V_r) and die cavity volume (V_d) shown in **Figure 5.17** (d)(e). When the D_1 was 10.0 mm, the V_d (142.84 mm³) was much greater than the V_r (90.0 mm³). Due to the large unfilled die cavity space, the 1.0 mm bottom sheet with a low rigidity was pressed backward rather than pierced by the rivet shank as shown in **Figure 5.17** (a). Whilst as shown in **Figure 5.17** (c), the 2.0 mm bottom sheet with a sufficient rigidity effectively prevented too much backward movement, and therefore allowed the rivet shank to flare deeply into the bottom sheet. So, the tested interlock rapidly increased from only 0.16 mm to 0.49 mm with the increment of the T_2 . In contrast, when the D_1 was 8.0 mm, the V_d (89.07 mm³) was almost equal to the V_r (90.0 mm³). The small die diameter effectively limited the large movement of the bottom sheets, especially the 1.0 mm one in **Figure 5.17** (g). Almost the same backward movements of the bottom sheets were observed as presented in **Figure 5.17** (g)(h)(i), and the rivet shank deeply flared into the bottom sheet in all of the three joints. Thus, the tested interlock just slightly increased from 0.48 mm to 0.51 mm with the increment of the T_2 .

In addition, the different gradients of contour lines also suggested that the interlock was more sensitive to the D_1 in SPR joints with a thin bottom sheet (e.g., 1.0 mm at the points g to a) than with a thick one (e.g., 2.0 mm at the points i to c). This phenomenon is also caused by

the combined effects of the bottom sheet rigidity and the differentiation between the rivet and die volumes, and hence not discussed in detail.

5.4.1.2. Between the rivet length (L_1) and die diameter (D_1)

When the T_1 , T_2 and H_1 were fixed at 1.2 mm, 1.8 mm and 2.0 mm, the contour graph of the interlock with varying L_1 and D_1 is shown in **Figure 5.18** (a). The non-parallel contour lines indicated the apparent interaction effects between the L_1 and D_1 on the interlock. With the different D_1 , the interlock always showed an increasing trend when the L_1 increased from 5.0 mm to 6.0 mm. Meanwhile, a slightly larger increment speed of the interlock was discovered with the $D_1=10.0$ mm than with the $D_1=8.0$ mm. In contrast, with the different L_1 , the changing trends of the interlock varied when the D_1 increased from 8.0 mm to 10.0 mm. For example, the interlock demonstrated a decreasing trend with the 5.0 mm long rivets, but first increased and then decreased with the 6.0 mm long rivets. **Figure 5.19** shows the cross-sectional profiles of joints corresponding to the points a~i from experimental tests and FEA simulations. Among the nine profiles, four of them were experimentally obtained using the accessible dies. By comparing **Figure 5.18** (a) and **Figure 5.19**, it can be seen that, although the interlock value at the point i was underestimated by the ANN, the predicted changing trends of the interlock from the ANN still showed reasonable agreements with that from both of the experimental tests and FEA simulations.

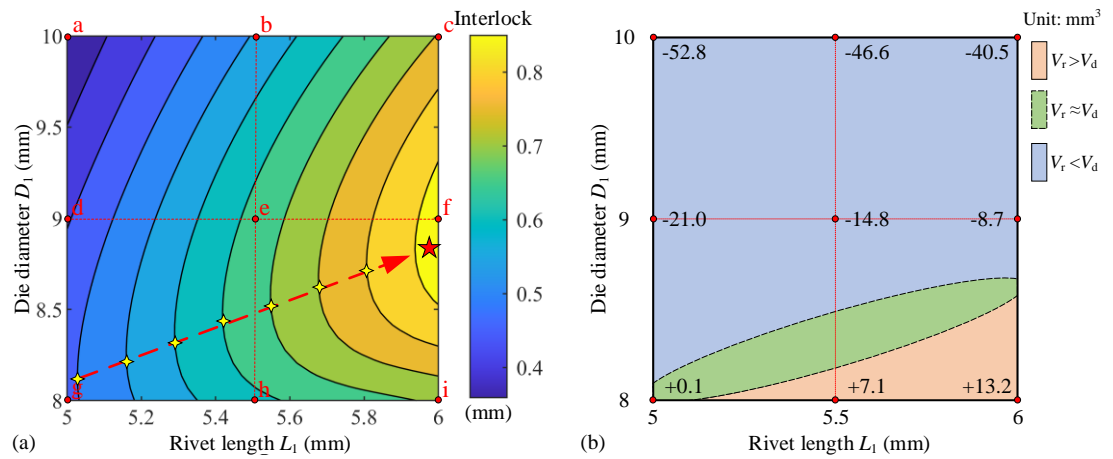


Figure 5.18 Contour graphs of the (a) interlock and (b) $V_r - V_d$ with varying rivet lengths L_1 and die diameters D_1 ($T_1=1.2$ mm, $T_2=1.8$ mm, $H_1=2.0$ mm)

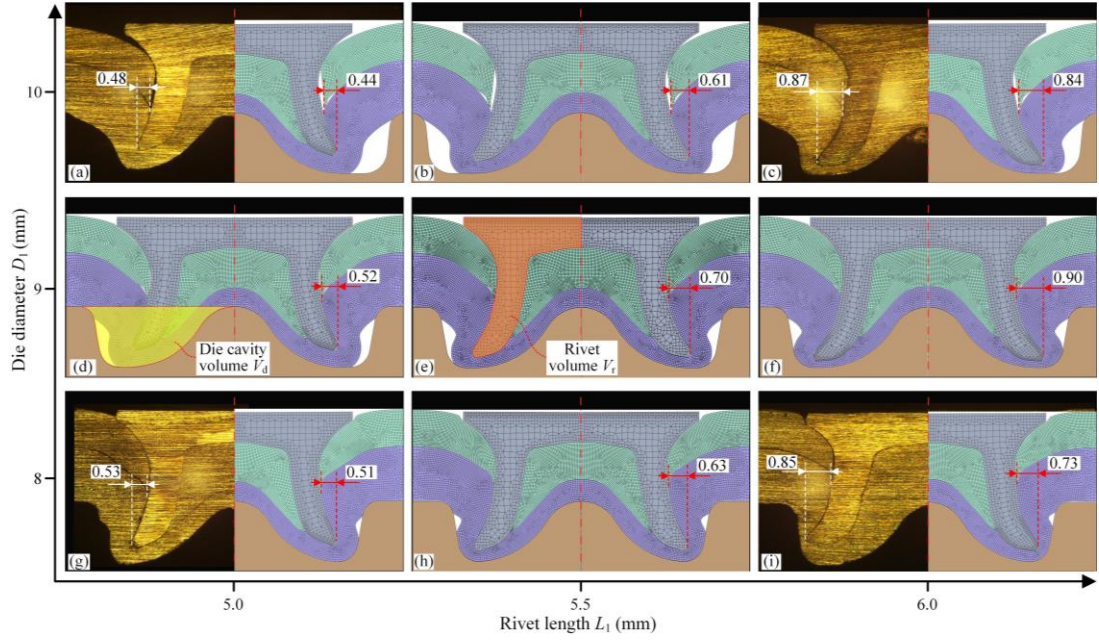


Figure 5.19 Joint cross-sectional profiles with different rivet lengths L_1 and die diameters D_1 ($T_1=1.2$ mm, $T_2=1.8$ mm, $H_1=2.0$ mm)

The interaction effect between the D_1 and L_1 on the interlock is also highly associated with the relative magnitudes of the V_r and V_d . **Figure 5.18** (b) illustrates the contour graph of the difference between the rivet and die cavity volumes ($V_r - V_d$) with varying D_1 and L_1 . With the 8.0 mm die diameter, the V_r of the 5.0 mm long rivet (90.0 mm^3) was almost equal to the V_d (89.07 mm^3). Further increment of the L_1 led to a greater V_r than the V_d . The rivet shank underwent a high pressure after the die cavity was fully filled, and therefore was inevitably buckled as shown in **Figure 5.19** (i). At the same time, the relatively small die diameter ($D_1=8.0$ mm) also limited the rivet shank flare. In contrast, with the 10.0 mm die diameter, the V_r was always smaller than the V_d (142.84 mm^3) as shown in **Figure 5.18** (b). The 1.8 mm bottom sheet was rigid enough to prevent large backward movements, and the rivet shank still flared effectively into the bottom sheet, as shown in **Figure 5.19** (a)(b)(c). As a result, with the increment of the L_1 from 5.0 mm to 6.0 mm, the interlock showed a larger increasing speed with the 10.0 mm die diameter than with the 8.0 mm one. Similarly, when the D_1 increased from 8.0 mm to 10.0 mm, the different interlock changing patterns with varying L_1 can also be explained by the changes of the rivet shank flare and buckling degrees induced by the different volumes between the rivet and die. To avoid repetition, detailed discussions about this part are omitted.

The contour graph not only demonstrated the interaction effects but also visualized the maximum interlock values with possible optimal rivet and die combinations under the pre-defined conditions. For example, the yellow stars marked in **Figure 5.18** (a) presented the maximum interlock values with the optimal D_1 for rivets of different lengths. From the positions of these yellow stars, it can be seen that the optimal D_1 slightly increased with the

increment of L_1 , and the maximum interlock occurred (i.e., red star) when the L_1 reached its maximum value 6.0 mm. Due to such strong interactions between the L_1 and D_1 , the influences of the L_1 and D_1 on the interlock should be considered simultaneously.

5.4.1.3. Between the die diameter (D_1) and die depth (H_1)

When the T_1 , T_2 and L_1 were fixed at 1.2 mm, 1.8 mm and 5.0 mm, the contour graph of the interlock with varying D_1 and H_1 is shown in **Figure 5.20** (a). The non-parallel contour lines confirmed the apparent interaction effects between the D_1 and H_1 on the interlock. It can be seen that the changing trend of the interlock varied with the changes of the D_1 and H_1 . For example, when the D_1 increased from 8.0 mm to 10.0 mm, the interlock first increased and then decreased with the $H_1=1.6$ mm, while it demonstrated a decline trend with the $H_1=2.0$ mm. Similarly, when the H_1 increased from 1.6 mm to 2.0 mm, the interlock also demonstrated different variation trends with the $D_1=8.0$ mm and $D_1=10.0$ mm. The cross-sectional profiles of joints corresponding to the points a~i obtained from the experimental tests and FEA simulations are presented in **Figure 5.21**. Four of the nine joints were made experimentally using the accessible dies. By comparing the contour graph with the joint cross-sectional profiles, it can be concluded that the predicted changing trends of the interlock from the ANN showed reasonable agreements with that from both of the experimental SPR tests and FEA simulations.

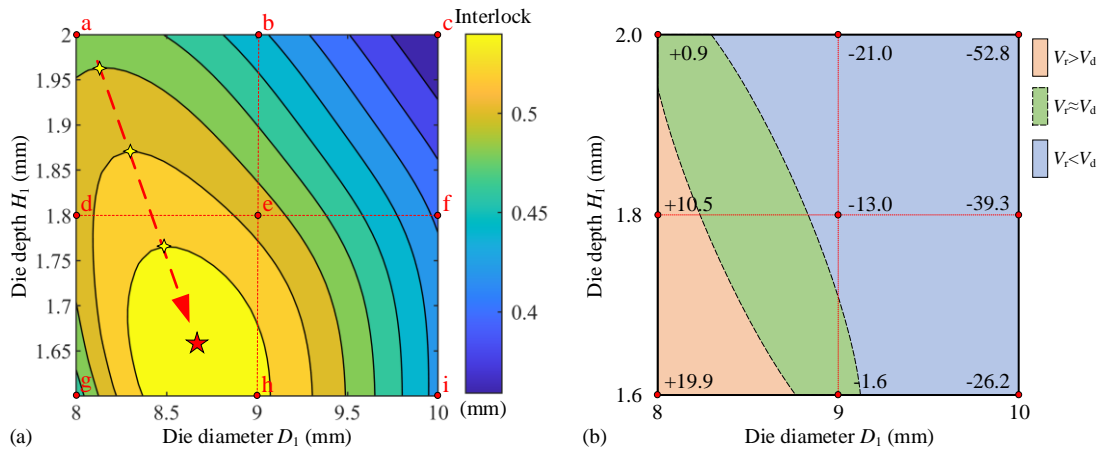


Figure 5.20 Contour graphs of the (a) interlock and (b) $V_r - V_d$ with varying die diameters D_1 and die depths H_1 ($T_1=1.2$ mm, $T_2=1.8$ mm, $L_1=5.0$ mm)

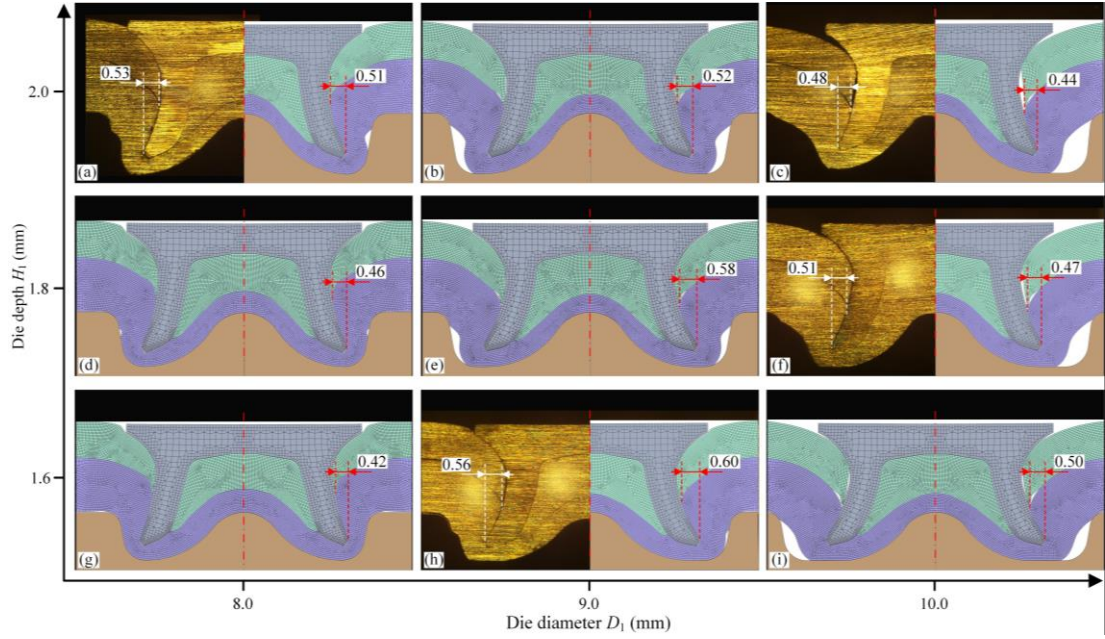


Figure 5.21 Joint cross-sectional profiles with different die diameters D_1 and die depths H_1 ($T_1=1.2$ mm, $T_2=1.8$ mm, $L_1=5.0$ mm)

The interaction effects between the D_1 and H_1 on the interlock are also highly associated with the relative magnitude of the V_r and V_d . **Figure 5.20** (b) illustrates the contour graph of the difference between the V_r and V_d with varying D_1 and H_1 . As mentioned above, if the V_d is smaller than the V_r , it would be very difficult for the rivet shank to further flare into the bottom sheet after the die cavity is fully filled. Instead, the rivet shank buckling happens and imposes negative influences on the interlock formation. On the other hand, if the V_d is greater than the V_r , the bottom sheet would undergo a large displacement towards the die cavity and thus could not be effectively pierced by the rivet shank. This would also impose a negative influence on the interlock formation. The increment of the H_1 from the points g to a effectively increased the V_d as shown in **Figure 5.20** (b). This provides enough volume for the rivet shank to flare, but not too much for the bottom sheet to deform freely into the die cavity. As a result, the rivet shank buckling degree was effectively reduced as shown in **Figure 5.21** (g)(d)(a), which led to the increasing trend of the interlock with the 8.0 mm die diameter. In contrast, from the points h to b and from the points i to c, the increment of the H_1 led to an increasingly larger V_d compared with the V_r as shown in **Figure 5.20** (b). As a result, the interlock showed decreasing tendencies with the 9.0 mm and 10.0 mm die diameters. The same principles can also be applied to explain the different changing trends of interlock when the D_1 increased from 8.0 mm to 10.0 mm. As shown in **Figure 5.20** (a), when the $H_1=1.6$ mm, the interlock first increased due to the reduction of rivet shank bulking degree and then decreased because of the increasingly larger backward movement of the bottom sheet. Whilst when the $H_1=2.0$ mm, the interlock showed a decreasing trend because the V_d became increasingly larger than the V_r .

Similar to the previous section, the contour graph also visualized the maximum interlock values with possible optimal combinations of the D_1 and H_1 under the pre-defined conditions. For example, the yellow stars marked in **Figure 5.20** (a) presented the maximum interlock values with the optimal D_1 for different H_1 . From the positions of these yellow stars, it can be seen that the optimal D_1 slightly increased with the decrease of H_1 , and the maximum interlock occurred (i.e., red star) when the H_1 reached around 1.65 mm. By observing the relative rivet and die volumes in **Figure 5.20** (b) corresponding to the locations of these yellow stars in **Figure 5.20** (a), the importance of choosing similar rivet and die volumes to maximise the interlock for a SPR joint was highlighted.

5.4.2. Interaction effects on the T_{cen} and T_{tip}

As mentioned above, strong interaction effects on the T_{cen} and T_{tip} were only discovered between the T_1 and T_2 . When the L_1 , D_1 and H_1 were fixed at 5.0 mm, 10.0 mm, 1.8 mm, the contour graph of the T_{cen} with varying T_1 and T_2 is shown in **Figure 5.22** (a). The apparent interaction effects between the T_1 and T_2 on the T_{cen} were highlighted by the non-parallel contour lines. The tested and FEA simulated cross-sectional profiles of joints corresponding to the points a ~ i are shown in **Figure 5.23**. Five of the nine joints were made experimentally due to the availability of dies. It can be seen that the predicted changing trends of the T_{cen} from the ANN showed reasonable agreements with that from the experimental SPR tests and the FEA simulations. With the different T_2 , the T_{cen} always decreased when the T_1 increased from 1.2 mm to 1.8 mm. A slightly greater decreasing speed of T_{cen} was captured with a larger T_2 . The decline of the T_{cen} is because the thicker top sheet takes a longer time to be penetrated by the rivet shank [41], whilst the greater speed of the T_{cen} might be mainly attributed to the relatively higher rigidity of the thicker bottom sheet. In contrast, with the different T_1 , the T_{cen} always increased when the T_2 changed from 1.2 mm to 1.8 mm. A larger increasing speed of T_{cen} was found with a smaller T_1 . The increment of the T_{cen} is directly linked with the increment of the initial bottom sheet thickness at the joint centre, whilst the larger speed of the T_{cen} might be attributed to the relatively lower pressure applied around the centre of the bottom sheet by the thinner top sheet. The largest T_{cen} was captured on the top left corner while the smallest value was observed on the lower right corner of the contour graph.

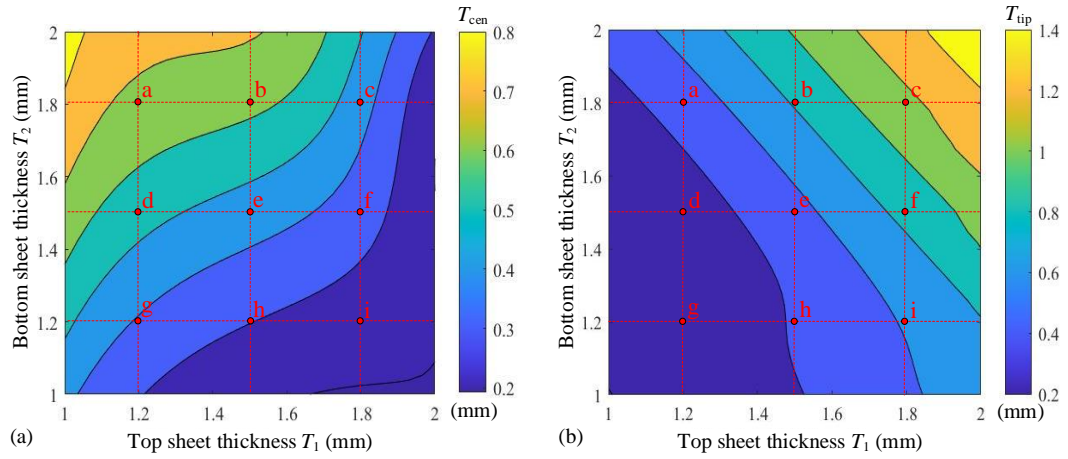


Figure 5.22 Contour graph of the (a) T_{cen} and (b) T_{tip} with varying top and bottom sheet thicknesses ($L_1=5.0$ mm, $D_1=10.0$ mm, $H_1=1.8$ mm)

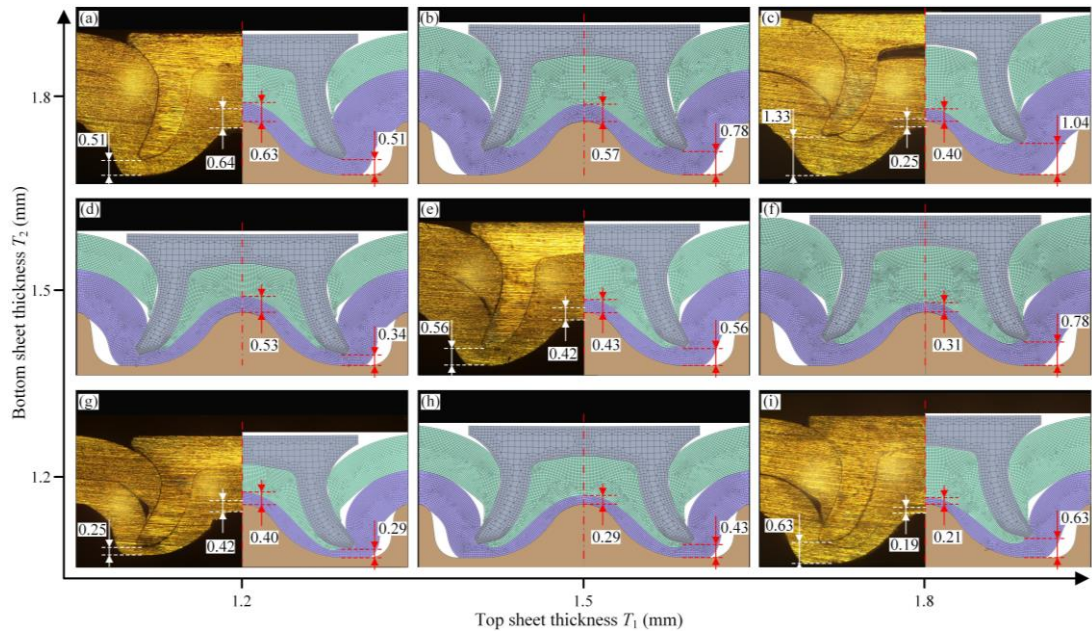


Figure 5.23 Joint cross-sectional profiles with varying top and bottom sheet thicknesses ($L_1=5.0$ mm, $D_1=10.0$ mm, $H_1=1.8$ mm)

When the L_1 , D_1 and H_1 were fixed at 5.0 mm, 10.0 mm, 1.8 mm, the contour graph of the T_{tip} with varying T_1 and T_2 is shown in **Figure 5.22** (b). The non-parallel contour lines demonstrated the interaction effects between the T_1 and T_2 on the T_{tip} . The predicted changing trends of the T_{tip} from the ANN in **Figure 5.22** (b) showed reasonable agreements with that from the experimental SPR tests and the FEA simulations in **Figure 5.23**. It can be seen that the T_{tip} always showed an increasing trend with the increments of the T_1 and T_2 . This is because the increment of the T_1 or T_2 increased the total sheet thickness and led to a larger distance between the final position of the rivet tip and the bottom of the die cavity. When the T_2 increased from 1.2 mm to 1.8 mm, a larger increasing speed of T_{tip} was found with a thicker top sheet. Similarly, when the T_1 changed from 1.2 mm to 1.8 mm, a larger increment speed of T_{tip} was also observed with a thicker bottom sheet. This phenomenon is attributed to the

different impact degrees of the sheet thickness changes on the rivet shank flare. For instance, **Figure 5.24** shows the rivet shank deformations from the points a to c with $T_2=1.8$ mm and from the points g to i with $T_2=1.2$ mm. An apparent increase of the deformed rivet length along the vertical direction was found from the points g to i due to the smaller rivet shank flare. Whilst the deformed rivet length along the vertical direction kept almost constant from the points a to c. The increment of the deformed rivet length directly led to a smaller T_{tip} . Thus, with the increment of the T_1 , a larger increment speed of T_{tip} was observed with a thicker bottom sheet. Different from the T_{cen} , the largest T_{tip} was found on the top right corner while the smallest value was observed on the lower left corner of the contour graph.

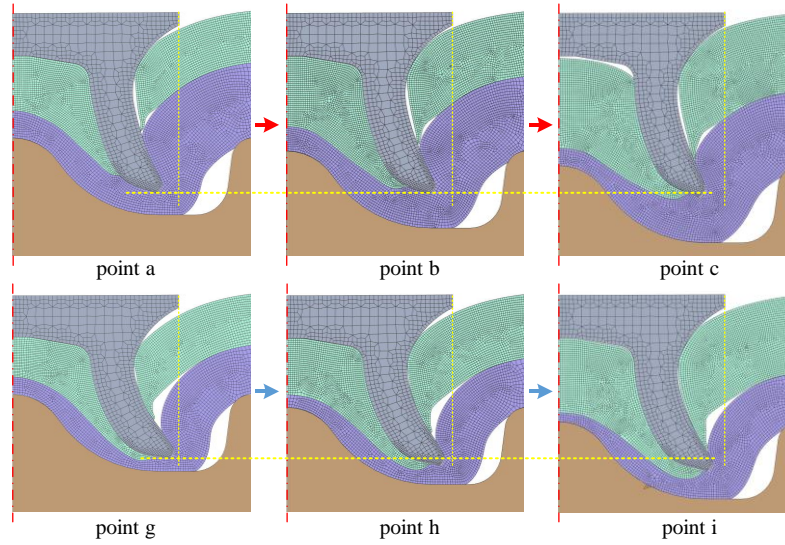


Figure 5.24 Deformed rivet shank in the SPR joints with different top and bottom sheet thicknesses

5.5. Summary

In this chapter, ANN models involving five critical joining parameters were developed to predict the SPR joint quality. An innovative approach, which combines the developed ANN models and the genetic algorithm (GA), was also proposed to automatically optimize the rivet and die for new sheet combinations. In addition, the interaction effects between five joining parameters on the joint quality indicators were also discussed with the contour graphs plotted by the developed ANNs. The main conclusions are summarised below:

1. Three ANN models for the interlock, T_{cen} and T_{tip} were established respectively for prediction of the SPR joint quality. The varying optimal ANN structures suggested that developing an individual ANN model for each quality indicator could maximise the prediction accuracy. The verified FEA model of SPR process can be used to collect training and testing data for ANN model development.
2. The accuracy of developed ANNs was validated with experimental SPR tests. The MAE, MAPE and r for the interlock between the experimental SPR test and ANN were 0.058

mm, 14.2 % and 0.978 respectively. The corresponding MAE, MAPE and r for the T_{cen} were 0.075 mm, 22.4 % and 0.881. The MAE, MAPE and r for the T_{tip} were 0.059 mm, 10.9 % and 0.996 respectively.

3. The GA combined with the developed ANNs can be used to simplify and optimize the selection of rivet and die for new sheet combinations. With the generated Pareto optimal solution set, the suitable rivet and die combinations can be easily selected to achieve the optimal joint quality according to different quality standards.
4. The developed ANNs showed very good performances in the interaction analysis between different joining parameters. Under the studied joint configurations, significant interaction effects on the interlock were identified between the D_1 and any of the other three parameters (T_2 , L_1 and H_1), whilst only the T_1 and T_2 demonstrated apparent interaction effects on the T_{cen} and T_{tip} . The strong interaction effects on the three quality indicators were discovered to be highly associated with the relative magnitude of the rivet and die volumes, the rivet shank flare and the sheet rigidity.

6. Auto-selection of rivet/die combinations for multiple SPR joints based on deep neural network

To further simplify the design process for new SPR joints, this chapter proposed two novel approaches to select the minimum rivet/die combinations automatically and quickly for multiple sheet combinations with the deep neural network (DNN). Firstly, a fast response prediction tool for SPR joint quality was developed using the DNN, and then its prediction performance was verified by experimental SPR tests. Afterwards, the developed DNN model combined with the Monto Carlo method was employed to evaluate the robustness of designed joints by considering the manufacturing tolerances of rivet, sheets and die. Finally, two different approaches were proposed to quickly select the minimum rivet/die combinations for multiple new sheet combinations. The first approach realizes the auto-selection of suitable rivet/die combinations with the developed DNN model and a proposed automatic selection algorithm, whilst also considers the joint robustness. The second method was developed based on the application range maps of different rivet/die combinations, and can be used to quickly select the suitable rivet/die combinations once established. The effectiveness of the proposed two approaches was validated through experimental SPR tests. Strategies developed in this chapter can speed up the design process for multiple SPR joints, and also effectively reduce the dependence on engineers' experience.

6.1. Introduction

The vehicle body structure consists of many parts, and thus there are a considerable number of different sheet combinations. In addition to ensuring the desired quality for each sheet combination, the total number of employed rivet/die combinations for all the sheet combinations should also be considered during the joint design process. Due to the inflexibility of changing rivet and die during the SPR operation, the more rivet/die combinations are employed, the more robots for SPR joining are required as shown in **Figure 6.1**. The total number of rivet/die combinations will directly influence the layout complexity, the initial investment and the subsequent maintenance of the manufacturing line for a specific product (e.g., the vehicle BIW). Therefore, to facilitate the manufacturing process, it is necessary to minimise the number of rivet/die combinations for multiple new sheet combinations. To the author's knowledge, there is still not an effective way to solve this problem and few studies relevant to this issue were reported in the public domain. Moreover, because of the intrinsic properties of SPR joints, the manufacturing tolerances of rivet, sheets

and die will unavoidably affect the SPR joint quality [47,48]. To ensure the reliability of connected structures, the robustness of each designed SPR joint should also be considered carefully during the selection of rivet and die. So far, the only study relevant to robustness design of SPR joints was reported by Tassler et al. [48], in which the variations of five joining parameters (i.e., sheet yield stress, sheet thickness, rivet length, clamping force and rivet head position) were considered during the rivet selection. More efforts are still required to improve the robustness of designed new SPR joints. It will be a great contribution to the design of new SPR joints if the above two problems can be resolved.

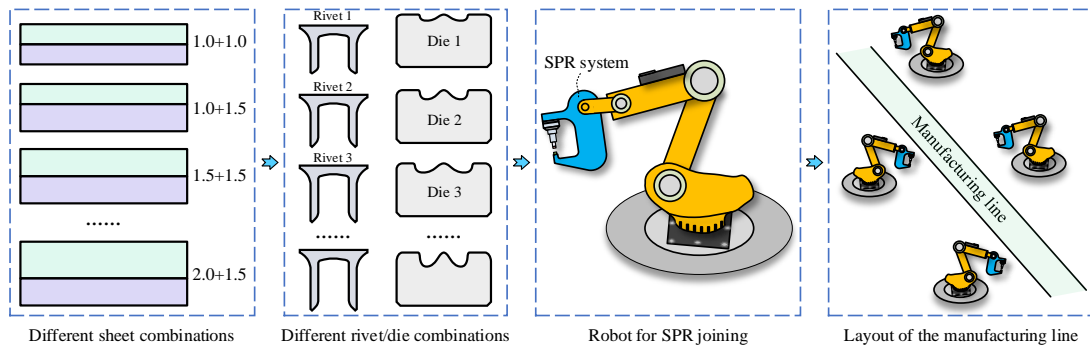


Figure 6.1 Factors affecting the layout of a manufacturing line

In order to solve the above problems, the fast quality prediction tool for SPR joints needs to be developed firstly to replace the experimental SPR tests and offer a prediction result immediately. Compared to FEA model and mathematic prediction model, advantages of the ANN in SPR joint quality prediction have been systematically discussed in Chapter 5. Therefore, the ANN was also selected in this chapter as the fast quality prediction tool. Actually, different types of ANNs have been applied to solve practical problems raised from different industrial sectors [47,140,144]. The structure of ANN, especially the number of hidden layers, has significant influences on its fitting ability and training difficulty. Compared with the SNN (one hidden layer, namely the ANN developed in Chapter 5), the DNN (two or more hidden layers) usually demonstrates a stronger fitting ability but is more difficult to be trained due to its complex network structure. Thus, in this chapter, the performances of SNNs and DNNs with different structures were compared to determine the optimal network structure for the fast joint quality prediction tool.

The manufacturing errors of the rivet, sheets and die usually vary from batch to batch. To experimentally evaluate the joint robustness, a large number of experimental SPR tests will be required for each SPR joint. This experimental approach might become unaffordable for a great number of new SPR joints due to the high investment in time and money. In contrast, the fast quality prediction tool (i.e., the ANN prediction model) can offer a prediction result almost immediately and is more suitable for the evaluation of joint robustness. Therefore, with

the help of the developed DNN prediction model and the Monte Carlo method, an approach was proposed to quantitatively predict the robustness of new SPR joints in this chapter.

To find out the minimise rivet/die combinations for multiple sheet combinations, the simplest way is to try all the possible rivet/die combinations experimentally and then select the suitable ones according to the joint quality results. However, even for experienced joining engineers, this method still costs a huge amount of time and money because of the large number of experimental SPR tests required. In contrast, the quality prediction tool developed with the ANN is capable of carrying out this task owing to its fast prediction ability. Meanwhile, the joint robustness can also be taken into consideration during the rivet and die selection process. Therefore, in this chapter, two different approaches that can quickly identify the minimum rivet/die combinations for multiple new sheet combinations were proposed by using the developed fast quality prediction tool. These two rivet/die selection approaches effectively simplify and speed up the SPR joint design process, reduce the dependence on engineers' experience and facilitate the design of manufacturing process. For clarity, the research structure of this chapter is illustrated in **Figure 6.2**.

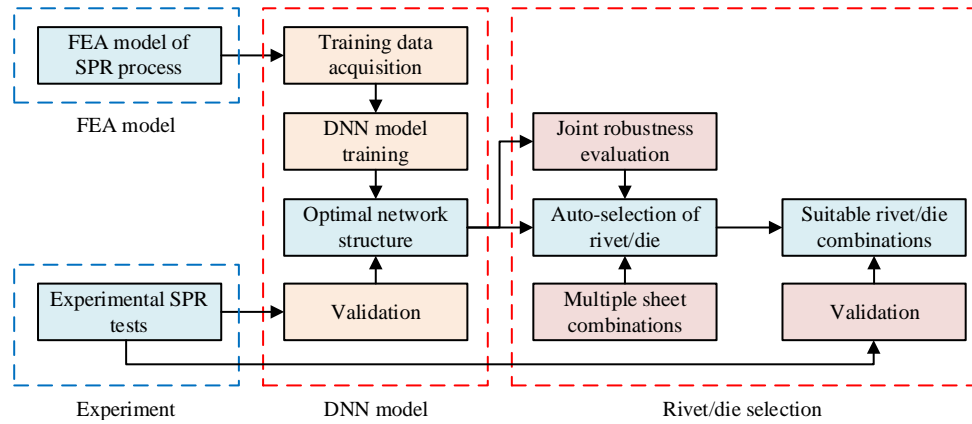


Figure 6.2 Schematic of the research structure for auto-selection of rivet/die for multiple sheet combinations

6.2. DNN models for SPR joint quality prediction

The multiple-layer structure of the DNN allows it to learn representations of data with multiple levels of abstraction [170]. It has a strong ability to describe complex relationships between the input (independent variables) and output (dependent variables)) features [171]. Therefore, the DNN was employed in this chapter to develop a fast joint quality prediction tool, which was then employed to develop the auto-selection system of rivet/die combinations for multiple sheet combinations.

6.2.1. Joint quality data collection

The DNN is a data-driven machine learning method, and thus a large enough training and testing database is required in order to achieve a high prediction performance [172]. The joint quality data (i.e., the 243 joints in **Table 5.1**) collected in Chapter 5 with the developed FEA model was also used as the training and testing data for SNN/DNN models development in this chapter. Five joining parameters, including the top sheet thickness (T_1), bottom sheet thickness (T_2), rivet length (L_1), die diameter (D_1) and die depth (H_1), were involved in the DNN as input variables. Three quality indicators, including the interlock (I), the remaining bottom sheet thickness under the rivet tip (T_{tip}) and the remaining bottom sheet thickness at the joint centre (T_{cen}), were selected as the outputs of the DNN. Moreover, to eliminate the influences of scope difference between the inputs/outputs on the DNN performance [173], all the five input parameters and three output variables of the 243 SPR joints were normalized using the min-max normalization (see Eq. (6.1)).

$$a_{norm} = \frac{a - a_{min}}{a_{max} - a_{min}} \quad (6.1)$$

where a_{norm} denotes the normalized input/output value. a is the original input/output value. a_{min} and a_{max} are the minimum and maximum values among the original input/output values.

6.2.2. DNN architecture design

Figure 6.3 shows the basic structure of a DNN, including one input layer, multiple hidden layers and one output layer. The neurons in each layer are connected to all neurons in the adjacent layers. The weights $W_{ij}^{(k)}$ assigned to each connection indicate the intensity of signal transmission between the connected neurons [174]. The i and j in the $W_{ij}^{(k)}$ denote the numbers of two connected neurons from the later layer and the previous layer respectively, and the k represents the layer number in the DNN. By optimizing the magnitudes of $W_{ij}^{(k)}$ and $B_{ij}^{(k)}$, the network performance can be effectively improved. As mentioned above, five input variables (i.e., T_1 , T_2 , L_1 , D_1 and H_1) and three output variables (i.e., I , T_{cen} and T_{tip}) were involved in the DNN model. It has been widely proved that the DNNs with two or three hidden layers are capable of dealing with complex practical problems, such as mechanical property prediction of hot rolled steel plates [173], material defects prediction [172] and soil moisture prediction [175]. Considering the relatively small sizes of inputs and outputs for the SPR joint quality prediction, the optimal DNN structure was selected from the DNNs with two or three hidden layers. To provide a comprehensive comparison between different neural network structures, SNN with one hidden layer was also developed.

The performances of DNN and SNN are significantly affected by the numbers of neurons in the hidden layers. To determine the optimal network structure for the joint quality prediction, DNNs and SNNs with different hidden neurons were established and their performances were compared. For the SNN, the number of neurons in the hidden layer changed from 3 to 12. For the DNN with two or three hidden layers, the number of neurons in each hidden layer also varied from 3 to 12, and the neurons in the current hidden layer were always no less than that in the following hidden layer. For clarity, the numbers of neurons in the first, second and third hidden layers are denoted by the variables m , n and q respectively ($m \geq n \geq q$).

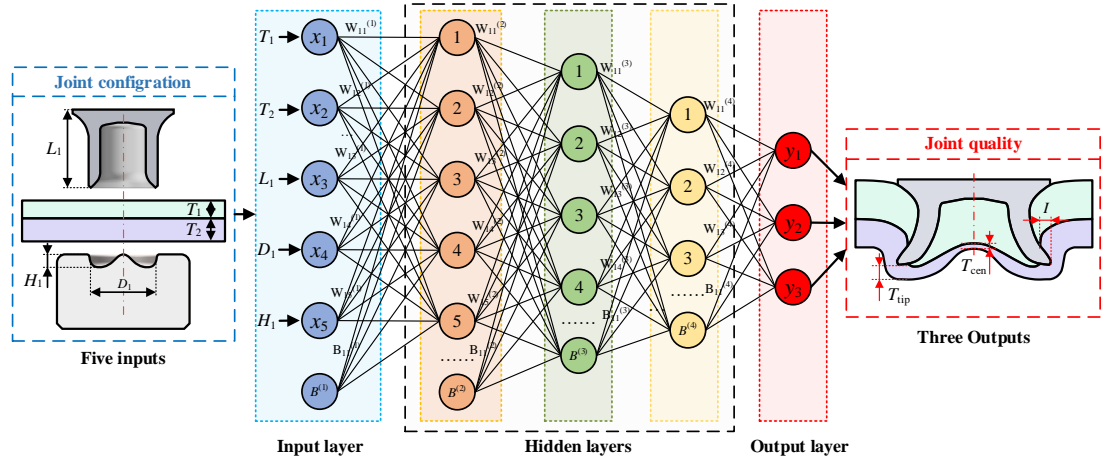


Figure 6.3 Schematic of the DNN structure with multiple hidden layers

6.2.3. Establishment of SNNs and DNNs

All the networks were developed using the software MATLAB 2020. The structure of SNN is relatively simple and thus was directly trained using the back-propagation (BP) algorithm. With multiple hidden layers to learn representations at different levels of abstraction, the DNN demonstrates an advanced ability to solve complex problems but also meets difficulties during the network training. With randomly initialized weights and biases, the gradient-based optimization more likely gets stuck in poor solutions (e.g., local optimum) for such complex network structures. It has been proved that this problem can be effectively solved by embedding a stacked autoencoder (SAE) [33,37]. Therefore, the SAE proposed in [182,183] was introduced in this chapter to facilitate the training of DNNs.

Figure 6.4 (a) shows the structure of a SAE. It consists of several sparse autoencoders, and the outputs of hidden layer in the previous autoencoder are used as the inputs of the following autoencoder. These autoencoders are trained in an unsupervised manner separately according to their sequences within the SAE. The basic structure of a single sparse autoencoder is shown in **Figure 6.4** (b). It contains an encoder and a decoder, and can be simply regarded as a SNN aimed at generating outputs as close as possible to its original inputs [178]. The encoder converts the input data x into a different representation h with the function $f(x)$ shown in Eq.

(6.2). The $w^{(1)}$ and $b^{(1)}$ denote the weight matrix and bias vector of the first layer. The decoder converts the h back into a reconstruction \hat{x} with the function $g(h)$ shown in Eq. (6.3). The $w'^{(1)}$ and $b'^{(1)}$ are the weight matrix and bias vector of the second layer. The sparse autoencoder can contain more neurons in the hidden layer than in the input layer, but only a limited number of hidden neurons are allowed to be active (marked in orange) for one training sample by controlling the sparsity penalty term $\Omega(h)$. It is trained using the scaled conjugate gradient back-propagation algorithm, and its performance is assessed with the loss function in Eq. (6.4).

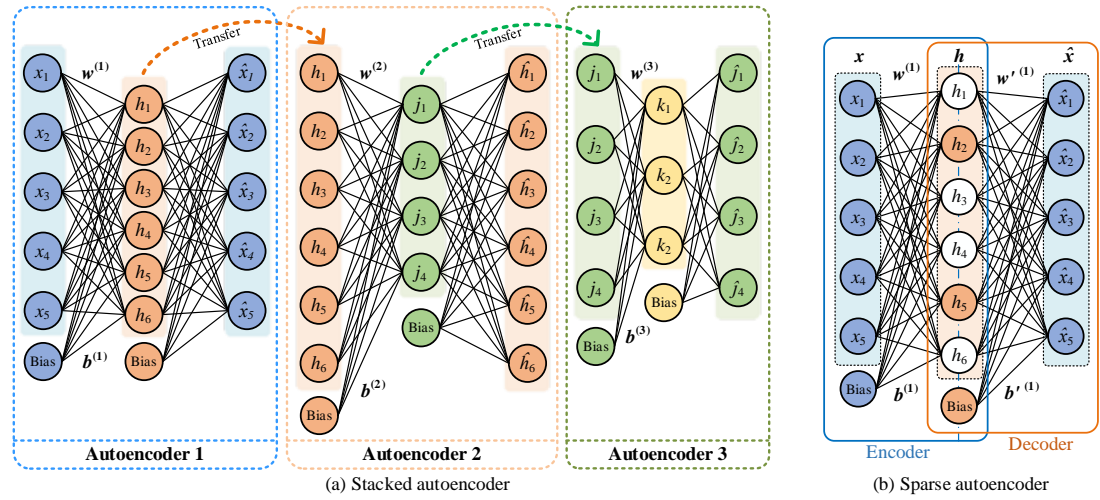


Figure 6.4 Schematic diagrams of (a) a SAE and (b) a single sparse autoencoder

$$h = f(w^{(1)}x + b^{(1)}) \quad (6.2)$$

$$\hat{x} = g(w'^{(1)}h + b'^{(1)}) \quad (6.3)$$

$$E(x, \hat{x}) = \|x - \hat{x}\|^2 + \Omega(h) = \|x - (gw'^{(1)}(w^{(1)}x + b^{(1)}) + b'^{(1)})\|^2 + \Omega(h) \quad (6.4)$$

In this section, each DNN was firstly pre-trained with a SAE to initialize the weights and biases in the first and second hidden layers. The weights and biases in other layers were initialized with random small numbers. **Figure 6.5** illustrates the relationships between the SAE and a DNN with three hidden layers. To obtain matched weights and biases, the number of hidden neurons in each autoencoder was kept the same as that in the corresponding hidden layer of the DNN. The default maximum epochs 1000 were used for the SAE network training. Then, the DNN was fine-tuned with the scaled conjugate gradient back-propagation algorithm. The default minimum performance gradient $1.0e-6$ was used, and the maximum number of iterations was set to 10000 during the network training. The activation function ‘*logsig*’ was implemented for the hidden layers, and the activation function ‘*purelin*’ was applied for the output layer. **Figure 6.6** shows the detailed training procedures for the DNN with two or three hidden layers. The MSE as shown in Eq. (6.5) between the actual output matrix and the

predicted output matrix was selected as the performance function during the DNN training. After completing the network training, for every quality indicator, the corresponding MAE and the correlation coefficients (r) between the FEA simulated and the DNN predicted results for the training and testing data were calculated to evaluate the DNN performance.

$$MSE = \frac{\sum_{j=1}^N (Y_{j,s} - Y_{j,p})^2}{N} \quad (6.5)$$

where the $Y_{j,s}$ and $Y_{j,p}$ denote the matrix of simulated values by the FEA model (i.e., actual value) and the predicted values by the DNN model of the j th SPR joint. The N is the total number of the SPR joints.

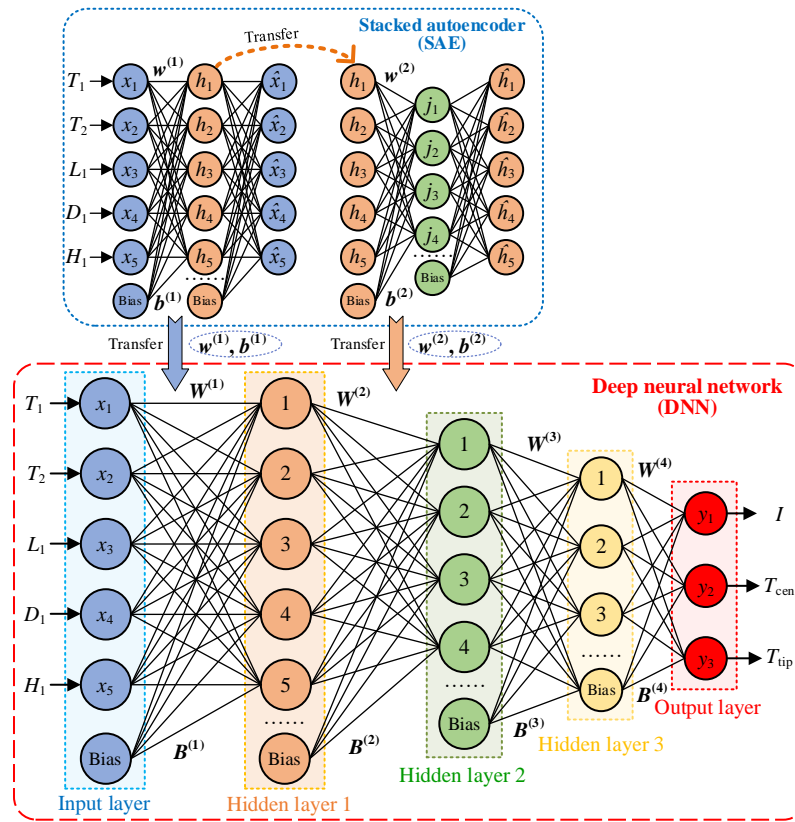


Figure 6.5 Schematic diagram of the relationships between the DNN and the SAE

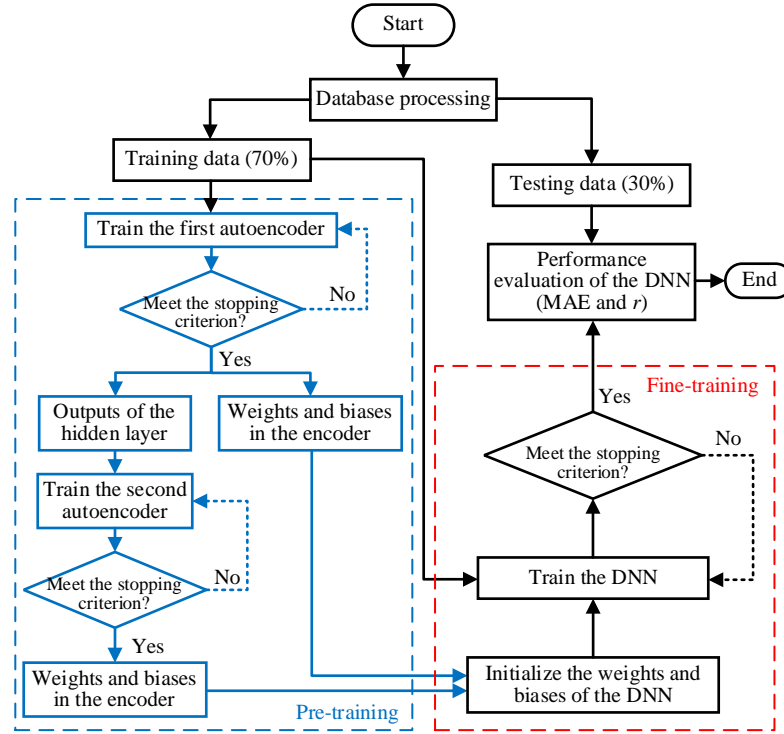


Figure 6.6 Illustration of detailed training procedures for the DNN with two or three hidden layers

Figure 6.7 shows the flow chart to determine the optimal structure of the DNN with three hidden layers. To properly evaluate the performance of each DNN, the training and testing procedures were repeated twenty-five times. The mean values of the MAE and the r for each DNN were calculated for further network performance comparison. Considering the huge number of DNNs, three loops were designed to automatically change the DNN structures and train the DNNs. After all the designed DNNs with different neurons in the hidden layers ($12 \geq m \geq n \geq q \geq 3$) were trained, the optimal DNN was selected by comparing the MAE and r of these DNNs. For the DNNs with two hidden layers and SNNs, similar procedures were also conducted to find out the optimal DNN with two hidden layers and the optimal SNN.

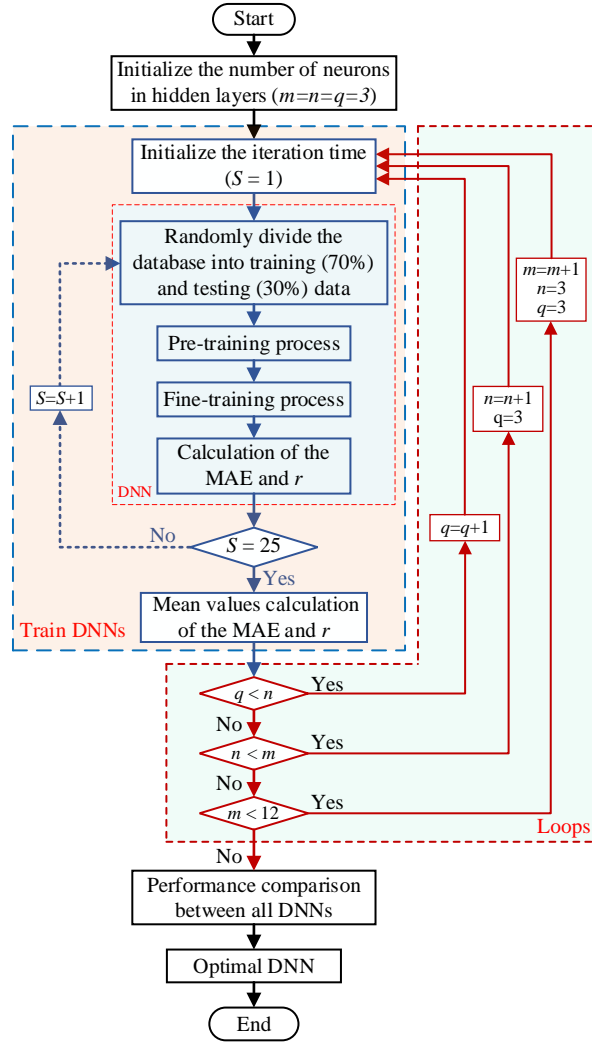


Figure 6.7 Flow chart to select the optimal DNN with three hidden layers

6.2.4. Optimal network structure

6.2.4.1. Performance of SNNs (One hidden layer)

The calculated mean values of the MAE and r for SNNs with different numbers of hidden neurons ($m=3\sim 12$) are illustrated in **Figure 6.8**. It can be seen that, for the training data (black lines), the MAE for the three quality indicators always decreased with the increment of the m . In contrast, the corresponding r for the three quality indicators showed increasing trends. This is because the fitting ability of SNN for the training data effectively improved with the increment of involved hidden neurons. However, too many hidden neurons will cause the overfitting problem and lead to worse performance of SNN for the testing data. As shown in **Figure 6.8**, for the testing data (red dash lines), the MAE for the three quality indicators firstly decreased but then slightly increased with the increment of the m . The corresponding r firstly increased but then slightly decreased. By analysing the variation trends of the MAE and r for the testing data, the optimal structures of SNN (i.e., minimum MAE & maximum r) for the

three quality indicators were identified. For the interlock (I), the SNN with 10 or 12 hidden neurons achieved the best performance. The corresponding MAE and r for the testing data were 0.024 mm and 0.989 respectively. For the T_{tip} , the SNN with 12 hidden neurons achieved the best performance. The corresponding MAE and r were 0.033 mm and 0.994 respectively. For the T_{cen} , the SNN with 12 hidden neurons was also the optimal one. The corresponding MAE and r were 0.022 mm and 0.993 respectively. Based on the above analysis results, the SNN with structure 5-12-3 was selected as the optimal one-hidden-layer network for joint quality prediction.

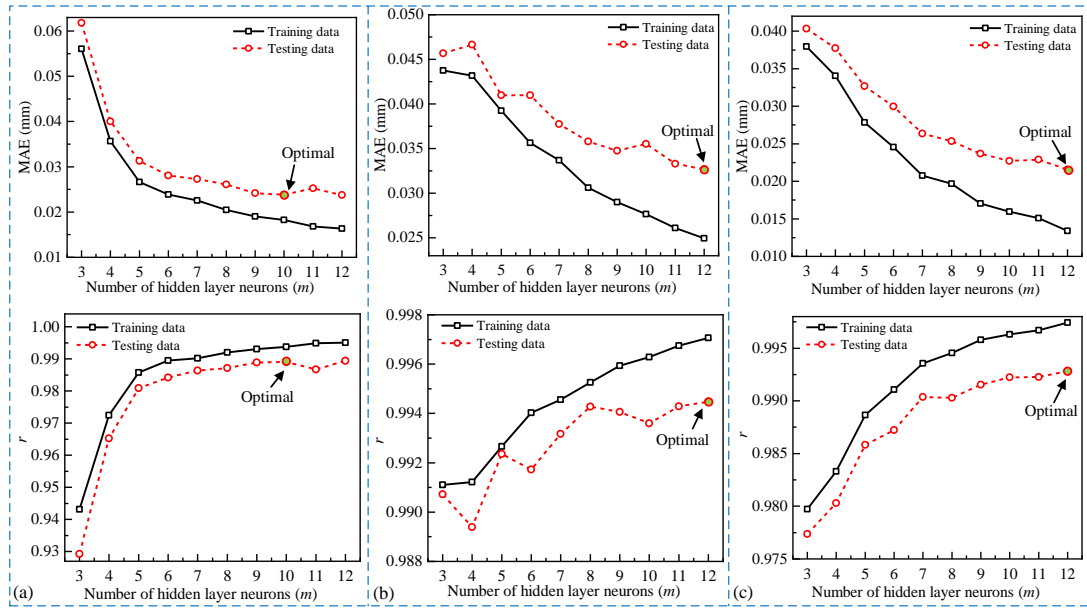


Figure 6.8 Performance evaluation of SNNs with varying hidden neurons for the training data and testing data (a) interlock I , (b) T_{tip} and (c) T_{cen}

6.2.4.2. Performance of DNNs with two hidden layers

The calculated mean values of the MAE and r for DNNs with varying numbers of neurons in the two hidden layers ($m=3\sim 12$, $n=3\sim 12$, $m \geq n$) are illustrated in **Figure 6.9**. Similar to the SNNs with different numbers of hidden neurons, for the training data (solid lines), the MAE for the three quality indicators always decreased with the increment of the m or n , whilst the corresponding r always increased. However, due to the overfitting problem with too many hidden neurons, for the testing data (dash lines), the MAE for the three quality indicators always first decreased and then fluctuated with the increment of the m or n . The corresponding r also first increased and then fluctuated with the increment of the m or n . The optimal DNN with two hidden layers should achieve the best fitting performance for the testing data (i.e., the minimum MAE & the maximum r). By evaluating the performances of all these DNNs, the optimal structures of DNN for the three quality indicators were identified. For the I , the DNN with 10 and 6 neurons in the first and second hidden layers (i.e., network structure 5-

10-6-3) achieved the best performance. The corresponding MAE and r for the testing data were 0.022 mm and 0.991 respectively. For the T_{tip} , the DNN with structure 5-10-6-3 also achieved the best performance. The corresponding MAE and r for the testing data were 0.029 mm and 0.996 respectively. While for the T_{cen} , the DNN with structure 5-12-5-3 was the optimal one, and the corresponding MAE and r for the testing data reached 0.018 mm and 0.995 respectively. Besides, the DNN with structure 5-10-6-3 also achieved a good prediction performance for the T_{cen} , and the corresponding MAE and r for the testing data were 0.020 mm and 0.994 respectively. Considering the performances of DNN for the three joint quality indicators simultaneously, the DNN with structure 5-10-6-3 was selected as the optimal two-hidden-layer network for joint quality prediction.

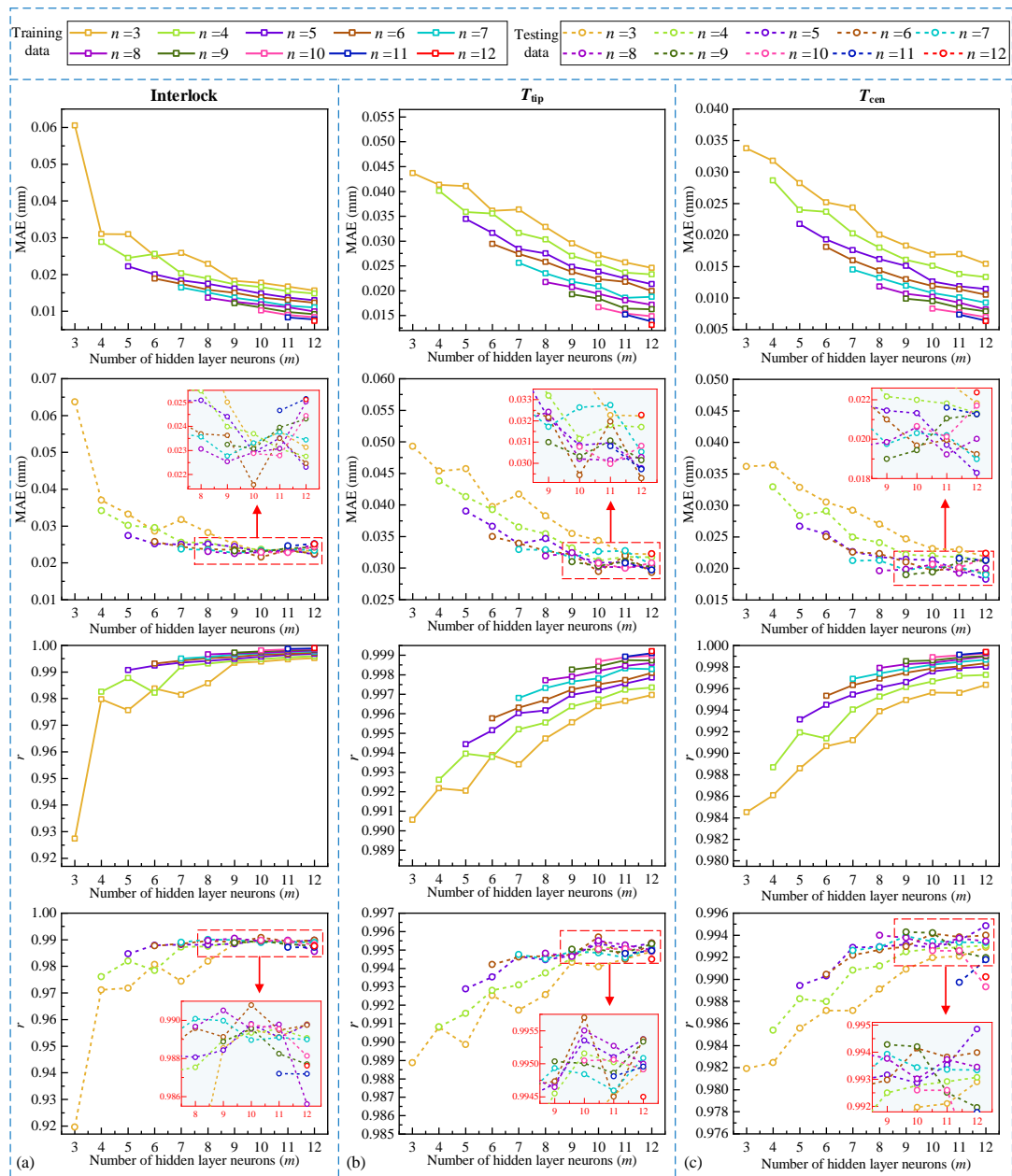


Figure 6.9 Performance evaluation of DNNs with two hidden layers for the training and testing data (a) interlock I , (b) T_{tip} and (c) T_{cen}

6.2.4.3. Performance of DNNs with three hidden layers

By comparing all the DNNs with three hidden layers, it was found that the optimal DNN had 11 neurons in the first hidden layer ($m=11$). Therefore, to avoid presenting large amounts of data, only the calculated MAE and r values for DNNs with $m=11$ were illustrated in **Figure 6.10**. The optimal DNN for the three quality indicators was also selected by analysing the changing trends of MAE and r for the testing data. For the I , both of the DNN with structure 5-11-6-6-3 and the DNN with structure 5-11-7-3-3 can be regarded as the optimal one due to their similar performances. The corresponding MAE and r for the testing data were 0.022 mm, 0.022 mm, 0.990 and 0.991 respectively. For the T_{tip} , the DNN with structure 5-11-10-4-3 achieved the best performance. The corresponding MAE and r for the testing data were 0.029 mm and 0.995 respectively. For the T_{cen} , the DNN with the structure 5-11-10-4-3 also achieved the best performance. The corresponding MAE and r for the testing data were 0.019 mm and 0.994 respectively. Therefore, the DNN with structure 5-11-10-4-3 was selected as the optimal three-hidden-layer network for joint quality prediction due to its good performance for the I (i.e., MAE=0.023 mm, $r=0.990$ for the testing data).

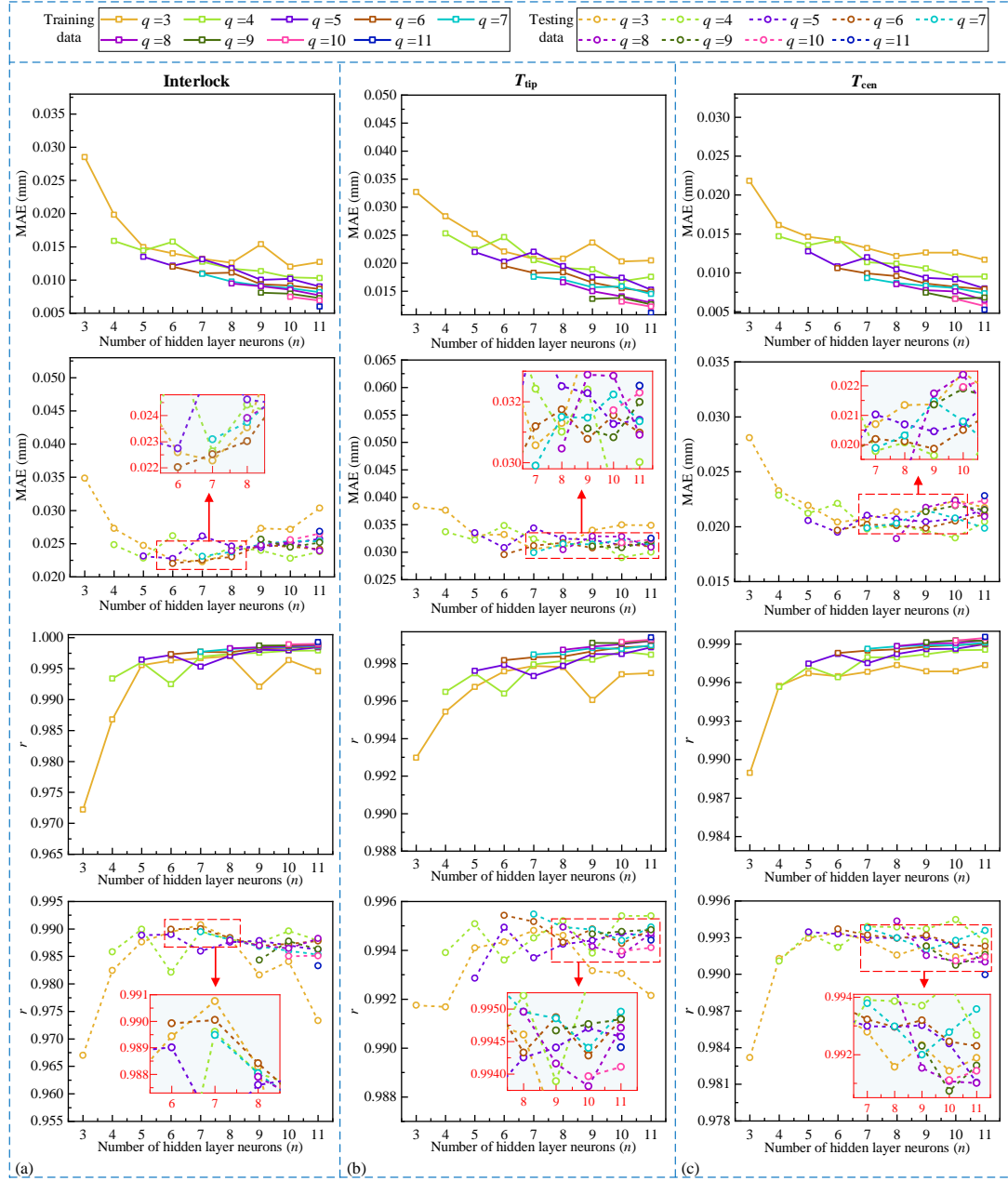


Figure 6.10 Performance evaluation of DNNs with three hidden layers for the training and testing data ($m=11$) (a) interlock I , (b) T_{tip} and (c) T_{cen}

6.2.4.4. Comparisons of the three optimal SNN and DNNs

To find out the optimal network structure for the joint quality prediction, performances of the optimal SNN (5-12-3), the optimal two-hidden-layer DNN (5-10-6-3) and the optimal three-hidden-layer DNN (5-11-10-4-3) for the testing data were compared as shown in **Figure 6.11**. It can be seen that the two DNNs obviously showed a higher prediction accuracy than the SNN, especially for the T_{tip} . For the DNNs, the additional third hidden layer did not apparently improve the DNN performance. The two-hidden-layer DNN even demonstrated a slightly higher prediction accuracy than the three-hidden-layer DNN. Therefore, in this section, the

DNN with structure 5-10-6-3 was selected as the optimal network for the quality prediction of SPR joints within the studied design space.

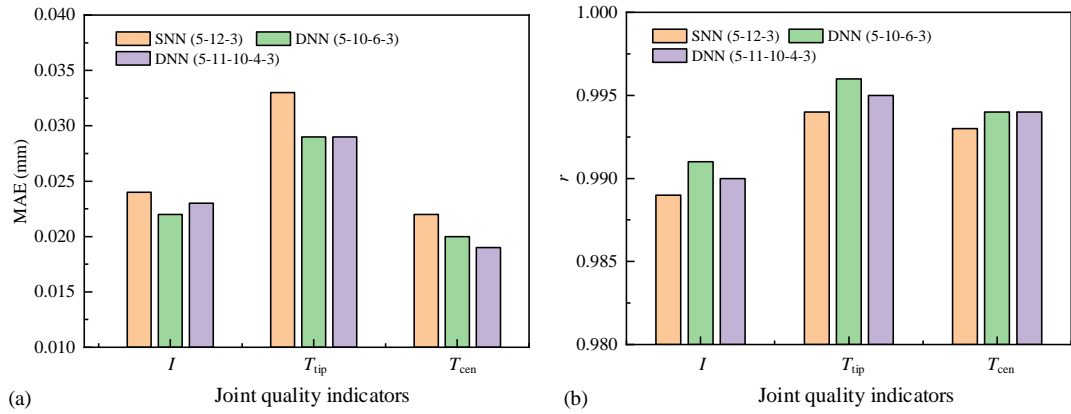


Figure 6.11 Performance comparison between the three optimal SNN and DNNs for the testing data (a) MAE and (b) r

To demonstrate the fitting degree of the optimal DNN model (5-10-6-3), comparisons between the FEA simulated and the DNN predicted joint quality are shown in **Figure 6.12**. Good agreements were found for the training data and the testing data. For the training data, the MAE for the I , T_{tip} and T_{cen} were 0.014 mm, 0.022 mm and 0.012 mm respectively. The corresponding r were 0.997, 0.998 and 0.998 respectively. For the testing data, the MAE for the I , T_{tip} and T_{cen} reached 0.022 mm, 0.029 mm and 0.020 mm respectively. The corresponding r were 0.991, 0.996 and 0.994 respectively. Therefore, it can be concluded that the developed optimal DNN achieved high prediction accuracies for the three joint quality indicators.

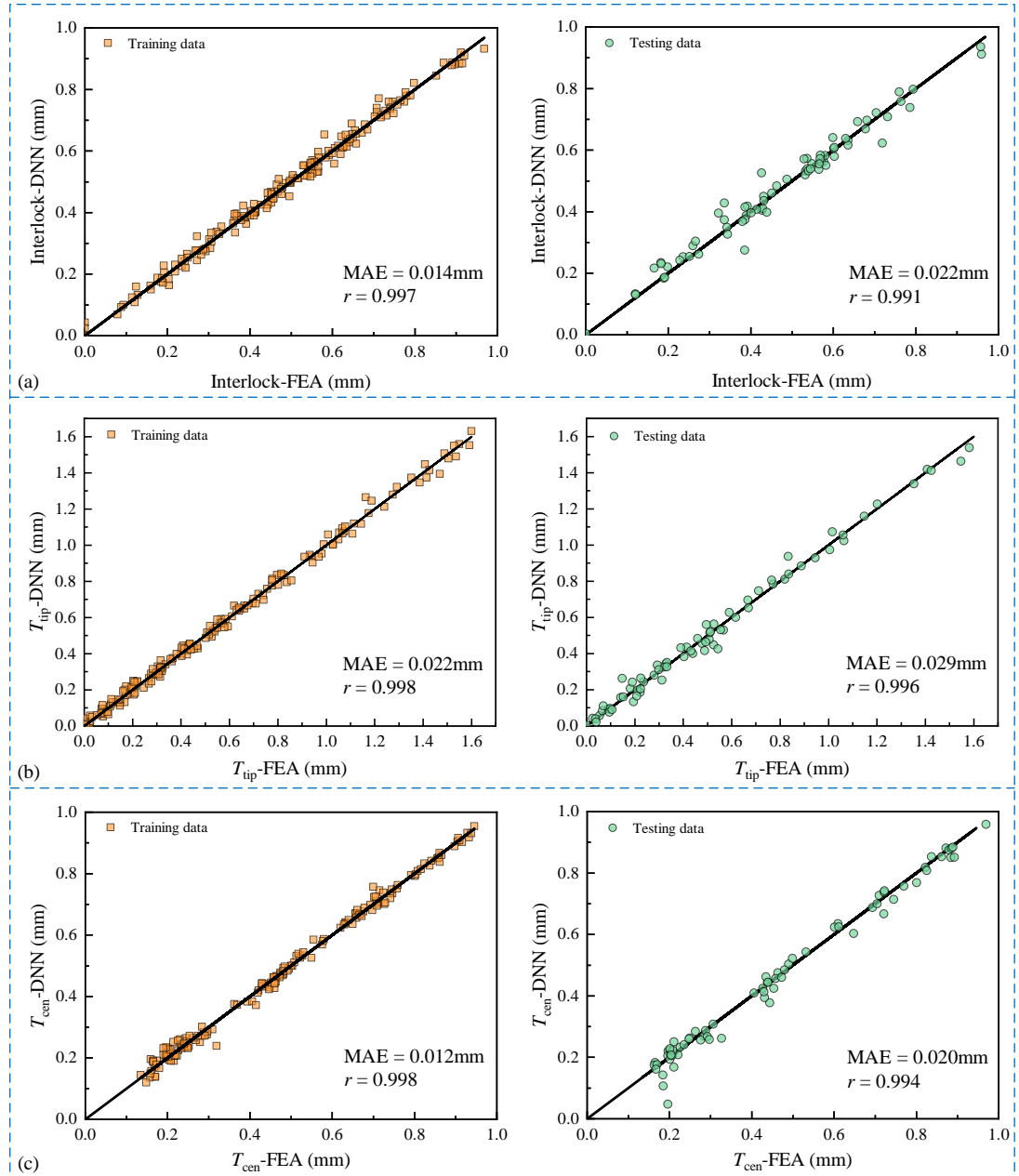


Figure 6.12 Comparisons between the optimal DNN (5-10-6-3) predicted and FEA simulated (a) interlock I , (b) T_{tip} and (c) T_{cen}

6.2.5. Validation of the DNN model

To evaluate the performance of the developed DNN model, twenty-two SPR joints with different configurations were adopted as shown in Table 6.1. Different top sheet thicknesses (T_1), bottom sheet thicknesses (T_2), rivet lengths (L_1), die diameters (D_1) and die depths (H_1) were used to enhance the reliability of the model evaluation result. All of the experimental conditions were the same as that used in the validation tests for the FEA model in 3.3. To ensure the effectiveness of the experimental test results, three repeats for each joint configuration were performed. The mean values of these indicators from the three repetitions were calculated for each joint configuration and also shown in Table 6.1. Meanwhile, the three

quality indicators of the 22 joints were also predicted with the FEA model and the developed DNN, as shown in Table 6.1. For easier comparisons, the joint quality data in Table 6.1 are also plotted in line graphs as shown in **Figure 6.13**.

Table 6.1 Experiment design and results for validation of DNN model

Joint configurations					Experiment, prediction and simulation results								
Joint no.	Stack /mm	Rivet Length L_1 /mm	Die		Interlock/mm			T_{tip} /mm			T_{cen} /mm		
			Diameter D_1 /mm	Depth H_1 /mm	Predicted (DNN)	Simulated (FEA)	Tested (Mean)	Predicted (DNN)	Simulated (FEA)	Tested (Mean)	Predicted (DNN)	Simulated (FEA)	Tested (Mean)
6-1	1.2+1.0	5.0	8.0	2.0	0.48	0.50	0.48	0.14	0.14	0.12	0.35	0.34	0.33
6-2	1.2+1.5	5.0	8.0	2.0	0.51	0.52	0.51	0.29	0.32	0.34	0.59	0.56	0.35
6-3	1.2+2.0	5.0	8.0	2.0	0.50	0.55	0.52	0.72	0.73	0.80	0.75	0.72	0.62
6-4	1.2+1.0	5.0	10.0	2.0	0.19	0.23	0.16	0.31	0.24	0.27	0.33	0.32	0.41
6-5	1.2+1.5	5.0	10.0	2.0	0.33	0.36	0.34	0.40	0.37	0.41	0.56	0.51	0.56
6-6	1.2+2.0	5.0	10.0	2.0	0.41	0.46	0.49	0.74	0.71	0.83	0.80	0.72	0.68
6-7	1.0+1.8	5.0	8.0	2.0	0.56	0.58	0.59	0.32	0.35	0.39	0.74	0.66	0.70
6-8	1.5+1.8	5.0	8.0	2.0	0.44	0.37	0.41	0.86	0.75	0.90	0.42	0.56	0.22
6-9	2.0+1.8	5.0	8.0	2.0	0.20	0.18	0.30	1.37	1.24	1.51	0.03	0.16	0.02
6-10	1.0+1.8	5.0	10.0	2.0	0.46	0.51	0.49	0.39	0.38	0.47	0.75	0.70	0.76
6-11	1.5+1.8	5.0	10.0	2.0	0.27	0.31	0.33	0.87	0.8	0.93	0.55	0.57	0.50
6-12	2.0+1.8	5.0	10.0	2.0	0.19	0.19	0.18	1.40	1.40	1.54	0.16	0.18	0.11
6-13	1.2+1.2	5.0	10.0	1.8	0.28	0.32	0.36	0.30	0.29	0.24	0.47	0.40	0.49
6-14	1.2+1.8	5.0	10.0	1.8	0.41	0.47	0.47	0.52	0.51	0.50	0.70	0.63	0.64
6-15	1.5+1.5	5.0	10.0	1.8	0.25	0.27	0.33	0.59	0.56	0.63	0.45	0.43	0.48
6-16	1.8+1.2	5.0	10.0	1.8	0.09	0.13	0.13	0.66	0.63	0.63	0.25	0.21	0.19
6-17	1.8+1.8	5.0	10.0	1.8	0.22	0.25	0.26	1.12	1.04	1.26	0.41	0.40	0.21
6-18	1.2+1.8	5.0	8.0	2.0	0.52	0.51	0.53	0.51	0.50	0.57	0.67	0.64	0.55
6-19	1.2+1.8	6.0	8.0	2.0	0.69	0.73	0.86	0.30	0.33	0.36	0.75	0.75	0.67
6-20	1.2+1.8	5.0	10.0	2.0	0.38	0.44	0.47	0.57	0.55	0.63	0.69	0.63	0.66
6-21	1.2+1.8	6.0	10.0	2.0	0.76	0.84	0.90	0.25	0.24	0.29	0.75	0.69	0.71
6-22	1.2+1.8	5.0	9.0	1.6	0.53	0.60	0.59	0.43	0.46	0.47	0.71	0.61	0.73

By comparing the magnitudes and variation trends of the three quality indicators from the experimental tests (black dot lines) and the DNN (red lines) in **Figure 6.13(a)(c)(e)**, it can be found that the DNN predicted joint quality matched well with that from the experimental SPR tests. Meanwhile, the developed DNN demonstrated better performance for the I and T_{tip} than for the T_{cen} . The calculated MAE and MAPE for the I were 0.053 mm and 13.2 % respectively. Except for the joints 6-9, 6-19 and 6-21, the predicted interlock values were quite close to the experimentally tested ones. The calculated MAE and MAPE for the T_{tip} reached 0.062 mm and 11.1 % respectively. The calculated MAE and MAPE for the T_{cen} were 0.073 mm and 24.1 % respectively. The relatively large MAPE for the T_{cen} is caused by the great relative percentage errors in the joints 6-2, 6-8 and 6-17 (i.e., 68.6 %, 90.0 % and 95.2 %). Overall, the developed DNN can provide an accurate prediction of SPR joint quality within the studied design space.

It is worth noting that the DNN was developed with the training data and testing data obtained from the FEA model. Therefore, the prediction accuracy of the FEA directly affects the performance of the developed DNN. As shown in **Figure 6.13** (b)(d)(f), the simulated three quality indicators (green dash lines) matched well with the experimentally tested ones (black dot lines). For the FEA simulated and the experimentally tested joint quality results, the calculated MAE and MAPE for the I were 0.035 mm and 9.2 % respectively. The calculated MAE and MAPE for the T_{tip} reached 0.078 mm and 11.7 % respectively. The calculated MAE and MAPE for the T_{cen} were 0.087 mm and 26.0 % (excluding the joint 6-9) respectively. These values matched well with the values calculated from the comparison between the DNN predicted and experimentally tested results. This indicated that the prediction accuracy of the DNN reached almost the same level as that of the FEA model. Therefore, the performance of the DNN can be further improved with the improvement of the employed FEA model.

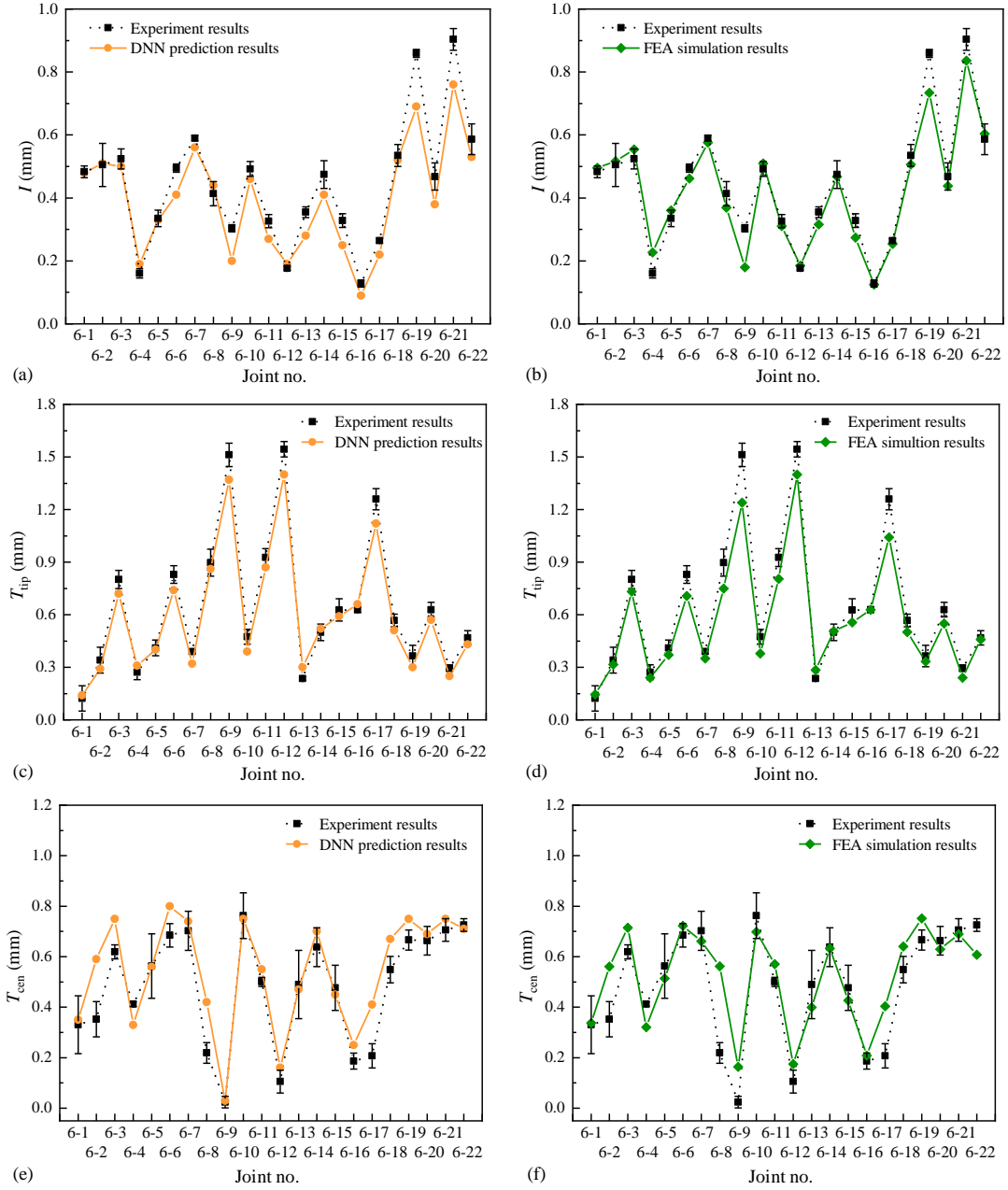


Figure 6.13 Comparisons of the I , T_{tip} and T_{cen} from the experimental SPR tests, the FEA model and the optimal DNN (5-10-6-3)

6.3. Joint robustness evaluation

The Monte Carlo method is good at solving problems that might be deterministic in principle with randomness and generating results from a probability distribution [179]. In this section, by combining the developed DNN with the Monte Carlo method, a strategy was firstly proposed to evaluate the robustness of designed SPR joints.

In practice, the dimensions of rivet, sheet and die always fluctuate within the allowable manufacturing tolerances. This will inevitably affect the final quality of obtained SPR joints. To improve the reliability of designed SPR joints, it is necessary to consider the influences of

these variations on the joint quality during the selection of rivet/die. The FEA model [113], mathematical model and the DNN can predict the quality of a SPR joint based on nominal dimensions of the employed rivet, sheet and die. But they are not capable of directly evaluating the joint robustness. In this research, with the help of the Monte Carlo method, the developed DNN was used to quantitatively evaluate the robustness of SPR joints.

For the studied SPR joints of this research, tolerance bands of the five joining parameters (i.e., T_1 , T_2 , L_1 , D_1 and H_1) are listed in **Table 6.2**. According to the standard EN 485-4:1993 [180], the width of tolerance band for the AA5754 sheet slightly increases with the increment of the nominal sheet thickness. The tolerance bands for the L_1 , D_1 and H_1 are assumed to be ± 0.10 mm, ± 0.10 mm and ± 0.05 mm respectively. Given that the manufactured dimensions of the rivet, sheets and die obey the normal distribution (i.e., $X \sim N(\mu, \sigma^2)$), the normal distribution equations for the T_1 , T_2 , L_1 , D_1 and H_1 were deduced according to their tolerance bands (2σ standard deviations, or 95 % confidence interval) as listed in **Table 6.2**. The procedures to evaluate the robustness of designed SPR joints are shown in **Figure 6.14**. Firstly, 10^6 samples were generated randomly obeying the corresponding normal distributions of the five joining parameters. Then, the joint quality of each sample was predicted by the developed DNN (structure 5-10-6-3). Next, the frequency distributions of the three quality indicators were obtained by processing all the quality results of 10^6 samples. Finally, the joint robustness can be calculated according to the selected joint quality standard.

Table 6.2 Tolerance bands and normal distribution equations for the five joining parameters [180]

Variable	Nominal value /mm	Tolerance band /mm	Normal distribution
Sheet thickness (T_1 and T_2)	[1.0, 1.2)	± 0.10	$\sim (\mu, 0.050^2)$
	[1.2, 1.5)	± 0.12	$\sim (\mu, 0.060^2)$
	[1.5, 1.8)	± 0.13	$\sim (\mu, 0.065^2)$
	[1.8, 2.0)	± 0.14	$\sim (\mu, 0.070^2)$
Rivet length (L_1)	[5.0, 6.0]	± 0.10	$\sim (\mu, 0.050^2)$
Die diameter (D_1)	[8.0, 10.0]	± 0.10	$\sim (\mu, 0.050^2)$
Die depth (H_1)	[1.6, 2.0]	± 0.05	$\sim (\mu, 0.025^2)$

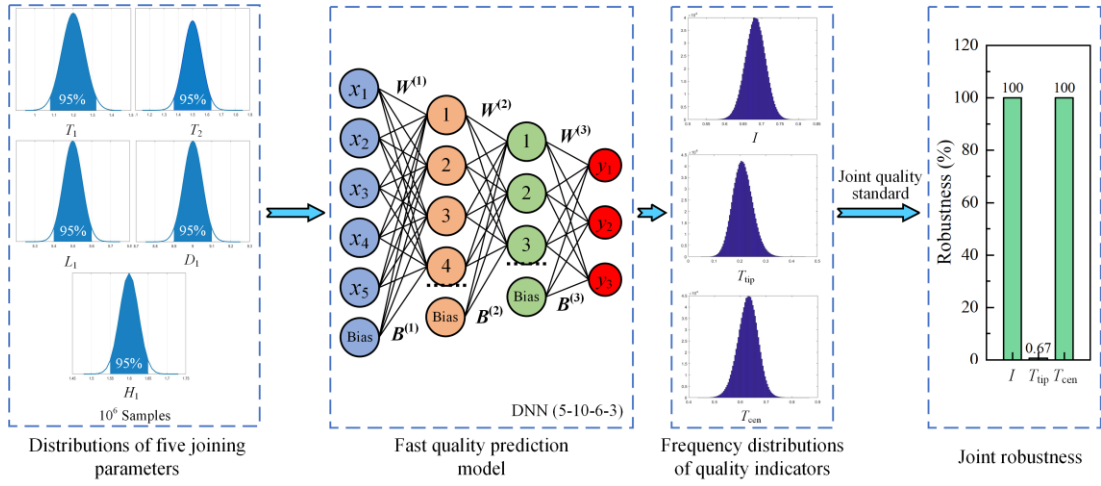
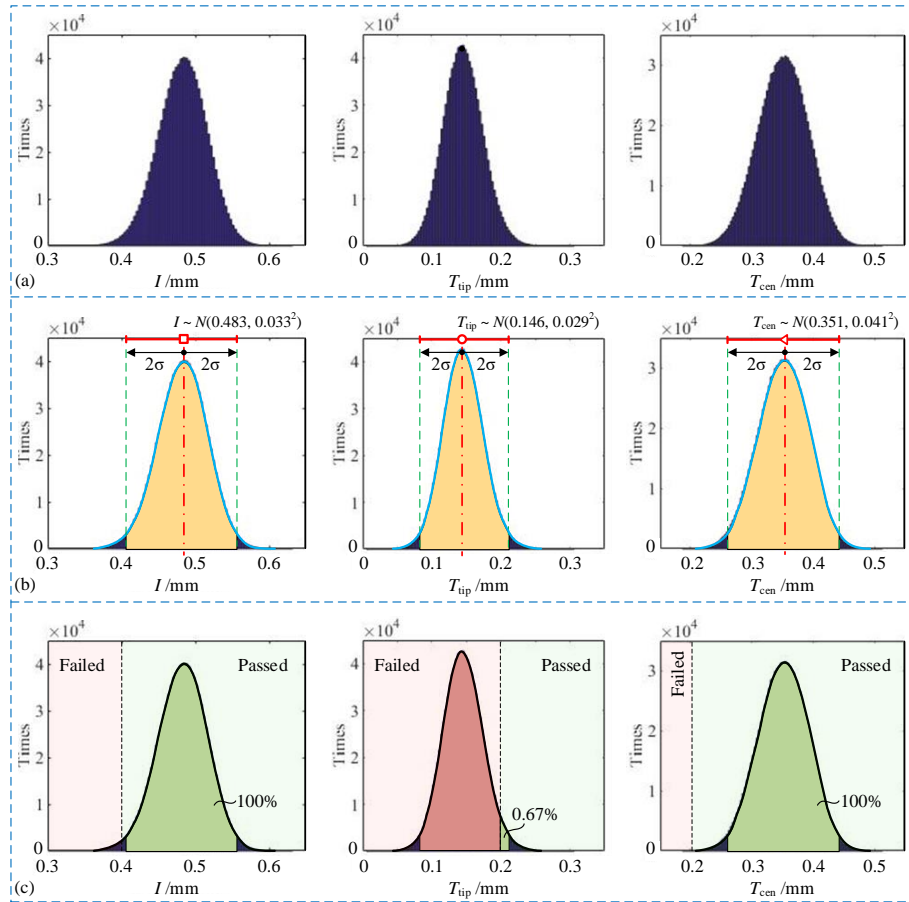


Figure 6.14 Schematic diagram of joint robustness evaluation procedures with the Monte Carlo method and the DNN

Taking the SPR joint 6-1 in **Table 6.3** as an example, detailed steps to calculate the joint robustness from the frequency distributions of quality indicators were demonstrated. **Figure 6.15** (a) shows the DNN predicted frequency distributions of the three quality indicators (i.e., I , T_{tip} and T_{cen}) after involving variations of the five joining parameters. Through data analysis, it was discovered that all the three indicators obey the normal distributions approximately, and the identified normal distribution functions were $I \sim N(0.483, 0.033^2)$, $T_{tip} \sim N(0.146, 0.029^2)$ and $T_{cen} \sim N(0.351, 0.041^2)$ as shown in **Figure 6.15** (b). By selecting the 2σ confidence interval (i.e., 95 % confidence level), the upper and lower boundaries of the variation range for each joint quality indicator were also obtained. The identified quality variation ranges for the I , T_{tip} and T_{cen} were 0.483 ± 0.066 mm, 0.146 ± 0.057 mm and 0.351 ± 0.081 mm respectively. Then, based on the selected joint quality standard (e.g., $I > 0.4$ mm and $T_{min} > 0.2$ mm), the robustness of I , T_{tip} and T_{cen} in the joint 6-1 were identified by calculating the probability that the quality indicator satisfies the quality standard (i.e., dark green regions in **Figure 6.15** (c)). The calculated robustness for the I , T_{tip} and T_{cen} were 100 %, 0.67 % and 100 % respectively. Finally, the smallest one (i.e., 0.67 %) was employed as the robustness of the joint 6-1. Due to the undesired robustness (<50 %), it can be concluded that the design of joint 6-1 is not acceptable, and the current rivet/die combination is not suitable for the 1.2 mm+1.0 mm sheet combination.

Table 6.3 Twelve SPR joints for the robustness evaluation

Joint no.	Stack /mm (AA5754)	Rivet length L_i /mm	Die diameter D_i /mm	Die depth H_i /mm
6-1	1.2+1.0	5.0	8.0	2.0
6-2	1.2+1.5	5.0	8.0	2.0
6-3	1.2+2.0	5.0	8.0	2.0
6-10	1.0+1.8	5.0	10.0	2.0
6-11	1.5+1.8	5.0	10.0	2.0
6-12	2.0+1.8	5.0	10.0	2.0
6-14	1.2+1.8	5.0	10.0	1.8
6-18	1.2+1.8	5.0	8.0	2.0
6-19	1.2+1.8	6.0	8.0	2.0
6-20	1.2+1.8	5.0	10.0	2.0
6-21	1.2+1.8	6.0	10.0	2.0
6-22	1.2+1.8	5.0	9.0	1.6

**Figure 6.15** Schematics of (a) frequency distributions, (b) identified normal distribution functions and (c) robustnesses of three quality indicators for the joint 6-1

Robustness of all the rest eleven joints in **Table 6.3** was also calculated to compare the reliabilities of SPR joints with different configurations as shown in **Figure 6.16**. **Figure 6.16** (a) illustrates the DNN predicted quality indicators with variation ranges and the experimentally tested quality indicators. It can be found that the predicted variation range of each quality indicator varies from joint to joint. This indicates that the SPR joints with different configurations have different sensitivities to the dimension variations of rivet, sheet and die. The greater the predicted variation range is, the more sensitive the joint quality

indicator is to the parameter variations. In addition, no obvious correlation was found between the predicted variation range and the magnitude of the quality indicator. By adding reference lines of the selected quality standard, the robustness of each designed joint can be roughly evaluated according to the relative position of the variation range and the quality reference line. **Figure 6.16** (b) shows the calculated robustness of the three quality indicators for the twelve SPR joints. Then, the predicted robustness of each designed SPR joint was obtained as shown in **Figure 6.16** (c). It can be seen that the designed joints 6-1, 6-11 and 6-12 are not acceptable because they have very low robustness and cannot meet the selected quality standard. The joints 6-14 and 6-20 satisfy the quality standard but are not reliable due to the relatively low robustness (i.e., 66.8 % for the 6-14 and 51.6 % for the 6-20) to the variations of the five joining parameters. The joints 6-2, 6-3, 6-10, 6-18, 6-19, 6-21 and 6-22 are very reliable considering their high robustness. Overall, by combining the DNN with the Monto Carlo method, both of the quality and robustness of a designed SPR joint can be quickly evaluated.

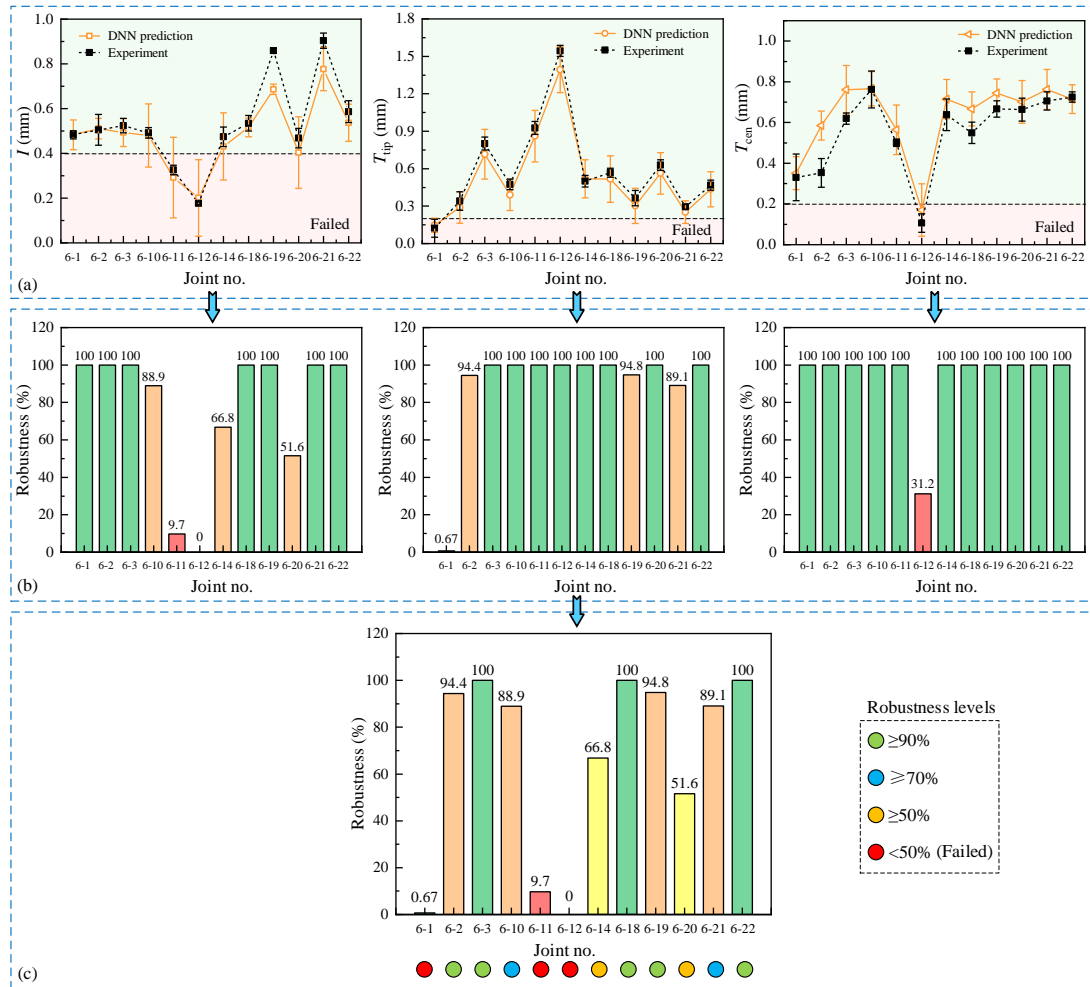


Figure 6.16 (a) Comparisons between the experimentally tested and DNN predicted joint quality indicators with variation ranges, (b) DNN predicted robustness of three quality indicators and (c) DNN predicted robustness of each SPR joint

6.4. Auto-selection of rivet/die combinations for multiple SPR sheet combinations

In this section, two approaches based on the DNN model were developed to simplify the selection of rivet/die and to minimise the number of rivet/die combinations required for multiple new sheet combinations. The joint robustness was considered in the first approach to improve the reliability of the designed new joints. Finally, the effectiveness of the proposed two rivet/die selection approaches was verified by experimental SPR tests.

6.4.1. Approach one

6.4.1.1. Method description

The first approach for quick selection of rivet/die was realized based on the developed DNN model and the Monte Carlo method. As shown in **Figure 6.17**, the performance of each rivet/die combination for all the target sheet combinations is firstly determined. Then, by comparing the performance of different rivet/die combinations, the minimum rivet/die combinations are identified. This selection approach considers the robustness of each SPR joint, and can be achieved manually or automatically.

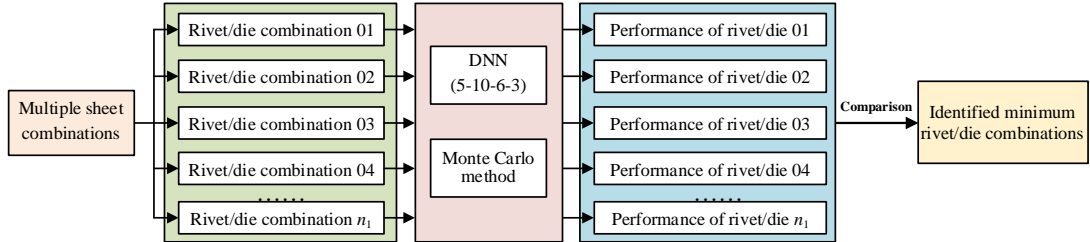


Figure 6.17 Schematic of the approach one for the rivet/die selection for multiple sheet combinations

For the manual method, the performance plot of a rivet/die combination for the target sheet combinations can be obtained straightforwardly from the DNN model, as shown in **Figure 6.18**. The manufacture tolerances of the rivet, sheets and die are considered with the Monte Carlo method to evaluate the robustness of each joint. By overlapping reference lines according to the selected joint quality standard (i.e black dot line for the I and blue/red line for the T_{\min}), the successfully connected sheet combinations with the specific rivet/die combination can be easily determined (green region) on the performance plot. Once the performance plots for all the potential rivet/die combinations are generated, the minimum suitable rivet/die combinations can be quickly selected by visually comparing these performance plots.

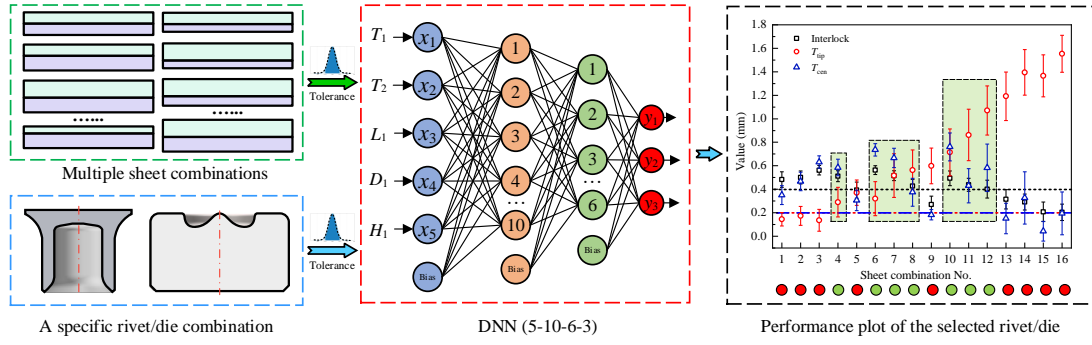


Figure 6.18 Performance plot of a specific rivet/die combination for new sheet combinations using the DNN

For the automatic method, a selection algorithm illustrated in **Figure 6.19** was proposed in this research to automatically compare the performances of different rivet/die combinations and identify the minimum rivet/die combinations. This effectively simplifies and speeds up the selection of rivet/die. For the convenience of practical applications, a GUI, which integrates the automatic selection algorithm and the rivet/die selection approach one, was developed in MATLAB 2020b and its performance was demonstrated in the next section.

The advantage of this approach is that the predicted values of the I , T_{cen} and T_{tip} can be accessed, and the robustness of each joint design can also be evaluated. Whilst the limitation is that the DNN model is always required during the selection process.

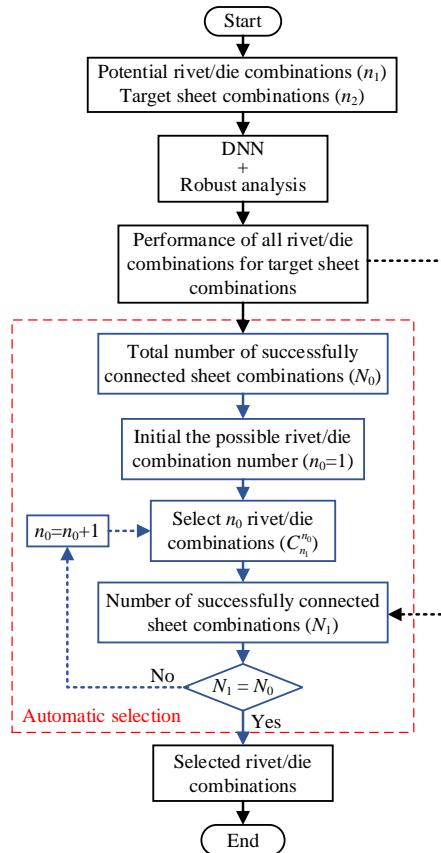


Figure 6.19 Schematic diagram for automatic selection of minimum rivet/die combinations for multiple sheet combinations

6.4.1.2. Performance demonstration

Taking the sixteen sheet combinations in **Table 6.4** as an example, performance of the approach one for the selection of rivet/die was demonstrated. The suitable rivet/die combinations would be identified from the eight frequently used rivet/die combinations for AA5754 sheets as listed in **Table 6.5**. The selected quality standard for the aluminium alloy AA5754 joints is $I > 0.4$ mm and $T_{\min} > 0.2$ mm [30]. Both of the manual method and automatic method were employed, and the identified rivet/die combinations for the target sixteen sheet combinations were compared.

Table 6.4 Sixteen sheet combinations (AA5754) to be self-piercing riveted

Sheet combination No.	Top sheet thickness T_1 /mm	Bottom sheet thickness T_2 /mm
1	1.2	1.0
2	1.2	1.2
3	1.0	1.5
4	1.2	1.5
5	1.5	1.2
6	1.0	1.8
7	1.2	1.8
8	1.5	1.5
9	1.8	1.2
10	1.2	2.0
11	1.5	1.8
12	1.5	2.0
13	1.8	1.8
14	1.8	2.0
15	2.0	1.8
16	2.0	2.0

Table 6.5 Eight rivet/die combinations frequently used for AA5754 sheets

Rivet/die combination No.	Rivet length L_1 /mm	Die diameter D_1 /mm	Die depth H_1 /mm
I	5.0	8.0	2.0
II	5.0	9.0	1.6
III	5.0	10.0	1.8
IV	5.0	10.0	2.0
V	6.0	8.0	2.0
VI	6.0	9.0	1.6
VII	6.0	10.0	1.8
VIII	6.0	10.0	2.0

Following the procedures illustrated in **Figure 6.18**, the performance plots of the eight different rivet/die combinations for the sixteen sheet combinations were obtained as shown in **Figure 6.20**. In this section, a SPR joint is regarded as a passed one (green background and labelled as a green circle) if the predicted quality of this SPR joint with designed nominal dimensions complies with the selected joint quality standard. Otherwise, a SPR joint is

regarded as a failed one (marked as a red circle). By comparing the numbers of passed joints with the eight rivet/die combinations, it was found that the rivet/die combinations with $L_1=5.0$ mm (i.e I~IV) showed poorer performances for the target sixteen sheet combinations than the rivet/die combinations with $L_1=6.0$ mm (i.e V~VIII). The main failure reason of SPR joints in **Figure 6.20** (a)~(d) is the unsatisfied interlock, whilst the main failure reason of SPR joints in **Figure 6.20** (e)~(h) is the too small remaining bottom sheet thickness (T_{cen} or T_{ip}). For the passed joints, the joint robustness can be roughly estimated according to the relative positions between the variation ranges of quality indicators and the quality reference lines.

For an easier selection of minimum rivet/die combinations, the prediction results of the 128 joints without considering the robustness are shown in **Figure 6.21** (a). By comparing the performances of different rivet/die combinations, two solutions were identified to connect all the sixteen sheet combinations with a minimum of three different rivet/die combinations. The rivet/die combinations II, IV and VI were selected as the Solution-01, whilst the rivet/die combinations II, III and VI were selected as the Solution-02. For the sixteen sheet combinations, some of them (i.e., sheet combinations No. 1~5, 8~9 and 13~16) can only be connected by one rivet/die combination (marked as blue background). The rest (i.e., the sheet combinations No. 6~7 and 10~12) can be successfully connected by two or three rivet/die combinations (marked as yellow background). The prediction results of the 128 joints considering the robustness are shown in **Figure 6.21** (b). By comparing the joint robustness in Solution-01 and Solution-02, it was found that Solution-02 was more reliable than Solution-01. Because higher joint robustness could be achieved for sheet combination No.3 with the rivet/die combination No. III than with the rivet/die combination No. IV. Based on the joint robustness results, a more reliable Solution-03 was obtained by slightly adjusting the Solution-02. The rivet/die combination No. II is more suitable for sheet combination No.7, whilst the rivet/die combination No. VI is more suitable for sheet combinations No.11~12. Meanwhile, it was also noticed that the designed joints with sheet combinations No.1~3 had relatively lower robustness than the remaining thirteen joints.

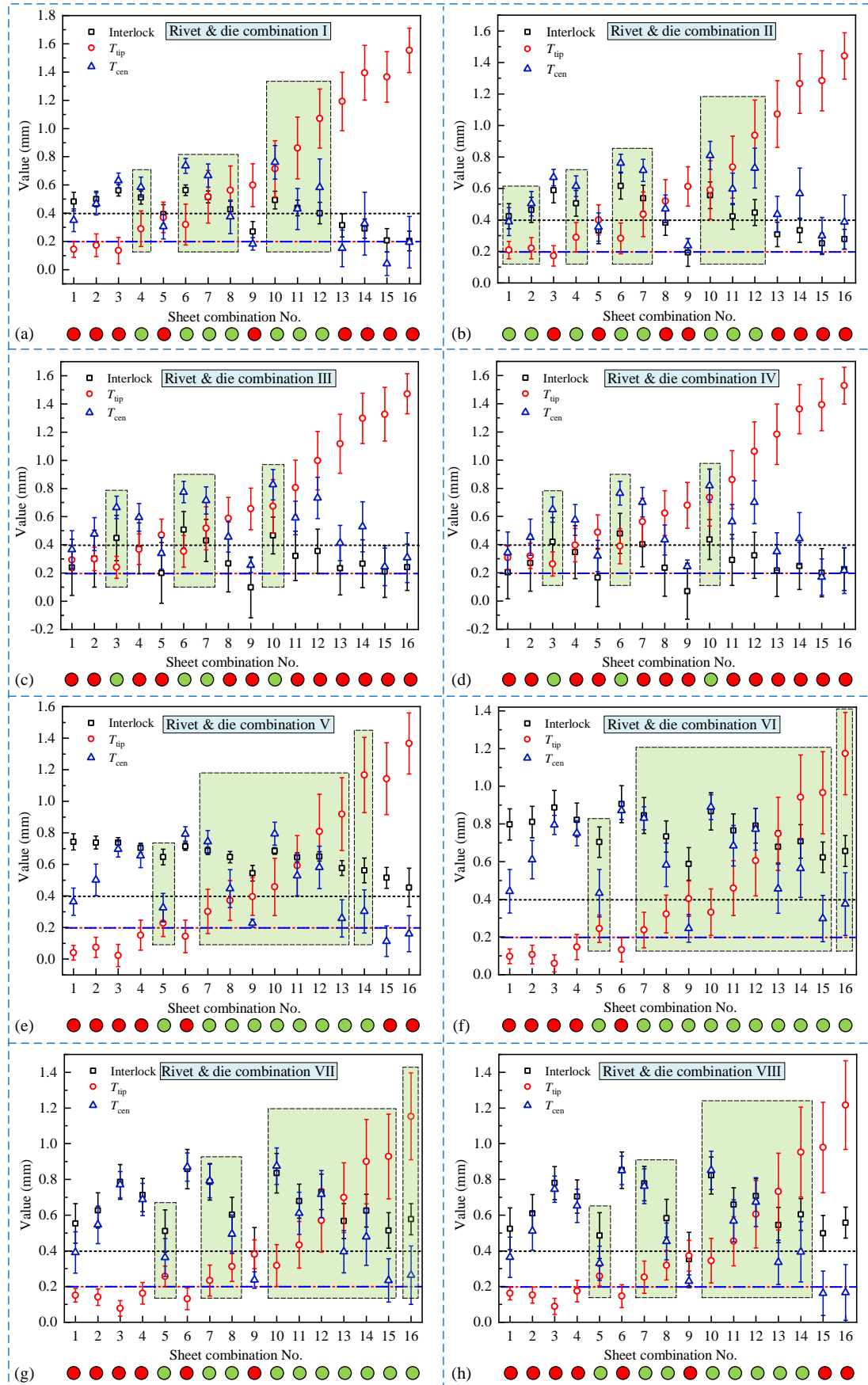


Figure 6.20 Performance plots of the eight different rivet/die combinations for the target sixteen sheet combinations

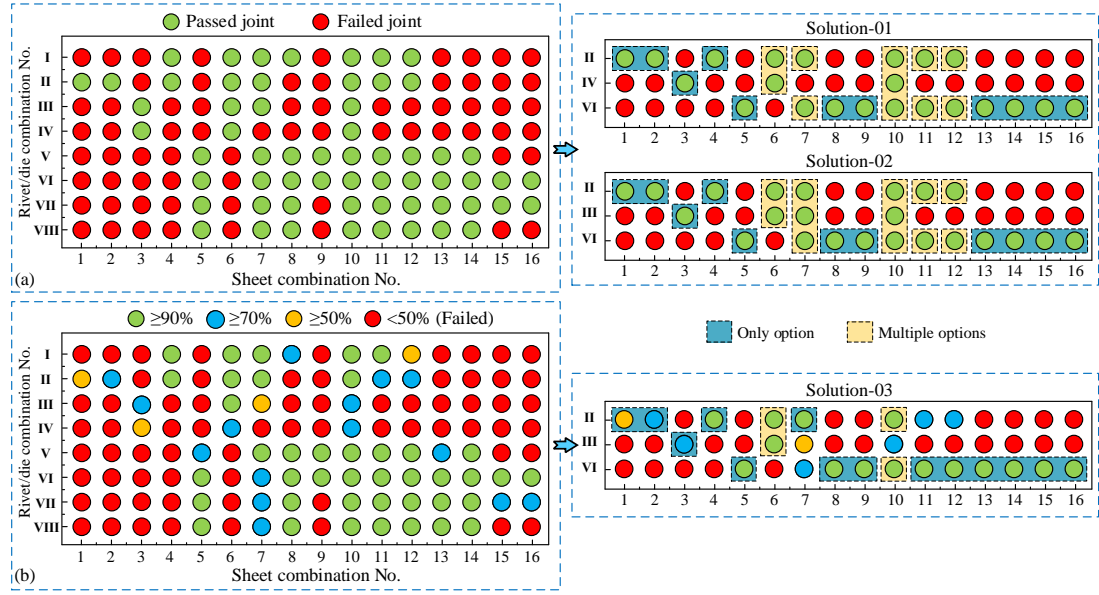


Figure 6.21 Performances of the eight different rivet/die combinations and corresponding solutions for the target sixteen sheet combinations (a) without considering the joint robustness and (b) considering the joint robustness

Figure 6.22 shows the developed GUI of rivet/die auto-selection system for multiple sheet combinations. By entering all the target sheet combinations and the potential rivet/die combinations, the GUI can call the DNN to predict the quality of each joint configuration and then automatically identify the minimum rivet/die combinations for the target multiple sheet combinations. It can be seen that the automatically selected rivet/die combinations are the same as that from the manually identified ones shown in **Figure 6.21**. This automatic system effectively reduces the complexity of rivet/die selection for new sheet combinations. From the above analysis, the effectiveness of the first rivet/die selection approach was fully demonstrated. The results indicated that it is very important to consider the joint robustness during the rivet/die selection for multiple sheet combinations.

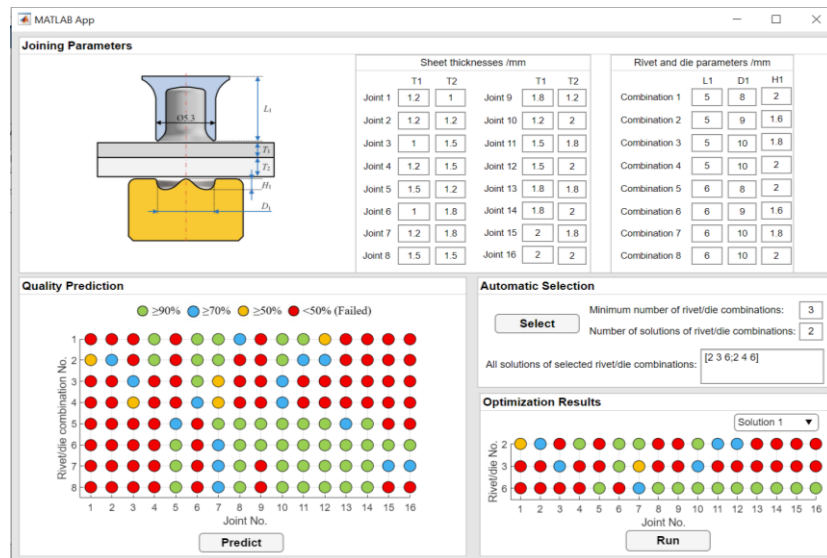


Figure 6.22 The GUI of automatic rivet/die selection for multiple sheet combinations

6.4.2. Approach two

6.4.2.1. Method description

The approach two for quick rivet/die selection was proposed on the basis of application range maps of different rivet/die combinations. As shown in **Figure 6.23**, this approach is divided into the preparation step and the application step. During the preparation step, the application range maps of potential rivet/die combinations are obtained with the developed DNN model. For a specific rivet/die combination, a large number of sheet combinations within the pre-defined design space (i.e., T_1 and T_2) are selected and the corresponding joint quality indicators are predicted with the DNN model. Then, each joint is classified into passed group or failed group according to the selected joint quality standard (e.g., $I > 0.4$ mm, and $T_{\min} > 0.2$ mm). Finally, the application range map for this rivet/die combination is obtained by plotting the joint quality results (green region for passed joints and orange regions for failed joints). During the application step, positions of the target sheet combinations are located on the application range map and the performance of the corresponding rivet/die combination is immediately evaluated (passed joints marked as green blocks and failed joints marked as red blocks). By comparing the performances of all the potential rivet/die combinations for the target sheet combinations, the minimum suitable rivet/die combinations can be easily identified.

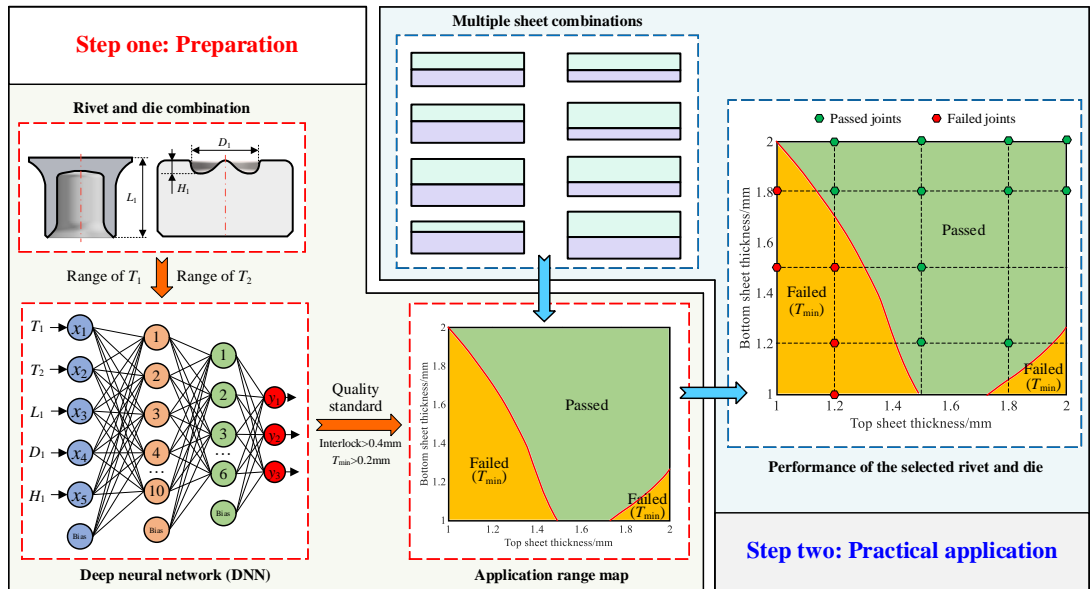


Figure 6.23 Application range map of a rivet/die combination and the corresponding performance for multiple sheet combinations

The advantage of this approach is that the DNN is not needed during the application step, where the application range maps for potential rivet/die combinations have already been established. It is very convenient to reuse these application range maps to quickly select rivet/die combinations for multiple sheets combinations in practice. Meanwhile, the failure

reason for each designed joint can also be identified from these maps. The limitation of this approach is that the specific predicted values of quality indicators for the designed joints are not accessible. The robustness of each SPR joint could only be estimated roughly according to its relative positions to the boundary lines.

6.4.2.2. Performance demonstration

Using the sixteen sheet combinations in **Table 6.4** and the eight rivet/die combinations in **Table 6.5**, performance of the approach two for the selection of rivet/die was also demonstrated. Following the procedures in **Figure 6.23**, the application range maps of the eight rivet/die combinations were successfully generated as shown in **Figure 6.24**. From the different patterns of these maps, it can be found that the rivet/die combinations No. I~IV ($L_1=5.0$ mm) are mainly workable for sheet combinations with a thin top sheet but a thick bottom sheet as shown in **Figure 6.24** (a)~(d). The rivet/die combinations No. I~II demonstrate wider application ranges than that of the rivet/die combinations No. III~IV. This is because the die cavity volume ($V_d=129.3$ mm³ or 142.8 mm³) is much greater than the rivet volume ($V_r=90.0$ mm³) in the rivet/die combinations No. III~IV, which has negative effects on the interlock formation. Rivet/die combinations with similar rivet and die cavity volumes more likely achieve better performance for the target sheet combinations and therefore have a broader joining range [45]. The rivet/die combinations No. V~VIII work well for sheet combinations with a large total sheet thickness as shown in **Figure 6.24** (e)~(h). Compared with the 5.0 mm long rivets, the 6.0 mm long rivets can effectively pierce into the bottom sheet to form a desired interlock. However, the 6.0 mm long rivets also increase the risk of undesired T_{\min} for sheet combinations with a relatively small total sheet thickness.

By locating the positions of the target sixteen sheet combinations on these application range maps, the performances of the eight rivet/die combinations can be easily identified as shown in **Figure 6.24**. The rivet/die combination No. VI successfully connected 11 of 16 sheet combinations as shown in **Figure 6.24** (f), and therefore was first selected. For the remaining 5 sheet combinations, the rivet/die combination No. II successfully connected 4 of them and thus was also selected. For the last sheet combination No.3, the rivet/die combination No. III was selected due to its better performance than the rivet/die combination No. IV. Therefore, the rivet/die combinations No. II, III and IV were quickly identified to successfully connect all the target sixteen sheet combinations. By overlapping the three application range maps in **Figure 6.24** (b)(c)(f), the overall application map of the selected three rivet/die combinations can be obtained as shown in **Figure 6.25** (a). It can be seen that some sheet combinations can only be connected by one rivet/die combinations, but the rest can be successfully joined by multiple rivet/die combinations. For clarity, all the joining results are illustrated in **Figure**

6.25 (b) and this identified solution is labelled as Solution-04. It can be found that the Solution-04 identified with the approach two is the same as the Solution-02 identified with the approach one. This proves the same effectiveness of the two different rivet/die selection approaches.

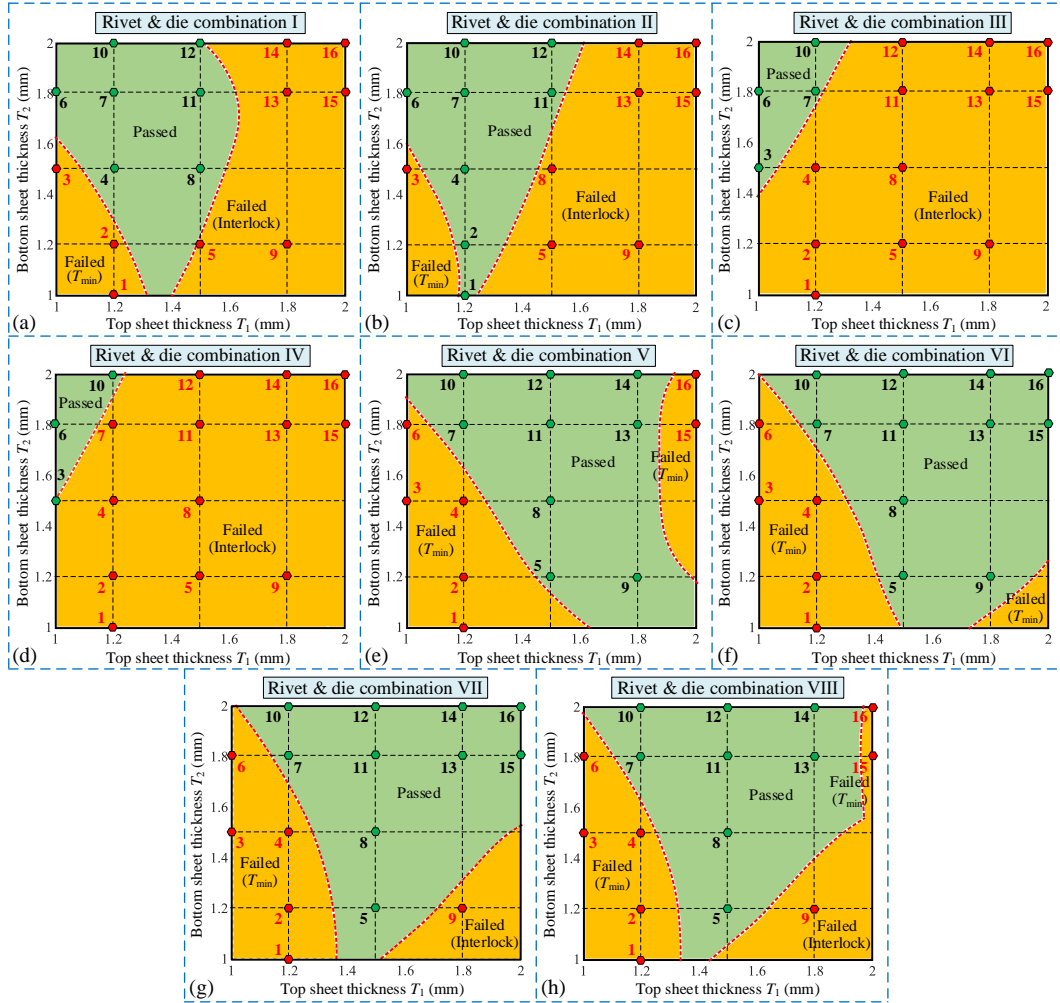


Figure 6.24 Application range maps of the eight rivet/die combinations and performance evaluations for the target sixteen different sheet combinations

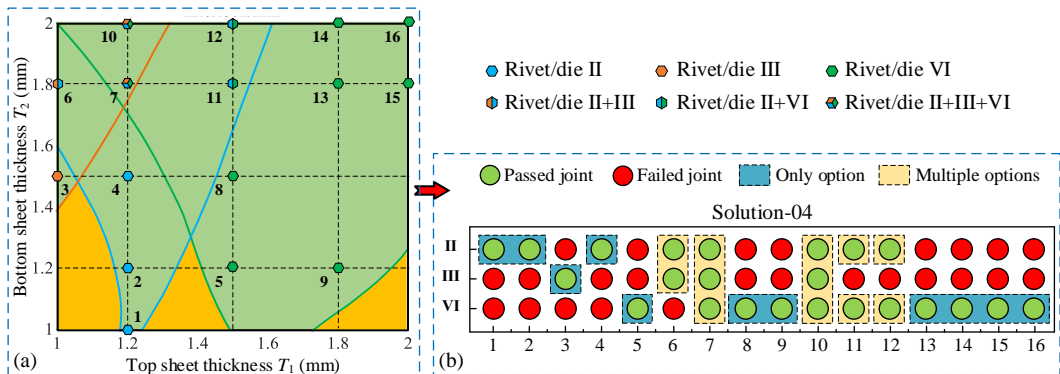


Figure 6.25 The identified minimum rivet/die combinations for the target sixteen sheet combinations with the approach two

6.4.3. Experimental validation

To validate the effectiveness of the proposed two rivet/die selection approaches, 32 of 128 joint configurations (i.e., $8 \times 16 = 128$) as listed in **Table 6.6** were experimentally tested. All the joint quality results from the experimental tests, DNN prediction and application range maps are recorded in **Table 6.6**. For an easier comparison, all these results are also illustrated in **Figure 6.26**. It can be seen that the quality of 31 joint configurations was successfully predicted with the DNN model and the application range maps. Only the quality of the joint 6-20 with sheet combination No.7 and rivet/die combination No. IV was not successfully predicted. Although the predicted interlock (0.38 mm) for this joint showed a reasonable agreement with that from the experimental test (0.47 mm), it is still difficult for the DNN to accurately assess the joint quality (passed or failed) if the joint quality indicator is close to the threshold value of the selected quality standard (e.g., $I > 0.4$ mm, $T_{\min} > 0.2$ mm). Overall, the DNN and application range maps show very good prediction performances for the joint quality. Therefore, it is reasonable to believe that the proposed two approaches are capable of accurately identifying the minimum suitable rivet/die combinations for the target multiple sheet combinations.

With the proposed two approaches, the cycle time of rivet/die selection can be dramatically shortened, and the number of experimental SPR tests can also be significantly reduced. The dependence on engineers' experience for new joint design can also be effectively minimised. Therefore, the two selection methods are promising to change the way of how engineers assess and implement new joint designs in the industry sector, especially the automotive industry.

Table 6.6 Validation of the proposed two rivet/die selection approaches

Joint no.	Joint configuration		Experimental results /mm				DNN prediction results /mm				Application Range map
	Sheet combination No.	Rivet/die combination No.	I	T_{tip}	T_{cen}	Joint quality	I	T_{tip}	T_{cen}	Joint quality	Joint quality
6-1	1	I	0.48	0.12	0.33	Failed	0.48	0.14	0.35	Failed	Failed
6-2	4	I	0.51	0.34	0.35	Passed	0.51	0.29	0.59	Passed	Passed
6-7	6	I	0.59	0.39	0.70	Passed	0.56	0.32	0.74	Passed	Passed
6-18	7	I	0.53	0.57	0.55	Passed	0.52	0.51	0.67	Passed	Passed
6-3	10	I	0.52	0.80	0.62	Passed	0.50	0.72	0.75	Passed	Passed
6-8	11	I	0.41	0.90	0.22	Passed	0.44	0.86	0.42	Passed	Passed
6-9	15	I	0.30	1.51	0.02	Failed	0.20	1.37	0.03	Failed	Failed
6-23	1	II	0.43	0.23	0.32	Passed	0.42	0.21	0.39	Passed	Passed
6-24	2	II	0.50	0.23	0.37	Passed	0.46	0.22	0.51	Passed	Passed
6-25	4	II	0.51	0.35	0.52	Passed	0.50	0.29	0.61	Passed	Passed
6-22	7	II	0.59	0.47	0.73	Passed	0.53	0.43	0.71	Passed	Passed
6-26	10	II	0.66	0.71	0.70	Passed	0.55	0.58	0.81	Passed	Passed
6-13	2	III	0.36	0.24	0.49	Failed	0.28	0.30	0.47	Failed	Failed
6-14	7	III	0.47	0.50	0.64	Passed	0.41	0.52	0.70	Passed	Passed
6-15	8	III	0.33	0.63	0.48	Failed	0.25	0.59	0.45	Failed	Failed
6-16	9	III	0.13	0.63	0.19	Failed	0.09	0.66	0.25	Failed	Failed
6-17	13	III	0.26	1.26	0.21	Failed	0.22	1.12	0.41	Failed	Failed

6-4	1	IV	0.16	0.27	0.41	Failed	0.19	0.31	0.33	Failed	Failed
6-5	4	IV	0.34	0.41	0.56	Failed	0.33	0.40	0.56	Failed	Failed
6-10	6	IV	0.49	0.47	0.76	Passed	0.46	0.39	0.75	Passed	Passed
6-20	7	IV	0.47	0.63	0.66	Passed	0.38	0.57	0.69	Failed	Failed
6-6	10	IV	0.49	0.83	0.68	Passed	0.41	0.74	0.8	Passed	Passed
6-11	11	IV	0.33	0.93	0.50	Failed	0.27	0.87	0.55	Failed	Failed
6-12	15	IV	0.18	1.54	0.11	Failed	0.19	1.40	0.16	Failed	Failed
6-19	7	V	0.86	0.36	0.67	Passed	0.69	0.30	0.75	Passed	Passed
6-27	5	VI	0.70	0.22	0.33	Passed	0.70	0.24	0.43	Passed	Passed
6-28	8	VI	0.77	0.46	0.69	Passed	0.73	0.32	0.58	Passed	Passed
6-29	10	VI	0.95	0.43	0.88	Passed	0.86	0.33	0.89	Passed	Passed
6-30	12	VI	0.92	0.77	0.53	Passed	0.79	0.60	0.77	Passed	Passed
6-31	14	VI	0.71	1.42	0.39	Passed	0.71	0.94	0.56	Passed	Passed
6-32	16	VI	0.65	1.41	0.42	Passed	0.65	1.18	0.37	Passed	Passed
6-21	7	VIII	0.90	0.29	0.71	Passed	0.76	0.25	0.75	Passed	Passed

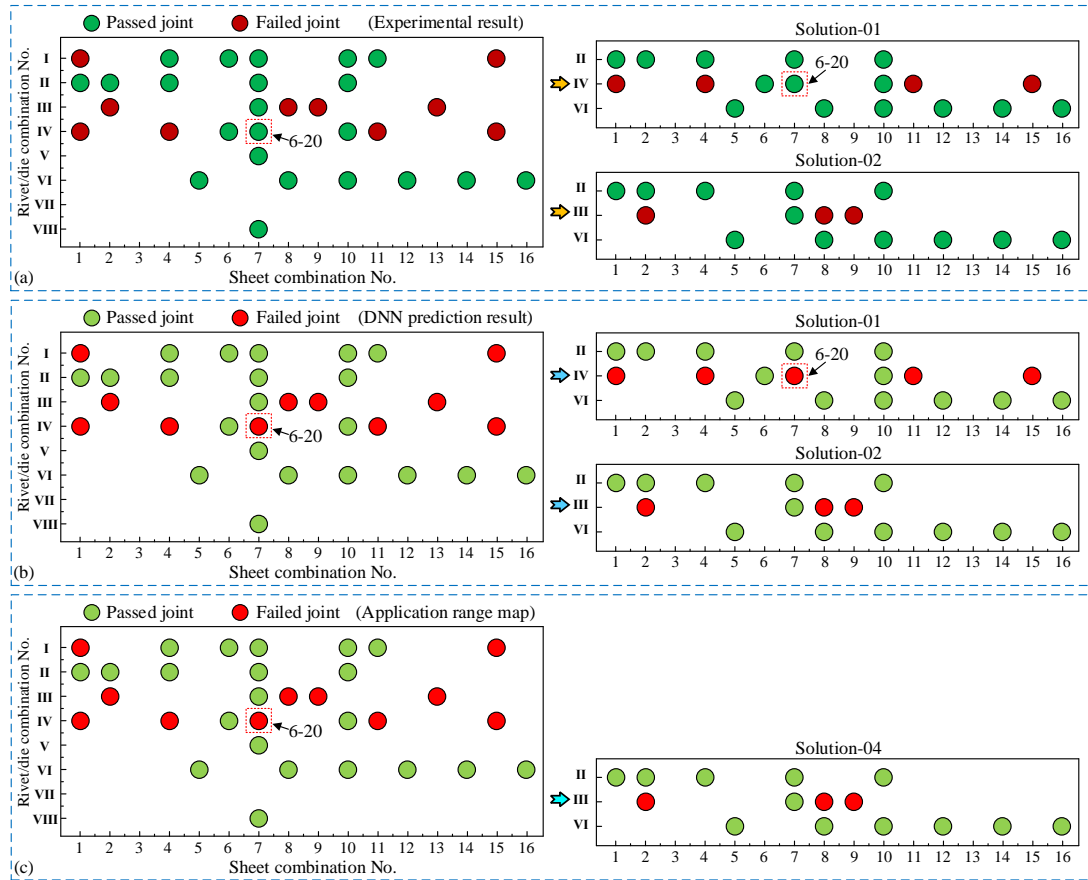


Figure 6.26 Comparisons between the (a) experimentally tested, (b) DNN predicted and (c) application range maps identified joint quality results

6.5. Summary

In this chapter, a high accuracy and fast response prediction tool for SPR joint quality was developed with the DNN. Robustness analysis was also carried out to assess the reliability of each SPR joint during the joint design process. In addition, two novel approaches were proposed to quickly and automatically select the minimum suitable rivet/die combinations for multiple sheet combinations. The main conclusions are summarised below:

1. The DNN with two hidden layers (5-10-6-3) achieved the best prediction performance for the studied SPR joints. The calculated MAE and MAPE for the interlock (I) between the experimental SPR test and the DNN were 0.053 mm and 13.2 % respectively. The MAE and MAPE for the T_{tip} were 0.062 mm and 11.1 %. The corresponding MAE and MAPE for the T_{cen} were 0.073 mm and 24.1 %.
2. By combining the developed DNN model with the Monte Carlo method, the robustness of designed SPR joints can be conveniently assessed. Manufacturing tolerances of rivet, sheets and die could impose obvious influences on the final joint quality, and therefore the joint robustness should be considered carefully during the selection of rivet/die for new sheet combinations.
3. With the DNN model, Monte Carlo method and the proposed automatic selection algorithm, the minimum rivet/die combinations for multiple sheet combinations can be quickly and automatically identified. The joint robustness can be considered when using this selection approach. The predicted values of the I , T_{cen} and T_{tip} for each designed joint are also accessible.
4. With the application range maps of different rivet/die combinations, the minimum rivet/die combinations for multiple sheet combinations can also be quickly identified. This approach is easy-to-use because it does not need the DNN model during the application stage. However, the joint robustness could only be roughly evaluated, and the specific values of quality indicators are not accessible.
5. The proposed two approaches apparently simplify the selection of rivet/die for multiple new sheet combinations, and reduce the dependence on engineers' joint design experience. The time required for design and implementation of multiple SPR joints can also be significantly reduced.

7. Conclusions and future work

This chapter summarises the major research conclusions from this thesis, and the potential future work or research directions that might be beneficial for the development of the SPR technique.

7.1. Research conclusions

This thesis provides in-depth research on the development of fast quality prediction tools for SPR joints, and on the simplification of rivet/die selection during the new joint design process. A FEA model of SPR process was firstly developed and utilized to acquire enough joint quality data for training and testing of the fast quality prediction models. Then, three types of models, including the multiple regression model, the SNN model and the DNN model, were employed to develop fast quality prediction tools, and their performances were evaluated through experimental SPR tests. With the developed regression models and the SNNs, interaction effects between the rivet, sheet and die parameters on the final SPR joint quality indicators were systematically studied to facilitate the selection of rivet and die. By combining the developed SNNs with the GA, optimization of the rivet and die parameters for new sheet combinations was also conducted to maximise the joint quality. With the help of the developed DNN model and the Monte Carlo method, procedures to evaluate the robustness of designed SPR joints were proposed. Meanwhile, two novel approaches suitable for inexperienced engineers to simplify the selection of rivet/die for multiple new sheet combinations were also proposed in combination with the DNN. Moreover, the formation mechanism of SPR joints with varying joining parameters was also numerically investigated with the FEA model.

The main conclusions from this thesis are summarised as follows:

1. The developed FEA model for SPR process was proved capable of predicting the final quality of joints with AA5754 sheets, and thus is an excellent alternative to experimental SPR tests to collect joint quality data for the development of fast quality prediction tools. The FEA model accurately captured the deformation behaviours of rivet and sheets, the changing trend of riveting force and the formation processes of joint quality indicators. Thus, it is also a perfect substitute for the interrupted experimental SPR test to investigate the influences of different joining parameters on the SPR joint formation. Meanwhile, the results also indicated that the FEA model is a powerful tool to facilitate the analysis of experimental SPR tests.

2. For the studied joint configurations, increment of the top sheet thickness (T_1) showed negative influences on the interlock formation by mainly affecting the position of the inner interlock boundary, negative effects on the formation of remaining bottom sheet thickness at the joint centre (T_{cen}) and positive influences on the remaining bottom sheet thickness under the rivet tip (T_{tip}). Increment of the bottom sheet thickness (T_2) was beneficial for the interlock formation by affecting both the inner and outer interlock boundaries, and imposed positive influences on the formations of the T_{cen} and T_{tip} . Increment of the rivet length (L_1) also had positive influences on the interlock formation by mainly altering the position of the outer interlock boundary, whilst showed limited influences on the T_{cen} and negative influences on the T_{tip} . The rapid decline of the T_{cen} mainly occurred before the top sheet was completely penetrated and after the rivet cavity was fully filled. In addition, when piercing the top sheet, flare behaviour of the rivet shank was significantly affected by the T_1 , but just slightly affected by the T_2 and L_1 . When piercing the bottom sheet, the flare speed of the rivet shank decreased with the increment of the T_1 and T_2 , but remained almost constant with the increment of the L_1 .
3. The developed multiple regression models, SNNs and DNN demonstrated good performances in fast prediction of SPR joint quality. Compared with the multiple regression model, the SNN and DNN have stronger fitting abilities and can conveniently involve more inputs (i.e., joining parameters) and outputs (i.e., joint quality indicators). At the same time, they also have simpler development procedures and are more suitable to be used to develop fast quality prediction tools. Furthermore, the DNN has greater fitting ability than that of the SNN and can achieve higher accuracy when predicting multiple quality indicators with a single network. Different from the FEA model, all the proposed fast quality prediction tools do not require professional knowledge to run and can be conveniently used by general engineers from the industry sector. They are helpful to speed up the design process of new SPR joints, and lay a foundation for the quick joint robustness evaluation, for the optimization of rivet and die parameters and for the simplification of rivet and die selection.
4. By plotting contour graphs of quality indicators with the developed fast quality prediction tools (i.e., regression models and SNNs), it is very convenient to analyse the interaction effects between different rivet, sheet and die parameters on the final joint quality. Under the studied joint configurations, significant interaction effects on the interlock were identified between the D_1 and any of the other three parameters (T_2 , L_1 and H_1), whilst only the T_1 and T_2 demonstrated apparent interaction effects on the T_{cen} and T_{tip} . The results also indicated that strong interaction effects between different joining parameters were highly associated with the Die-to-Rivet volume ratio (R) and the sheet rigidity, which directly affect the deformations of rivet and sheets, and therefore alter the formation of

joint quality indicators. It was found that a greater interlock was more likely to be achieved when the R was close to 1.0.

5. By combining the developed SNNs with the GA, the proposed optimization approach effectively simplifies the selection of rivet and die for new sheet combinations. With the generated Pareto optimal solution set, the suitable rivet and die parameters can be easily and quickly determined to achieve the optimal joint quality according to different quality standards. Moreover, with the help of the developed DNN model and the Monte Carlo method, the manufacturing tolerances of rivet, sheets and die were successfully considered to assess the robustness of designed SPR joints. This provides a simple but effective way to predict the joint robustness, and offers useful information for the selection of rivet/die to improve the design reliability of new SPR joints.
6. Finally, the proposed two approaches for rivet/die selection were proved effective to apparently simplify the selection of rivet/die for multiple new sheet combinations, and to reduce the dependence on the engineers' experience. The first approach, which was developed based on the DNN model, the Monte Carlo method and the proposed automatic selection algorithm, successfully takes the joint robustness into account and can automatically identify the minimum rivet/die combinations for multiple new sheet combinations. The predicted values of joint quality indicators (i.e., I , T_{cen} and T_{tip}) for each designed joint are also accessible. The second approach, which was developed based on the application range maps of different rivet/die combinations, can also be used to quickly determine the minimum rivet/die combinations. It is convenient to use because the DNN model is not needed anymore during the application stage. However, the joint robustness can only be evaluated roughly with this method, and the specific quality indicator values for each joint are not accessible.

7.2. Future work

Based on the work process and research results presented in this thesis, some potential research topics/directions that might be beneficial for the development of the SPR technique are summarised as follows:

1. In practical applications, the rivet head height (H) is usually adjusted within the allowed range (i.e., $-0.5 \sim +0.3$ mm) to optimize the SPR joint quality as shown in **Figure 7.1**. The fast quality prediction models developed in this thesis can only predict the joint quality when the H equals 0.0 mm. To further improve the application range of the quality prediction tools, it is necessary to take the H into account when developing the prediction tools.

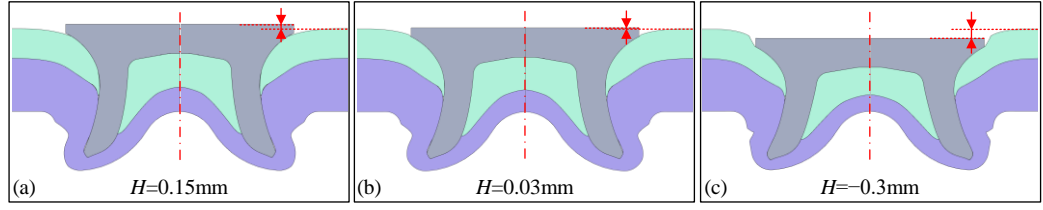


Figure 7.1 Cross-sectional profiles of SPR joints with different rivet head heights

2. The quality prediction models and rivet/die selection approaches in this thesis are designed for SPR joints with AA5754 sheets and the pip die. Other sheet materials (e.g., AA6xxx series, magnesium alloy and steel), rivet parameters (e.g., the rivet hardness level and rivet diameter) and die types (e.g., flat die) can be involved in the prediction models to widen their application area. Meanwhile, ranges of the joining parameters in the proposed models can also be further enlarged to meet the scope of practical applications.
3. Compared with the interlock, the prediction of T_{\min} is much more difficult due to its uncertain positions. The remaining bottom sheet thicknesses at two locations where the T_{\min} most likely appears (i.e., under the rivet tip and at the joint centre as shown in **Figure 7.2** (a)) were predicted by the proposed prediction models. However, in practice, the T_{\min} can appear at any position on the deformed bottom sheet. To accurately predict the magnitude of T_{\min} , the remaining bottom sheet thickness at more locations as shown in **Figure 7.2** (b) can be involved in the prediction model.

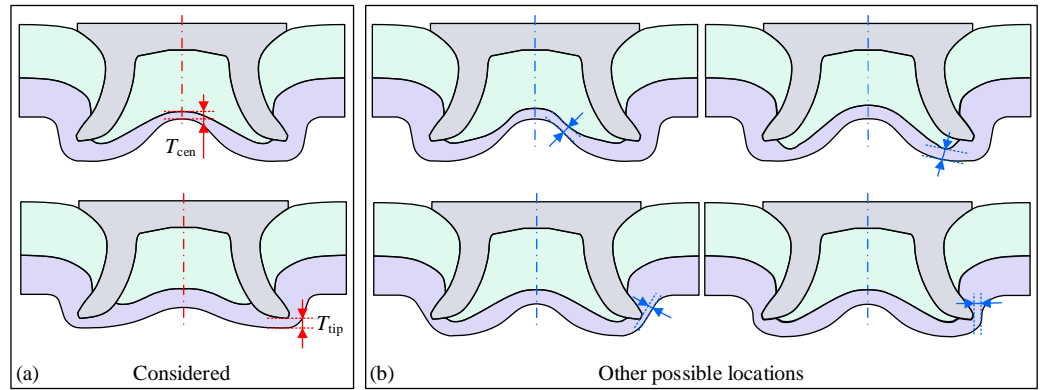


Figure 7.2 Schematics of locations the T_{\min} may appear (a) two locations considered in this thesis and (b) other possible locations can be further involved

4. With the increment of inputs (i.e., joining parameters) and outputs (i.e., joint quality indicators) that are involved in the fast quality prediction model, the size of joint quality data required for model training and testing will significantly increase. Manually establishing all the FEA models and extracting all the simulation results will be a time-consuming job. To simplify the data collection process and speed up the prediction model development, it is necessary to propose a strategy to automatically build new simulations and extract the required joint quality data (e.g., co-simulation between Simufact.Forming

and Matlab [181]) as shown in **Figure 7.3**. This will be a big contribution to not only the development of fast quality prediction tools but also the auto-selection of rivet and die.

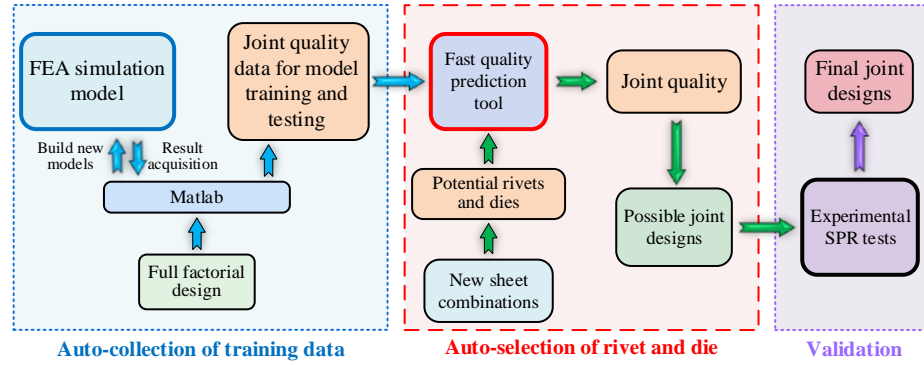


Figure 7.3 Schematic diagram of procedures to facilitate the rivet and die selection in practical applications

5. This thesis developed fast joint quality prediction models to facilitate the design of new SPR joints. Following the same procedures, fast prediction models for joint mechanical strength can also be developed. To achieve this goal, FEA model for joint mechanical strength should be firstly developed to collect necessary training and testing data, then fast prediction models based on ANN can be established as shown in **Figure 7.4**.

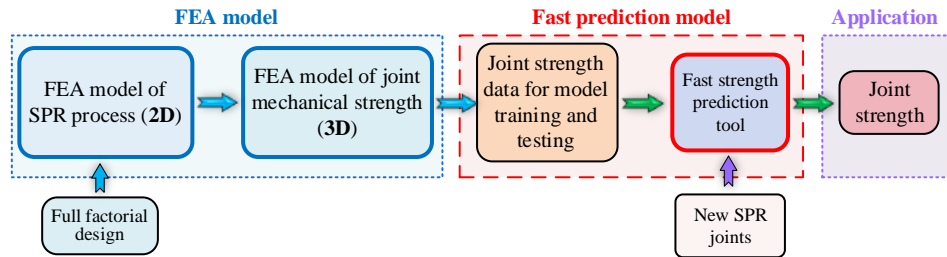


Figure 7.4 Schematic diagram for the development and application of fast joint mechanical strength prediction model

6. To facilitate practical applications in the industry sector, an expert system integrating the proposed fast joint quality prediction models and rivet/die selection strategies can be developed. In future, more prediction models for different sheet materials can be gradually developed and integrated into this expert system to widen its application range and enhance its performance.

References

- [1] M.Á.P. Salaverría, Intensive use of aluminium in car body construction, 12th EAEC Eur. Automot. Congr. Bratislava. (2009) 15.
- [2] D. Li, A. Chrysanthou, I. Patel, G. Williams, Self-piercing riveting-a review, *Int. J. Adv. Manuf. Technol.* 92 (2017) 1777–1824. <https://doi.org/10.1007/s00170-017-0156-x>.
- [3] Z. Wang, Survey of optimization methods for BIW lightweight design, *MATEC Web Conf.* 128 (2017) 05002. <https://doi.org/10.1051/mateconf/201712805002>.
- [4] M. Tisza, I. Czinege, Comparative study of the application of steels and aluminium in lightweight production of automotive parts, *Int. J. Light. Mater. Manuf.* 1 (2018) 229–238. <https://doi.org/10.1016/j.ijlmm.2018.09.001>.
- [5] A. Kelkar, R. Roth, J. Clark, Automobile bodies: Can aluminum be an economical alternative to steel?, *Jom.* 53 (2001) 28–32. <https://doi.org/10.1007/s11837-001-0131-7>.
- [6] R.J. Urbance, F. Field, R. Kirchain, R. Roth, J.P. Clark, Market model simulation: The impact of increased automotive interest in magnesium, *Jom.* 54 (2002) 25–33. <https://doi.org/10.1007/BF02711863>.
- [7] J. Agarwal, S. Sahoo, S. Mohanty, S.K. Nayak, Progress of novel techniques for lightweight automobile applications through innovative eco-friendly composite materials: A review, *J. Thermoplast. Compos. Mater.* 33 (2020) 978–1013. <https://doi.org/10.1177/0892705718815530>.
- [8] K. Mori, Y. Abe, T. Kato, Mechanism of superiority of fatigue strength for aluminium alloy sheets joined by mechanical clinching and self-pierce riveting, *J. Mater. Process. Technol.* 212 (2012) 1900–1905. <https://doi.org/10.1016/j.jmatprotec.2012.04.017>.
- [9] W.S. Miller, L. Zhuang, J. Bottema, A.J. Wittebrood, P. De Smet, A. Haszler, A. Vieregge, Recent development in aluminium alloys for the automotive industry, *Mater. Sci. Eng. A.* 280 (2000) 37–49. [https://doi.org/10.1016/S0921-5093\(99\)00653-X](https://doi.org/10.1016/S0921-5093(99)00653-X).
- [10] A. Weber, Assembling ford’s aluminum wonder truck, *Assembly.* 58 (2015).
- [11] Y. Abe, T. Kato, K. Mori, Joinability of aluminium alloy and mild steel sheets by self piercing rivet, *J. Mater. Process. Technol.* 177 (2006) 417–421. <https://doi.org/10.1016/j.jmatprotec.2006.04.029>.

-
- [12] A. Kochan, Audi moves forward with all-aluminium cars, *Assem. Autom.* 20 (2000) 132–135. <https://doi.org/10.1108/01445150010321751>.
- [13] P. Reinhert, The new Jaguar XJ - The first all aluminium car in monocoque design, *Alum. Int. Today.* 16 (2004) 21–24. <http://www.scopus.com/inward/record.url?eid=2-s2.0-1042292857&partnerID=40&md5=bd6d1e6bb3d44dcbfa94d78a09441aac>.
- [14] M. White, Aluminium used in Jaguar Land Rover vehicles helps meet sustainability targets, *Alum. Int. Today.* 27 (2015) 24–25. <http://0-search.proquest.com.pugwash.lib.warwick.ac.uk/docview/1656619789?accountid=14888>.
- [15] Applications - Car body – Body structures, *Alum. Automot. Man.* 6 (2013) 1–84. https://www.european-aluminium.eu/media/1543/1_aam_body-structures.pdf.
- [16] S.M. Manladan, F. Yusof, S. Ramesh, M. Fadzil, Z. Luo, S. Ao, A review on resistance spot welding of aluminum alloys, *Int. J. Adv. Manuf. Technol.* 90 (2017) 605–634. <https://doi.org/10.1007/s00170-016-9225-9>.
- [17] A. Ambroziak, M. Korzeniowski, Using resistance spot welding for joining aluminium elements in automotive industry, *Arch. Civ. Mech. Eng.* 10 (2010) 5–13. [https://doi.org/10.1016/s1644-9665\(12\)60126-5](https://doi.org/10.1016/s1644-9665(12)60126-5).
- [18] Z. Rao, L. Ou, Y. Wang, P.C. Wang, A self-piercing-through riveting method for joining of discontinuous carbon fiber reinforced nylon 6 composite, *Compos. Struct.* 237 (2020) 111841. <https://doi.org/10.1016/j.compstruct.2019.111841>.
- [19] X. He, L. Zhao, C. Deng, B. Xing, F. Gu, A. Ball, Self-piercing riveting of similar and dissimilar metal sheets of aluminum alloy and copper alloy, *Mater. Des.* 65 (2015) 923–933. <https://doi.org/10.1016/j.matdes.2014.10.002>.
- [20] W. Cai, P.C. Wang, W. Yang, Assembly dimensional prediction for self-piercing riveted aluminum panels, *Int. J. Mach. Tools Manuf.* 45 (2005) 695–704. <https://doi.org/10.1016/j.ijmachtools.2004.09.023>.
- [21] B. Wang, C. Hao, J. Zhang, H. Zhang, A New Self-Piercing Riveting Process and Strength Evaluation, *J. Manuf. Sci. Eng.* 128 (2006) 580–587. <https://doi.org/10.1115/1.2137746>.
- [22] L. Han, M. Thornton, M. Shergold, A comparison of the mechanical behaviour of self-piercing riveted and resistance spot welded aluminium sheets for the automotive industry, *Mater. Des.* 31 (2010) 1457–1467. <https://doi.org/10.1016/j.matdes.2009.08.031>.

- [23] P. Briskham, N. Blundell, L. Han, R. Hewitt, K. Young, D. Boomer, Comparison of self-pierce riveting, resistance spot welding and spot friction joining for aluminium automotive sheet, SAE Tech. Pap. (2006). <https://doi.org/10.4271/2006-01-0774>.
- [24] H.R. Kotadia, A. Rahnema, I.R. Sohn, J. Kim, S. Sridhar, Performance of dissimilar metal Self-Piercing Riveting (SPR) joint and coating behaviour under corrosive environment, J. Manuf. Process. 39 (2019) 259–270. <https://doi.org/10.1016/j.jmapro.2019.02.024>.
- [25] J. Mortimer, Jaguar uses X350 car to pioneer use of self-piercing rivets, Ind. Robot An Int. J. 28 (2001) 192–198. <https://doi.org/10.1108/01439910110389344>.
- [26] L. Han, Y.K. Chen, A. Chrysanthou, J.M. O’Sullivan, Self-pierce riveting - A new way for joining structures, Am. Soc. Mech. Eng. Press. Vessel. Pip. Div. PVP. 446 (2002). <https://doi.org/10.1115/PVP2002-1495>.
- [27] W. Leitemann, J. Christlein, The 2nd-generation Audi Space Frame of the A2: A trendsetting all- aluminium car body concept in a compact class car, in: Seoul 2000 FISITA World Automot. Congr., Seoul, Korea, 2000: pp. 1–5.
- [28] R. Haque, Quality of self-piercing riveting (SPR) joints from cross-sectional perspective: A review, Arch. Civ. Mech. Eng. 18 (2018) 83–93. <https://doi.org/10.1016/J.ACME.2017.06.003>.
- [29] Y. Liu, L. Han, H. Zhao, X. Liu, Evaluation and correction of cutting position’s effects on quality indicator measurement of self-piercing riveted joint, Mater. Des. (2021) 109583. <https://doi.org/10.1016/J.MATDES.2021.109583>.
- [30] L. Han, M. Thornton, D. Li, M. Shergold, Effect of setting velocity on self-piercing riveting process and joint behaviour for automotive applications, SAE Tech. Pap. (2010). <https://doi.org/10.4271/2010-01-0966>.
- [31] D.H. Kam, T.E. Jeong, M.G. Kim, J. Shin, Self-piercing riveted joint of vibration-damping steel and aluminum alloy, Appl. Sci. 9 (2019) 4575. <https://doi.org/10.3390/app9214575>.
- [32] N.H. Hoang, R. Porcaro, M. Langseth, A.G. Hanssen, Self-piercing riveting connections using aluminium rivets, Int. J. Solids Struct. 47 (2010) 427–439. <https://doi.org/10.1016/j.ijsolstr.2009.10.009>.
- [33] X. Zhang, X. He, B. Xing, W. Wei, J. Lu, Quasi-static and fatigue characteristics of self-piercing riveted joints in dissimilar aluminium-lithium alloy and titanium sheets, J. Mater. Res. Technol. 9 (2020) 5699–5711. <https://doi.org/10.1016/j.jmrt.2020.03.095>.

-
- [34] D. Li, L. Han, M. Thornton, M. Shergold, An evaluation of quality and performance of self-piercing riveted high strength aluminium alloy AA6008 for automotive applications, SAE Tech. Pap. (2010). <https://doi.org/10.4271/2010-01-0223>.
- [35] Y. Xu, Effects of factors on physical attributes of self-piercing riveted joints, Sci. Technol. Weld. Join. 11 (2006) 666–671. <https://doi.org/10.1179/174329306X131866>.
- [36] Y. Abe, T. Kato, K. Mori, Self-piercing riveting of high tensile strength steel and aluminium alloy sheets using conventional rivet and die, J. Mater. Process. Technol. 209 (2009) 3914–3922. <https://doi.org/10.1016/j.jmatprotec.2008.09.007>.
- [37] L. Han, A. Chrysanthou, Evaluation of quality and behaviour of self-piercing riveted aluminium to high strength low alloy sheets with different surface coatings, Mater. Des. 29 (2008) 458–468. <https://doi.org/10.1016/j.matdes.2006.12.020>.
- [38] B. Uhe, C.M. Kuball, M. Merklein, G. Meschut, Improvement of a rivet geometry for the self-piercing riveting of high-strength steel and multi-material joints, Prod. Eng. (2020). <https://doi.org/10.1007/s11740-020-00973-w>.
- [39] R. Haque, J.H. Beynon, Y. Durandet, Characterisation of force–displacement curve in self-pierce riveting, Sci. Technol. Weld. Join. 17:6 (2012) 476–488. <https://doi.org/10.1179/1362171812Y.0000000036>.
- [40] J.H. Deng, F. Lyu, R.M. Chen, Z.S. Fan, Influence of die geometry on self-piercing riveting of aluminum alloy AA6061-T6 to mild steel SPFC340 sheets, Adv. Manuf. 7 (2019) 209–220. <https://doi.org/10.1007/s40436-019-00250-9>.
- [41] Y. Liu, H. Li, H. Zhao, X. Liu, Effects of the die parameters on the self-piercing riveting process, Int. J. Adv. Manuf. Technol. 105 (2019) 1–16. <https://doi.org/10.1007/s00170-019-04567-4>.
- [42] M. Jäckel, T. Falk, D. Landgrebe, Concept for Further Development of Self-pierce Riveting by Using Cyber Physical Systems, Procedia CIRP. 44 (2016) 293–297. <https://doi.org/10.1016/J.PROCIR.2016.02.073>.
- [43] K. Mori, Y. Abe, T. Kato, Self-pierce riveting of multiple steel and aluminium alloy sheets, J. Mater. Process. Technol. 214 (2014) 2002–2008. <https://doi.org/10.1016/j.jmatprotec.2013.09.007>.
- [44] J. Mucha, A study of quality parameters and behaviour of self-piercing riveted aluminium sheets with different joining conditions, Stroj. Vestnik/Journal Mech. Eng. 57 (2011) 323–333. <https://doi.org/10.5545/sv-jme.2009.043>.

- [45] Y.W. Ma, M. Lou, Y.B. Li, Z.Q. Lin, Effect of rivet and die on self-piercing rivetability of AA6061-T6 and mild steel CR4 of different gauges, *J. Mater. Process. Technol.* 251 (2018) 282–294. <https://doi.org/10.1016/j.jmatprotec.2017.08.020>.
- [46] M. Jäckel, T. Grimm, R. Niegsch, W.-G. Drossel, Overview of current challenges in self-pierce riveting of lightweight materials, *Proceedings.* 2 (2018) 384. <https://doi.org/10.3390/icem18-05206>.
- [47] Y. Fang, L. Huang, Z. Zhan, S. Huang, W. Han, Effect analysis for the uncertain parameters on self-piercing riveting simulation model using machine learning model, *SAE Tech. Pap.* 2020-April (2020) 1–10. <https://doi.org/10.4271/2020-01-0219>.
- [48] T. Tassler, M. Israel, M.F. Goede, K. Dilger, K. Dröder, Robust joining point design for semi-tubular self-piercing rivets, *Int. J. Adv. Manuf. Technol.* 98 (2018) 431–440. <https://doi.org/10.1007/s00170-018-2238-9>.
- [49] H.Q. Ang, An overview of self-piercing riveting process with focus on joint failures, corrosion issues and optimisation techniques, *Chinese J. Mech. Eng.* 34 (2021) 1–25. <https://doi.org/10.1186/s10033-020-00526-3>.
- [50] X. Sun, Optimization of the strength of self-piercing rivets (SPRs), Woodhead Publishing Limited, 2014. <https://doi.org/10.1533/9780857098849.2.149>.
- [51] Y. Durandet, R. Deam, A. Beer, W. Song, S. Blacket, Laser assisted self-pierce riveting of AZ31 magnesium alloy strips, *Mater. Des.* 31 (2010) S13–S16. <https://doi.org/10.1016/j.matdes.2009.10.038>.
- [52] L. Ying, T. Gao, M. Dai, P. Hu, J. Dai, Towards joinability of thermal self-piercing riveting for AA7075-T6 aluminum alloy sheets under quasi-static loading conditions, *Int. J. Mech. Sci.* 189 (2021) 105978. <https://doi.org/10.1016/j.ijmecsci.2020.105978>.
- [53] J. Mucha, A study of quality parameters and behaviour of self-piercing riveted aluminium sheets with different joining conditions, *Stroj. Vestnik/Journal Mech. Eng.* 57 (2011) 323–333. <https://doi.org/10.5545/sv-jme.2009.043>.
- [54] D. Li, Influence of aluminium sheet surface modification on the self-piercing riveting process and the joint static lap shear strength, *Int. J. Adv. Manuf. Technol.* 93 (2017) 2685–2695. <https://doi.org/10.1007/s00170-017-0710-6>.
- [55] Y. Abe, T. Maeda, D. Yoshioka, K.I. Mori, Mechanical clinching and self-pierce riveting of thin three sheets of 5000 series aluminium alloy and 980 MPa grade cold rolled ultra-high strength steel, *Materials (Basel)*. 13 (2020) 1–22. <https://doi.org/10.3390/ma13214741>.

- [56] L. Han, A. Chrysanthou, Evaluation of quality and behaviour of self-piercing riveted aluminium to high strength low alloy sheets with different surface coatings, *Mater. Des.* 29 (2008) 458–468. <https://doi.org/10.1016/j.matdes.2006.12.020>.
- [57] J.F.C. Moraes, J.B. Jordon, X. Su, M.E. Barkey, C. Jiang, E. Ilieva, Effect of process deformation history on mechanical performance of AM60B to AA6082 self-pierce riveted joints, *Eng. Fract. Mech.* 209 (2019) 92–104. <https://doi.org/10.1016/j.engfracmech.2018.12.020>.
- [58] Y. Ma, S. Niu, H. Shan, Y. Li, N. Ma, Impact of stack orientation on self-piercing riveted and friction self-piercing riveted aluminum alloy and magnesium alloy joints, *Automot. Innov.* 3 (2020) 242–249. <https://doi.org/10.1007/s42154-020-00108-y>.
- [59] A.A. Luo, T.M. Lee, J.T. Carter, Self-pierce riveting of magnesium to aluminum alloys, *SAE Int. J. Mater. Manuf.* 4 (2011) 158–165. <https://doi.org/10.4271/2011-01-0074>.
- [60] G. Di Franco, L. Fratini, A. Pasta, V.F. Ruisi, On the self-piercing riveting of aluminium blanks and carbon fibre composite panels, *Int. J. Mater. Form.* 3 (2010) 1035–1038. <https://doi.org/10.1007/s12289-010-0947-1>.
- [61] M.A. Karim, J.H. Bae, D.H. Kam, C. Kim, W.H. Choi, Y. Do Park, Assessment of rivet coating corrosion effect on strength degradation of CFRP/aluminum self-piercing riveted joints, *Surf. Coatings Technol.* 393 (2020) 125726. <https://doi.org/10.1016/j.surfcoat.2020.125726>.
- [62] H.M. Rao, J. Kang, G. Huff, K. Avery, Impact of specimen configuration on fatigue properties of self-piercing riveted aluminum to carbon fiber reinforced polymer composite, *Int. J. Fatigue.* 113 (2018) 11–22. <https://doi.org/10.1016/j.ijfatigue.2018.03.031>.
- [63] G. Di Franco, L. Fratini, A. Pasta, Influence of the distance between rivets in self-piercing riveting bonded joints made of carbon fiber panels and AA2024 blanks, *Mater. Des.* 35 (2012) 342–349. <https://doi.org/10.1016/j.matdes.2011.09.036>.
- [64] L. Han, K.W. Young, A. Chrysanthou, J.M. O’Sullivan, The effect of pre-straining on the mechanical behaviour of self-piercing riveted aluminium alloy sheets, *Mater. Des.* 27 (2006) 1108–1113. <https://doi.org/10.1016/j.matdes.2005.04.002>.
- [65] L. Deng, M. Lou, Y. Li, B.E. Carlson, Thermally assisted self-piercing riveting of AA6061-T6 to ultrahigh strength steel, *J. Manuf. Sci. Eng. Trans. ASME.* 141 (2019). <https://doi.org/10.1115/1.4044255>.
- [66] M. Lou, Y. Li, Y. Li, G. Chen, Behavior and quality evaluation of electroplastic self-piercing riveting of aluminum alloy and advanced high strength steel, *J. Manuf. Sci. Eng. Trans. ASME.* 135 (2013). <https://doi.org/10.1115/1.4023256>.

- [67] Z. Du, L. Duan, L. Jing, A. Cheng, Z. He, Numerical simulation and parametric study on self-piercing riveting process of aluminium–steel hybrid sheets, *Thin-Walled Struct.* 164 (2021) 107872. <https://doi.org/10.1016/J.TWS.2021.107872>.
- [68] L. Zhao, X. He, B. Xing, Y. Lu, F. Gu, A. Ball, Influence of sheet thickness on fatigue behavior and fretting of self-piercing riveted joints in aluminum alloy 5052, *Mater. Des.* 87 (2015) 1010–1017. <https://doi.org/10.1016/J.MATDES.2015.08.121>.
- [69] R. Haque, Y. Durandet, Strength prediction of self-pierce riveted joint in cross-tension and lap-shear, *Mater. Des.* 108 (2016) 666–678. <https://doi.org/10.1016/j.matdes.2016.07.029>.
- [70] Z. Xie, W. Yan, C. Yu, T. Mu, L. Song, Improved shear strength design of cold-formed steel connection with single self-piercing rivet, *Thin-Walled Struct.* 131 (2018) 708–717. <https://doi.org/10.1016/j.tws.2018.03.025>.
- [71] Z. Xie, A. Zhang, W. Yan, Y. Zhang, T. Mu, C. Yu, Study on shear performance and calculation method for self-pierce riveted joints in galvanized steel sheet, *Thin-Walled Struct.* 161 (2021) 107490. <https://doi.org/10.1016/j.tws.2021.107490>.
- [72] L. Han, K.W. Young, R. Hewitt, M.R. Alkahari, A. Chrysanthou, Effect of sheet material coatings on quality and strength of self-piercing riveted joints, *SAE Tech. Pap.* (2006). <https://doi.org/10.4271/2006-01-0775>.
- [73] L. Han, A. Chrysanthou, J.M. O’Sullivan, Fretting behaviour of self-piercing riveted aluminium alloy joints under different interfacial conditions, *Mater. Des.* 27 (2006) 200–208. <https://doi.org/10.1016/j.matdes.2004.10.014>.
- [74] Henrob T-Rivet, (n.d.) 1–3. <https://www.atlascopco.com/content/dam/atlas-copco/industrial-technique/general/documents/brochures-leaflets/joining-solutions/t-rivet-pdf.pdf> (accessed September 12, 2021).
- [75] Y. Abe, T. Kato, K. Mori, Aluminium alloy self-pierce riveting for joining of aluminium alloy sheets, *Key Eng. Mater.* 410–411 (2009) 79–86. <https://doi.org/10.4028/www.scientific.net/KEM.410-411.79>.
- [76] B. Uhe, C.M. Kuball, M. Merklein, G. Meschut, Strength of self-piercing riveted joints with conventional rivets and rivets made of High Nitrogen Steel, in: *Esaform 2021*, 2021: pp. 1–8. <https://doi.org/10.25518/esaform21.1911>.
- [77] B. Uhe, C.M. Kuball, M. Merklein, G. Meschut, Self-piercing riveting using rivets made of stainless steel with high strain hardening, *Form. Futur.* (2021) 1495–1506. https://doi.org/10.1007/978-3-030-75381-8_124.

- [78] N.H. Hoang, O.S. Hopperstad, M. Langseth, I. Westermann, Failure of aluminium self-piercing rivets: An experimental and numerical study, *Mater. Des.* 49 (2013) 323–335. <https://doi.org/10.1016/J.MATDES.2013.01.034>.
- [79] M. Fu, P.K. Mallick, Effect of process variables on the static and fatigue properties of self-piercing riveted joints in aluminum alloy 5754, in: *SAE Tech. Pap.*, 2001. <https://doi.org/10.4271/2001-01-0825>.
- [80] Y. Chen, M. Li, X. Yang, W. Luo, Damage and failure characteristics of CFRP/aluminum single lap joints designed for lightweight applications, *Thin-Walled Struct.* 153 (2020) 106802. <https://doi.org/10.1016/j.tws.2020.106802>.
- [81] X. Jin, Y.B. Li, M. Lou, Y. Wang, Process optimization of self-piercing riveting aluminum to high strength steel using DOE method, *Chinese J. Automot. Eng.* 1 (2011) 185–191.
- [82] D. Li, L. Han, M. Shergold, M. Thornton, G. Williams, Influence of rivet tip geometry on the joint quality and mechanical strengths of self-piercing riveted aluminium joints, *Mater. Sci. Forum.* 765 (2013) 746–750. <https://doi.org/10.4028/www.scientific.net/MSF.765.746>.
- [83] H. Jiang, S. Gao, G. Li, J. Cui, Structural design of half hollow rivet for electromagnetic self-piercing riveting process of dissimilar materials, *Mater. Des.* 183 (2019) 108141. <https://doi.org/10.1016/j.matdes.2019.108141>.
- [84] M.A. Karim, T.E. Jeong, W. Noh, K.Y. Park, D.H. Kam, C. Kim, D.G. Nam, H. Jung, Y. Do Park, Joint quality of self-piercing riveting (SPR) and mechanical behavior under the frictional effect of various rivet coatings, *J. Manuf. Process.* 58 (2020) 466–477. <https://doi.org/10.1016/j.jmapro.2020.08.038>.
- [85] M. Esfahani, Y. Durandet, J. Wang, Y. Wong, Effect of joining process on the coatings of self-piercing rivets, *Adv. Mater. Res.* 488–489 (2012) 1501–1505. <https://doi.org/10.4028/www.scientific.net/AMR.488-489.1501>.
- [86] C. Kraus, T. Falk, R. Mauermann, W.G. Drossel, Development of a new self-flaring rivet geometry using finite element method and design of experiments, *Procedia Manuf.* 47 (2020) 383–388. <https://doi.org/10.1016/j.promfg.2020.04.295>.
- [87] Z. Huang, S. Xue, J. Lai, L. Xia, J. Zhan, Self-piercing riveting with inner flange pipe rivet, *Procedia Eng.* 81 (2014) 2042–2047. <https://doi.org/10.1016/j.proeng.2014.10.278>.
- [88] Z. Huang, Q. Yao, J. Lai, J. Zhao, Z. Jiang, Developing a self-piercing riveting with flange pipe rivet joining aluminum sheets, *Int. J. Adv. Manuf. Technol.* 91 (2017) 2315–2328. <https://doi.org/10.1007/s00170-016-9938-9>.

-
- [89] L.M. Alves, R.M. Afonso, P.A.F. Martins, Double-sided self-pierce riveting of polymer sheets, *J. Adv. Join. Process.* 3 (2021) 100051. <https://doi.org/10.1016/j.jajp.2021.100051>.
 - [90] L.M. Alves, R.M. Afonso, P.T. Pereira, P.A.F. Martins, Double-sided self-pierce riveting of dissimilar materials, *Int. J. Adv. Manuf. Technol.* 115 (2021) 3679–3687. <https://doi.org/10.1007/s00170-021-07426-3>.
 - [91] Z. Du, B. Wei, Z. He, A. Cheng, L. Duan, G. Zhang, Experimental and numerical investigations of aluminium–steel self-piercing riveted joints under quasi-static and dynamic loadings, *Thin-Walled Struct.* 169 (2021) 108277. <https://doi.org/10.1016/j.tws.2021.108277>.
 - [92] Z. Huang, Y. Jia, J. Lai, Fatigue characteristics and failure mechanism of self-piercing riveted joints of DP590 and AA6061 plates, in: *Miner. Met. Mater. Ser.*, Springer, Cham, 2021: pp. 1423–1436. https://doi.org/10.1007/978-3-030-75381-8_118.
 - [93] Z. Xie, W. Zhang, T. Chen, D. Zhou, L. Shi, Y. Tang, C. Yu, Comparative analysis and design method of shear strength for hybrid SPR-SDS joints in thin-walled steel structures, *Structures.* 33 (2021) 4313–4329. <https://doi.org/10.1016/J.ISTRUC.2021.07.003>.
 - [94] X. Zhang, X. He, B. Xing, W. Wei, J. Lu, Pre-holed self-piercing riveting of carbon fibre reinforced polymer laminates and commercially pure titanium sheets, *J. Mater. Process. Technol.* 279 (2020) 116550. <https://doi.org/10.1016/J.JMATPROTEC.2019.116550>.
 - [95] X. Zhang, X. He, F. Gu, A. Ball, Self-piercing riveting of aluminium–lithium alloy sheet materials, *J. Mater. Process. Technol.* 268 (2019) 192–200. <https://doi.org/10.1016/j.jmatprotec.2019.01.019>.
 - [96] X. He, Y. Wang, Y. Lu, K. Zeng, F. Gu, A. Ball, Self-piercing riveting of similar and dissimilar titanium sheet materials, *Int. J. Adv. Manuf. Technol.* 80 (2015) 2105–2115. <https://doi.org/10.1007/s00170-015-7174-3>.
 - [97] J. Zhang, S. Yang, Self-piercing riveting of aluminum alloy and thermoplastic composites, *J. Compos. Mater.* 49 (2015) 1493–1502. <https://doi.org/10.1177/0021998314535456>.
 - [98] D. Li, L. Han, Z. Lu, M. Thornton, M. Shergold, Influence of die profiles and cracks on joint buttons on the joint quality and mechanical strengths of high strength aluminium alloy joint, *Adv. Mater. Res.* 548 (2012) 398–405. <https://doi.org/10.4028/www.scientific.net/AMR.548.398>.

- [99] S.L. Han, Z.Y. Li, Y. Gao, Q.L. Zeng, Numerical study on die design parameters of self-pierce riveting process based on orthogonal test, *J. Shanghai Jiaotong Univ.* 19 (2014) 308–312. <https://doi.org/10.1007/s12204-014-1504-8>.
- [100] K. Mori, T. Kato, Y. Abe, Y. Ravshanbek, Plastic joining of ultra high strength steel and aluminium alloy sheets by self piercing rivet, *CIRP Ann. - Manuf. Technol.* 55 (2006) 283–286. [https://doi.org/10.1016/S0007-8506\(07\)60417-X](https://doi.org/10.1016/S0007-8506(07)60417-X).
- [101] Y. Ma, M. Lou, Y. Li, Z. Lin, Effect of rivet and die on self-piercing rivetability of AA6061-T6 and mild steel CR4 of different gauges, *J. Mater. Process. Technol.* 251 (2018) 282–294. <https://doi.org/10.1016/J.JMATPROTEC.2017.08.020>.
- [102] M. Lou, Y.B. Li, S.Y. Huang, G.L. Chen, Influence of die-rivet volume ratio on forming performance of self-piercing riveting joints of dissimilar materials, *China Mech. Eng.* 20 (2009) 1873–1876.
- [103] L. Han, A. Chrysanthou, K.W. Young, Mechanical behaviour of self-piercing riveted multi-layer joints under different specimen configurations, *Mater. Des.* 28 (2007) 2024–2033. <https://doi.org/10.1016/j.matdes.2006.06.015>.
- [104] D. Li, L. Han, M. Thornton, M. Shergold, Influence of rivet to sheet edge distance on fatigue strength of self-piercing riveted aluminium joints, *Mater. Sci. Eng. A.* 558 (2012) 242–252. <https://doi.org/10.1016/j.msea.2012.07.119>.
- [105] K.Y. Kim, J. Sim, N.E. Jannat, F. Ahmed, S. Ameri, Challenges in riveting quality prediction: A literature survey, *Procedia Manuf.* 38 (2019) 1143–1150. <https://doi.org/10.1016/j.promfg.2020.01.203>.
- [106] E. Atzeni, R. Ippolito, L. Settineri, Experimental and numerical appraisal of self-piercing riveting, *CIRP Ann. - Manuf. Technol.* 58 (2009) 17–20. <https://doi.org/10.1016/j.cirp.2009.03.081>.
- [107] X. He, B. Xing, K. Zeng, F. Gu, A. Ball, Numerical and experimental investigations of self-piercing riveting, *Int. J. Adv. Manuf. Technol.* 69 (2013) 715–721. <https://doi.org/10.1007/s00170-013-5072-0>.
- [108] N.H. Hoang, M. Langseth, R. Porcaro, A.G. Hanssen, The effect of the riveting process and aging on the mechanical behaviour of an aluminium self-piercing riveted connection, *Eur. J. Mech. A/Solids.* 30 (2011) 619–630. <https://doi.org/10.1016/j.euromechsol.2011.02.006>.
- [109] S.G. Qu, W.J. Deng, Finite element simulation of the self-piercing riveting process, *ASME Int. Mech. Eng. Congr. Expo. Proc.* 4 (2009) 243–249. <https://doi.org/10.1115/IMECE2008-67017>.

-
- [110] R. Cacko, P. Czyzewski, C.P. Cacko R., Verification of numerical modelling of the SPR joint by experimental stack-up, *Comput. Methods Mater. Sci.* 7 (2007) 124–129.
- [111] G. Testa, N. Bonora, G. Iannitti, A. Ruggiero, D. Gentile, Numerical simulation of self-piercing riveting process (SRP) using continuum damage mechanics modelling, *Frat. Ed Integrita Strutt.* 12 (2018) 161–172. <https://doi.org/10.3221/IGF-ESIS.44.13>.
- [112] P.O. Bouchard, T. Laurent, L. Tollier, Numerical modeling of self-pierce riveting-From riveting process modeling down to structural analysis, *J. Mater. Process. Technol.* 202 (2008) 290–300. <https://doi.org/10.1016/j.jmatprotec.2007.08.077>.
- [113] M. Carandente, R.J. Dashwood, I.G. Masters, L. Han, Improvements in numerical simulation of the SPR process using a thermo-mechanical finite element analysis, *J. Mater. Process. Technol.* 236 (2016) 148–161. <https://doi.org/10.1016/J.JMATPROTEC.2016.05.001>.
- [114] F. Hönsch, J. Domitner, C. Sommitsch, B. Götzinger, M. Kölz, Numerical simulation and experimental validation of self-piercing riveting (SPR) of 6xxx aluminium alloys for automotive applications, *J. Phys. Conf. Ser.* 1063 (2018) 012081. <https://doi.org/10.1088/1742-6596/1063/1/012081>.
- [115] L. Huang, J.F.C. Moraes, D.G. Sediako, J.B. Jordon, H. Guo, X. Su, Finite-element and residual stress analysis of self-pierce riveting in dissimilar metal sheets, *J. Manuf. Sci. Eng. Trans. ASME.* 139 (2017) 021007. <https://doi.org/10.1115/1.4034437>.
- [116] E. Atzeni, R. Ippolito, L. Settineri, FEM modeling of self-piercing riveted joint, *Key Eng. Mater.* 344 (2007) 655–662. <https://doi.org/10.4028/www.scientific.net/kem.344.655>.
- [117] L. Huang, J. V. Lasecki, H. Guo, X. Su, Finite element modeling of dissimilar metal self-piercing riveting process, *SAE Int. J. Mater. Manuf.* 7 (2014) 2014-01–1982. <https://doi.org/10.4271/2014-01-1982>.
- [118] R. Porcaro, A.G. Hanssen, A. Aalberg, M. Langseth, Joining of aluminium using self-piercing riveting: Testing, modelling and analysis, *Int. J. Crashworthiness.* 9 (2004) 141–154. <https://doi.org/10.1533/ijcr.2004.0279>.
- [119] G. Testa, A. Ruggiero, G. Iannitti, N. Bonora, D. Gentile, Modification of the bonora damage model for shear failure, *Frat. Ed Integrita Strutt.* 12 (2018) 140–150. <https://doi.org/10.3221/IGF-ESIS.44.11>.
- [120] S. Fayolle, P.O. Bouchard, K. Mocellin, Joining and mechanical strength of self-piercing riveted structure - numerical modeling and experimental validation, *Exp. Anal. Nano Eng. Mater. Struct.* (2007) 813–814. https://doi.org/10.1007/978-1-4020-6239-1_404.

-
- [121] S. Fayolle, P.O. Bouchard, K. Mocellin, Modelling the strength of self-piercing riveted joints, Woodhead Publishing Limited, 2014. <https://doi.org/10.1533/9780857098849.1.79>.
- [122] N. Bonora, G. Iannitti, G. Testa, A. Ruggiero, Damage mechanics modelling of material separation in self- pierce riveting (SPR) process, J. Phys. Conf. Ser. 1063 (2018). <https://doi.org/10.1088/1742-6596/1063/1/012153>.
- [123] S. Wituschek, C.M. Kuball, M. Merklein, M. Lechner, Test method for friction characterization of rivets, Defect Diffus. Forum. 404 (2020) 132–137. <https://doi.org/10.4028/www.scientific.net/DDF.404.132>.
- [124] S.L. Han, X.D. Tang, Y. Gao, Q.L. Zeng, Effects of friction factors on flat bottom self-pierce riveting joints of AZ31 magnesium alloy, Mater. Res. Innov. 19 (2015) S10-235–238. <https://doi.org/10.1179/1432891715Z.0000000002155>.
- [125] R. Porcaro, A.G. Hanssen, M. Langseth, A. Aalberg, Self-piercing riveting process: An experimental and numerical investigation, J. Mater. Process. Technol. 171 (2006) 10–20. <https://doi.org/10.1016/j.jmatprotec.2005.05.048>.
- [126] J.F.C. Moraes, J.B. Jordon, E.I. Ilieva, Influence of the friction coefficient in self-pierce riveting simulations: a statistical analysis, SAE Int. J. Mater. Manuf. 11 (2018) 123–130. <https://doi.org/10.4271/05-11-02-0013>.
- [127] R. Cacko, Review of different material separation criteria in numerical modeling of the self-piercing riveting process - SPR, Arch. Civ. Mech. Eng. 8 (2008) 21–30. [https://doi.org/10.1016/S1644-9665\(12\)60190-3](https://doi.org/10.1016/S1644-9665(12)60190-3).
- [128] A. Pirondi, F. Moroni, Clinch-bonded and rivet-bonded hybrid joints: Application of damage models for simulation of forming and failure, J. Adhes. Sci. Technol. 23 (2009) 1547–1574. <https://doi.org/10.1163/156856109X433063>.
- [129] R. Porcaro, M. Langseth, A.G. Hanssen, H. Zhao, S. Weyer, H. Hooputra, Crashworthiness of self-piercing riveted connections, Int. J. Impact Eng. 35 (2008) 1251–1266. <https://doi.org/10.1016/j.ijimpeng.2007.07.008>.
- [130] T. Sadowski, P. Golewski, M. Kneć, Experimental investigation and numerical modelling of spot welding–adhesive joints response, Compos. Struct. 112 (2014) 66–77. <https://doi.org/10.1016/J.COMPSTRUCT.2014.01.008>.
- [131] G. Casalino, A. Rotondo, A. Ludovico, On the numerical modelling of the multiphysics self piercing riveting process based on the finite element technique, Adv. Eng. Softw. 39 (2008) 787–795. <https://doi.org/10.1016/j.advengsoft.2007.12.002>.

-
- [132] S. Ishikawa, H. Aihara, Modelling of self-piercing riveting with ALE, CEL and SPH based on abaqus/explicit, in: Proc. 14th Int. Conf. Comput. Plast. - Fundam. Appl. COMPLAS 2017, 2017: pp. 682–691.
- [133] L. Huang, Y. Wu, G. Huff, S. Huang, A. Ilinich, A. Freis, G. Luckey, Self-piercing rivet insertion using smoothed particle galerkin method, in: 15th Int. LS-DYNA User Conf., 2018: pp. 1–11.
- [134] J. Mucha, Analysis of stress distribution in the die during the self-piercing riveting process, *Adv. Manuf. Sci. Technol.* 40 (2016) 43–54. <https://doi.org/10.2478/amst-2016-0021>.
- [135] Y.H. Zhang, B.J. Shi, J.B. Zhong, Multi-parameter joint optimization of self-piercing riveting on aluminum alloy plate, in: *J. Phys. Conf. Ser.*, 2020. <https://doi.org/10.1088/1742-6596/1605/1/012093>.
- [136] X. Sun, M.A. Khaleel, Performance optimization of self-piercing rivets through analytical rivet strength estimation, *J. Manuf. Process.* 7 (2005) 83–93. [https://doi.org/10.1016/S1526-6125\(05\)70085-2](https://doi.org/10.1016/S1526-6125(05)70085-2).
- [137] R. Haque, N.S. Williams, S.E. Blacket, Y. Durandet, A simple but effective model for characterizing SPR joints in steel sheet, *J. Mater. Process. Technol.* 223 (2015) 225–231. <https://doi.org/10.1016/j.jmatprotec.2015.04.006>.
- [138] W. Yan, Z. Xie, C. Yu, L. Song, H. He, Experimental investigation and design method for the shear strength of self-piercing rivet connections in thin-walled steel structures, *J. Constr. Steel Res.* 133 (2017) 231–240. <https://doi.org/10.1016/j.jcsr.2017.02.022>.
- [139] M. Paliwal, U.A. Kumar, Neural networks and statistical techniques: A review of applications, *Expert Syst. Appl.* 36 (2009) 2–17. <https://doi.org/10.1016/j.eswa.2007.10.005>.
- [140] F. Lambiase, V. Grossi, A. Paoletti, Machine learning applied for process design of hybrid metal-polymer joints, *J. Manuf. Process.* 58 (2020) 92–100. <https://doi.org/10.1016/J.JMAPRO.2020.08.016>.
- [141] A. Sedki, D. Ouazar, E. El Mazoudi, Evolving neural network using real coded genetic algorithm for daily rainfall-runoff forecasting, *Expert Syst. Appl.* 36 (2009) 4523–4527. <https://doi.org/10.1016/j.eswa.2008.05.024>.
- [142] D. Katherasan, J. V. Elias, P. Sathiya, A.N. Haq, Simulation and parameter optimization of flux cored arc welding using artificial neural network and particle swarm optimization algorithm, *J. Intell. Manuf.* 25 (2014) 67–76. <https://doi.org/10.1007/s10845-012-0675-0>.

-
- [143] C. Chen, S. Zhao, X. Han, M. Cui, S. Fan, Optimization of a reshaping rivet to reduce the protrusion height and increase the strength of clinched joints, *J. Mater. Process. Technol.* 234 (2016) 1–9. <https://doi.org/10.1016/j.jmatprotec.2016.03.006>.
- [144] L. Jiang, L. Huang, X. Wang, Z. Zhan, S. Huang, G. Huff, A. Freis, A crack detection method for self-piercing riveting button images through machine learning, *SAE Tech. Pap.* 2020-April (2020) 1–8. <https://doi.org/10.4271/2020-01-0221>.
- [145] D. Mylavarapu, R. Ganesh Narayanan, M. Das, Temperature prediction during self-pierce riveting of sheets by FEA-ANN hybrid model, Springer Singapore, 2019. https://doi.org/10.1007/978-981-32-9072-3_24.
- [146] M. Jäckel, T. Falk, J. Georgi, W.G. Drossel, Gathering of process data through numerical simulation for the application of machine learning prognosis algorithms, *Procedia Manuf.* 47 (2020) 608–614. <https://doi.org/10.1016/j.promfg.2020.04.186>.
- [147] T. Udayakumar, K. Raja, T.M. Afsal Husain, P. Sathiya, Prediction and optimization of friction welding parameters for super duplex stainless steel (UNS S32760) joints, *Mater. Des.* 53 (2014) 226–235. <https://doi.org/10.1016/j.matdes.2013.07.002>.
- [148] B. Zhang, X. Chen, K. Pan, J. Wang, Multi-objective optimization of friction stir spot-welded parameters on aluminum alloy sheets based on automotive joint loads, *Metals (Basel)*. 9 (2019) 520. <https://doi.org/10.3390/met9050520>.
- [149] Y.W. Park, S. Rhee, Process modeling and parameter optimization using neural network and genetic algorithms for aluminum laser welding automation, *Int. J. Adv. Manuf. Technol.* 37 (2008) 1014–1021. <https://doi.org/10.1007/s00170-007-1039-3>.
- [150] D.S. Nagesh, G.L. Datta, Genetic algorithm for optimization of welding variables for height to width ratio and application of ANN for prediction of bead geometry for TIG welding process, *Appl. Soft Comput. J.* 10 (2010) 897–907. <https://doi.org/10.1016/j.asoc.2009.10.007>.
- [151] U. Zuperl, F. Cus, Optimization of cutting conditions during cutting by using neural networks, *Robot. Comput. Integr. Manuf.* 19 (2003) 189–199. [https://doi.org/10.1016/S0736-5845\(02\)00079-0](https://doi.org/10.1016/S0736-5845(02)00079-0).
- [152] E. Atzeni, R. Ippolito, L. Settineri, FEM modeling of self-piercing riveted joint, *Key Eng. Mater.* 344 (2007) 655–662. <https://doi.org/10.4028/www.scientific.net/kem.344.655>.
- [153] M. Carandente, FE simulation of the SPR process to predict joint characteristics: innovation report, University of Warwick, 2016.

- [154] D. Li, L. Han, M. Thornton, M. Shergold, Influence of edge distance on quality and static behaviour of self-piercing riveted aluminium joints, *Mater. Des.* 34 (2012) 22–31. <https://doi.org/10.1016/j.matdes.2011.07.046>.
- [155] R. Haque, Y. Durandet, Investigation of self-pierce riveting (SPR) process data and specific joining events, *J. Manuf. Process.* 30 (2017) 148–160. <https://doi.org/10.1016/j.jmapro.2017.09.018>.
- [156] R.K. Bhushan, Optimization of cutting parameters for minimizing power consumption and maximizing tool life during machining of Al alloy SiC particle composites, *J. Clean. Prod.* 39 (2013) 242–254. <https://doi.org/10.1016/j.jclepro.2012.08.008>.
- [157] B. Singh, N. Ahuja, Development of controlled-release buccoadhesive hydrophilic matrices of Diltiazem hydrochloride: Optimization of bioadhesion, dissolution, and diffusion parameters, *Drug Dev. Ind. Pharm.* 28 (2002) 431–442. <https://doi.org/10.1081/DDC-120003004>.
- [158] E.M. Anawa, A.G. Olabi, Using Taguchi method to optimize welding pool of dissimilar laser-welded components, *Opt. Laser Technol.* 40 (2008) 379–388. <https://doi.org/10.1016/j.optlastec.2007.07.001>.
- [159] C. Bitondo, U. Prisco, A. Squilace, P. Buonadonna, G. Dionoro, Friction-stir welding of AA 2198 butt joints: Mechanical characterization of the process and of the welds through DOE analysis, *Int. J. Adv. Manuf. Technol.* 53 (2011) 505–516. <https://doi.org/10.1007/s00170-010-2879-9>.
- [160] D. Zhao, Y. Wang, D. Liang, P. Zhang, Modeling and process analysis of resistance spot welded DP600 joints based on regression analysis, *Mater. Des.* 110 (2016) 676–684. <https://doi.org/10.1016/j.matdes.2016.08.038>.
- [161] M. Paliwal, U.A. Kumar, Neural networks and statistical techniques: A review of applications, *Expert Syst. Appl.* 36 (2009) 2–17. <https://doi.org/10.1016/j.eswa.2007.10.005>.
- [162] A.M. Khorasani, I. Gibson, A.H. Ghasemi, A. Ghaderi, Modelling of laser powder bed fusion process and analysing the effective parameters on surface characteristics of Ti-6Al-4V, *Int. J. Mech. Sci.* 168 (2020) 105299. <https://doi.org/10.1016/j.ijmecsci.2019.105299>.
- [163] H. Wang, Z. Zhang, L. Liu, Prediction and fitting of weld morphology of Al alloy-CFRP welding-rivet hybrid bonding joint based on GA-BP neural network, *J. Manuf. Process.* 63 (2021) 109–120. <https://doi.org/10.1016/j.jmapro.2020.04.010>.
- [164] J. Liu, Z. Zhao, Y. Bi, H. Dong, Prediction and compensation of force-induced deformation for a dual-machine-based riveting system using FEM and neural network,

- Int. J. Adv. Manuf. Technol. 103 (2019) 3853–3870. <https://doi.org/10.1007/s00170-019-03826-8>.
- [165] S. Katoch, S.S. Chauhan, V. Kumar, A review on genetic algorithm: past, present, and future, *Multimed. Tools Appl.* 80 (2021) 8091–8126. <https://doi.org/10.1007/s11042-020-10139-6>.
- [166] Y. Wang, J. Yu, Y. Song, F. Chen, Parameter optimization of the composite honeycomb tip in a turbine cascade, *Energy*. 197 (2020) 117236. <https://doi.org/10.1016/j.energy.2020.117236>.
- [167] B. Xu, H. Zhang, Z. Wang, H. Wang, Y. Zhang, Model and algorithm of BP neural network based on expanded multichain quantum optimization, *Math. Probl. Eng.* 2015 (2015). <https://doi.org/10.1155/2015/362150>.
- [168] J.D. Olden, D.A. Jackson, A comparison of statistical approaches for modelling fish species distributions, *Freshw. Biol.* 47 (2002) 1976–1995. <https://doi.org/10.1046/j.1365-2427.2002.00945.x>.
- [169] K. Deb, Multi-objective optimisation using evolutionary algorithms: An introduction, in: *Multi-Objective Evol. Optim. Prod. Des. Manuf.*, Springer, London, 2011: pp. 3–34. https://doi.org/10.1007/978-0-85729-652-8_1.
- [170] Y. Lecun, Y. Bengio, G. Hinton, Deep learning, *Nature*. 521 (2015) 436–444. <https://doi.org/10.1038/nature14539>.
- [171] W. Samek, A. Binder, G. Montavon, S. Lapuschkin, K.R. Müller, Evaluating the visualization of what a deep neural network has learned, *IEEE Trans. Neural Networks Learn. Syst.* 28 (2017) 2660–2673. <https://doi.org/10.1109/TNNLS.2016.2599820>.
- [172] S. Feng, H. Zhou, H. Dong, Using deep neural network with small dataset to predict material defects, *Mater. Des.* 162 (2019) 300–310. <https://doi.org/10.1016/j.matdes.2018.11.060>.
- [173] Q. Xie, M. Suvarna, J. Li, X. Zhu, J. Cai, X. Wang, Online prediction of mechanical properties of hot rolled steel plate using machine learning, *Mater. Des.* 197 (2021) 109201. <https://doi.org/10.1016/j.matdes.2020.109201>.
- [174] J.D. Olden, M.K. Joy, R.G. Death, An accurate comparison of methods for quantifying variable importance in artificial neural networks using simulated data, *Ecol. Modell.* 178 (2004) 389–397. <https://doi.org/10.1016/j.ecolmodel.2004.03.013>.
- [175] Y. Cai, W. Zheng, X. Zhang, L. Zhangzhong, X. Xue, Research on soil moisture prediction model based on deep learning, *PLoS One*. 14 (2019) 1–19. <https://doi.org/10.1371/journal.pone.0214508>.

- [176] X. Li, L. Peng, Y. Hu, J. Shao, T. Chi, Deep learning architecture for air quality predictions, *Environ. Sci. Pollut. Res.* 23 (2016) 22408–22417. <https://doi.org/10.1007/s11356-016-7812-9>.
- [177] Y. Bengio, P. Lamblin, D. Popovici, H. Larochelle, Greedy layer-wise training of deep networks, in: *Adv. Neural Inf. Process. Syst.*, 2007: pp. 153–160. <https://doi.org/10.7551/mitpress/7503.003.0024>.
- [178] G.E. Hinton, R.R. Salakhutdinov, Reducing the dimensionality of data with neural networks, *Science* (80-.). 313 (2006) 504–507. <https://doi.org/10.1126/science.1127647>.
- [179] A. Seifi, M. Dehghani, V.P. Singh, Uncertainty analysis of water quality index (WQI) for groundwater quality evaluation: Application of Monte-Carlo method for weight allocation, *Ecol. Indic.* 117 (2020) 106653. <https://doi.org/10.1016/j.ecolind.2020.106653>.
- [180] EN485-4:1993, Aluminium and aluminium alloys - Sheet, strip and plate - Part 4: Tolerances on shape and dimensions for cold-rolled products, 1993.
- [181] C.M. Tamasco, M. Rais-Rohani, A. Buijk, Coupled finite element simulation and optimization of single- and multi-stage sheet-forming processes, *Eng. Optim.* 45 (2013) 357–373. <https://doi.org/10.1080/0305215X.2012.675062>.